

# **Spatial Distortion in MRI with Application to Stereotactic Neurosurgery**

Paul S. Morgan

May 1999

Submitted for the degree of Doctor of Philosophy

The University of Nottingham

# Contents

<b>1</b>	<b>Introduction</b>	<b>1</b>
<b>2</b>	<b>An Introduction to Nuclear Magnetic Resonance Imaging</b>	<b>5</b>
2.1	Introduction . . . . .	5
2.2	Fundamentals of NMR . . . . .	6
2.2.1	Spin-lattice and Spin-spin Relaxation . . . . .	9
2.2.2	NMR signal . . . . .	13
2.2.3	Chemical Shift . . . . .	15
2.2.4	Pulse Sequences . . . . .	16
2.3	NMR Imaging Techniques . . . . .	23
2.3.1	Spatial Encoding . . . . .	23
2.3.2	Two Dimensional Fourier Techniques and $k$ Space . . . . .	27
2.3.3	Rapid MRI with Multiple Echoes . . . . .	37
2.4	MR Imaging Considerations . . . . .	44
2.4.1	Digital Fourier Transform and Aliasing . . . . .	44
2.4.2	Bandwidth . . . . .	46
2.4.3	Flow Effects . . . . .	47
2.5	Instrumentation for MRI . . . . .	50
2.5.1	Main Magnetic Field . . . . .	50
2.5.2	Magnetic Gradients . . . . .	51
2.5.3	RF System . . . . .	53
2.5.4	Control System . . . . .	54
2.5.5	MRI Systems . . . . .	55
2.6	Safety . . . . .	55
2.6.1	Static Main Magnetic Field . . . . .	55
2.6.2	Time Varying Magnetic Field . . . . .	56
2.6.3	RF Electromagnetic Field . . . . .	56
2.6.4	Other Risks . . . . .	57
<b>3</b>	<b>Neurosurgical Stereotactic Techniques</b>	<b>58</b>
3.1	Origins of Neurology and Neurosurgery . . . . .	58
3.2	Stereotaxis . . . . .	59
3.3	Radiotherapy and Radiosurgery . . . . .	63
3.4	The BRW and CRW Stereotactic Systems . . . . .	67
3.5	Application of MRI to the BRW System . . . . .	72

## CONTENTS

---

3.6	Discussion of Advantages and Disadvantages of Using MRI for Stereotactic Treatment Planning . . . . .	74
3.7	Conclusion . . . . .	77
<b>4</b>	<b>Spatial Distortion in MRI</b>	<b>79</b>
4.1	Introduction . . . . .	79
4.2	Sources and Description of Spatial Distortion in MRI . . . . .	80
4.2.1	Spatial Distortion in Spin Warp Acquisitions . . . . .	81
4.2.2	Spatial Distortion in EPI Acquisitions . . . . .	85
4.3	Methods for the Correction of Spatial Distortion . . . . .	89
4.3.1	Phase Map Correction Method . . . . .	90
4.3.2	Reversed Gradient Correction Method . . . . .	95
4.3.3	Implementation of Reversed Gradient Correction Method . . . . .	99
4.3.4	Results and Discussion of Reversed Gradient Correction Method (single slice) . . . . .	105
4.3.5	Results and Discussion of Reversed Gradient Correction Method (volume) . . . . .	108
4.3.6	Validity of Reversed Gradient Correction Method . . . . .	111
4.4	Comparison of Correction Methods . . . . .	112
4.4.1	Method for Comparison . . . . .	112
4.4.2	Results and Discussion of Comparison . . . . .	114
4.5	Distortion Caused by Stereotactic Apparatus . . . . .	118
4.6	Applications of Distortion Correction to Contemporary EPI Techniques . . . . .	121
4.6.1	ADC Maps . . . . .	121
4.6.2	BOLD Functional Imaging . . . . .	126
4.7	Modifications to Chang & Fitzpatrick's Correction Method . . . . .	131
4.7.1	New Volume Correction Method One . . . . .	132
4.7.2	New Volume Correction Method Two . . . . .	134
4.8	Conclusions . . . . .	138
<b>5</b>	<b>Quantification of Errors in Stereotaxis</b>	<b>141</b>
5.1	Introduction . . . . .	141
5.2	Direct Phantom Measurements . . . . .	144
5.2.1	Materials and Method . . . . .	145
5.2.2	Theory and Implementation . . . . .	149
5.2.3	Results and Discussion . . . . .	154
5.3	Comparison of MR Sequences and Scanners . . . . .	155
5.3.1	Method . . . . .	156
5.3.2	Results from Bandwidth Comparison and Discussion . . . . .	158
5.3.3	Results from Scanner Comparison and Discussion . . . . .	159
5.3.4	Results from Sequence Comparison and Discussion . . . . .	160
5.4	Application of Distortion Correction to Stereotaxis . . . . .	162
5.4.1	Method . . . . .	162
5.4.2	Results from Phantom and Discussion . . . . .	163

## CONTENTS

---

5.4.3	Results from Patient and Discussion . . . . .	165
5.5	Determination of Sources of Distortion . . . . .	167
5.5.1	Method . . . . .	167
5.5.2	Results from Tufnol Base Plate and Discussion . . . . .	169
5.5.3	Results from Phantom Translation and Discussion . . . . .	169
5.5.4	Results from Interchanging Frequency and Phase Encoded Axes and Discussion . . . . .	170
5.5.5	Results from Apparatus Reassembly and Discussion . . . . .	172
5.5.6	Discussion of Sources of Distortion . . . . .	172
5.6	Conclusions . . . . .	174
<b>6</b>	<b>Propagation of Errors in Stereotaxis</b>	<b>176</b>
6.1	Introduction . . . . .	176
6.2	Estimation of Fiducial Localization Error . . . . .	184
6.3	TRE due to FLE and TLE in MRI . . . . .	188
6.3.1	TLE and FLE in MR Images from Reversed Gradient Cor- rection . . . . .	189
6.3.2	Calculation of STM's and TRE's . . . . .	193
6.4	Discussion and Conclusions . . . . .	199
<b>7</b>	<b>Conclusion</b>	<b>203</b>

## **Abstract**

The aim of this work was to implement a thorough method for quantifying the errors introduced to frame-based neurosurgical stereotactic procedures by the use of MRI. Chang & Fitzpatrick's reversed gradient distortion correction method was used, in combination with a phantom, to measure these errors. Spatial distortion in MR images of between 1 mm and 2 mm was measured. Further analysis showed that this typically introduced an additional error in the coordinate of the actual treatment point of 0.7 mm. The implications of this are discussed.

The main source of distortion in the MR images used for stereotaxis was found to be the head ring. A comparison between imaging sequences and MR scanners revealed that the spatial distortion depends mainly on the bandwidth per pixel of the sequence rather than other differences in the imaging sequences.

By comparison with a phase map distortion correction technique, the imaging parameters required to allow successful distortion correction with the reversed gradient method were identified. The most important was the use of full Fourier spin echo acquisitions.

The reversed gradient correction method was applied to two contemporary EPI techniques. Considerable improvement was seen in the production of ADC maps after the images had been corrected for distortion. The method also was shown to be valid in application to BOLD fMRI data.

# Chapter 1

## Introduction

The field of Magnetic Resonance Imaging (MRI) has experienced rapid growth in the 25 years since its foundation. In particular, its application as a tool for medical imaging has led to many advances in the understanding and diagnosis of disease processes. Its unique view of the living human body, both anatomically and physiologically, has allowed new insights and helped to forge a new relationship between men and women and their bodies.

The range of medical disciplines which benefit from the extra information contained within a MR image is wide and expanding. However great the potential gain from applying MRI to a particular field, it is still vital that its use is validated. The role of physics research within the field of MRI is not just limited to the physics of the production of MR images or various MRI techniques, but also to the use of that knowledge and understanding to study the suitability and validity of new applications.

One of the first regions of the body to be imaged with MRI, and for which MRI remains a *primary diagnostic tool*, is the brain. The high spatial resolution and excellent contrast between different tissues, allows MRI to provide localized diagnostic anatomical information unavailable from other imaging modalities. In the same imaging session, MRI can also provide a plethora of physiological information, covering blood flow, brain function, and relative chemical content, as well as information directly related to the fundamental physical parameters involved in MRI. The basic physical principles of MRI are described in Chapter 2.

The information available in neurological MR images is of direct interest to neurosurgeons, among others. Imaging of the brain plays an important role

## 1. Introduction

---

in planning a neurosurgical procedure. The more precisely the location and dimensions of the surgical target is known, the less invasive the surgery can be. A number of systems have been developed for reproducibly and accurately physically locating a three dimensional point within the human brain. This is known as stereotaxis. If the target can be visualized using a medical imaging technique, the target position may be transferred from the images onto the stereotactic system and used to guide the neurosurgeon during surgery. Surgery may take the form of an invasive operation, or the concentrated delivery of high energy x-rays from an external source to sterilize the target. Traditionally, stereotactic procedures have been planned using x-ray imaging modalities. It would be desirable to use MRI in this process. Further details of performing stereotactic procedures planned from medical images are given in Chapter 3.

However, the use of MRI in the planning of stereotactic procedures is not without its problems. Conventional stereotactic systems using x-ray images usually require apparatus to be attached to the patient for the duration of the imaging session. MRI is sensitive to metallic objects placed close to the region being imaged. Therefore, modified apparatus is required. Furthermore, MR images usually exhibit some degree of spatial shift at various points throughout the image. This results in images which may be distorted and spatially incorrect. While this is not usually a problem in images to be interpreted diagnostically, it may result in an incorrect target being calculated in a stereotactic procedure planned from MR images.

The aim of this thesis is twofold. Firstly, to implement methods to quantify the amount of spatial distortion present in MRI and if possible correct it. This may then be applied to MR images acquired especially for planning stereotactic neurosurgery. Any errors introduced by the spatial distortion in the MR images can be measured and their effect discussed. MRI has been used for stereotactic planning in a few centres throughout this decade, and the effect of spatial distortion has been studied previously. However, it is felt that much of this previous work either has considered the errors from spatial distortion in isolation, has not measured the distortion using representative apparatus, has not considered the effects of different MRI acquisition schemes or MR scanners, and has not con-

## 1. Introduction

---

sidered the source of spatial distortion. These points are addressed in this thesis hopefully forming a more coherent analysis. The work is outlined below.

Sources of spatial distortion in MRI are outlined in Chapter 4. A method proposed by Chang & Fitzpatrick<sup>17</sup> for correcting spatial distortion (the reversed gradient correction method) is implemented. This method can be used to quantify the amount of distortion present, as well as to produce corrected images. In this work it is used to measure the amount of distortion caused by various items of MRI compatible stereotactic apparatus so as to assess their individual contribution to spatial distortion.

Spatial distortion is present in all MR images and may cause various problems depending on the subsequent use of the images. Distortion is usually worse in Echo Planar Imaging (EPI) acquisitions<sup>101</sup> and often causes problems when these images undergo further processing. Two contemporary fields where this is the case are the *measurement of the diffusion of water within the brain*,<sup>58</sup> and the detection of localized brain activation by a technique called BOLD functional MRI (fMRI).<sup>56</sup> As well as applying the distortion correction method to MR images for use with stereotaxis, it was also applied to correct EP images acquired for these two purposes. This is reported in Chapter 4.

A number of methods are available to correct spatial distortion in MRI. Chapter 4 also briefly describes a comparison performed between the reversed gradient correction method and a phase map correction method. As well as comparing correction of real MR images, a computer simulation of a MRI acquisition was implemented in order to individually vary various parameters. This allowed the imaging parameters required for optimal correction to be determined, as well as the limitations of both methods to be appreciated.

Finally, Chapter 4 describes two modifications to the reversed gradient distortion correction method which theoretically appear to improve the correction of distortion present in a volumetric MRI acquisition.

In order to aid the measurement of distortion present in MR images used for stereotaxis, a mock stereotactic set-up was constructed for MR imaging. This involved a plastic 'phantom' head surrounded by the MR compatible stereotactic apparatus. The actual dimensions of the phantom were determined by imaging

## 1. Introduction

---

it with x-rays. This allows the spatial distortion in MR images to be measured by two independent methods: by direct comparison with the actual dimensions of the phantom, and by applying the reversed gradient correction method. This is reported in Chapter 5. With a relationship established between distortion from direct phantom measurements and from the reversed gradient distortion correction method, the distortion within a patient's brain could be estimated. A small number of patients undergoing stereotactic procedures were imaged using MRI as well as x-ray techniques. The reversed gradient correction method could be used to quantify the distortion present in the patient's brain compared to the phantom.

MR images may be acquired using a wide range of contrast mechanisms. In identifying a particular target in the brain, one contrast mechanism may be preferable. A comparison is performed using the stereotactic phantom in order to assess whether the amount of spatial distortion varies with MR imaging sequence, and the results presented in Chapter 5. It also was possible to repeat the same comparison using a different MRI scanner with the same magnetic field strength. The comparison between sequences and between scanners not only verified the validity of their use, but also help to identify the sources which cause the spatial distortion.

With methods for measuring spatial distortion in MR images used for stereotaxis established, Chapter 6 considers the effect of these errors on the final stereotactic treatment coordinate. It is this final error which is needed to convince neurosurgeons of the validity in using MRI.

This thesis presents a thorough method for measuring the spatial distortion in MR images used for the planning of frame-based stereotactic procedures and the effect of that distortion on the final treatment coordinate. It also was possible to apply the methods used to study the validity of the reversed gradient correction method and to apply it to correct distortion in contemporary EPI techniques.

# Chapter 2

## An Introduction to Nuclear Magnetic Resonance Imaging

### 2.1 Introduction

The phenomenon of Nuclear Magnetic Resonance (NMR) was first reported in 1946 by Bloch *et al.*<sup>6</sup> and Purcell *et al.*<sup>93</sup> Two discoveries in 1950, that of the spin echo by Hahn,<sup>33</sup> and the chemical shift by Dickinson<sup>25</sup> and Procter & Yu,<sup>92</sup> allowed NMR to be used as a high resolution non-destructive spectroscopic technique. In 1971, Damadian<sup>23</sup> reported that a parameter measurable by NMR ( $T_1$  recovery) may have a larger value for cancerous tissue than for healthy tissue *in vitro*. This led to an interest in applying NMR to medical diagnosis. As the impact of x-ray Computed Tomography (CT) imaging was beginning to be felt in the medical world, in 1973 methods for spatially localising NMR signals were proposed (independently by Lauterbur<sup>57</sup> and Mansfield & Grannell<sup>66</sup>). This quickly led to the ability to produce two dimensional NMR images of a sample. While these were small at first, as the technology of producing strong uniform magnetic fields improved, samples of up to nearly one metre in diameter could be imaged. By 1980, with the advent of imaging schemes based on spin warp<sup>28</sup> Fourier imaging<sup>55</sup> techniques, diagnostically useful medical NMR imaging of the human body became a reality.<sup>37</sup> Once in a medical imaging environment, the term Magnetic Resonance Imaging (MRI) became increasingly common to describe

## 2. An Introduction to Nuclear Magnetic Resonance Imaging

---

NMR imaging of humans and animals. The demands of the medical community along with those of the practicalities of mass production of the hardware required have helped to fuel the rapid expansion of MRI throughout the last two decades, to the stage where it now is seen as an equal diagnostic partner with CT. However, while the growth of new applications and techniques involving CT has slowed, the range of new MRI techniques and applications continues to grow rapidly, suggesting a diverse, interesting and exciting future.

### 2.2 Fundamentals of NMR

Nuclei which possess spin and an odd number of nucleons are observed to have a non-zero angular momentum,  $\mathbf{J}$ . This results in a nuclear magnetic moment,  $\boldsymbol{\mu}$ , such that  $\boldsymbol{\mu} = \gamma\mathbf{J}$  where  $\gamma$  is the gyromagnetic ratio, which is a constant for a particular isotope (see Table 2.1). In the absence of an external magnetic field the eigenfunctions describing a nucleus are energetically degenerate. However, if it is placed in a magnetic field,  $\mathbf{B}_0$ , then Zeeman splitting of its energy levels occurs. The direction of  $\mathbf{B}_0$  may be used to define the direction of a  $z$  axis. Quantum Mechanics predicts the shift in each energy level as

$$E_m = -m_z \gamma \hbar B_0 \quad (2.1)$$

where the eigenvalue  $m_z = -I, -(I-1), \dots, I-1, I$  and  $\hbar$  is Planck's constant divided by  $2\pi$ . For a proton the spin quantum number  $I = \frac{1}{2}$  and so  $m_z = \pm\frac{1}{2}$  (i.e., two energy levels, denoted 'spin up' and 'spin down').

A transition between these energy levels will occur with the absorption or emission of a photon with energy  $\hbar\omega_0$  (where  $\omega_0$  is the angular frequency of the photon) where the energy of the photon equals the difference between the energy levels, i.e.,

$$\begin{aligned} \hbar\omega_0 &= \frac{1}{2}\gamma\hbar B_0 - -\frac{1}{2}\gamma\hbar B_0 \\ \Rightarrow \quad \omega_0 &= \gamma B_0 \end{aligned} \quad (2.2)$$

Thus the frequency of the electromagnetic radiation involved in a transition between the two energy levels is directly proportional to the magnitude of the magnetic field strength  $\mathbf{B}_0$  and is known as the Larmor frequency (see Figure 2.1).

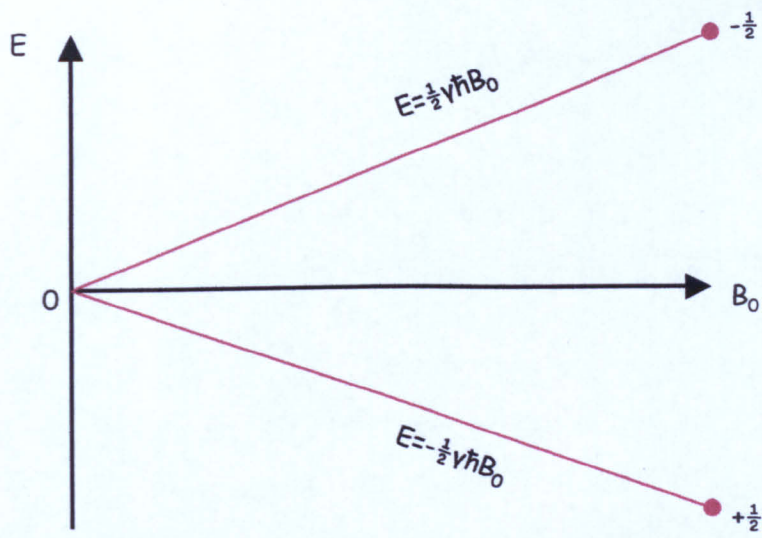


**Figure 2.1** Zeeman splitting of proton energy levels under the influence of a magnetic field  $B_0$ .

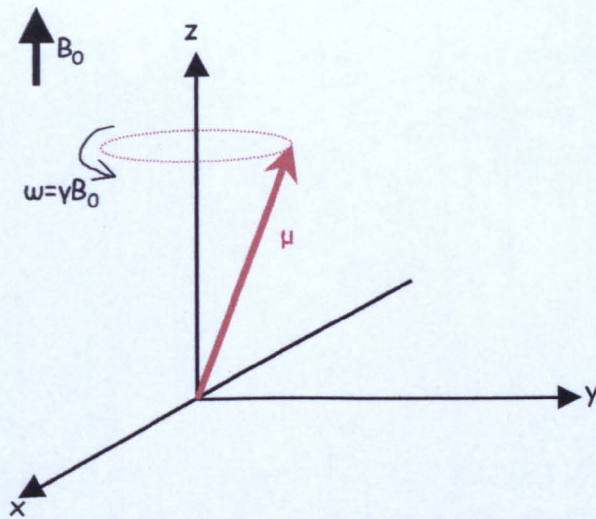


**Figure 2.2** The precession of a magnetic moment  $\mu$  around a magnetic field  $B_0$  aligned parallel to the  $z$  axis.

## 2. An Introduction to Nuclear Magnetic Resonance Imaging

---

The above description can also be given from a consideration of classical mechanics. This is useful as it allows certain phenomena to be described using a more visual picture. The application of a magnetic field,  $B_0$ , to a nucleus with angular momentum  $J$  results in a torque,  $\mu \times B_0$ , being exerted on it. From the same analysis as that performed on a spinning gyroscope, the nucleus remains tilted at the same angle relative to the magnetic field, but precesses around an axis parallel to  $B_0$  (see Figure 2.2). The frequency of rotation can be calculated and is found to be the same as in Equation 2.2. If an electromagnetic field of this frequency is applied to the sample perpendicular to  $B_0$ , resonance with the magnetic field will occur and the angle of tilt of the magnetic moment relative to  $B_0$  will be increased. Electromagnetic radiation of other frequencies will not resonate and so not alter this angle.

In practice it is always a collection of nuclei which is considered rather than a single nucleus. A sample can be considered as a group of non-interacting nuclei. In the absence of an external magnetic field, the degenerate energy state of the nuclei (or classically, the random orientation of the individual magnetic moments) result in no overall magnetization of the sample. When the sample is placed in a magnetic field, Zeeman splitting of the nuclear energy levels results in populations of nuclei in the various energy levels, being described by Boltzmann statistics. For a proton (with two energy levels) the difference in the fraction of nuclei in the higher energy state ('spin down') to the lower ('spin up') is given by

$$\frac{\Delta n}{n} = \tanh\left(\frac{\gamma\hbar B_0}{2kT}\right) \quad (2.3)$$

where  $k$  is Boltzmann's constant,  $T$  is the temperature,  $\Delta n$  is the difference between the number of nuclei in the lower and upper energy levels, and  $n$  is the total number of nuclei in both energy levels. It is interesting to note that at the temperature of the human body (about 310 K) in a magnetic field of 1 T, the fraction of proton nuclei in the higher energy state<sup>79</sup> is roughly  $3.3 \times 10^{-6}$ .

Due to the differing populations in each energy state, a net magnetization of the sample,  $M_0$ , is produced. Classically, this is the sum of the magnetization due to the precessing magnetic moments. When equilibrium has been achieved in the presence of  $B_0$ , the phase of each precessing nuclear magnetic moment is

## 2. An Introduction to Nuclear Magnetic Resonance Imaging

---

uncorrelated to other magnetic moments and so no magnetic moment would be expected in the  $x$ - $y$  plane resulting in  $M_0$  being parallel to  $B_0$ .

As  $\gamma\hbar B_0 \ll kT$  the fraction  $\frac{\Delta n}{n}$  (called the polarization) can be approximated to

$$\frac{\Delta n}{n} \approx \frac{\gamma\hbar B_0}{2kT} \quad (2.4)$$

The net magnetization of a sample of nuclei, each with magnetic moments  $\mu$  would be  $M_0 = \mu\Delta n$ . As  $\mu = \gamma J$  and  $J$  is quantized in units of  $\frac{1}{2}\hbar$  (for a proton) then  $M_0 = \frac{1}{2}\gamma\hbar\Delta n$  or

$$M_0 \approx \frac{n\gamma^2\hbar^2 B_0}{4kT} \quad (2.5)$$

The nuclear susceptibility  $\chi$  is defined as the ratio of  $M_0$  to  $B_0$  and so in this case

$$\chi \approx \frac{n\gamma^2\hbar^2}{4kT} \quad (2.6)$$

NMR involves manipulation and detection of the populations of nuclei in these energy levels in a magnetic field by the use of electromagnetic radiation of an appropriate (resonant) frequency. Nuclei which take part in this NMR are commonly referred to as 'spins'. The amplitude of the NMR signal received from the sample will depend on the difference in population between the energy levels. The small value of  $\Delta n$  results in an inherently poor sensitivity seen in NMR experiments compared to other spectroscopic techniques, as in NMR a signal effectively is received from only one nucleus in about  $10^5$ . However, Equation 2.3 shows that the NMR sensitivity can be increased by increasing  $B_0$  or by decreasing the temperature of the sample.

As will be described later, a MR image is composed of voxels, of which a typical size in a proton image of a human is 0.010 ml. In humans, water constitutes between 60% and 90% of the weight of soft tissues, therefore a voxel may typically contain 0.0075 ml of water. 1 mole of water has a mass of 18 g and contains two moles of hydrogen in a volume of 18 ml. Therefore, the typical excess in the number of proton spins per voxel in the lower energy state compared to the higher state, due to exposure to a static 1 T magnetic field, would be  $2 \times (6.02 \times 10^{23}) \times 0.0075 \times (3.3 \times 10^{-6}) \div 18 = 1.7 \times 10^{15}$ .

## 2. An Introduction to Nuclear Magnetic Resonance Imaging

Species	Nuclear spin quantum number ( $I$ )	Gyromagnetic ratio $\frac{\gamma}{2\pi}$ ( $\text{MHzT}^{-1}$ )	NMR sensitivity relative to $^1\text{H}$	Measurement sensitivity relative to $^1\text{H}$
$^1\text{H}$	$\frac{1}{2}$	42.573	1	1
$^{13}\text{C}$	$\frac{1}{2}$	10.705	$2.5 \times 10^{-4}$	$3 \times 10^{-7}$
$^{19}\text{F}$	$\frac{1}{2}$	40.052	$8.5 \times 10^{-1}$	$9 \times 10^{-5}$
$^{23}\text{Na}$	$\frac{3}{2}$	11.263	$1.3 \times 10^{-1}$	$1 \times 10^{-3}$
$^{31}\text{P}$	$\frac{1}{2}$	17.237	$8.3 \times 10^{-2}$	$4 \times 10^{-5}$

Table 2.1: Some NMR Characteristics of Nuclei Commonly of Interest in MRI.<sup>53,79</sup> NMR Sensitivity is the relative size of the NMR signal per nucleus at constant  $B_0$ . Measurement Sensitivity is the product of the NMR Sensitivity with the relative abundance of the particular nucleus in the human body, and so gives an indication of the size of the signal obtainable in MRI.

In the description of NMR given in this section, the magnetic field,  $B_0$ , was responsible for both causing Zeeman splitting of nuclear energy levels, and the population difference between those energy levels (*i.e.*, the magnetization of the sample). As shown above, the amount of polarization obtained by placing a sample of water in a magnetic field of 1 T is only  $3.3 \times 10^{-6}$ . While it is usual in practice to use the same magnetic field to polarize and perform NMR, it need not be the case. The spins may be polarized by a magnetic field of one strength and NMR may occur in a magnetic field of a different strength. Other methods of magnetizing samples than by placement in a magnetic field also exist. It has been known for some time that nuclei in a noble gas in a magnetic field may be polarized to a high degree (close to 100%) by exposure to a laser beam of an appropriate frequency. This allows NMR of high sensitivity to be performed on these gases. As the magnetic field used is only required to cause Zeeman splitting and not the polarization itself, a range of field strengths may be used and in particular high magnetic fields are not required as the amount of polarization is independent of  $B_0$ .

### 2.2.1 Spin-lattice and Spin-spin Relaxation

If a sample is placed in a static magnetic field  $B_0$  and a magnetic field  $B_1$  rotating in the  $x$ - $y$  plane at the Larmor frequency is applied, photons will be

## 2. An Introduction to Nuclear Magnetic Resonance Imaging

---

absorbed in the transfer of spins from the lower to the higher energy state. This results in a change in the magnetization of the sample. In classical terms, the electromagnetic radiation (applied for a time  $t$ ) would resonate with the precessing magnetic moments and tip them away from the  $z$  axis. This results<sup>111</sup> in  $\mathbf{M}_0$  being tipped through an angle  $\theta$  where  $\theta = \gamma B_1 t$  (see Figure 2.3).

Following cessation of the electromagnetic field, the relative populations of the energy levels return to their equilibrium state through time with the emission of photons. This energy is absorbed and dissipated in the molecules surrounding the nucleus, and this surrounding environment is termed the lattice. This return to equilibrium is named spin-lattice (or longitudinal) relaxation and is described by an exponential recovery with a time constant  $T_1$ . In classical terms, spin-lattice relaxation can be described as the return of  $\mathbf{M}_0$  to its equilibrium position, parallel to  $\mathbf{B}_0$ .

In the classical description, the application of resonant electromagnetic radiation is thought of as tipping  $\mathbf{M}_0$  away from the  $z$  axis by an angle  $\theta$ . Thus, components of  $\mathbf{M}_0$  will be seen in the  $x$ - $y$  plane. During the application of the electromagnetic field, all magnetic moments will be resonating in phase with the  $B_1$  field. However, after its cessation, each nucleus will precess freely with a frequency which depends on the local magnetic field which it experiences. Due to interactions with the magnetic moments of neighbouring nuclei, the local magnetic field will be slightly inhomogeneous from nucleus to nucleus. Hence each nucleus will precess with a slightly different frequency. The result will be a dephasing of the magnetic moments in the  $x$ - $y$  plane, resulting in a decrease in the net magnetization in this plane. The irreversible loss of net magnetization in the  $x$ - $y$  plane is called spin-spin (or transverse) relaxation and is described as an exponential decay with time constant  $T_2$ .

In practice the local magnetic field depends on more than contributions from neighbouring magnetic moments. A larger variation is produced by inhomogeneities in the external magnetic field,  $\mathbf{B}_0$ , which causes spins to dephase more rapidly than they would otherwise. The time constant describing the observed

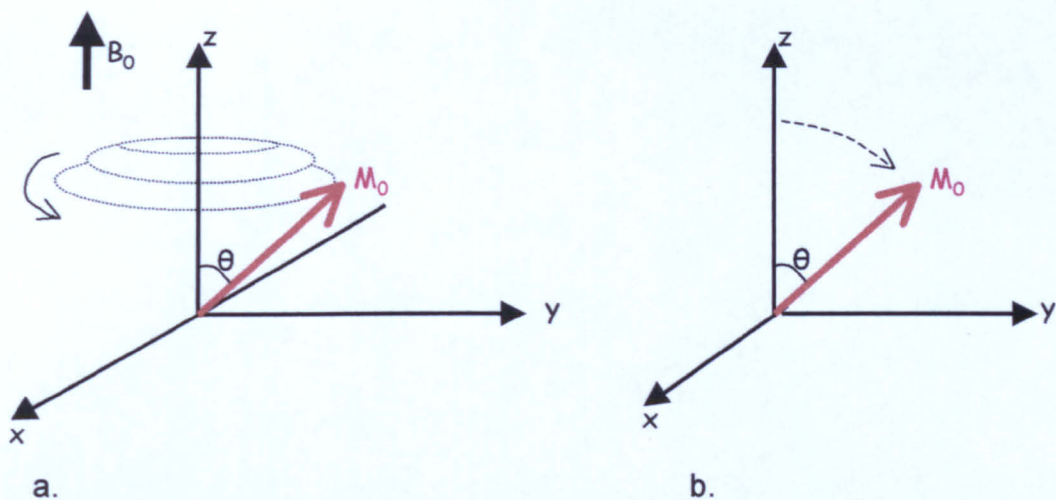


**Figure 2.3** The tipping of  $M_0$  away from the z axis under the influence of electromagnetic radiation at the Larmor frequency in the x-y plane. a) in the laboratory reference frame. b) in a reference frame rotating at the Larmor frequency.

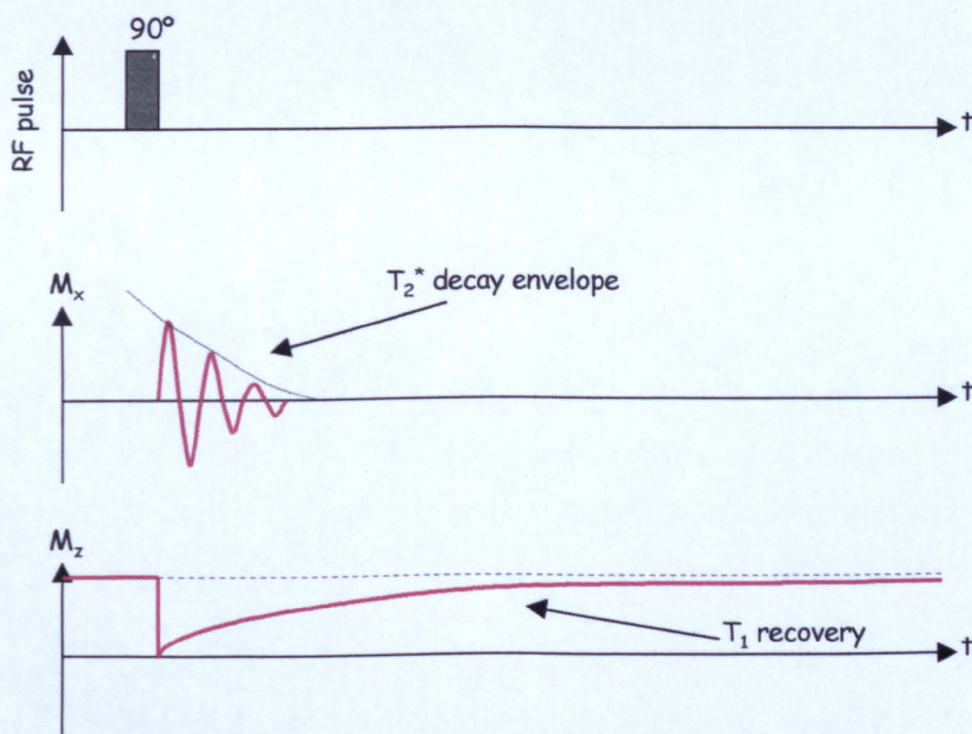


**Figure 2.4** Free Induction Decay,  $M_x$  in the laboratory frame, after the application of a  $90^\circ$  RF pulse. The FID envelope is  $T_2^*$  exponential decay, and would be the NMR signal observed in the rotating frame.  $T_1$  recovery of  $M_z$  occurs more slowly than  $T_2^*$  decay.

## 2. An Introduction to Nuclear Magnetic Resonance Imaging

---

dephasing is denoted by  $T_2^*$  and it can be related to  $T_2$  by

$$\frac{1}{T_2^*} = \frac{1}{T_2} + \frac{1}{T_2^{\text{magnet}}} + \frac{1}{T_2^{\text{susceptibility}}} + \dots \quad (2.7)$$

It is found that the relaxation time constants  $T_1$  and  $T_2$  depend on a number of parameters, indeed it was the belief that  $T_1$  has a different range of values for normal tissue than for cancerous tissue that lead to the initial involvement of NMR in medical diagnosis.

The exponential  $T_1$  and  $T_2$  relaxations described above may be combined into a single set of equations which describe the behaviour of the spins in a sample through time under the influence of  $B_1$  and  $B_0$ , in the rotating frame of reference. These are the Bloch equations<sup>15,46</sup> and are given below (Equation 2.8). While these equations are extremely important in NMR, they are not used directly by the work in this thesis and so will not be discussed further.

$$\begin{aligned} \frac{dM_x}{dt} &= \gamma M_y \left( B_0 - \frac{\omega}{\gamma} \right) - \frac{M_x}{T_2} \\ \frac{dM_y}{dt} &= \gamma M_z B_1 - \gamma M_x \left( B_0 - \frac{\omega}{\gamma} \right) - \frac{M_y}{T_2} \\ \frac{dM_z}{dt} &= -\gamma M_y B_1 - \frac{(M_z - M_0)}{T_1} \end{aligned} \quad (2.8)$$

MRI is mainly concerned with imaging biological systems where the majority of molecules are in the liquid state, Also, due to the high proportion of water in tissue and the relatively high NMR sensitivity of hydrogen compared to other elements (see Table 2.1), MRI is almost exclusively applied to imaging water. Hence, unless otherwise stated, the following description will only consider NMR of protons in liquids.

The values of  $T_1$  and  $T_2$  for free water are both of the order of several seconds at a magnetic field strength of the order of 1 T. However, once the water is placed in an environment such as a biological system, or is bound with other molecules, then the values for these two parameters are reduced so that  $T_1$  is typically of the order of hundreds of milliseconds and  $T_2$  is of the order of tens of milliseconds.

The reduction of  $T_2$  can be explained by noting that the resonating molecules in tissue have a reduced mobility. Hence they will experience a particular local inhomogeneous magnetic field for longer. The greater mobility of the identical

## 2. An Introduction to Nuclear Magnetic Resonance Imaging

---

molecules in free water result in an 'averaging out' of some of the local field inhomogeneities caused by neighbouring nuclei, leading to a larger  $T_2$  value for a particular region of the sample.

Spin-lattice relaxation requires a transfer of energy between the spins and the lattice, which is mediated by fluctuations in magnetic field caused by molecular motion. This transfer will be more efficient when more molecular motion can be resolved into a fluctuation at the Larmor frequency, resulting in a smaller value for  $T_1$ . Hence spin-lattice relaxation is also dependant on molecular motion and mobility. The fluctuating magnetic fields can have various sources, including resonating nuclei, paramagnetic molecules, and chemically shifted molecules. This results in  $T_1$  values which depend on the local chemical environment of the spins.

Variations in  $T_1$  values are observed with the value of  $B_0$ . An increase in  $B_0$  generally results in an increase in  $T_1$  for a particular sample. Variations of  $T_1$  with  $B_0$  would be expected because, as described above,  $T_1$  partly depends on mobility with respect to the Larmor frequency. A change in  $B_0$  results in a different Larmor frequency relative to the same molecular motion and hence a different amount of stimulated emission. As well as increasing with  $B_0$  different values of  $T_1$  for different samples are seen to converge to the value of  $T_1$  observed for free water. However  $T_2$  is not found to vary greatly with various values of  $B_0$ .

Descriptions of the relaxation processes in a biological system are complex and incomplete. A simple hypothesis (the two phase model<sup>68</sup>) considers water in tissue to consist of free water and water bound to macromolecules (e.g., proteins), in various proportions. The bound water, having reduced mobility, has a shorter  $T_1$ . An exchange of water molecules between the free and bound states is assumed. If this exchange is fast, (as it would appear to be in simple solutions) then the observed  $T_1$  can be approximated by considering the fraction of free and bound water,<sup>79</sup> such that

$$\frac{1}{T_1} = \frac{1}{T_1^{\text{free}}} + b \left( \frac{1}{T_1^{\text{bound}}} - \frac{1}{T_1^{\text{free}}} \right) \quad (2.9)$$

where  $b$  is the fraction of bound tissue water,  $T_1^{\text{free}}$  is the spin-lattice relaxation time for free water, and  $T_1^{\text{bound}}$  is the spin-lattice relaxation time for bound water.

## 2. An Introduction to Nuclear Magnetic Resonance Imaging

Hence  $\frac{1}{T_1}$  is directly proportional to the fraction of bound water. However, this model is not always a suitable one, and does not explain the multi-exponential relaxation which can be observed, suggesting that a more complex process is occurring.

The dependence of  $T_1$  on proportions of free and bound water led to initial hopes that NMR could be used to discriminate between tissues, especially between healthy and cancerous tissues.<sup>23</sup> Large variations are observed between different tissues and differing pathology resulting in high contrast in MRI between tissues compared to other diagnostic imaging tools, especially between soft tissues and white and grey matter in the brain. However, characterization of pathology by absolute  $T_1$  and  $T_2$  values has not yet proven to have any clinical value.<sup>111</sup>

### 2.2.2 NMR signal

As described in the previous section, the application of resonating electromagnetic radiation,  $B_1$ , to a sample of nuclei in a magnetic field,  $B_0$ , will tip the net magnetization,  $M_0$ , away from the  $z$  axis. After the cessation of the electromagnetic radiation the magnetic moments will relax back to their equilibrium state. If any component of  $M_0$  is present in the  $x$ - $y$  plane then due to its precession around the  $z$  axis, electromagnetic radiation will be emitted. In NMR imaging, magnetic field strengths of the order of a Tesla are used, resulting in a Larmor frequency for the proton in hydrogen of the order of  $10^7$  Hz. A photon of this frequency lies in the radiowave section of the electromagnetic spectrum. One method of detecting this is to place a coil with its axis in the  $x$ - $y$  plane into which an oscillating e.m.f. is induced. This e.m.f. is the NMR signal, and all other NMR parameters (such as  $T_1$  and  $T_2$ ) must be deduced from it.

For NMR imaging, short bursts of electromagnetic radiation are usually applied to the sample. These are normally termed radiofrequency (RF) pulses, and their strength and duration define the angle  $\theta$  through which  $M_0$  is tipped, where  $\theta = \gamma B_1 t$ . Thus a  $90^\circ$  pulse would result in  $M_0$  being tipped from the  $z$  axis into the  $x$ - $y$  plane (see Figure 2.3).

The rotating magnetic field  $B_1$  ideally would be applied as a circularly po-

## 2. An Introduction to Nuclear Magnetic Resonance Imaging

larized RF pulse. Practically, the RF pulse is often only linearly polarized. This magnetic field can be resolved into two counter-rotating fields of frequency  $\omega$ , one of which is rotating in the same sense as the spins and thus resonates with them. The other field has no result other than reducing the efficiency of the RF pulse.

After the application of a RF pulse which results in a component of  $M_0$  in the  $x$ - $y$  plane, a NMR signal can be observed, either in the same coil which supplied the RF pulse, or in a separate receiver coil. The signal obtained is usually called a Free Induction Decay (FID) as it shows spin-spin decay in the absence of input RF (see Figure 2.4). The individual oscillations in the signal correspond to a rotation of  $M_0$  around the  $z$  axis.

The dephasing of individual magnetic moments in the  $x$ - $y$  plane is characterised by  $T_2^*$  decay, which occurs more rapidly in tissue water than  $T_1$  recovery. As the NMR signal is from a rotating net magnetization in the  $x$ - $y$  plane, the duration of each FID is governed by  $T_2^*$ . The initial amplitude of the FID depends on the density of resonating protons in the sample, and on the magnitude of the component of  $M_0$  in the  $x$ - $y$  plane.

It is usual to convert the NMR signal into a frame of reference rotating at the Larmor frequency. This is achieved by passing the signal through two phase sensitive detectors (p.s.d.) prior to digitization (known as quadrature detection).<sup>79</sup> Each p.s.d. takes a reference signal at the expected Larmor frequency, with the phase of the reference signal to one p.s.d.  $90^\circ$  different to that of the other. If an input NMR signal is in phase with the reference then a positive output, proportional to the input signal strength, is obtained. If the phases are  $90^\circ$  or  $270^\circ$  apart then there is no output, and if they are  $180^\circ$  apart a negative output is obtained. Hence the frequencies present in the output of a p.s.d. are the difference between the frequencies of the input source and the reference frequency. If the reference signal is at the same frequency as the spins then one channel will show an exponential decay (the envelope of the FID, with time constant  $T_2^*$ , often called the real signal) and the other channel will contain no signal (the imaginary channel) as there is no component of the NMR signal which is  $90^\circ$  out of phase with the reference. In practice, not all the nuclei will be spinning at the

## 2. An Introduction to Nuclear Magnetic Resonance Imaging

---

same frequency (for the same reasons as  $T_2 \neq T_2^*$ ) and so the signal will contain a range of frequencies, resulting in both real and imaginary signals. Acquiring both real and imaginary signals results in a  $\sqrt{2}$  improvement in the signal to noise ratio (SNR) during subsequent processing due to the ability to distinguish between positive and negative frequencies relative to the reference frequency.

For NMR imaging techniques it is often necessary to excite only those nuclei spinning with a certain frequency. This requires a RF pulse with a small bandwidth of frequencies. If this is desired (*i.e.*, a rectangular step function in frequency space) then it is necessary to apply the RF pulse modulated by a sinc envelope (as a sinc function is the Fourier transform of a single period of a square wave). In practice, the application of finite sinc modulation still results in undesirable frequency components, hence the sinc function often is modulated further, typically with a Gaussian function.

### 2.2.3 Chemical Shift

Perturbations in the local magnetic field experienced by individual nuclei can be caused by interactions with the electrons in the surrounding chemical environment. This results in a reduction in the local magnetic field, resulting in a new local magnetic field strength  $B$  where

$$B = (1 - \sigma) B_0 \quad (2.10)$$

where  $\sigma$  is the shielding parameter. This results in the nucleus resonating with a different Larmor frequency,  $\omega$ . The chemical shift,  $\delta$ , is the fractional shift in Larmor frequency relative to a reference compound (often tetramethylsilane if the chemical shift of  $^1\text{H}$  is being considered) expressed in parts per million (p.p.m.). That is

$$\delta = \frac{\omega - \omega_{\text{ref}}}{\omega_{\text{ref}}} \times 10^6 \quad (2.11)$$

In MRI the chemical shift manifests itself mainly in the different frequencies obtained from free water ( $\text{H}_2\text{O}$ ) and fat (containing  $\text{CH}_2$ ), the two main sources of proton NMR signals in biological tissue. At 1.5 T, it is observed that the resonant frequency of the hydrogen in fat is about 224 Hz below that of the

## 2. An Introduction to Nuclear Magnetic Resonance Imaging

---

hydrogen in water, since  $\delta \approx 3.5$  p.p.m. During image construction, considered below, this can result in two shifted, but overlapping, images; a water and a fat image. Also, the high intensity from fat in many MR images can often mask abnormal signal from juxtaposed pathology. Therefore it often is desirable to selectively acquire a NMR signal from either water or fat and a number of methods exist to allow this to be performed during MRI acquisitions.<sup>15, 79, 85</sup> One such method is described at the end of the following section.

### 2.2.4 Pulse Sequences

The FID NMR signal described above only contains information concerning  $\rho$  (resonating proton density, from its initial amplitude) and  $T_2^*$ . In order to gain information relating to  $T_1$  and  $T_2$ , as well as other parameters which may be measured by NMR, a sequence of RF pulses can be applied to a sample, resulting in the amplitude of the NMR signal being weighted by the required parameters.

#### Saturation Recovery

The simplest sequence used in MRI is known as saturation recovery. In this,  $90^\circ$  RF pulses are applied to the sample every TR seconds (see Figure 2.5). If TR is large compared to the sample's  $T_1$  then most of the spins will have relaxed and the amplitude of each FID will depend on  $\rho$ . If TR is approximately equal to  $T_1$  then not all of the spins will have relaxed by the time that the subsequent  $90^\circ$  RF pulse is applied. Fewer magnetic moments will be orientated along the  $z$  axis to be tipped into the  $x$ - $y$  plane, resulting in a FID with a smaller amplitude. The actual value of  $T_1$  could be obtained by repeating the pulse sequence with a different TR, and using both signals in the following equation. The amplitude of the FID's obtained from this pulse sequence,  $S_{sr}$ , (after the first few FID's) can be described by

$$S_{sr} \propto \rho \left( 1 - \exp \left( -\frac{TR}{T_1} \right) \right) \quad (2.12)$$

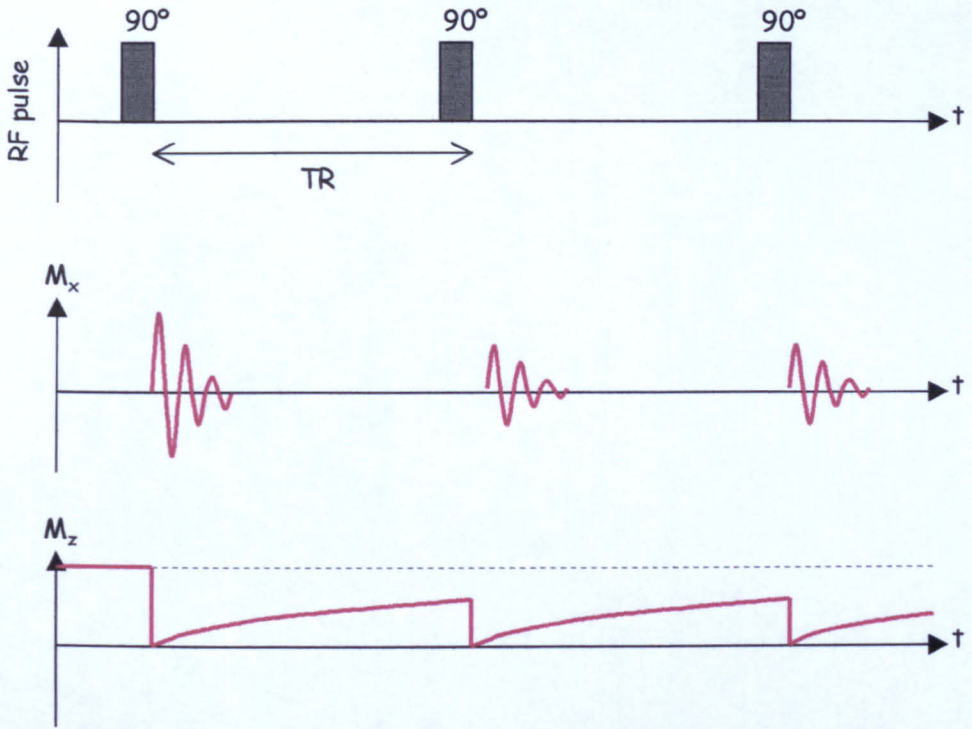


**Figure 2.5** Saturation recovery.  $90^\circ$  RF pulses occur more rapidly than complete  $T_1$  recovery. Subsequent FID's have a smaller amplitude, the value of which depends on  $T_1$ .

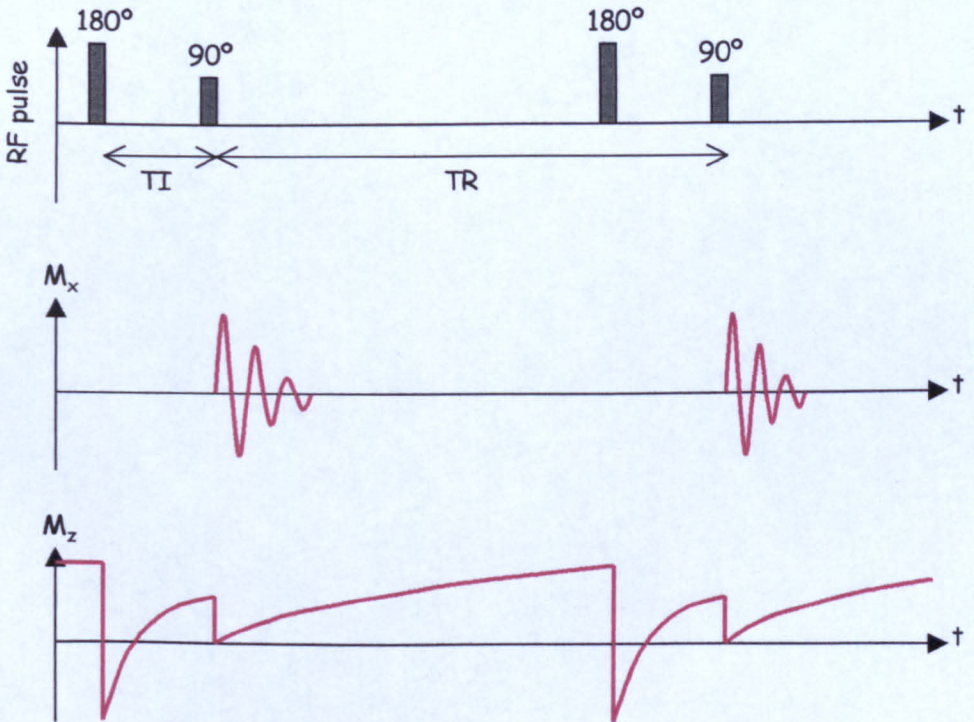


**Figure 2.6** Inversion recovery. The amplitude of the FID depends on the amount of  $T_1$  recovery which has occurred during  $TI$ .

## 2. An Introduction to Nuclear Magnetic Resonance Imaging

---

### Inversion Recovery

To improve the  $T_1$  weighting, the inversion recovery sequence can be used. In this, a  $180^\circ$  RF pulse is applied at a time  $TI$  before the  $90^\circ$  pulse of the saturation recovery sequence (see Figure 2.6). After the  $180^\circ$  pulse the spins relax from being aligned parallel to the  $-z$  axis back to being aligned with the  $+z$  axis with spin-lattice interactions, but with twice the range of the saturation recovery sequence. The  $90^\circ$  pulse tips and rephases the  $z$  axis component of  $M_0$  into the  $x$ - $y$  plane so that its FID can be observed. The amplitude of the FID obtained from inversion recovery,  $S$ , can be described by

$$S_{ir} \propto \rho \left( 1 - 2 \exp\left(-\frac{TI}{T_1}\right) + \exp\left(-\frac{TR}{T_1}\right) \right) \quad (2.13)$$

and if  $TR \gg T_1$  then

$$S_{ir} \propto \rho \left( 1 - 2 \exp\left(-\frac{TI}{T_1}\right) \right) \quad (2.14)$$

The signal may be negative or positive. MR images are usually displayed as modulus images; in this case the negative portion is mirrored around the zero level.

### Spin Echoes

To gain information on the value of  $T_2$  for a sample, a sequence involving an echo must be used, such as the spin-echo pulse sequence described in Figure 2.7. The initial  $90^\circ$  pulse tips  $M_0$  into the  $x$ - $y$  plane. The transverse magnetization then starts to relax with a time described by  $T_2^*$ . To extract  $T_2$ , effects due to the magnetic field inhomogeneity need to be cancelled out. This is achievable as they depend on the spatial location of the spins. By applying a  $180^\circ$  pulse (after a time  $\frac{1}{2}TE$ ) all the magnetic moments are effectively mirrored about an axis in the  $x$ - $y$  plane (see Figure 2.8) Each stationary nucleus still feels the same local magnetic field as it did before the  $180^\circ$  pulse, and hence still rotates at its own Larmor frequency. This results in a 'refocusing' of magnetic moments at a time  $TE$  after the  $90^\circ$  pulse, producing a NMR signal called an echo. The amplitude of this echo will depend on  $T_2$  (because  $T_2$  dephasing can not be refocused, as its source is not spatially fixed) as well as  $T_1$  and  $\rho$ . Repeated  $180^\circ$

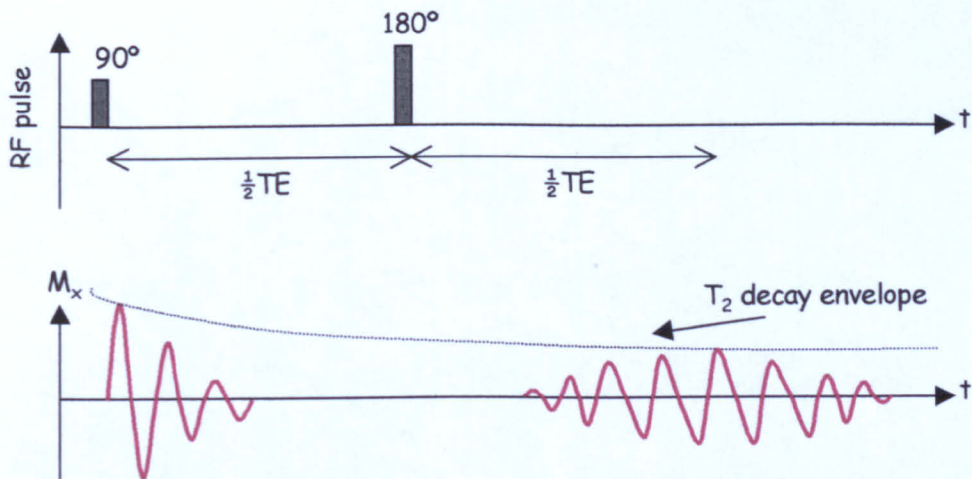


**Figure 2.7** Spin echo pulse sequence. The centre of the echo occurs at a time  $TE$  after the  $90^\circ$  RF pulse.

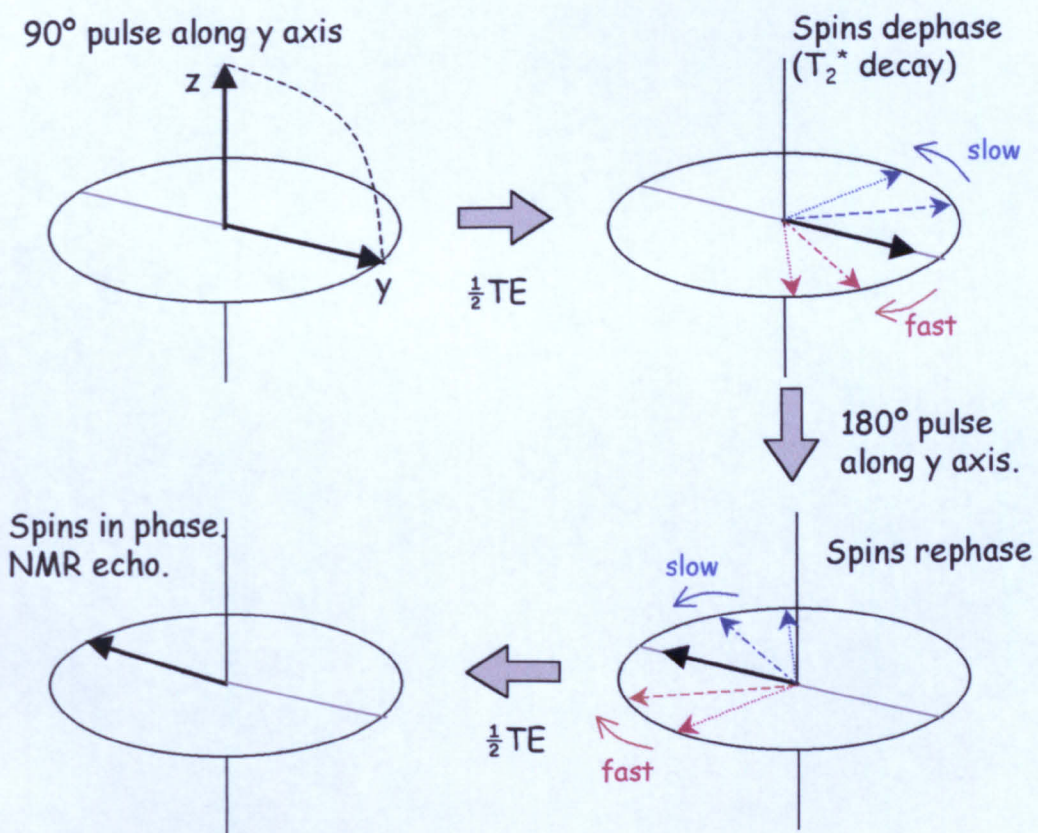


**Figure 2.8** Spin echo formation, in the rotating frame of reference.

## 2. An Introduction to Nuclear Magnetic Resonance Imaging

---

pulses (the Carr-Purcell-Meiboom-Gill (CPMG) sequence<sup>16,72</sup>) result in repeated echoes which allow any multiexponential  $T_2$  behaviour to be seen. The envelope covering the echo peaks is the  $T_2$  decay curve, and after at least one repetition of the pulse sequence, its amplitude at the first echo,  $S_{se}$ , is given by

$$S_{se} \propto \rho \left[ 1 - 2 \exp\left(-\frac{TR - \frac{TE}{2}}{T_1}\right) + \exp\left(-\frac{TR}{T_1}\right) \right] \exp\left(-\frac{TE}{T_2}\right) \quad (2.15)$$

If  $TE \ll TR$  then

$$S_{se} \propto \rho \left[ 1 - \exp\left(-\frac{TR}{T_1}\right) \right] \exp\left(-\frac{TE}{T_2}\right) \quad (2.16)$$

and if  $TR \gg T_1$

$$S_{se} \propto \rho \exp\left(-\frac{TE}{T_2}\right) \quad (2.17)$$

The spin-echo pulse sequence, with or without an initial inversion pulse, is one of the most popular sequences to be used on clinical MRI units. By varying  $T_1$ ,  $TR$ , and  $TE$ , the NMR signal can be weighted more or less by  $\rho$ ,  $T_1$ , or  $T_2$ . Long  $TR$ 's and short  $TE$ 's with no inversion pulse result in  $\rho$  weighting; short  $TE$ 's and either short  $TR$ 's or an inversion pulse result in  $T_1$  weighting; long  $TR$ 's and long  $TE$ 's without an inversion pulse result in  $T_2$  weighting. For imaging biological tissue using a static magnetic field of about 1 T then typical ranges for  $TR$  are 300–2000 ms,  $T_1 = 100$ –1200 ms, and  $TE = 5$ –100 ms. If a sample has a short  $T_1$  then after the pulse sequence repetition time  $TR$ , more of the spins will have relaxed to be excited in the next pulse, resulting in a larger NMR signal amplitude. Hence in a saturation recovery MR image, short  $T_1$  areas usually appear bright. A short  $T_2$  results in the amplitude of the echoes decreasing more rapidly and so in an image, short  $T_2$  areas normally appear dark.

The flip angle of the refocusing RF pulse does not need to be  $180^\circ$  for a spin echo to form. Supposing the first RF pulse tips the spins from the  $z$  axis to the  $+x$  axis in the  $x$ - $y$  plane. Through a time  $\frac{TE}{2}$ , the spins will dephase by  $T_2^*$  decay. In the rotating frame of reference, the slow spins will move towards (say) the  $-y$  axis and the fast spins towards the  $+y$  axis. Another RF pulse along the  $+x$  axis will tip the component of spins remaining along the  $x$  axis back to the  $z$  axis while the component of spins along the  $y$  axis will remain in the  $x$ - $y$

## 2. An Introduction to Nuclear Magnetic Resonance Imaging

---

plane. These will form a spin echo along the  $-y$  axis after a further time  $\frac{TE}{2}$ . Spin echoes formed by refocusing RF pulses of less than  $180^\circ$  are often called Hahn echoes. The amplitude of the echo will be a maximum for a  $180^\circ$  RF refocusing pulse; less for lower flip angles.

### Stimulated Echoes

If three or more non- $180^\circ$  RF pulses are applied in rapid succession, an echo is formed in addition to the Hahn echoes described above. If, after the Hahn echo described above, a further RF pulse is applied, the spins which had been tipped along the  $z$  axis by the second RF pulse will be tipped back into the  $x$ - $y$  plane, along the  $x$  axis. While they had been 'stored' along the  $z$  axis, they had been experiencing slower  $T_1$  relaxation rather than  $T_2$  decay. Following the convention used for the description of the Hahn echo above, the fast spins will fall on the  $+x$  axis and the slow spins along the  $-x$  axis. This will combine to form a new echo along the  $-x$  axis at a time  $\frac{TE}{2}$  where  $\frac{TE}{2}$  is the time between the first two RF pulses. This is called a stimulated echo. The third RF pulse will also cause Hahn echoes; one from the first RF pulse and one from the second RF pulse. The third RF pulse will also refocus the Hahn echo cause by the first two RF pulses, resulting in a secondary Hahn echo. In order to observe all these echoes, the time between the first two RF pulses must be different from the time between the second two RF pulses; if these times are the same, some echoes will occur at the same time and interfere with each other. This is shown in Figure 2.9.

An appreciation of various echo processes is important in MRI. As will be seen below, to acquire a MR image, RF pulses may be applied in rapid succession (*i.e.*, short TR). Stimulated and secondary echoes may appear when they are not required and interfere with subsequent NMR signals, which in turn may result in artefacts in the final MR image. Even for MRI acquisitions which use  $90^\circ$ – $180^\circ$  RF pulses, unwanted echoes may still cause a problem. Slice selective RF pulses (described in Section 2.3.1 below) never result in a uniform flip angle across the slice profile, especially at the edges, and so an imaged slice will always contain a small number of spins with flip angles lower than expected.

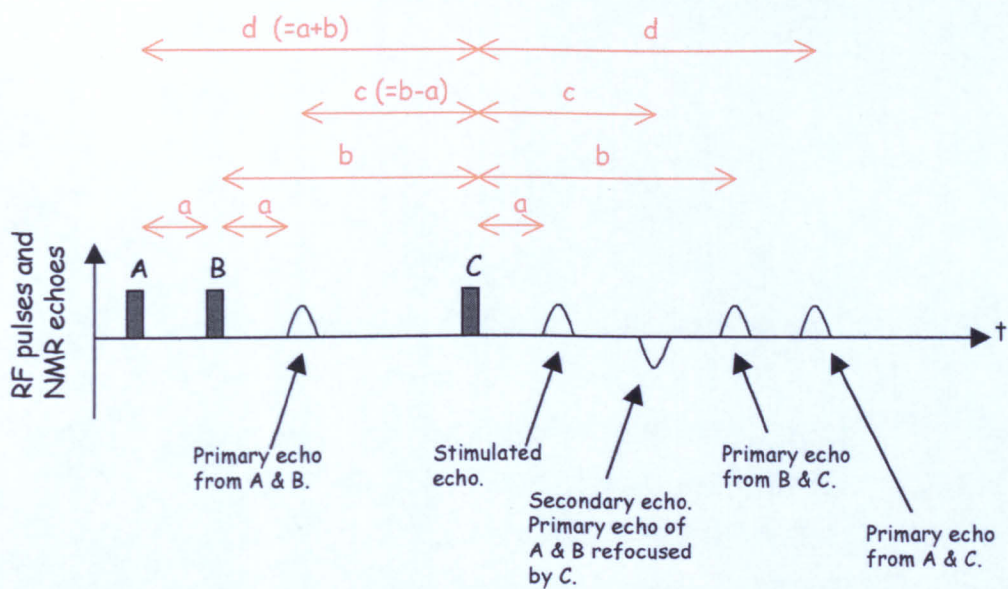


**Figure 2.9** Echoes from three low angle RF pulses, A, B, & C.

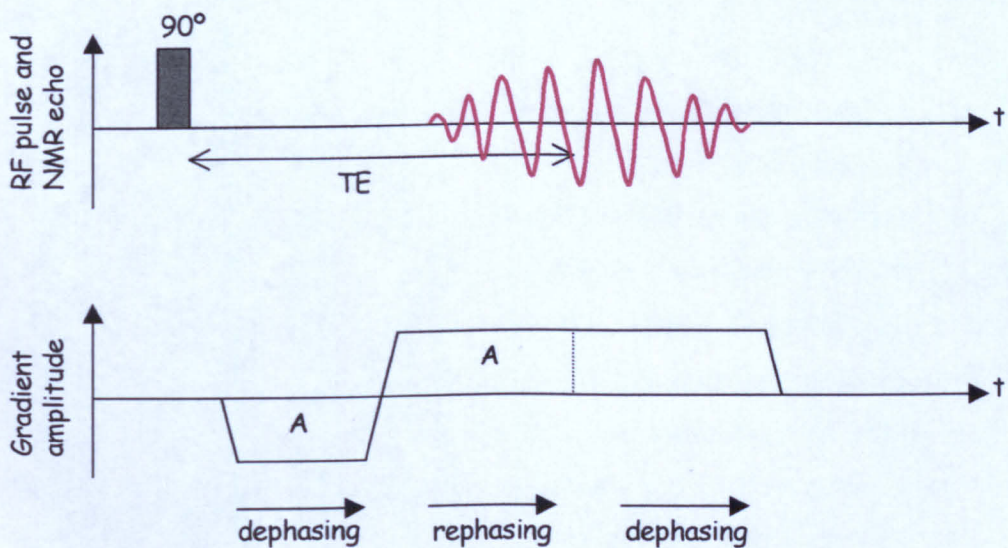


**Figure 2.10** Gradient echo. Equal gradient-time areas are labelled A.

## 2. An Introduction to Nuclear Magnetic Resonance Imaging

---

### Gradient Echoes

An echo formed by the application of a RF pulse is termed a spin echo. A similar echo can be formed by applying an additional relatively small spatially varying magnetic field to the sample. This additional magnetic field is termed a magnetic field gradient. Application of a magnetic gradient increases the heterogeneity of the local magnetic field and hence causes dephasing of the spins at an increased rate. Spins that experience an increased local magnetic field rotate with a higher Larmor frequency, and *vice versa*. This dephasing appears similar to that which occurs as a result of  $T_2^*$  decay but the magnetic field gradient causes it to occur far more rapidly. If the magnitude of this magnetic gradient is then reversed while its spatial distribution remains the same, then the spins which experienced an increased local magnetic field now experience a lower magnetic field, and so now rotate with a lower Larmor frequency. Spins which had rotated more slowly now rotate more rapidly. As these spins rephase, an NMR signal is observed and termed a gradient echo (see Figure 2.10). In practice, magnetic field gradients may be applied and reversed in order to form a gradient echo in a shorter duration of time than the application of a  $180^\circ$  RF pulse, especially in the case of acquiring NMR echoes for the formation of a MR image, described in later sections. This results in shorter achievable TE times for gradient echoes compared with spin echoes, which allows the faster acquisition of a MR image. However, a gradient echo is not as 'complete' as a spin echo. While a spin echo rephases stationary spins dephased by all sources other than those causing  $T_2$  decay, a gradient echo only rephases spins which were dephased by the magnetic gradient applied to cause the echo. Dephasing caused by sources such as an inhomogeneous  $B_0$  magnetic field are not rephased by a gradient echo. As such, the amplitude of the gradient echo is smaller than that of a spin echo and does not describe the  $T_2$  decay envelope.

The use of echoes is extremely important in NMR. Because a FID occurs immediately after the application of a RF pulse, it is technically difficult to acquire the beginning of the NMR signal and hence its initial amplitude is difficult to determine. More importantly, when magnetic gradients are applied in order to form a MR image, the FID dephases very rapidly resulting in little or no NMR

## 2. An Introduction to Nuclear Magnetic Resonance Imaging

---

signal being detected. However, by use of an echo, the NMR signal is separated in time from the RF pulse and may be measured in its entirety. Also, as the spins are in phase at the centre of the echo, the NMR signal is measured both prior to and after a time when the spins are in phase. In a NMR signal of a FID, data can only be acquired at times after the spins were in phase (which was at the time of application of the RF pulse). The extra information contained in an echo results in improved NMR image quality than would be obtained from just FID's, as will be described later. Unless stated otherwise, further references in this thesis to the NMR signal will refer to the echo rather than the initial FID.

### Chemical Presaturation

As mentioned in the previous section, proton NMR signals for imaging of biological systems mainly come from the hydrogen in free water or fat. To discriminate between these signals it is possible to modify a pulse sequence to suppress the NMR signal from either water or fat. One method of doing this is to apply a RF pulse to excite only water or fat immediately before the imaging sequence.<sup>85</sup> For example, if it is desired to suppress the NMR signal from the hydrogen in fat at a magnetic field strength of 1.5 T, a RF pulse may be applied with a bandwidth of 200 Hz and a frequency offset from the resonant frequency of hydrogen in water of -224 Hz. The flip angle is typically 100° to 120° which tips the  $M_0$  of fat just below the  $x$ - $y$  plane but leaves the  $M_0$  of water unchanged along the  $z$  axis. Unipolar magnetic gradients are then applied to dephase the fat  $M_0$  in the  $x$ - $y$  plane, but as they are not reversed, they do not refocus it in a gradient echo. Use of gradients to dephase  $M_0$  in the  $x$ - $y$  plane is often called spoiling or crushing. This is termed a fat saturation pulse. The imaging pulse sequence is applied immediately afterwards; for this, the frequencies and bandwidths of the RF pulses used will be determined to produce an image (as described in sections below) rather than selectively excite water, hence both water and fat will interact with the imaging RF pulses. However, as the fat  $M_0$  has been dephased in the  $x$ - $y$  plane, it will not be rephased by the imaging sequence at the same times as the  $M_0$  of water and hence not contribute coherently to the NMR signal; it has been suppressed. However, as the  $T_1$  of fat is relatively short, the fat suppression

## 2. An Introduction to Nuclear Magnetic Resonance Imaging

pulse must occur as close as possible in time before the start of the imaging sequence for its effect to be observed.

### **Magnetization Transfer**

The proton NMR signals for imaging of biological systems mainly come from the hydrogen in free water or fat. One method of saturating the signal from fat and hence only imaging the signal from water, is described above. However, there is a considerable amount of hydrogen present in biological systems in other molecules other than  $H_2O$  and  $CH_2$ . In particular, hydrogen is present in large protein macromolecules. Because they are tightly bound, they do not contribute directly to the observed NMR signal (their  $T_2$ 's are much shorter than a millisecond). However, they still magnetically interact with the hydrogen in water and fat, which are resonating with similar frequencies. This is termed magnetization transfer (MT). The magnetization of hydrogen in water will be influenced by the density of hydrogen-bearing macromolecules in its local environment. The amount of MT occurring may be observed in MRI. The short  $T_2$  of hydrogen in macromolecules result in them having a large bandwidth of resonant frequencies\*. The hydrogen in macromolecules may be saturated by application of a RF saturation pulse prior to imaging. At 1.5 T, this RF pulse typically may be applied with a central frequency offset from that of water by 1500 Hz and with a bandwidth of 500 Hz. This is called MT saturation (MTS). In the time following the MT saturation RF pulse, MT occurs between the hydrogen in water to the hydrogen in macromolecules, but the macromolecules do not possess coherent magnetization to transfer back to the water hydrogen. Therefore, in the following MR image, signal intensity in regions containing a high density of macromolecules will be lower. The difference between an image acquired with MTS and one acquired without will highlight the amount of MT occurring in each pixel and give rise to MT contrast (MTC).

---

\*The FT of a rapidly decaying FID, or echo, (*i.e.*, short  $T_2$  or  $T_2^*$ ) gives a spectrum containing a wide range of frequencies.

### 2.3 NMR Imaging Techniques

In the previous section a basic introduction to NMR has been given. Until 1973, NMR was used and developed mainly as a spectroscopic tool and method for measuring various parameters such as  $T_1$  and  $T_2$ . However, once the possibility of using NMR to produce non-destructive images arose, new techniques were devised in order to produce images from the NMR signal. A brief introduction to the methods used to produce NMR images is given in this section, with emphasis on contemporary techniques used in medical MRI and the background behind them.

#### 2.3.1 Spatial Encoding

One of the landmarks in the history of NMR was the realization in 1973 of methods of spatially encoding NMR signals,<sup>57,66</sup> and later of spatially localizing NMR signals.<sup>31</sup> This allowed an image consisting of the NMR signal from various spatially localized volumes throughout the sample to be constructed. This is done by applying linear magnetic gradients and RF pulses to the sample. Various techniques have been used but the most popular ones at the present time for acquiring two dimensional images (slices) through a sample are the spin warp technique and its high speed variants such as FLASH, and Echo Planar Imaging (EPI). These techniques are described below. The RF pulse sequences described in Section 2.2.4 above can be used with these to create images with their pixel intensities weighted by  $\rho$ ,  $T_1$ , or  $T_2$  as desired.

#### Slice Selection

To image a plane slice through a sample it is desirable that an NMR signal is only received from that slice. This can be achieved by selective excitation of only the spins in the required slice. It is assumed that the required slice is perpendicular to the  $z$  axis. If the sample is placed in a static magnetic field  $\mathbf{B}_0$  and a smaller uniform magnetic field gradient  $G_z$  is also applied, such that the magnetic field along the  $z$  axis is described by

$$B_z = \mathbf{B}_0 + zG_z \quad (2.18)$$

## 2. An Introduction to Nuclear Magnetic Resonance Imaging

---

where

$$G_z = \frac{\partial B_z}{\partial z} \quad (2.19)$$

then the Larmor frequency of spins will depend on their position along the  $z$  axis such that

$$\omega(z) = \gamma(B_0 + zG_z) \quad (2.20)$$

Hence the Larmor frequency has been spatially encoded along the  $z$  axis (see Figure 2.11). If a RF pulse of a certain frequency is applied then only the nuclei precessing at that frequency will be excited. The thickness of the slice excited depends on the bandwidth of the RF pulse and the magnitude of  $G_z$ . A wider bandwidth or a weaker gradient will result in a thicker slice. This process is called slice selection.

As explained at the end of Section 2.2.2, it is usual to modulate finite RF pulses used for MRI with a sinc envelope. A finite sinc RF pulse may be considered to affect  $M_0$  instantaneously at the centre of the duration of its application. However, to ensure slice selection occurs,  $G_z$  must be applied throughout the whole application of the RF pulse. This results in the spins in the excited slice being dephased at the end of the application of  $G_z$ . The spins must be brought back into coherent phase in order for a NMR signal to be detected. This is performed in the same manner as the formation of a gradient echo, described in Section 2.2.4 and is referred to as slice refocusing. If the RF pulse was considered to act at the mid-point of its application, then the dephasing occurs from this point onwards under the influence of  $G_z$ , forming an area  $A_s$  (being the product of  $G_z$  and time). To rephase the spins, a gradient of opposite sign must be applied with equal modulus area to  $A_s$ .

A feature of MRI not available with any other non-destructive tomographic imaging technique is the ability to acquire images with any orientation through the sample, without moving the sample or imaging apparatus. Although this section relates the  $x$ ,  $y$ , and  $z$  axes with the frequency, phase, and slice axes, this need not be the case. It may be required that the latter axes are rotated relative to the physical  $x$ ,  $y$ , and  $z$  axes of the magnet, to obtain an oblique slice.

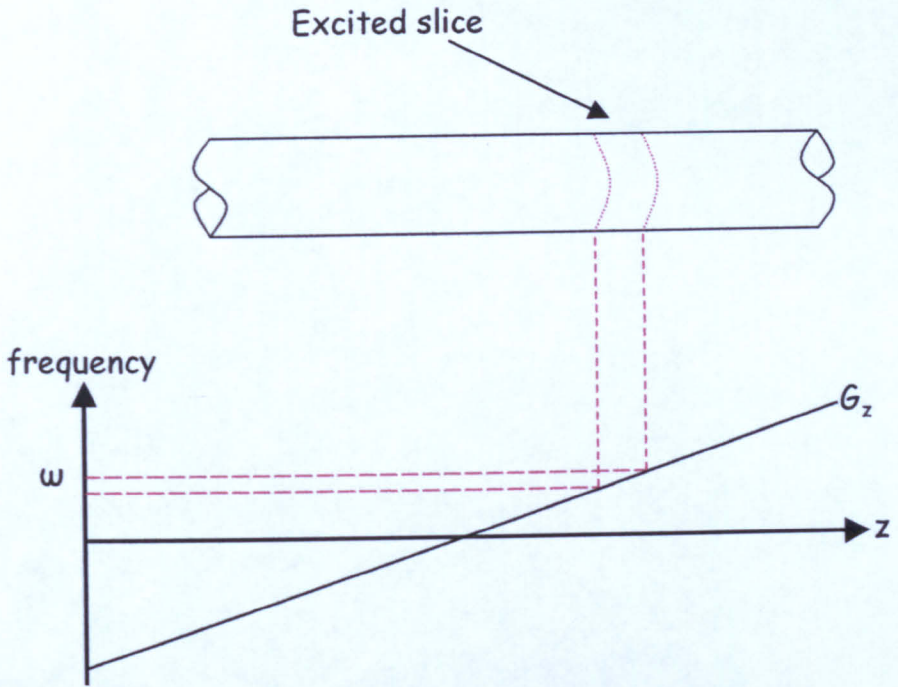


**Figure 2.11** Slice selection. A RF pulse with frequency  $\omega$  applied while  $G_z$  is active, selectively excites a slice in the sample.

## 2. An Introduction to Nuclear Magnetic Resonance Imaging

---

This is done by simultaneously applying combinations of the physical  $x$ ,  $y$ , and  $z$  axis magnetic gradients so that the combination of three magnetic gradients result in a gradient in the required direction.

### Frequency Encoding

It can be seen that if selective excitation is successively applied with magnetic gradients along the  $x$ ,  $y$ , and  $z$  directions, then it would be possible to excite just one volume element (voxel) in the sample. However to construct a NMR image by consecutively exciting different voxels is very time consuming, inefficient, and will result in a relatively poor image. If a magnetic gradient is applied after the RF pulse and  $G_z$  have ceased, along the  $x$  axis (for example) then the frequency of each resonating nucleus is encoded along the  $x$  axis, where

$$\omega(x) = \gamma(B_0 + xG_x) \quad (2.21)$$

where

$$G_x = \frac{\partial B_z}{\partial x} \quad (2.22)$$

The NMR signal is collected simultaneously to the application of  $G_x$  and consists of a band of frequencies corresponding to the NMR signals of precessing nuclei across the  $x$  axis. This is the sum of the individual NMR signals of spins rotating at different frequencies and weighted by the number of spins at each frequency. If the Fourier transform (FT) is taken of this signal, the frequencies and weightings will be revealed. As the Larmor frequency is a linear function of the displacement along the  $x$  axis (see Equation 2.21) then the FT will be a projection of the resonating nuclei along the  $x$  axis. The NMR signal has been spatially encoded, and this method is termed frequency encoding, as the spatial position depends on the frequency of the spins at that point. This is shown in Figure 2.12. The gradient applied while the NMR signal is acquired is the frequency encoding, or read, gradient.

The usefulness of acquiring NMR signals as echoes rather than FID's can now be seen. If the NMR signal and spatial projection are considered as a Fourier transform pair, then to fully describe the projection in real space, both positive

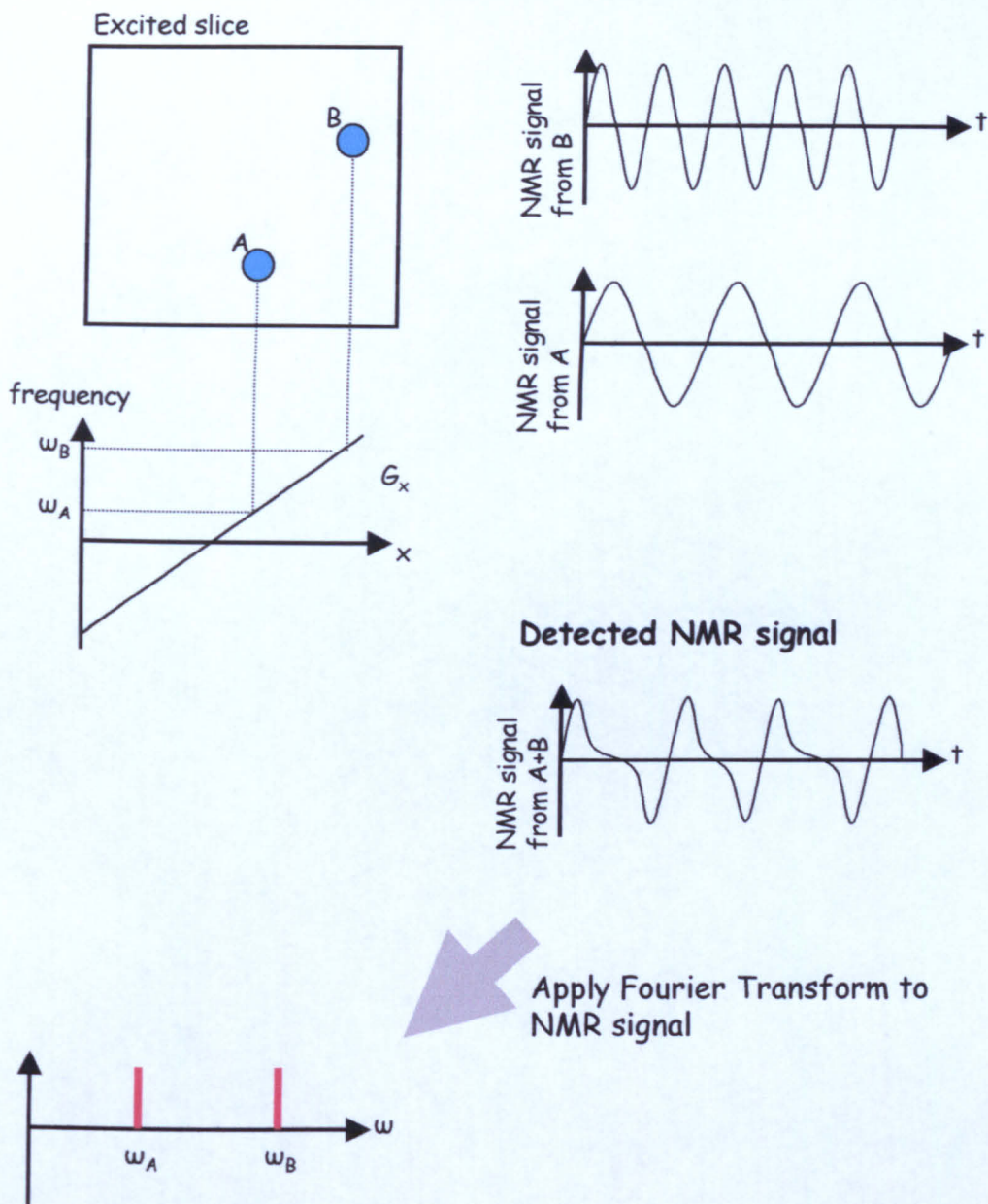


**Figure 2.12** Frequency encoding. During acquisition of the NMR signal, a gradient  $G_x$  is applied to the sample containing two objects. The FT of the NMR signal yields the projection of the sample on the  $x$  axis. Only the positive portion of the FT is shown. The envelope of the NMR signal is not included for clarity.

## 2. An Introduction to Nuclear Magnetic Resonance Imaging

---

and negative 'spatial frequencies' are required in the NMR signal. The origin of the NMR signal in relation to the Fourier transform, is when all the spins are in phase. This occurs at the centre of an echo, and hence the NMR signal of an echo contains both negative (before the centre of the echo) and positive (after the centre of the echo) components. An FID only contains a dephasing NMR signal, *i.e.*, the positive components. In practice, this results in artefacts in the projection of the sample; these are described more fully in the section dealing with half Fourier MR images below.

The idealized frequency encoded NMR signal can be described mathematically. In the presence of only the uniform static magnetic field  $B_0$ , the NMR signal amplitude will depend on the density of spins within the sample,  $\rho(x)$ , the Larmor frequency, and the relaxation processes. If the relaxation processes are ignored, then the NMR signal in the laboratory frame is

$$S(t) \propto e^{i\gamma B_0 t} \int \rho(x) dx \quad (2.23)$$

where  $t$  is the time during the NMR signal acquisition, with its origin when the spins are in phase, at the centre of an echo. The application of a linear frequency encoding gradient,  $G_x$ , as described by Equation 2.21 results in a NMR signal of

$$S(t) \propto \int e^{i\gamma(B_0 + xG_x)t} \rho(x) dx \quad (2.24)$$

Equation 2.24 is a Fourier transform, where  $S$  is the FT of  $\rho$ . Therefore, the inverse FT of  $S(t)$  yields  $\rho(x)$ .

To achieve frequency encoding requires the application of a magnetic gradient, as described above. However, this gradient will cause dephasing of the spins, as described in Section 2.2.4 referring to gradient echoes. This will result in a spin echo with reduced amplitude. To overcome this, a gradient echo is formed along the frequency encoded axis and arranged to peak at the centre of the spin echo. This is achieved by applied a gradient along the same axis but of opposite sign to the frequency encoding gradient, prior to application of the frequency encoding gradient itself. The dephasing caused by the initial gradient is refocused by the frequency encoding gradient to form an echo.

### Projection Reconstruction

By applying magnetic gradients along both the  $x$  and  $y$  axes simultaneously during collection of the NMR signal, a projection of the sample can be collected at any chosen in-slice angle. Hence a two dimensional image can be constructed using similar methods to those used for x-ray CT image construction, *i.e.*, using filtered backprojection or iterative algebraic reconstruction techniques (ART). This method of acquiring MR images is termed projection reconstruction. Although methods involving projections were used to create two dimensional NMR images in the early days of MRI, they have been superseded by spin warp techniques in the vast majority of MRI techniques.

In order to obtain all the projections required for image reconstruction, at least one iteration of the pulse sequence is required for each projection. As outlined in Section 2.2.4 above, after acquiring a NMR signal, it is necessary to wait some time,  $TR$ , before repeating the pulse sequence. This allows sufficient  $T_1$  recovery to occur so that a significant component of  $M_0$  is parallel to  $B_0$  and available to be tipped into the  $x$ - $y$  plane by the next  $90^\circ$  RF pulse. To obtain a sufficiently large NMR signal in biological tissue this repetition time between acquisitions,  $TR$ , is between 300 ms and several seconds, resulting in imaging times of several minutes. Hence imaging moving structures (*e.g.*, the human chest or abdomen) proves to be difficult, as these structures will not be in the same spatial location for the acquisition of each projection and the reconstructed image will suffer from artefacts.

### 2.3.2 Two Dimensional Fourier Techniques and $k$ Space

In the description of the projection reconstruction technique for producing MR images, given above, one dimensional FT's are performed to obtain projections of the sample at many angles, from which a two dimensional image can be produced. This relationship between a NMR signal (in the time domain) and a one dimensional projection of the sample obtained by the Fourier transform of the NMR signal, can be extended to two dimensions.<sup>55</sup> That is, a two dimensional Fourier transform pair exists between the two dimensional image and a two dimensional data set of NMR signals. In order to produce a MR image, the correct

## 2. An Introduction to Nuclear Magnetic Resonance Imaging

---

set of NMR signals must be collected to fill this data set.

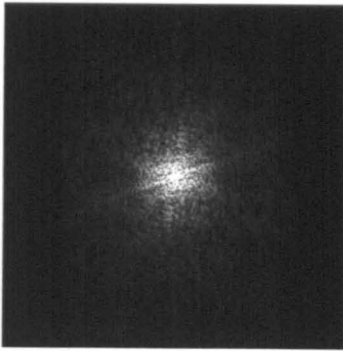
From the outset of work on the spatial localization of NMR signals<sup>66</sup> it was realized that a useful concept was that of a variable to describe the 'reciprocal lattice' of the image, and with reference to optics, this was termed  $k$ . This variable references the Fourier transform of the image space (*i.e.*, the NMR signals) and is in units of distance<sup>-1</sup>, representing a spatial frequency. The set of NMR signals which it describes is termed  $k$  space.

The acquisition of a MR image by projection reconstruction method can be described in terms of  $k$  space. When the frequency encoding gradient is applied solely along the  $x$  axis, the NMR signal acquired is sampling  $k$  space along the  $k_x$  axis. When the frequency encoding gradient is entirely along the  $y$  axis, a line along the  $k_y$  axis is acquired. For projections of intermediate angles, the gradient is applied along both  $x$  and  $y$  axes resulting in the NMR signal sampling  $k$  space in an oblique direction, but always passing through the origin of  $k$  space. This results in  $k$  space being sampled in a star type pattern, being densely sampled near the origin (*i.e.*, low spatial frequencies, contributing mainly to the contrast of the MR image) and sparsely near the edges (high spatial frequencies, contributing mainly to the edges of the MR image). Although not a projection reconstruction MRI acquisition, Figure 2.13 shows the contribution of high and low spatial frequencies in  $k$  space to the final MR image.

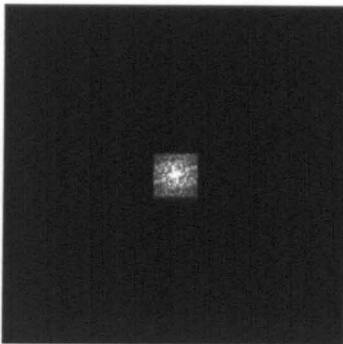
The sampling of  $k$  space is controlled by application of the  $x$  and  $y$  magnetic gradients. This means that any manner of trajectory through  $k$  space may be devised by appropriate manipulation of the gradients. A FT of the acquired  $k$  space will result in a MR image. In particular, an even rectilinear sampling of  $k$  space is desirable as it reduces some of the artefacts observed in projection reconstruction images, which are due to the varying combinations of inhomogeneities in the  $x$  and  $y$  magnetic field gradients. Such a trajectory is produced by a spin warp technique.

### Spin Warp

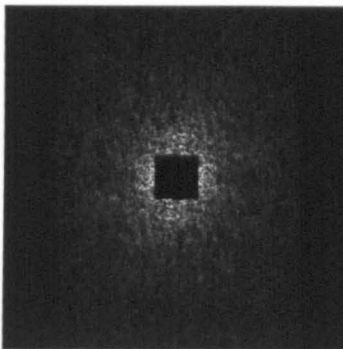
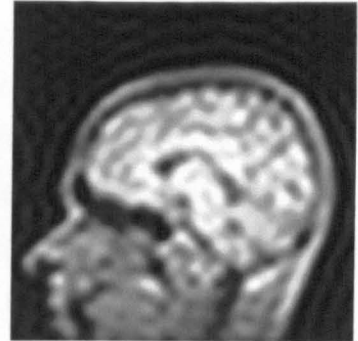
The spin warp imaging sequence<sup>28</sup> was first introduced in 1980, and is performed as follows. A 90° RF pulse followed by a 180° pulse is used to create a spin



a) complete  $k$  space



b) low spatial frequencies  
of  $k$  space



c) high spatial frequencies  
of  $k$  space

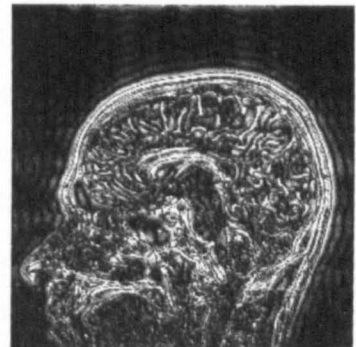


**Figure 2.13** Contributions of low and high spatial frequencies to a MR image. Low spatial frequencies contain contrast information; high spatial frequencies contain edge information. No smoothing was applied to the partial  $k$  space maps, so images suffer from ringing artefacts.

## 2. An Introduction to Nuclear Magnetic Resonance Imaging

---

echo, during which a frequency encoded projection along the  $x$  axis is acquired as described above (hence the  $x$  axis is termed the frequency encoded axis). However, after the  $90^\circ$  pulse but before the application of the  $x$  axis (read) gradient, a magnetic gradient is briefly applied along the  $y$  axis. This has the effect of changing the phase of all the rotations of the spins within the excited slice by a known amount (hence the  $y$  axis is termed the phase encoding axis). The NMR signal is then acquired as before, representing one line in  $k$  space, parallel to the  $k_x$  axis. The sequence is repeated with the phase encoding gradient set to produce a different phase offset by applying a different strength gradient for the same period of time, resulting in another line of data in  $k$  space parallel to the  $k_x$  axis but with a different  $k_y$  value. This is repeated until sufficient scans through  $k$  space have been made to produce a satisfactory image. The phase encoding usually starts with the gradient with the most negative value and steps linearly through zero to the most positive value. A two dimensional Fourier transform of this  $k$  space data set results in a two dimensional image of the sample.

A qualitative description of phase encoding spatial information is given in Figure 2.14 and a typical spin warp pulse sequence is shown in Figure 2.15. This method typically is used to produce images with matrix sizes of  $256 \times 256$  or  $512 \times 512$ , resulting in pixel dimensions of less than one millimetre.

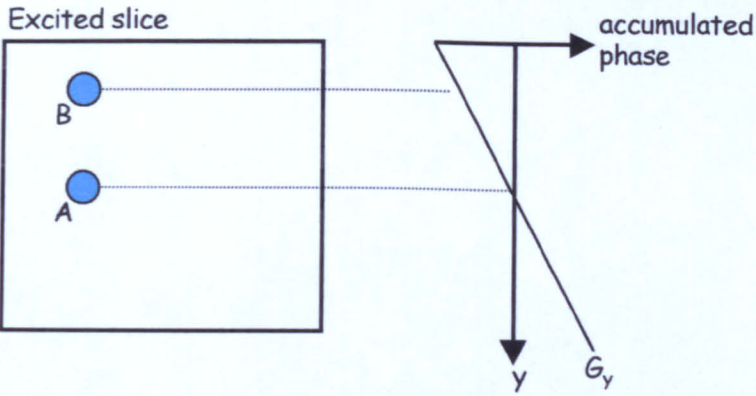
The idealized NMR signal from one frequency encoding line is given in Equation 2.24 above. This can be modified to include the effect of the phase encoding gradient,  $G_y$ , which has a different value for each frequency encoding line acquired, being  $G_y(n)$  for the  $n^{\text{th}}$  phase encoding line. Assuming  $G_y$  can be applied as a square pulse for a constant duration,  $t_y$ , then

$$S_{sw}(t, n) \propto \iint \rho(x, y) e^{i\gamma(B_0 + xG_x)t} e^{i\gamma G_y(n)t_y} dx dy \quad (2.25)$$

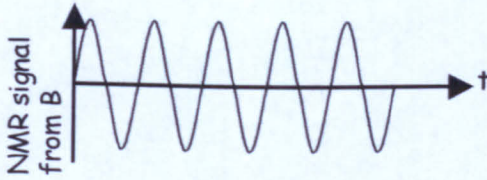
As the position of any point in  $k$  space is determined by a product of the gradient strength and the duration for which it has been applied (the area under the gradient),  $\mathbf{k}$  can be generally defined as

$$\mathbf{k} = \gamma \int \mathbf{G}(t') dt' \quad (2.26)$$

This allows representation of the more realistic case of gradient waveforms which are trapezoidal rather than square pulses through time. In certain cases the



*NMR signal with no phase encoding gradient applied.*



*NMR signal after application of phase encoding gradient.*

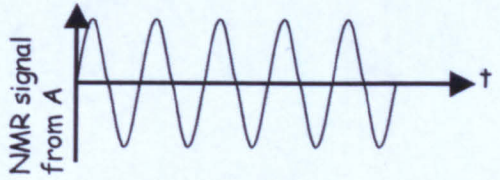
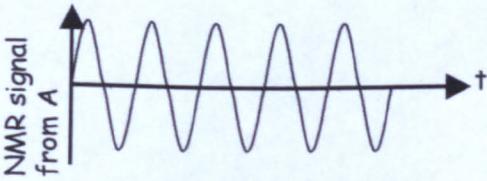
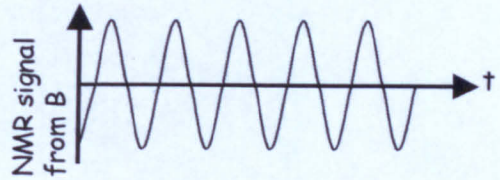


**Figure 2.14** Phase encoding. At the origin, A is unaffected by the application of a phase encoding gradient. The phase of B increases with increasing  $G_y$  and also depends on its  $y$  coordinate. After collecting a matrix of NMR signals with a range of  $G_y$ 's, the rate of change of phase (*i.e.*, a frequency) down a column of  $k$  space will give  $y$  positional information, which can be extracted using a discrete Fourier transform.

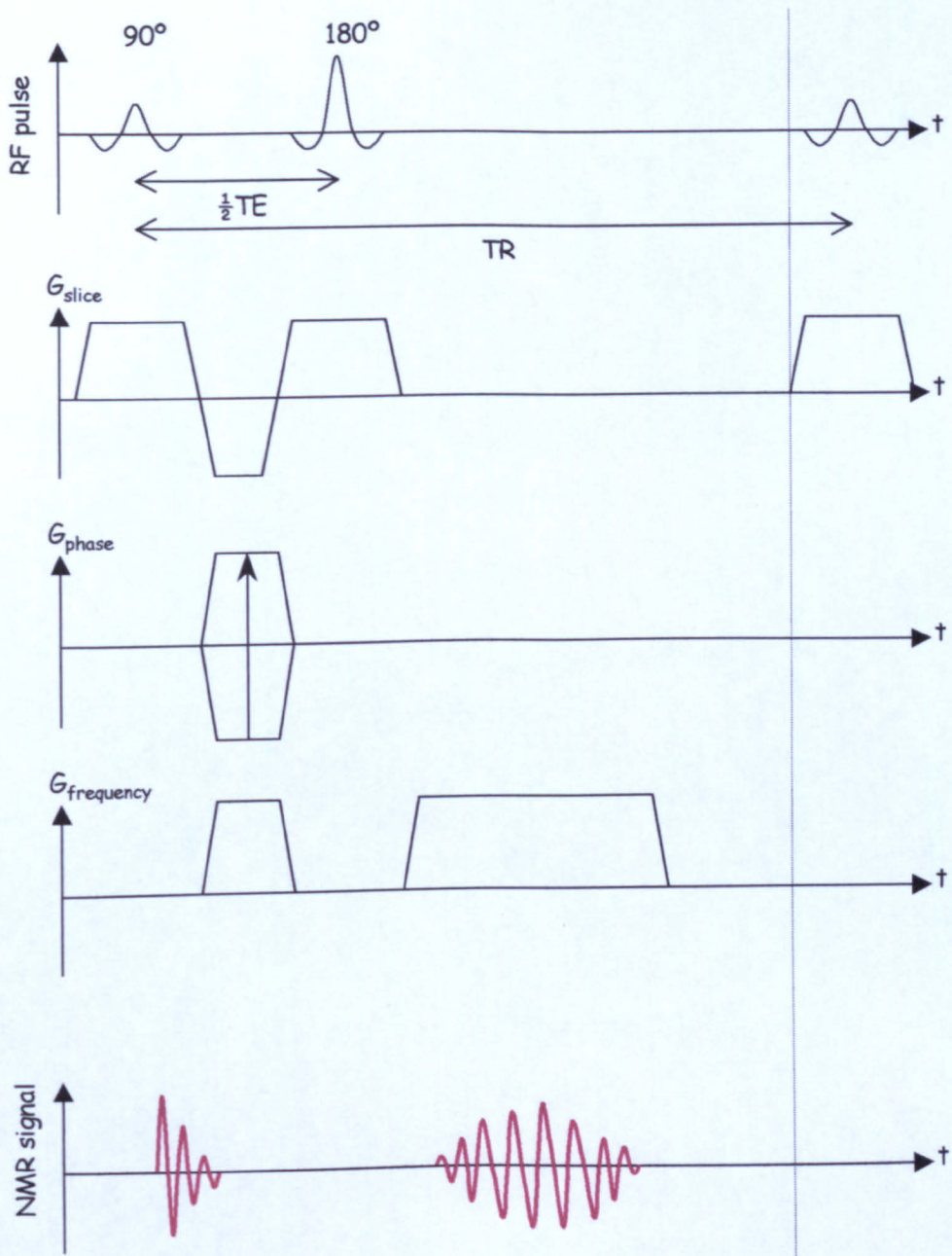


**Figure 2.15** Spin Warp MR imaging sequence. One frequency encoded line of  $k$  space is acquired per spin echo. After a time TR the sequence repeats with a different phase encoding gradient. The dephasing gradient along the frequency encoding axis, to create a gradient echo, is the same sign as the readout gradient as it is on the opposite side of the  $180^\circ$  RF pulse. Phase encoding gradients are indicated with an arrow to show that their amplitude changes with each TR period.

## 2. An Introduction to Nuclear Magnetic Resonance Imaging

---

gradient waveform may be deliberately non-linear, *e.g.*, when generated *via* a resonant circuit to allow rapid switching of the gradient.

Equation 2.25 for a spin warp acquisition can be rewritten as

$$S_{sw}(k_x, k_y) \propto \iint \rho(x, y) e^{ik_x x} e^{ik_y y} dx dy \quad (2.27)$$

where  $S_{sw}$  is now sampled in the rotating frame with the aid of p.s.d.'s, removing the frequency  $\gamma B_0$ , and where

$$k_x = \gamma \int_{-\frac{t_x}{2}}^t G_x(t') dt' \quad \text{and} \quad k_y = \gamma \int_0^{t_y} G_y(n, t') dt' \quad (2.28)$$

$\frac{t_x}{2}$  is the time before the centre of the echo in the frequency encoding direction at which the NMR signal acquisition is started.

It is not necessary to apply the gradients along all three axes at separate times; as they are orthogonal they may be applied simultaneously. For example, while the slice select gradient is ramping down or performing the slice refocusing lobe, the phase encoding gradient may be active, and the frequency encoding gradient may be ramping up to its plateau. However, while the NMR signal is being acquired, only the frequency encoding gradient should be active.

### Multislice Imaging

Often, several slices with different  $z$  axis positions are required during the study of a sample. If spin warp imaging is applied to each slice in turn, the total imaging time will be proportional to the number of slices acquired. This total study time can be reduced by interleaving the acquisition of multiple slices. The majority of the time in acquiring a spin warp image acquisition is spent after the NMR signal measurement, waiting for sufficient spin-lattice relaxation to have occurred before applying the next pulse (typically about 95% of the TR delay). During this time, another separate slice can be selectively excited and the NMR signal from it obtained independently from the first slice. This can be performed for several slices until TR for the first slice has elapsed. The total acquisition time for all the slices is then the same as the acquisition time for one slice. As described in Section 2.2.4 above, the choice of TR determines the  $T_1$  weighting of the MR image. For a chosen TR, only a certain number of multislice acquisitions

## **2. An Introduction to Nuclear Magnetic Resonance Imaging**

may be fitted into the period, before the first slice must be excited again. In practice, a compromise must be made between  $T_1$  weighting and the number of multiple slices to be acquired in one acquisition.

Section 2.3.1 above briefly described the process of slice selection. In practice, due to the finite duration of the RF pulse and the effect of inhomogeneous magnetic fields, the slice profile is never exactly rectangular. The width of the slice profile is usually defined by its width at half the maximum (or central) amplitude of the profile (FWHM). Hence, if slices are excited in turn in a multislice acquisition as described above, with no separation in between, interference will occur between the  $M_0$ 's of consecutive slices. This is known as slice 'cross-talk' and can lead to artefacts in the images. This effect may be reduced in a multislice acquisition by interleaving the slice excitation order so that the time between exciting adjacent slices is maximized, allowing as much spin-lattice relaxation as possible to occur. For example, in one TR period, the odd number slices are acquired first followed by the even numbered slices, in ascending order. To totally avoid any potential artefact of this kind, an abutting slice should not be excited until spin-lattice relaxation has occurred fully in any neighbouring slices. This may be done by performing two separate multislice acquisitions, the first acquiring the odd slices, the second acquiring the even. All slices are separated by one slice width, and a short TR may be used for both acquisitions.

### **FLASH**

As with the projection reconstruction method, to acquire a spin warp image takes several minutes. This time can be reduced by using a Fast-Low-Angle-SHot (FLASH) technique, first introduced in 1985 by Haase *et al.*<sup>32</sup> It is based on the spin warp sequence described above with two modifications. Firstly, a gradient echo is used rather than a spin echo, and secondly a RF pulse with a flip angle of less than  $90^\circ$  is used for excitation. Use of a gradient echo reduces the total time taken to acquire one frequency encoded line of  $k$  space, as no time is required to apply the refocusing  $180^\circ$  pulse and associated slice selective gradients. Shorter TE's may be obtained than with spin echo techniques. The use of a low flip angle RF pulse (typically between  $10^\circ$  and  $50^\circ$ ) results in  $M_0$

## 2. An Introduction to Nuclear Magnetic Resonance Imaging

---

not being tipped completely into the  $x$ - $y$  plane; a component remains parallel to  $B_0$ . This results in a relatively larger proportion of  $M_0$  being available for the next low flip angle RF pulse used for the next frequency encoding line. Hence, the TR between frequency encoding lines of  $k$  space in the same slice may be reduced and so the entire image may be acquired more rapidly. On a 1.5 T MR scanner imaging biological tissue, a reasonable FLASH image will be obtained with parameters such as TR=40 ms and a flip angle of  $30^\circ$  resulting in a  $256 \times 256$  matrix image being acquired in about ten seconds.

As short TR values are used, coherent transverse magnetization may remain at the end of a TR period and interfere with the subsequent RF pulse. To remove this effect, spoiler gradients are applied to dephase any remaining transverse magnetization. These are usually applied along the frequency encoding axis for reasons mentioned below.

The use of RF flip angles of less than  $90^\circ$  affects the quality of the image. As a smaller component of  $M_0$  is tipped into the  $x$ - $y$  plane, a smaller e.m.f. is induced into the RF coil during reception of the NMR signal, resulting in a lower signal relative to the constant noise. The lower the flip angle (in order to acquire images more rapidly) the lower the signal to noise ratio in the image. Also, the choice of flip angle will influence the amount of spin-lattice relaxation which can occur in the TR period. For the first few low flip angle RF pulses, the magnetization parallel to  $B_0$  will decline until eventually a steady state will arise where the fraction of  $M_0$  tipped into the  $x$ - $y$  plane is matched by that returning to be parallel to  $B_0$  from previous shots. The steady state value will depend on the flip angle, TR, and  $T_1$  of the sample. By fixing TR, the  $T_1$  weighting of the image may be varied by changing the flip angle alone. For a particular  $T_1$  and TR it is possible to optimize the flip angle to obtain maximum NMR signal; this angle is called the Ernst angle,  $\alpha_E$ , and is given by

$$\cos \alpha_E = e^{-\frac{TR}{T_1}} \quad (2.29)$$

MR imaging sequences based on the FLASH technique are very popular on clinical MR systems. However, an important drawback of FLASH techniques is the difficulty in adapting the sequence to obtain contrast from anything other than  $T_1$  saturation recovery mechanisms. The addition of a RF inversion pulse

## 2. An Introduction to Nuclear Magnetic Resonance Imaging

---

before acquiring each line of  $k$  space, to produce inversion recovery  $T_1$  contrast, is not possible without compromising the short imaging times. The TI effectively adds to the TR and with TI's typically between 150 ms and 800 ms on 1.5 T MR scanners, short TR's are not possible.  $T_2$  weighting is also difficult to obtain, since the long TE's required increase the TR. Also, as the gradient echo envelope decays more rapidly than the actual  $T_2$  envelope, true  $T_2$  weighting is not achieved, combined with less signal available in the gradient echo itself.

These limitations may be overcome with the use of so-called "TurboFLASH" (also called snapshot FLASH) techniques. These use the same sequence as described above for FLASH, but optimized for very low flip angles, and as short TR values as possible, typically  $5^\circ$  and 10 ms. There is no 'dead' time in a TR interval for multislicing to occur, so all the phase encoding lines for an image are acquired consecutively. While TurboFLASH MR images may be acquired in the order of one second, the signal to noise in the resulting image is very low. As very small RF flip angles are used, the vast majority of  $M_0$  remains parallel to  $B_0$  throughout the acquisition, resulting in images with only very small  $T_1$  weighting; the images being predominantly proton density weighted. As the sequence itself creates little  $T_1$  or  $T_2$  weighting, RF pulses may be applied prior to the TurboFLASH sequence to prime the spins with the desired weighting, such as those described in Section 2.2.4 above. Applying preparation pulses to invert the spin system prior to a TurboFLASH acquisition is often termed Magnetization Prepared Rapid Acquisition Gradient recalled Echo (MP-RAGE). Care must be taken when selecting the delay between the inversion RF pulse and the beginning of the TurboFLASH acquisition. Contrast in a MR image is mainly defined by the low  $k$  space spatial frequency components. Therefore, the effective TI (compared to spin warp MRI) will be the time between the inversion RF pulse and the frequency encoding line which traverses the centre of  $k$  space (*i.e.*, with no phase encoding). Single slice TurboFLASH sequences are typically used to image the heart within the duration of a breath-hold or to monitor the first pass of a blood contrast agent through a slice. Because a significant amount of magnetization remains along the axis parallel to  $B_0$ , not only are short TR times possible, but subsequent images may be acquired of the same slice in rapid

## 2. An Introduction to Nuclear Magnetic Resonance Imaging

succession. Their other main use is for three dimensional imaging, as described below.

The popularity of FLASH based MRI sequences has spawned a variety of modifications and wide range of acronyms to describe the same sequences.<sup>81</sup> Often, this has arisen due to competition between manufacturers of MRI systems, as well as due to issues of copyright and patents. These sequence variants are described in more detail elsewhere.<sup>15,81</sup> Because of the short TR's used between RF pulses, the transverse magnetization also reaches a steady state, as described above, and may involve stimulated and secondary echoes. The steady state may either be deliberately utilized or destroyed. To reach and maintain a steady state, the total gradient strength applied along each axis must remain constant for each line of  $k$  space acquired. As the phase encoding gradient changes with each line, an opposite gradient must be applied along the phase encoding axis after the NMR signal has been acquired to cancel out the effect of the first phase encoding gradient (*i.e.*, return to the  $k_y=0$  line in  $k$  space). This is called rewinding the phase. Sequences based on this FLASH variant are called GRASS (Gradient Recalled Acquisition in Steady State), FISP (Fast Imaging with Steady-state Precession), FAST (Fourier Acquired steady State). These sequences are arranged to only sample the primary gradient echo; stimulated and secondary echoes are made to occur outside the NMR sampling window. Similar steady state FLASH based techniques, which only sample the stimulated and secondary echoes are called SSFP (Steady State Free Precession), PSIF (mirrored 'FISP'), and CE-FAST (Contrast Enhanced 'FAST'). The contrast mechanisms for steady state FLASH based sequences are complex. To maintain only  $T_1$  weighting in a FLASH image, any build up of steady state transverse magnetization between TR periods must be destroyed. This is performed by use of pseudo random spoiler gradients along all axes (the original FLASH) and by varying the phase of the RF pulses by a pseudo random amount (SPGR – Spoiled 'GRASS', RF-FAST – RF spoiled 'FAST'). This results in  $T_1$  weighting at the expense of decreased signal to noise due to the lack of contribution from stimulated and secondary echoes.

## 2. An Introduction to Nuclear Magnetic Resonance Imaging

### Three Dimensional MRI Acquisitions

One of the advantages of MRI compared with other non-destructive imaging techniques is its ability to acquire multiple slices throughout the sample at any oblique angle. If contiguous multislices are acquired a three dimensional volume of the sample may be built up. However, to obtain MR images with a satisfactory signal to noise, the slice thickness is usually larger than the in-slice pixel dimensions resulting in a multislice volume with non-cubic voxels.

It is also possible to acquire NMR signal from throughout an excited volume resulting in a true MR volume acquisition. This is often performed using a modified TurboFLASH sequence. The slice selective portion excites the entire volume, or slab, to be imaged. If the entire sample is to be imaged in a single volume, slice selection is not required; all the spins in the sample are excited by the RF pulse. Phase encoding now occurs along two axes, one of which may be thought of as the usual in-plane phase encoding axis and the second axis as phase encoding in the slice selection direction. Phase encoding steps along the slice selective axis are often referred to as partitions, and the entire excited volume as a slab, in order to distinguish them from the excited slice in two dimensional imaging. Frequency encoding occurs along the third axis as normal. In order to acquire the entire volume, all the phase encoding steps in both axes must be stepped through, *i.e.*, for 256 in-plane phase encoded lines and 128 partitions, 32768 frequency encoding NMR signals must be acquired. In order to acquire all these data in an acceptable time, the repetition time for the frequency encoding axis must be very short. A three dimensional Fourier transform is performed on the entire three dimensional  $k$  space data set to produce the MR volume. This volume is usually stored as a series of contiguous images.

Volume acquisitions may be weighted with  $T_1$  contrast by application of a preparation inversion RF pulse. Phase encoding steps may increment most rapidly (per frequency encoding line) either in the partition or the in-plane phase encoding directions. The inversion pulse would be applied once per the most rapidly varying phase cycle. This sequence is called 3D MP-RAGE and shown in Figure 2.16 in its steady state form. Other steady state FLASH sequences may be modified for volumetric acquisitions, resulting in images weighted with a combi-

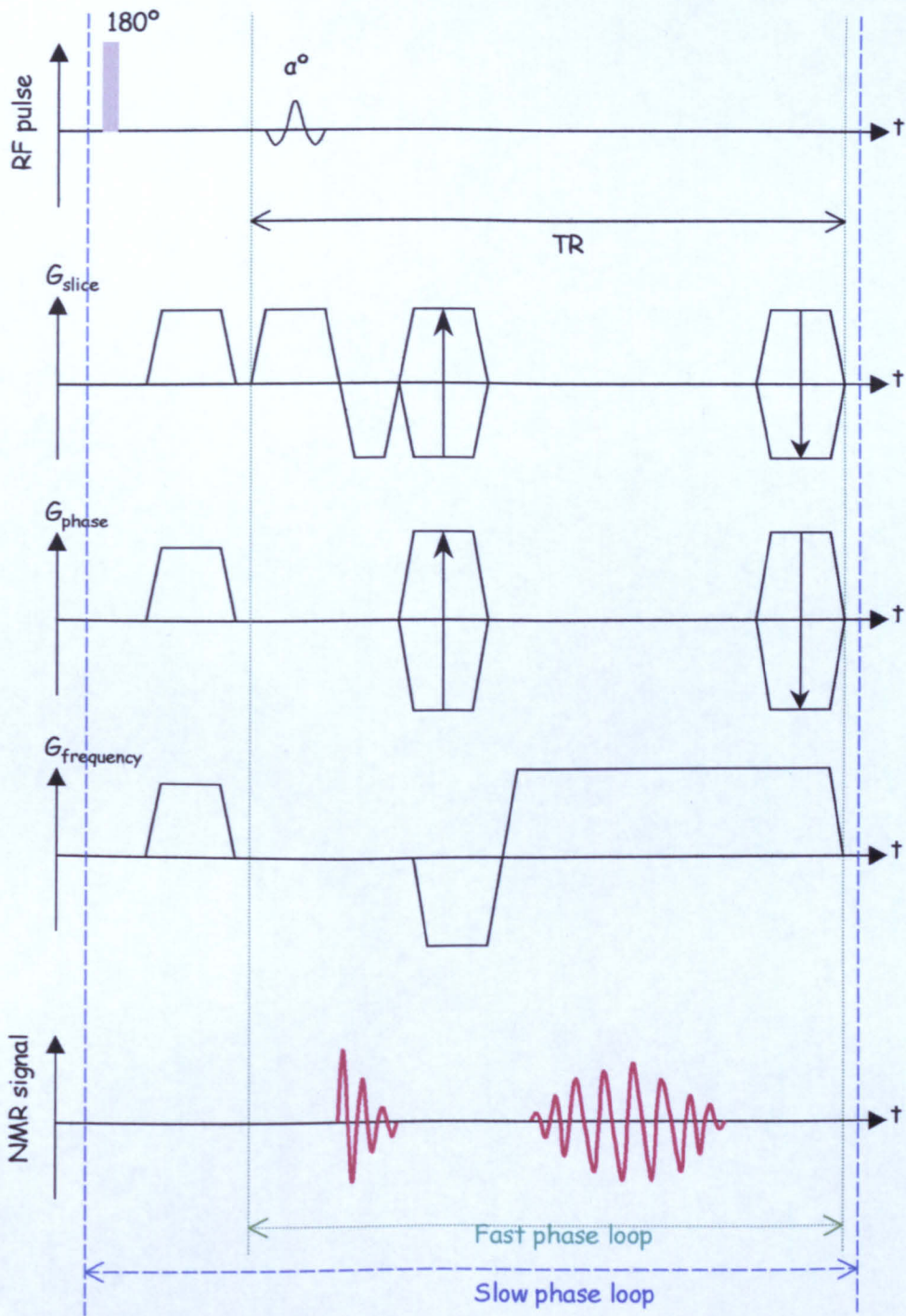


**Figure 2.16** 3D MP-RAGE imaging sequence.. One FLASH frequency encoded line of  $k$  space is acquired per gradient echo; the slice selective RF pulse excites the whole slab. Phase encoding occurs along both the in-plane phase encoding axis and the slice axis. For each phase encoding step of the 'slow' phase axis, a non selective RF inversion pulse is applied and spoiled. The section between the green dotted lines is then repeated with each repetition incrementing the 'fast' phase encoding axis until all 'fast' phase encoding steps have been performed. All phase encoding axes are rewound to preserve a steady state between repetitions. The frequency encoding gradient remains on to spoil any transverse magnetization.

## 2. An Introduction to Nuclear Magnetic Resonance Imaging

---

nation of  $T_1$  and  $T_2^*$  weighting. Two of these are called Constructive Interference in Steady State (3D CISS) and Double Echo Steady State (3D DESS).

At first, there may seem to be little gain in performing a volume acquisition in comparison to a multislice TurboFLASH acquisition with the same number of slices as there were partitions. However, volume acquisitions have several advantages compared to multislice imaging with the same voxel dimensions, as described below.

The signal to noise ratio (SNR) in a MR image depends on the voxel size and the number of times the acquisition is repeated (among other things). Consider a comparison between a single slice acquisition and a partition from a volume acquisition with identical acquisition parameters. The single slice thickness and partition thickness is  $v_z$ , and  $N_p$  partitions were acquired. In the single slice case, the  $SNR_{slice} \propto v_z$ . For the volume acquisition, the data from the slab is acquired  $N_p$  times, resulting in an improvement of  $\sqrt{N_p}$  in the SNR for the entire slab, giving  $SNR_{partition} \propto \frac{(v_z \times N_p)}{N_p} \sqrt{N_p}$ . The fractional increase in SNR for the partition compared to the single slice<sup>81</sup> is  $\sqrt{N_p}$ . Hence, volume acquisitions result in improved SNR, or alternatively thinner slices with the same SNR, compared to multislice acquisitions.

As mentioned above, in Section 2.3.1, in practice the profile of an excited slice is not rectangular. However, as the partitions in a volume acquisition are defined by phase encoding rather than selective excitation, their partition profile is far more rectangular. For the same reason, cross talk between partitions does not occur in volume acquisitions. Furthermore, as will be seen in Chapter 4, spatial distortion in MR images does not occur along the phase encoding axis. Hence, while a single slice may be distorted in two axes, a partition will only be distorted along one axis.

The main disadvantages of volume acquisitions are patient movement and the difficulty in adapting them for use with spin echoes. Isolated movement during a multislice TurboFLASH acquisition would only affect the slice being acquired at the time it occurred. For a volume acquisition, movement at any time throughout the acquisition will affect all partitions *via* the three dimensional FT. The use of spin echoes in volume acquisitions would be advantageous to further increase the

## 2. An Introduction to Nuclear Magnetic Resonance Imaging

SNR and provide  $T_2$  weighting. However, their use would considerably increase the acquisition time. Multiple spin echoes, as described below, may be used for volume acquisitions. While the prevalence of the 3D spin echo techniques may increase in the future, they are not currently in common use.

### **2.3.3 Rapid MRI with Multiple Echoes**

The spin warp based MRI sequences describe above all acquire one NMR signal per RF excitation pulse. However, in the vast majority of sequences the duration of the NMR signal acquisition is far shorter than  $T_2$ . Hence, there is still a coherent component of  $M_0$  in the  $x$ - $y$  plane. In the MRI sequences described above, this signal is usually not required and removed by dephasing. Rather than trying to eliminate it, multiple echo sequences refocus the transverse magnetization and use the subsequent echoes to acquire extra phase encoded lines of  $k$  space. This is a far more efficient use of the transverse magnetization than in spin warp based sequences. It results in more rapid imaging, as a new RF excitation is not required for each frequency encoding line. By choosing the amount of phase encoding for each echo, the resultant images may be weighted by  $T_1$ ,  $T_2$ , or  $T_2^*$ .

However, multiple echo techniques also introduce extra problems. In particular, each echo in the echo train occurs at a different time after the RF excitation pulse, and so will contain a unique  $T_2$  weighting. In a single echo spin warp image, each frequency encoding line is acquired at the same time after the RF excitation pulse; they will all have the same  $T_2$  weighting. The effect on the MR image of different lines of  $k$  space having different  $T_2$  weighting is not obvious, and in extreme cases may introduce artefacts. Multiple echo acquisitions are also less forgiving on imperfectly shaped gradient pulses and sequence timings. What may be only a small effect at the first echo may have increased to a larger and more serious effect in the later echoes.

#### **Multiple Spin Echo**

MR imaging sequences may be constructed by combining a spin warp imaging sequence with a CPMG<sup>16,72</sup> type RF pulse sequence (see Section 2.2.4 above). The first echo is acquired as for a normal spin warp sequence, described above.

## 2. An Introduction to Nuclear Magnetic Resonance Imaging

Further  $180^\circ$  RF pulses, separated by a time TE, refocus the previous echo into a new echo which also may be frequency encoded. Care must be taken to ensure that the repeated gradient echoes caused by the frequency encoding gradient always coincide with the spin echoes. Phase encoding is applied immediately before each frequency encoding line is acquired. In order to reduce image artefact, it is usual to 'rewind the phase' immediately after the cessation of the frequency encoding gradient and before the next  $180^\circ$  RF pulse is applied.

The number of echoes which may be formed from the FID following one RF excitation is limited by the  $T_2$  of the sample and the rate at which echoes may be formed. The time for one TE period depends on the time taken to apply a  $180^\circ$  pulse and to switch the various gradients on and off (ramping), as well as the maximum gradient strength achievable which with the ramping time defines the area contained under a gradient pulse and hence the maximum possible excursion in  $k$  space and the minimum image resolution. On a modern clinical MR scanner, TE values for multiple spin echo sequences are typically of the order of 10 ms, and unlikely to be shorter than 5 ms.

When these techniques were first introduced in routine clinical use, contemporary gradient systems could not switch as rapidly or achieve high amplitudes, compared with systems produced today. Only a few multiple echoes could be acquired before the NMR signal had dephased due to  $T_2$  decay. In this case, the echoes would be phase encoded to cover  $k$  space sparsely in the phase encoding direction. This process would be repeated with a slightly different initial phase encoding offset following a subsequent RF excitation pulse. The resulting data are interleaved to produce the final map of  $k$  space. For example, to acquire 256 phase encoding lines of  $k$  space when an echo train length of 8 echoes is possible, would require 32 interleaves. These acquisition schemes have acronyms such as Fast Spin Echo (FSE) or Turbo Spin Echo (TSE). They are of particular use in acquiring  $T_2$  weighted images in a shorter time than would be required for spin echo spin warp schemes. While waiting for the required TE to elapse before acquiring the frequency encoding line through the central region of  $k$  space, other echoes can be acquired of the higher spatial frequency components.

On more modern MR systems, echo train lengths of up to 128 echoes may

## **2. An Introduction to Nuclear Magnetic Resonance Imaging**

be acquired, following one RF excitation. This allows a spin echo image to be acquired in a single shot with an acquisition time of less than one second. If both positive and negative portions of  $k$  space are acquired in the phase encoding axis, the sequence often is called Rapid Acquisition with Relaxation Enhancement (RARE)<sup>40</sup> – which originally covered interleaved TSE sequences as well as the single shot method. If only just over half of  $k$  space is sampled in the phase encoding direction, the sequence is often called Half Fourier Acquisition with Single shot Turbo spin Echoes (HASTE).

Rapid multiple spin echo sequences with 180° refocusing pulses have probably reached their lower limit, in terms of decreasing imaging times. A RARE sequence with a TE value of 5 ms applies a considerable amount of RF power to the patient, and is very close to the level II safety limit for RF absorption, as described in Section 2.6 below. Increasing the performance of the gradients will not allow more rapid acquisitions as it still will be limited by the SAR. Refocusing RF pulses of less than 180° may be used,<sup>39</sup> but this causes the introduction of more complex echo evolution schemes which interfere with the primary echo being acquired.

### **Echo Planar Imaging**

The use of multiple gradient echoes rather than multiple spin echoes, would be expected to reduce imaging times still further. A method for acquiring a MR image in the duration of one FID was proposed by Mansfield in 1977 and termed Echo Planar Imaging (EPI).<sup>64,101</sup> Although it may appear to be a logical step from the MRI sequences described above, it should be appreciated that EPI was proposed, and implemented on dedicated MR scanners, before most of the imaging schemes mentioned above.

An echo train of multiple gradient echoes may be performed very rapidly while simultaneously acquiring frequency encoded lines of  $k$  space. After the first gradient echo has been produced, the remaining duration of the frequency encoding gradient dephases the spins. If, after this, the gradient is immediately switched to be applied with the opposite polarity, a second gradient echo will be formed and may be acquired, under a gradient of opposite sign to the first. This

## 2. An Introduction to Nuclear Magnetic Resonance Imaging

---

can be repeated very rapidly until the NMR signal has been completely dephased due to  $T_2^*$  decay.

To produce an image, each frequency encoded gradient echo must be given differing amounts of phase encoding. A phase encoding scheme similar to that used for RARE could be used, however this would take a significant amount of time to apply (and rewind). The use of gradient echoes rather than spin echoes reduces the artefacts seen if the phase encoding axis is not rewound prior to the formation of another echo. Mansfield proposed applying only small amounts of phase encoding to increment subsequent frequency encoded lines along  $k_y$ . In the most common contemporary form of EPI, the phase encoding gradient is applied as a brief 'blip' while the gradient along the frequency encoding axis is reversing its polarity. The portion of  $k$  space scanned by EPI in the phase encoding direction can be selected by applying a single gradient pulse in the phase encoding direction prior to the EPI readout echo train. This gradient, of opposite polarity to the phase encoding blips to follow, is called a pre  $k$  space excursion. If it is set to half the area of the sum of all subsequent phase encoding blips, then  $k$  space is sampled symmetrically, and the EPI acquisition termed Modulus Blipped EPI (MBEST).<sup>47</sup> A MBEST sequence is shown in Figure 2.17. For EPI acquisitions, the frequency encoding axis is often referred to as the switched axis, while the phase encoding axis as the blipped or broadening axis.

Before performing a two dimensional DFT (see Section 2.4.1) on  $k$  space, every alternate phase encoded line must be reversed. This is because it was acquired under a gradient of the opposite sign and so sampled  $k$  space in the opposite direction. This may introduce an artefact in EP images not seen in other MR imaging modalities. In practice, the gradient waveforms along the frequency encoding axis are not exactly the shape demanded. In particular, the positive gradients may not be symmetric to the negative gradients. Unlike other MRI techniques, EPI acquisitions sample under both positive and negative gradient echo lobes. As alternate lines must be reversed (left–right) before the DFT is performed, a mismatch may arise in the position of the NMR signal between every other phase encoded line. This 'ripple' is at the highest frequency measurable by the DFT and results in two images being produced, one shifted by half the image

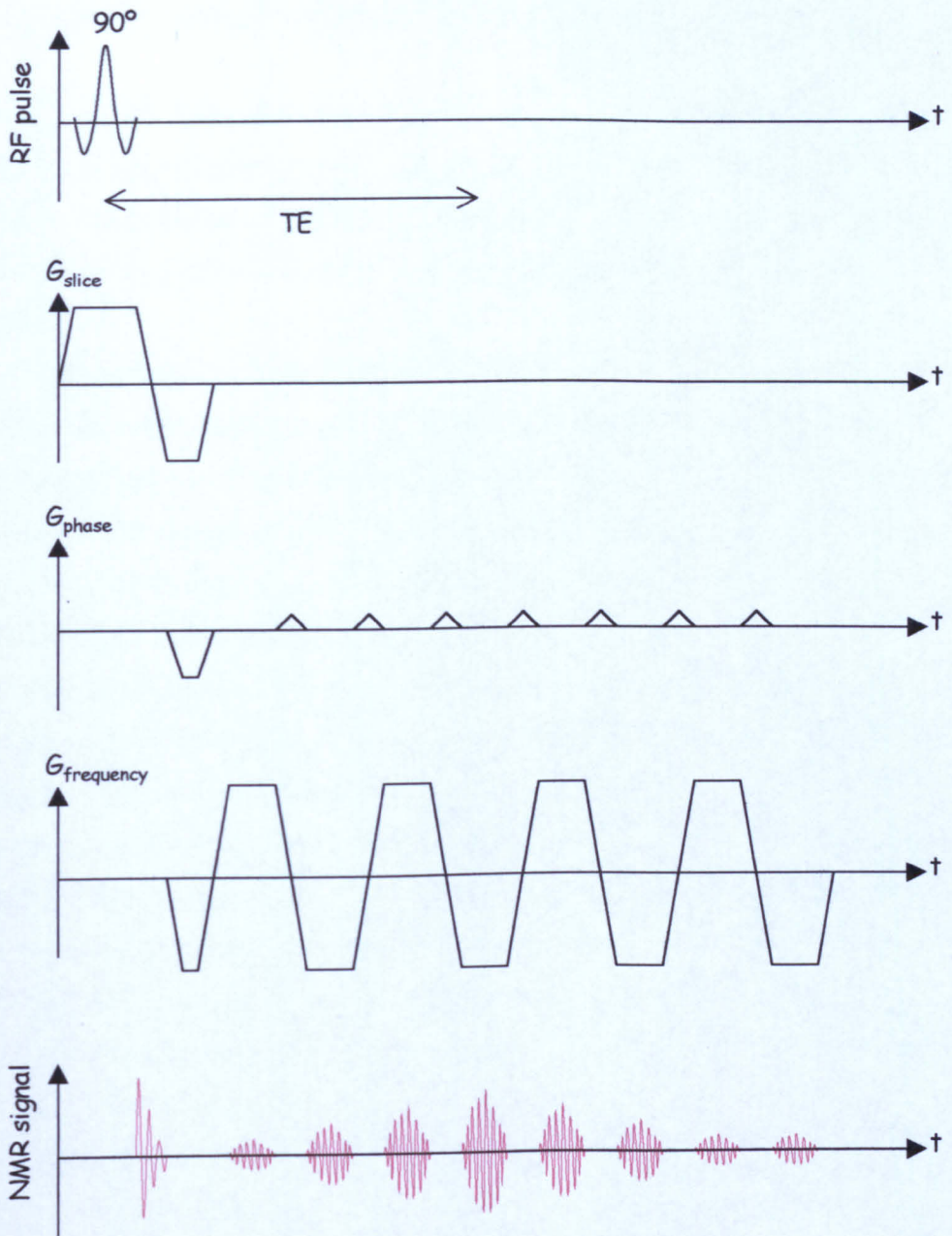


**Figure 2.17** MBEST EPI sequence. A train of gradient echoes are formed along the frequency encoding axis. Alternate echoes are of opposite sign. While the frequency encoding gradient is switching, a brief blip is applied along the phase encoding axis to increment the phase for the next echo. The sequence shown here would result in a MR image with an  $8 \times 8$  matrix.  $k$  space is sampled symmetrically for MBEST and a  $T_2^*$  weighted image is obtained.

## 2. An Introduction to Nuclear Magnetic Resonance Imaging

---

matrix compared to the other. The central image is considered the main image while the image shifted relative to it by half a matrix step is termed the Nyquist ghost. The fraction of the signal in the ghost relative to the main image may be reduced by careful calibration of the EPI acquisition and by post processing techniques.

The duration of EP acquisitions may be reduced further by acquiring the NMR signal under not just the uniform plateaus of the frequency encoding gradient, but under the rising and falling ramps also. It is usually desirable for a gradient to rise to its maximum value as fast as possible as this results in the maximum area for a fixed time under a particular gradient pulse. However, for the rapid switching of the frequency encoding gradient, required to acquire EP images as fast as possible, a significant time is spent ramping. Acquiring the NMR signal under a temporally varying gradient results in a non-uniform sampling of  $k$  space in the frequency encoding direction (see Equation 2.26). This introduces artefacts in the final image. A solution to this is to sample the NMR signal in a non-linear manner so that the acquired points in  $k$  space have a fixed spacing between them. Data is acquired more rapidly when the gradient is at its highest strengths. To enable non-linear sampling requires that the sampling window be aligned to the gradient waveform with greater accuracy than is usually required to avoid further image artefacts.

Typically, a frequency encoding line will be acquired in less than 1 ms, resulting in a total acquisition time for a  $128 \times 128$  image of the order of 100 ms. As only one excitation RF pulse is applied, this is usually a  $90^\circ$  pulse, maximizing the amount of magnetization in the  $x$ - $y$  plane available for imaging. A refocusing  $180^\circ$  pulse may be applied before the EPI readout to form a spin echo, usually to coincide with the acquisition of the frequency encoding line passing through the centre of  $k$  space in the phase encoding direction. The spin echo results in a  $T_2$  weighted EP image as opposed to the usual  $T_2^*$  weighting. In practice, EPI acquisitions of up to 128 echoes are routinely performed. Although more echoes can be acquired, they do not necessarily lead to the expected improvement in image resolution. Unlike most spin warp acquisitions, in EPI a significant amount of  $T_2$  decay can occur throughout the duration for which the NMR signal is acquired.

## 2. An Introduction to Nuclear Magnetic Resonance Imaging

---

This results in a relatively broad point spread function in the image in the phase encoding direction for each point in the sample.<sup>15</sup> For a typical EPI acquisition of 256 echoes, the point spread function is often larger than the size of a pixel, hence the resolution which appears to have been achieved is not real.

Acquiring MR images in such a short period of time has a number of applications. Movement of patients can introduce a number of artefacts in spin warp MRI techniques, which degrade their usefulness. In particular, techniques designed to measure movement itself, such as perfusion or diffusion, suffer from such movement artefacts. The use of EPI in these fields can be particularly advantageous. Fast MRI techniques have obvious application to imaging the heart. While TurboFLASH images either may acquire one or two images per heartbeat or images of several phases of the cardiac cycle acquired over several heartbeats, EPI is the only MRI technique capable of imaging many different phases of the cardiac cycle in the duration of a single heartbeat.<sup>18</sup> This may be particularly advantageous in performing cardiac imaging of patients with irregular heartbeats or ECG signals<sup>†</sup>, as TurboFLASH images of different phases of the cardiac cycle require a regular ECG signal in order to interleave data from different heartbeats. Also, its relatively high SNR in comparison with TurboFLASH techniques make it the sequence of choice for performing BOLD functional imaging experiments (briefly described in Section 4.6.2). However, EPI acquisitions are far more sensitive to inhomogeneous magnetic fields, the effect of which is to cause spatial distortion along the phase encoded axis. This important problem is described more fully in Chapter 4.

Technical requirements for EPI are higher than for conventional MRI. The number of echoes that may be acquired in an EPI acquisition is limited by the  $T_2^*$  of the sample. The  $T_2^*$  is reduced in the presence of inhomogeneous magnetic fields. Hence, to acquire as many echoes as possible,  $B_0$  should have a high level of homogeneity. To achieve a spatial resolution comparable with conventional MRI acquisitions, the strength of the frequency encoding gradient needs to be up to ten times higher and switched with a tenth of the duration, compared to that

---

<sup>†</sup>An electrocardiogram (ECG) shows the time varying electrical activity associated with a beating heart.<sup>98</sup>

## 2. An Introduction to Nuclear Magnetic Resonance Imaging

---

required for conventional MRI. As well as the technical difficulties in doing this, switching gradients quickly results in induced eddy currents in the magnet. These can cause opposing magnetic fields which interfere with the desired gradient waveform. However this problem was largely overcome by the development of active magnetic screening of gradient coils.<sup>65</sup> These almost completely eliminate the magnetic field outside the gradient set and so reduces the eddy currents induced. However, the advantage of having a MRI system capable of performing EPI extend beyond EPI itself, as the high performance gradients may be used to further optimize other MRI sequences, resulting in an overall improvement in image quality and reduction of imaging times.

### Half Fourier MRI

As described above, the measured NMR signal is usually recorded in quadrature resulting in a real and imaginary signal. After a Fourier transform of these signals, the image will be complex. Normally the final displayed image is the modulus of these real and imaginary images; a phase image, of the angle between the real and imaginary components of each pixel, may also be constructed.

As the NMR signal is generated by a real sample, it would be expected that the MR image also would contain only real components. If this is assumed to be the case then Fourier theory suggests that half the data in  $k$  space is related to the other half and therefore is redundant. Acquisition times of MR images can be reduced by only mapping half of  $k$  space in the phase encoding direction. Fourier theory<sup>3,91</sup> shows that if data contain only real components then there is a symmetry in its FT such that  $g(-\mathbf{k}) = g(\mathbf{k})^*$  where  $g(\mathbf{k})$  is the complex value of a point in  $k$  space and  $g(\mathbf{k})^*$  is its complex conjugate. Hence, only the positive or negative part of  $k$  space is required. The remaining half may be constructed from the conjugate symmetry given above, prior to applying the FT to produce a real-only image. Techniques that use this result are called Half Fourier (HF) methods.

In practice, it is never the case that a MR image consists of only real components. Imperfections in the imaging hardware including inhomogeneous static and gradient magnetic fields and flow effects result in an imaginary component

## **2. An Introduction to Nuclear Magnetic Resonance Imaging**

---

to the final MR image. The modulus image is usually calculated to remove phase effects. However, this is not possible in HF acquisitions as only the real component of the MR image is produced, and hence may contain phase artefacts. Also, the SNR is reduced by a factor of  $\sqrt{2}$  due to less unique NMR signals being acquired.

A compromise, to attempt to benefit from the reduced imaging times of HF techniques while reducing phase artefacts in the final image, is to acquire slightly more than half of  $k$  space. The central region of  $k$  space, which is sampled symmetrically, allows a crude, low resolution (in the phase encoding direction) MR image to be constructed containing true phase information. This can then be used to 'add' phase to the higher resolution real image produced by the HF technique described above. In practice, this can be implemented as a one stage process, such as the method of Margosian half Fourier reconstruction.<sup>67</sup> In many cases, this results in the production of images of very acceptable quality. This is especially true for non-compliant patients who are unlikely to keep still for the duration of a longer full Fourier acquisition. However, as the phase information is only contained in a low spatial resolution form, its use is not suitable for techniques requiring accurate high resolution phase information, such as phase contrast flow studies.

### **2.4 MR Imaging Considerations**

A number of issues arise when performing MRI in practice. It is useful to give a brief description of some of the more important areas. As well as aiding the experimental set up of MRI acquisitions and interpretation of the images, they also provide further insight into the processes involved in MRI.

#### **2.4.1 Digital Fourier Transform and Aliasing**

In order to produce a MR image from  $k$  space, a two or three dimensional Fourier transform must be performed. This is almost exclusively performed by a computer using a digital representation of the  $k$  space data. Therefore, the continuous NMR signal first must be digitized. This process is limited by the sampling rate and the number of bits used to store the amplitude of the signal.

## 2. An Introduction to Nuclear Magnetic Resonance Imaging

---

Of particular interest is the sampling rate as this defines the smallest unit of time which in turn relates to the interval between data points along the frequency encoding  $k$  axis (see Equation 2.26). Once a discrete matrix of  $k$  space has been acquired, a Discrete Fourier Transform (DFT) must be applied, of which the most efficient algorithm is the Fast Fourier Transform (FFT).<sup>91</sup> A limitation of the standard FFT algorithm is that it must be performed on a data set of a size which is an exact power of two. For this reason, most NMR signals are digitized into a number of points fulfilling this criterion, resulting in MR images contained in a matrix with each axis containing an exact power of two points.

The properties of a DFT define the physical dimensions of the final MR image.<sup>91</sup> If there are  $N$  discrete points along a particular  $k$  space axis, and each discrete point spans a portion of  $k$  space of size  $\Delta k$  then for a symmetric coverage of  $k$  space the maximum position along the  $k$  axis will be  $k_{max} = \frac{1}{2}N\Delta k$ .  $\Delta k$  depends on the amount of gradient area swept out per sampling interval. After performing the DFT, the corresponding axis in 'image' space will contain  $N$  pixels with pixel dimension  $\frac{1}{2k_{max}}$  or  $\frac{1}{N\Delta k}$  while the image will span a distance of  $\frac{N}{2k_{max}}$  or  $\frac{1}{\Delta k}$  along that axis. Hence, the sampling rate defines the size of the image and the maximum excursion in  $k$  space will define the dimensions of a pixel, *i.e.*, the image resolution.

The finite digital sampling rate introduces an effect not seen in continuous FT analysis. The digitized  $k$  space contains NMR signals oscillating with a range of frequencies. The highest frequency which can be represented uniquely is a sinusoidal wave with a maximum amplitude in one sample point and minimum values in adjacent sampling points. This frequency is  $\frac{2}{N}$ . Digitization of any frequencies higher than this will result in the signal appearing in the discrete matrix as a lower frequency. This effect is known as aliasing and described by the Nyquist sampling theorem. In MRI, spatial encoding relates frequency to position. Therefore, spins emitting a NMR signal with a frequency greater than the Nyquist frequency will appear aliased in the digitized  $k$  space as a lower frequency and the signal will appear in the wrong place in the image. This occurs if the field of view (FOV) of a MR image is set to be smaller than the physical size of the object being imaged. As the linear gradient extends through

## 2. An Introduction to Nuclear Magnetic Resonance Imaging

---

the sample outside the FOV, the NMR signal will contain frequencies from spins outside the desired FOV too. Aliasing in the frequency encoding direction may be eliminated by filtering the analogue NMR signal to remove frequencies outside the required range prior to digitization. The sampling rate may also be increased, doubling the FOV so that it covers the object; the extra peripheral regions may be removed from the image after the DFT has been performed. This latter technique is known as frequency oversampling.

Aliasing is more of a problem in the phase encoding direction, both in plane and to a lesser extent in the slab direction if a three dimensional volume acquisition is being acquired. As explained in Section 2.3.2, the rate of change of phase in the  $k_y$  direction (*i.e.*, a frequency) relates to spatial position along the phase encoding axis. In a MRI acquisition consisting of  $N_{pe}$  phase encoding steps, if the rate of change of phase along  $k_y$  exceeds the Nyquist frequency limit of  $\frac{2}{N_{pe}}$ , then aliasing will occur along the phase encoding axis. This is often referred to as phase wrap. This will occur if  $\Delta k_y$  is too large. The FOV in the phase encoding direction is  $\frac{1}{\Delta k_y}$  and hence acquiring a MR image with a smaller FOV (and fixed  $N_{pe}$ ) results in a larger  $\Delta k_y$ . Oversampling may be applied in the phase encoding direction too, however this results in an increase in the acquisition time as more lines of  $k$  space,  $N_{pe}$ , must be acquired.

### 2.4.2 Bandwidth

A range of spatial frequencies is contained within  $k$  space. The bandwidth of these frequencies depends on the duration for which  $k$  space is sampled and the gradient applied. The bandwidth,  $\Delta\omega_{fe}$ , of the actual NMR signal under a frequency encoding gradient acquired for a time  $t_{fe}$  can be calculated as follows. Consider the difference between the maximum and minimum frequencies,  $\Delta\omega_{fe}$ , in Equation 2.21 expected for a FOV of  $\frac{N}{2k_{max}}$ . Assuming a constant gradient,  $G_x$ , then  $k_{max} = \frac{1}{2}\gamma G_x t_{fe}$  and so  $\Delta\omega_{fe} = \frac{N}{t_{fe}}$ . It is often useful to express this in terms of bandwidth per pixel (or frequency per point), *i.e.*,  $\frac{1}{t_{fe}}$ .

The bandwidth per pixel may also be calculated in the phase encoding direction. For a spin warp type experiment acquiring one frequency encoding line per RF excitation, the phase evolution throughout the NMR signal will be the same

## 2. An Introduction to Nuclear Magnetic Resonance Imaging

---

for each frequency encoded line. This is because each frequency encoded line is acquired at the same time after the RF excitation which tips the magnetization into the  $x$ - $y$  plane with a defined phase. Only the phase offset is changed by the phase encoding gradient. The same is true for most multiple spin echo acquisitions, as the acquisition of each echo usually occurs at the same time after the previous refocusing RF pulse. As all points in a phase encoding column of  $k$  space were acquired at the same effective time, the bandwidth per pixel in this direction is effectively infinite.

However, this is not the case with EPI acquisitions. Phase encoding effectively occurs throughout the entire readout portion of the acquisition as there is no RF excitation to reset the phase. In this case, the time for which the spins evolve under the phase encoding gradient is  $t_{pe}$  which for  $n_e$  echoes typically is equal to  $n_e t_{fe}$ . Therefore, the bandwidth,  $\Delta\omega_{pe}$  is  $\frac{1}{n_e t_{fe}}$  or  $\frac{1}{n_e} \Delta\omega_{fe}$ .

The bandwidth per point can be used to calculate the effect of spins rotating with a different frequency to their neighbours. For example, a voxel may contain spins of both water and fat. At 1.5 T, they will resonant with a difference in frequency of 224 Hz. Although at the same physical location, the fat image will appear shifted relative to the water image, in the frequency encoding direction, by  $224 \times t_{fe}$  pixels. In the phase encoding direction, the shift will be  $224 \times t_{pe}$  pixels, which will be zero for spin warp acquisition and for EPI will be  $n_e$  times the shift in the frequency encoding direction. This highlights one of the problems of EPI compared to spin warp acquisition, *i.e.*, it is more sensitive to erroneous frequencies of spins. Fat saturation is often more important for EPI than for spin warp acquisitions. As well as chemical shift effects, the local frequency of spins may be shifted due to an inhomogeneous  $B_0$  magnetic field. Again, this usually affects EPI acquisitions more than spin warp schemes.

### 2.4.3 Flow Effects

In a living biological system, as well as movement artefacts due to the respiratory and cardiac cycles, the flow of liquids, especially blood, can have an effect on the resultant image. Understanding the effects caused by flow allows the flow itself to be quantified, allowing MR imaging to be used to study these dynamic

## 2. An Introduction to Nuclear Magnetic Resonance Imaging

---

effects. Flow can manifest itself in an image in one (or a combination) of four ways:<sup>9</sup> time-of-flight effects, reversible phase effects, turbulence, and stagnation.

Time-of-flight (TOF) effects only occur if a component of the flow is perpendicular to the slice (or slab) being imaged. It can either result in a signal gain in the pixels containing the flow at low velocities, or signal loss at higher velocities. Signal loss is usually only observed in sequences containing slice selective spin echoes. Neither TOF effect is readily observed in EPI acquisitions. At low velocities, the flowing liquid remains in the slice during the excitation and acquisition of (at least) one frequency encoding line. However by the time the next frequency encoded line is acquired, at a time TR later, the spins have flowed out of the slice and have been replaced by unsaturated ones. These fresh spins have a larger component of  $M_0$  along the  $z$  axis available to be tipped into the  $x$ - $y$  plane than spins which were previously in the slice because the magnetization of these latter spins would not have fully relaxed back to the  $z$  axis. Enhancement of signal in the voxels containing flow is seen. By repeating the pulse sequence with various values of TR, the flow can be quantified.

However, if the flow is fast enough to remove spins from the slice during the acquisition of a single spin echo frequency encoding line, then TOF signal loss occurs. In this case, some spins that were excited by the initial RF pulse have been replaced before the slice selective  $180^\circ$  refocusing RF pulse is applied. The spins which have left the slice do not feel the effect of the  $180^\circ$  RF pulse, are not refocused and so do not contribute to the NMR echo. Neither do the fresh unexcited spins that have replaced them. This effect is not so prominent in pulse sequences using gradient echoes (or spin echoes created using a non-slice-selective  $180^\circ$  RF pulse), as the flowing spins which experienced the initial excitation RF pulse are still refocused and contribute to an echo even when they have flowed out of the slice being imaged.

Flow contained in the slice (or slab) being imaged can lead to phase shifts in the MR image. During an echo pulse sequence, flowing spins will move from a volume experiencing one magnetic field strength to a region experiencing another, resulting in a change in the phase of their rotation. It can be shown that this phase change is directly proportional to the velocity of the nuclei<sup>11</sup> and this

## **2. An Introduction to Nuclear Magnetic Resonance Imaging**

information can be extracted from a phase map. Methods have also been devised, using multiple gradient echoes, to rephase moving spins and hence allow them to contribute to the MR image without exhibiting flow effects.<sup>81</sup>

When the flow is turbulent signal loss is seen and the phase change in the signal can not be modelled simply, hence flow information can not be extracted. At the other extreme, a 'false' flow signal can be seen from volumes from which flow is expected due to a brief stagnation of the flow. This can be seen if the MRI acquisitions are triggered from the cardiac cycle. A higher signal is seen in the arteries during diastole than during systole.<sup>9</sup>

These effects can be complicated in multislice acquisitions. In this case, there is the possibility than excited spins from one slice enter an adjacent slice and contribute to a signal there. However from this information, it can be deduced whether the flow is with or against the direction of multislice acquisition.

The time-of-flight (TOF) flow effect can be used to construct MR images containing angiographic information (MRA). FLASH acquisitions may be performed with a short TR and large flip angle. The signal for spins which remain in the slice for its entire acquisition are saturated after the first few RF pulses and hence contribute only a very small signal in the final image. In-flowing blood will bring a continual supply of unsaturated spins into the slice. These will give a high signal from the large RF flip angle. The final image will contain very low signal from stationary spins and a high signal from inflowing blood, highlighting the vascular system. This can be extended to three dimensional FLASH MRI, resulting in a volume in which the only voxels with high signal intensity are those containing rapid in-flowing blood. TOF MRA is a unique method for producing high resolution three dimensional angiograms without the use of additional contrast agents.

Spins may also undergo incoherent movement due to diffusion effects. While diffusion does not significantly affect normal MRI acquisitions, MRI sequences may be sensitized to diffusion and thus used to quantify it. A method for doing this is described in Section 4.6.1.

### 2.5 Instrumentation for MRI

A MR imaging unit may be considered as consisting of a main static magnet, magnetic gradient fields, RF system, and processing computers. Although the hardware is crucial for the production of high quality MR images, it does not form part of the work presented in this thesis, beyond that. Therefore, only a brief description is given below; it is described in more detail elsewhere.<sup>79</sup>

#### 2.5.1 Main Magnetic Field

The largest item is the main magnet. Its design is a complex process, as a highly uniform strong magnetic field is required over a region which also must allow easy access of the patient. Although resistive and permanent magnets have been used, their maximum field strengths (for whole body imaging) are approximately 0.15 T and 0.3 T respectively.<sup>53</sup> However the trend has been towards higher magnetic field strengths, and to achieve this, magnetic fields created by a superconducting solenoid are used. Coils, typically of niobium-titanium alloy in a copper matrix are surrounded by liquid helium, with a boiling point of 4.2 K. To reduce the helium's boil-off rate, it is often surrounded by liquid nitrogen (77.4 K boiling point) and all enclosed in a vacuum system for insulation. Modern magnets may not have a second insulating layer of liquid nitrogen, but instead compress the cold helium gas which has boiled off, to re-liquefy it.

For easy access of a patient lying on a couch, the bore of a whole body superconducting solenoid is aligned horizontally, resulting in the main magnetic field,  $B_0$ , of the MRI scanner also being horizontal. Once superconducting, if the temperature of the solenoid coil rises enough for it to gain resistance, the heat generated causes a rapid boiling of the cryogen and loss of magnetic field; this is known as quenching. To create as uniform a magnetic field as possible, smaller 'shimming' coils are used to change the main field, resulting in typical maximum inhomogeneities over a central 30 cm diameter region of less than 10 p.p.m. Shims are usually a combination of passive shims, often strategically placed ferromagnetic strips in trays around the circumference of the magnet's bore, and active shims, which are a series of up to 30 electromagnetic coils also

## **2. An Introduction to Nuclear Magnetic Resonance Imaging**

attached to the inside of the magnet's bore. Active shims may be adjusted, often under computer control, to fine tune the homogeneity of the static magnetic field.

The strength of the main magnetic field is an important consideration. Stronger main magnets are more expensive, but result in a higher SNR. However the  $T_1$  contrast between different regions in a sample decreases with increasing field strength. The ability to detect differing pathology depends on contrast as well as resolution and so a contrast-to-noise ratio may be a useful concept. Larger main magnetic field strengths also result in larger spatial distortions due to an increased inhomogeneous local magnetic field caused by magnetic susceptibility differences, for the same sample.

A strong static magnetic field will extend for some distance from the magnet itself. This is often a problem, as it can affect electrical equipment nearby, especially the computer system essential to control the MR scanner itself. In a clinical setting, the external magnetic field also could cause problems with medical equipment close to the magnet. It must be remembered that the field will extend upwards as well and may be felt in rooms above the magnet. The extent of this fringe field may be reduced by active or passive shielding. Passive shielding involves surrounding the magnet with a ferromagnetic shield. While this works, it adds a considerable amount of load to the floor as well as potentially interfering with the homogeneity of the main magnetic field. Active shielding drastically reduces the fringe field by surrounding the superconducting coils producing the main magnetic field by another set of superconducting coils producing a magnetic field of the opposite polarity. The outer coil effectively cancels the fringe field caused by the inner coil. However, as it also affects the field in the centre of the magnetic, the inner coil must generate a much higher primary magnetic field to overcome this. To produce a 1.5 T magnetic field, the inner coil alone may produce a 2.5 T field, of which 1 T is 'cancelled' by the outer coil.

### **2.5.2 Magnetic Gradients**

In order to spatially encode a NMR signal, magnetic field gradients are required, typically of strengths of a few tens of milliTesla per metre. A linear gradient is required and although a good approximation can be achieved near to the

## 2. An Introduction to Nuclear Magnetic Resonance Imaging

central volume of the magnet, departure from this will result in incorrect spatial encoding and image distortion. Again, the design of electromagnetic coils to produce gradient magnetic fields suffers from the opposing requirements of a uniform, linear field with good patient access. The gradient coils are inserted inside the magnet's bore. They are not superconducting, but may be water cooled.

The gradient along the main static magnetic field,  $G_z$ , can be achieved simply by the use of coils arranged in a Maxwell pair with currents circulating in opposite directions. This results in no contribution to the main magnetic field at the centre of the volume, and positive and negative contributions away from it. This also allows good access for large samples to be imaged.

Magnetic gradients along axes perpendicular to the main magnetic field can be generated by the use of saddle configuration wires. These produce a linear gradient up to three-quarters of the coil radius from the central axis and allow greater access to the imaging volume.

These designs can be improved by adding more coils, which can result in stronger and more uniform magnetic gradients. However this also increases the coils' inductance, which results in longer gradient switching times. Rapid switching of magnetic gradients also results in considerable forces exerted on the coils. As well as stressing the coils and their mountings, these can also result in high audible noise levels.

Gradient coil performance also may be limited by interactions of the gradient fields with the main magnet. This is a hindrance for gradient systems intended to be used for EPI acquisitions. Active shielding also may be employed for the gradients as well as the main magnetic field.<sup>65</sup> This reduces the magnetic gradient field outside the gradient set and hence reduces interactions with the main magnet. However, actively shielded magnetic gradients occupy more space in the limited volume inside the magnet's bore.

The design of gradient coils benefit greatly from numerical computer models. The high performance gradient systems present on modern MR systems are only possible through use of such models. In particular the use of actively shielded gradients require the use of computer calculations.<sup>113</sup>

### 2.5.3 RF System

To excite the nuclei, a RF electromagnetic field must be applied to the sample, oscillating perpendicularly (in the  $x$ - $y$  plane) to the main static magnetic field (which is parallel to the  $z$  axis). A solenoid coil as part of a resonant circuit is an efficient method of doing so, but if the main magnetic field is along the long axis of the MR imager, such as produced by superconducting solenoids, then a solenoid coil is not suitable. Saddle coils may be used, for both excitation and NMR signal detection, however a birdcage resonator design is more common as it results in greater RF field uniformity.<sup>15</sup> To obtain a high  $Q$  factor and hence a high SNR, the coil's 'filling factor' (the proportion of the coil's volume occupied by the sample) should be high. However if the sample is a conductor, induced currents in it will result in the RF coil being less efficient, hence lowering its  $Q$  factor, and so a compromise between the two has to be found.

Another factor to be considered is that if the RF is not homogeneously distributed throughout the sample then the tip angle of selective pulses will not be the same throughout the sample, resulting in modulated NMR signals from various volumes in the sample. However, RF attenuation in the body is not such a big problem as it may seem at first due to the compartmentalization of the body, reducing 'skin depth' effects. RF homogeneity is improved if the radius of the coil is large compared with the size of the sample; another consideration in coil design.

If only a small volume of the sample is to be imaged, such as an eye or breast, the final SNR can be improved by using RF surface coils. These are placed over the volume to be imaged and result in images up to a depth that is approximately equal to the radius of the coil.

In practice, a variety of RF coils are available for a whole body MR imaging system, to conform to the body part being imaged. In particular, a head coil which fits fairly close to the head, and a larger diameter body coil into which the trunk of a human will fit, are common on most clinical systems. In NMR, RF must be both applied and received. This is often performed by the same coil, which is electronically switched between transmit and receive modes. However, in some cases it may be preferential to transmit the RF pulses using one coil and

## **2. An Introduction to Nuclear Magnetic Resonance Imaging**

---

to receive on a separate coil system. This is often the case when surface coils are used, as they do not provide a uniform RF field. A larger coil may be used to transmit good RF pulses over the entire sample, while the surface coil is used to receive the NMR signal only. This is often the case when surface coils are positioned in a phased array configuration, where NMR signals from a number of spatially separate surface coils are combined to produce a more uniform MR image.

The RF amplifier attached to the transmission coil must be capable of accurately supplying RF over a range of frequencies, with defined phase, and modulated by generally shaped amplitude envelopes, such as a sinc waveform. It should also contain a power monitor to cut off the RF output if a fault would allow excessive transmission of RF power into the patient.

The RF receive channel must be capable of detecting the small NMR signal and should introduce as little noise as possible. The bandwidth of acceptable frequencies must be set to the bandwidth of frequencies expected in the NMR signal. Setting the bandwidth too wide will result in sampling of frequencies containing only noise and so reduce the SNR of the actual signal.

In order to reduce the amount of RF noise as well as image artefacts, the MR scanner should be placed within a Faraday cage, or screened room. This prevents radiowaves entering the room and being detected by the RF coil during MRI acquisition. Care must also be taken to filter all electrical cables entering the screened room to prevent RF entering the room through the cables. In particular, the cables carrying the high currents to drive the magnetic gradients must be filtered.

### **2.5.4 Control System**

To control the various pulse and gradient sequences, and to collect, process, and display the NMR signals and MR images, a fairly sophisticated set of electronic hardware and computer is required. It must be able to communicate and interface with the equipment producing the gradient and RF pulse sequences, and synchronously digitize the received NMR signals at a rapid rate. Once the NMR signals have been collected, they need to be processed (including Fourier trans-

## **2. An Introduction to Nuclear Magnetic Resonance Imaging**

forming) before being displayed on a suitable monitor. For rapid processing, not only is a fast computer required, but also one with a large amount of directly accessible memory and external storage devices.

### **2.5.5 MRI Systems**

Four whole body MRI scanners were used to acquire images for the work presented in this thesis; two research systems and two clinical units. A 0.5 T whole body superconducting magnet system and 3 T whole body magnet system (the latter with gradient coils to image the head) were used to acquire EP images, both built in-house and situated in the Magnetic Resonance Centre at the University of Nottingham. A clinical 1.5 T Vision MR scanner supplied by Siemens (Erlangen, Germany) was used at the Queen's Medical Centre University Hospital, Nottingham, as was a Siemens 1.5 T SP MR scanner.

## **2.6 Safety**

Unlike images formed from x-rays, MRI does not present any risk to the person being imaged from ionizing radiations. However an assessment of any potential hazards and risks is still important. As a diagnostic imaging tool applied to tens of thousands of people each year, even a relatively small risk could cause morbidity or mortality to a few people. Hazards in MRI are normally considered from three sources: the static magnetic field, switched magnetic gradients, and RF power. These have been considered by the National Radiation Protection Board (NRPB) who devised the limits mentioned below<sup>26</sup> for clinical MRI examinations. The proposed limits have been classified in to two levels, where exposure below level I is not believed to carry any risk, and exposure above level II is considered inadvisable. Exposures between the two levels are considered safe for healthy people.

### **2.6.1 Static Main Magnetic Field**

Static magnetic fields of strengths of a few Teslas are not thought to have a harmful biological effect. The NRPB has set the level I whole body limit for the

## 2. An Introduction to Nuclear Magnetic Resonance Imaging

Duration of field change $t$	$\frac{dB}{dt}$ ( $\text{Ts}^{-1}$ )	
	level I	level II
$3 \text{ ms} < t$	20	20
$120 \mu\text{s} < t < 3 \text{ ms}$	20	$\frac{60 \times 10^{-3}}{t}$
$45 \mu\text{s} < t < 120 \mu\text{s}$	$\frac{2.4 \times 10^{-3}}{t}$	$\frac{60 \times 10^{-3}}{t}$
$2.5 \mu\text{s} < t < 45 \mu\text{s}$	$\frac{2.4 \times 10^{-3}}{t}$	1300 ( $\equiv 2 \text{ Wkg}^{-1}$ )

Table 2.2: Limits for time varying magnetic fields.<sup>26</sup>

main static magnetic field of 2.5 T, with level II at 4.0 T. The main hazard from static magnetic fields is from loose ferromagnetic objects near, or in, the magnet. Unattached objects can be attracted towards the magnet, causing physical harm to a person in their path, or damage to the magnet or its housing. Special consideration must be given to emergency procedures such as fire or cardiac arrest, where the initial response may be to bring ferromagnetic equipment close to the magnet. Other objects such as cardiac pacemakers and other metallic implants, as well as external medical equipment, may cease to function correctly.

### 2.6.2 Time Varying Magnetic Field

The switching on and off of gradient magnetic fields in order to spatially encoding the MR image results in time varying magnetic fields. These cause a biological risk because of the current induced in the sample. This may interfere with cardiac ventricular fibrillation, other electrical signals and stimulation within the body, and may induce epilepsy. The most common effect is of nerve stimulation, especially in the shoulders and the optical nerve; nevertheless, these effects are rare and not believed to be hazardous. The NRPB limits are given in Table 2.2. With rapid imaging techniques such as EPI, these limits may frequently be reached.

### 2.6.3 RF Electromagnetic Field

RF power dissipated in tissue could cause damage due to local heating. A rise in local body temperature of 1 K is considered to be safe, and this value is used to set the level II limit on RF absorption (level I is set for a 0.5 K temperature rise). The lens of the eye has no blood supply to remove heat and so is chosen as the region of consideration. The levels are set in terms of Specific energy

## 2. An Introduction to Nuclear Magnetic Resonance Imaging

Duration of exposure t (min)	SAR of whole body ( $\text{Wkg}^{-1}$ )		SAR of head ( $\text{Wkg}^{-1}$ )	SAR of trunk ( $\text{Wkg}^{-1}$ )	SAR of limbs ( $\text{Wkg}^{-1}$ )
	level I	level II			
$30 < t$	1.0	2.0	2.0	4.0	6.0
$15 < t < 30$	$\frac{30}{t}$	$\frac{60}{t}$	$\frac{60}{t}$	$\frac{120}{t}$	$\frac{180}{t}$
$t < 15$	2.0	4.0	4.0	8.0	12.0

Table 2.3:  $B_1$  radiofrequency SAR limits.<sup>26</sup>

Absorption Rate (SAR) and are shown in Table 2.3. Again, these limits may be reached fairly easily during routine clinical MR scanning using rapid multiple spin echo acquisitions, such as RARE or HASTE.

Hazards from RF irradiation also include local heating caused by eddy currents induced into closed conducting loops (as opposed to direct RF absorption). Heating effects have been noted in metallic implants, monitoring equipment attached to the patient, e.g., ECG electrodes and leads used to monitor the cardiac cycle, and in patients' legs if their bare feet are touching, causing a large conducting loop.

### 2.6.4 Other Risks

There is no convincing evidence that MRI examinations of pregnant women causes any detrimental effect on the embryo or foetus. However, it is probably wise not to perform MRI during pregnancy unnecessarily, although it may be a preferable option to an x-ray examination, which is known to carry small risks.

Finally, MRI acquisitions are noisy. Rapid switching of the magnetic gradient coils causes them to move slightly resulting in emission of sound. This can be quite considerable and so ear protection, in the form of headphones or ear plugs, must be worn.

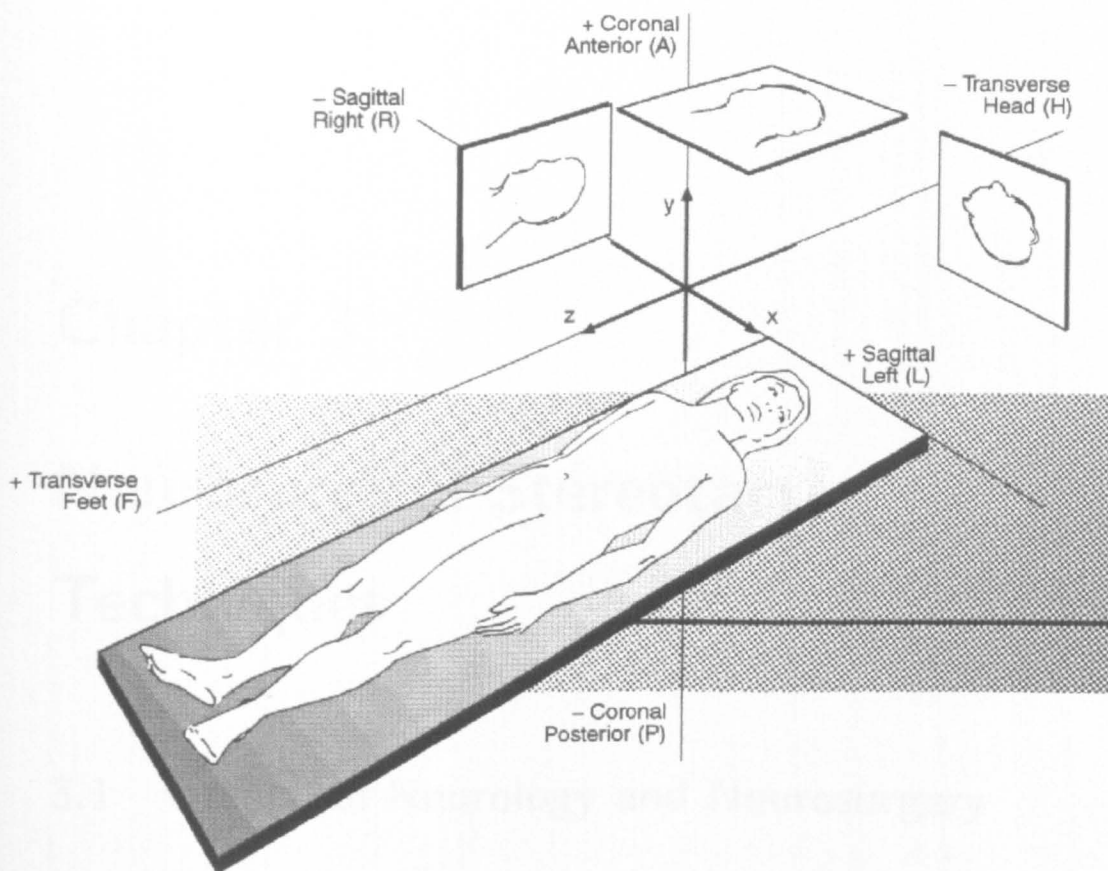


**Figure 2.18** Standard orthogonal imaging planes (transverse, coronal, and sagittal) relative to a supine person. The transverse plane also is often labelled transaxial. The magnet's three primary (x,y,z) axes are also given. For a typical whole body superconducting MRI system, the magnet's bore is horizontal as is the main magnetic field,  $B_0$ , both of which are parallel to the z axis.  
 (adapted from 'Application Guide for the Vision' by Siemens)

# Chapter 3

## Neurosurgical Stereotactic Techniques

### 3.1 Origins of Neurology and Neurosurgery

Throughout human history, man has been fascinated by the human brain, and diseases with which it may be associated. Archaeological evidence suggests that skull trepanation (removal of a portion of skull, leaving a hole) had been performed as long ago as 3000 BC., possibly to ease symptoms caused by trauma, or in the belief that it would allow the escape of troublesome daemons. In some cases, partial re-growth of the skull surrounding the trephine suggests that the patient survived the operation for several months.<sup>112</sup>

The understanding of the function of the brain was furthered during antiquity by Erasistratos in 300 BC., and Galen who believed it to be associated with intelligence, movement, and sensation. However, association between specific functions of the brain and particular physical regions within it was not made until the 17<sup>th</sup> century, when Descartes decided that the soul was located in a specific volume of the brain, the pineal gland.<sup>24</sup> Phrenology, hypothesized in the late 18<sup>th</sup> century by Gall, assumed the organization of the cerebral cortex\*, and throughout the 19<sup>th</sup> century, further postulates assumed the connection of various regions of the brain with particular functions. In particular, Broca

---

\*the outer layer of the brain.<sup>98</sup>

### 3. Neurosurgical Stereotactic Techniques

---

correlated speech impediments with the location of lesions found subsequently during post mortems, from 1861 onwards.<sup>5</sup> Animal experiments by a number of researchers observed that electrical stimulation of various regions of monkeys and dogs' brains resulted in distinct muscular movements, leading them to propose a functional map of the brain. In 1925, Foerster was the first to experiment on the human motor cortex, using electrical stimulation to evoke specific muscle movements. For the first time, the site of an abnormality in the brain could now be suggested from a diagnosis of the symptoms.<sup>112</sup>

From then on, the increasing ability to associate various regions within the human brain with its function or disease,<sup>86,87</sup> allowed the development of neurology, the study of the central nervous system (CNS), and neurosurgery. However, in order to proceed, a method for accurately locating a point within the brain was required. Functional atlases of the brain were constructed from the addition of data from several people, but with the variations in size and shape between individual brains, these could only result in accurate location of function on the visible surface of the cerebral cortex; the location of function in deeper regions of the brain was more uncertain, and its position (relative to the brain's surface) variable between people. For neurosurgery too, this accuracy was required. The less well defined the location of the target of the surgery is, the more invasive the surgery needs to be, in order to find it, which in turn is likely to increase the chance of morbidity and mortality in the patient.

## 3.2 Stereotaxis

Stereotaxis (from the Greek *stereos* solid, *taxis* arrangement<sup>112</sup>) refers to techniques for accurately and reproducibly physically locating a three dimensional coordinate within a solid body or volume. These techniques have been applied to many fields, including medicine where its primary use is to define fixed points within the human head. Neurological stereotactic apparatus typically consists of a frame which is rigidly attached to the head. The frame contains devices that allow accurate and reproducible positioning, typically of a needle point, at a range of three dimensional coordinates relative to the frame. If the target

### 3. Neurosurgical Stereotactic Techniques

---

point is known relative to the head<sup>†</sup> then, as the frame is rigidly attached to the head, its coordinate can be transferred to the frame system. The coordinate can then be 'dialled up' on the frame, to allow positioning of the needle tip at the desired target. Its use in neurosurgery falls into two categories: image directed surgery, and functional surgery. In image directed neurosurgery, one or more images through the head, acquired using a variety of medical diagnostic imaging modalities, are used to localize the target point. In functional neurosurgery, the target point is selected from anatomical atlases rather than individual images. The contemporary work in this thesis, relating to stereotaxis, is only concerned with the former use.

The first stereotactic system to examine the anatomy of the human head is believed to have been used at the University of Utrecht in 1861 by Harting.<sup>35</sup> In 1895, Rossilimo<sup>99</sup> used a stereotactic device to drain a lesion, later suggested to be a cystic glioma;<sup>48</sup> his apparatus was based upon the 'encephalometer' of Professor Zernov of Moscow University which was introduced in 1889. A device for reproducibly localizing points within monkeys' cerebella was constructed and used by Sir Victor Horsley and Richard Clarke<sup>21,45</sup> at University College London in 1906. This device, which is usually attributed as the first stereotactic frame, was used to guide electrodes to internal targets based on external anatomy; the frame was positioned on the head by locating plugs into the nose and ears, while plates fitted over the eyes. A stereotactic system was designed for human use in Canada in 1918 by Aubrey Mussen,<sup>88</sup> the target to be selected using an atlas of the head, but it was never used on a patient. It was not until 1933 that Kirschner devised a stereotactic method for guiding an electrocoagulation needle to treat tic douloureux in humans,<sup>54</sup> selecting the target using both x-ray radiographs and external landmarks; however its design was not suitable for extension to treat deeper targets.

The routine application of stereotactic devices to human neurosurgery was not realized until 1947 when Spiegel and Wycis<sup>105</sup> introduced their stereotactic frame. This was attached to the patient using a plaster cast of his or her head, and initially used to treat functional disorders. A system was developed in 1949

---

<sup>†</sup>or preferably, directly relative to the frame, after it has been rigidly attached to the head.

### 3. Neurosurgical Stereotactic Techniques

---

by Talirach and others<sup>109</sup> to allow the positioning of a needle within the head. It used a two point sighting system to align the frame, attached to the patient's head, with a x-ray beam. The resulting radiographs allowed a grid of holes to be aligned to the frame, one of which would guide the needle, and depth to be calculated. As the benefits of using a stereotactic system became more widely known, many designs were implemented; two of the most successful and popular were those designed by Lars Leksell in Stockholm in 1949,<sup>59</sup> and Riechert & Mundinger in Freiburg in 1955<sup>95</sup> (modified from an initial system by Riechert & Wolff, first used in 1950<sup>96</sup>). These two systems were initially designed to be used with planar x-ray systems, while requiring only a small amount of computation for each procedure. Their success can be judged from their usage; the Riechert-Mundinger system had been used for over 10,000 stereotactic operations by 1988.<sup>112</sup>

With the introduction into routine clinical use of x-ray computed tomography (CT) systems in the early 1970's, a new dimension in neurology was opened up. Both the Leksell and Riechert-Mundinger systems were adapted to make use of this new, richly informative medium. The new perspective offered by transverse CT images through the head, coupled with the availability of relatively cheap computers, allowed new stereotactic systems and protocols to be developed to take advantage of these factors. Since the early 1980's, the Brown-Robert-Wells (BRW) stereotactic system (produced by Radionics, Burlington, MA, USA) has become increasingly popular<sup>11-13</sup> due to its simplicity and quoted millimetric accuracy.<sup>97</sup> This system relies on computer calculations to determine the final target coordinate to be 'dialled up' on the frame. Although designed primarily to allow surgical planning to be conducted directly from CT images, it also allows planning from magnetic resonance (MR) images and planar x-ray angiograms. The details of the BRW stereotactic system are described more fully below. The increased availability of diagnostic imaging modalities which are compatible with stereotactic systems allows individual planning of each patient undergoing a stereotactic procedure. This is especially important for targets which do not occur at specific locations; the location varying from patient to patient, and for all targets deep within the brain, whose location can only be accurately

### 3. Neurosurgical Stereotactic Techniques

---

determined from diagnostic images. The accurate determination of the target from diagnostic images, pre-operatively, also allows the surgery to be far less invasive than it would otherwise have had to be, which is likely to decrease the chance of morbidity and mortality in the patient. In addition, many regions of the brain could now be operated upon for the first time, as the accurate location of not only the target, but other critical structures to be avoided, dramatically increased the chance of a successful outcome.

A typical contemporary stereotactic procedure, planned using a diagnostic imaging technique, would involve rigidly attaching a base ring to the patient's head, which remains in place for the entire duration of the operation. It is assumed that points within the patient's head remain at a constant, fixed, position relative to this head ring throughout the procedure. The ring is then attached to a specially designed frame during diagnostic imaging; the frame is visible on the images, allowing coordinates to be transformed from the image to the frame system, and hence to a coordinate system relative to the base head ring. The patient is then attached to a treatment jig *via* the base ring, which allows the target coordinate to be transferred to the calibrated treatment jig; usually defined as a needle tip. This procedure is described more fully below, with reference to the BRW system.

Stereotaxis has become a widely accepted and used diagnostic and surgical procedure in neurology. Its primary use is for obtaining intracranial biopsies, where small cores of tissue (typically  $5 \times 2 \text{ mm}^{112}$ ) through the target are removed using a needle entered through the skull *via* a small burr hole, often performed under only a local anaesthetic. These samples can then be analysed to aid the diagnosis of the patient's condition. Inaccuracies in the locations of the biopsy may cause brain damage, or lead to false negative diagnoses of the samples, resulting in incorrect diagnosis and treatment of the patient. One measure of the success of stereotactic biopsies is the rates of mortality, morbidity, and positive diagnosis; these are typically 0.5%, 2%, and over 90% respectively.<sup>112</sup> The mortality rate for radical neurosurgery is of the order of 5%.<sup>112</sup> Other neurosurgical applications for which stereotactic biopsy techniques have been widely applied include aspiration of cystic tumours, cerebral abscesses, and intracere-

### **3. Neurosurgical Stereotactic Techniques**

---

bral haematomas.<sup>112</sup> A stereotactic biopsy system may also be used to direct a craniotomy, although once the open surgery has begun, the inevitable distortion of normal brain anatomy means that the pre-operatively determined stereotactic target coordinate will probably no longer be correct. This highlights a further advantage to be gained from the decreased invasiveness of most stereotactic procedures, compared with traditional methods: that the target coordinate is less likely to be displaced due to the surgical procedure itself. Stereotactic techniques have also been used to place an electrode at a specific target within the brain, to treat aneurysms, functional disorders, and destroy epileptogenic foci.

### **3.3 Radiotherapy and Radiosurgery**

An application of stereotactic techniques which is becoming increasingly popular is its use to determine the target for external beam radiotherapy of the head. Radiotherapy of tumours is based upon the observation that a population of cancerous cells usually recovers more slowly after exposure to a high, but non-lethal dose of ionizing radiation, than does a population of healthy cells of the same tissue type. Repeated doses of radiation, preferably at about six hours intervals, but practically daily, reduce the surviving proportion of viable cancerous cells more rapidly than surround healthy cells. After a certain cumulative dose, the probability of any surviving viable cancerous cells is virtually zero, while the probability of surviving viable healthy cells is significantly greater than zero. This type of cumulative radiation treatment, consisting of many small treatments, is known as fractionated radiotherapy.<sup>119</sup> Ionizing radiation can also be delivered in just one, large amount, usually in a larger dose than the effective total dose of a fractionated treatment regime. This treatment is intended to sterilize all cells in the target volume, healthy or otherwise. This type of radiation treatment is often known as radiosurgery, as it can be considered as effectively 'burning out' the target volume. This technique is usually used to treat conditions other than cancer, however its use is limited to small volumes, as the body can not deal with a large volume of necrotic tissue.

For many years, stereotaxis has been used to position solid radioisotopes within a target in the brain using very similar techniques to a stereotactic biopsy.<sup>112</sup>

### 3. Neurosurgical Stereotactic Techniques

---

This interstitial irradiation, or brachytherapy, is intended to deliver a localized dose of ionizing radiation, and as such, the radioisotopes chosen are usually beta emitters, as beta particles have a limited range. Disadvantages of brachytherapy include a potentially high radiation dose to the neurosurgeon, and the difficulty in arranging the source accurately enough to result in a uniform delivery of dose to the target; 'hot spots' may result in unacceptably large volumes of necrosis, and underdosed volumes have a lower probability of successful treatment.

The advantage of external beam radiotherapy is that it is completely non-invasive, thereby removing the associated risks of surgery, including the risks of intracranial haemorrhage and infection, and results in the irradiation of only the patient. The ionizing radiation used is usually either x-rays, produced by the deceleration of electrons exiting a linear accelerator, or gamma rays, from a solid source<sup>‡</sup> with typical energies between one and ten mega-electron volts.<sup>51</sup> The problem of obtaining a uniform radiation dose throughout the target volume is reduced by placing the x-ray source at a distance from the target (typically 100 cm). It is highly desirable to minimize the volume of healthy tissue irradiated outside the target volume, in order to minimize the chance of morbidity. However, at depths greater than about one centimetre, the amount of energy deposited by an incident beam of x-rays as it penetrates tissue has been found empirically to vary approximately as a combination of the inverse square law (with distance from the x-ray source) and exponential attenuation (with depth in tissue).<sup>51</sup> This means that to deliver the required radiation dose to a target at depth in the head, using one incident x-ray beam, results in an even larger radiation dose to more superficial, healthy tissues. In order to reverse this effect, several collimated radiation beams are applied, either concurrently or in succession, from different angles around the target. These are arranged so that the cumulative dose, where all the beams cross, falls over the target volume. Generally, the more beams that are applied from different angles, the more uniform is the high dose target volume, and the lower is the dose absorbed at any point outside the target volume. By varying the weighting and dimensions of the various beams, a near uniform radiation dose can be applied over the whole target. This process

---

<sup>‡</sup>usually Cobalt-60.

### 3. Neurosurgical Stereotactic Techniques

---

is called radiotherapy treatment planning, and requires information regarding the x-ray beam characteristics, the dimensions and structure of the patient's head, and the target location within it. Due to the complexity of treating a patient stereotactically, relative to conventional radiotherapy, most patients are only treated on one occasion.

The stereotactic frame, attached to the patient's head during diagnostic imaging, is then attached to the x-ray delivery system (usually a couch) instead of to a surgical jig. As the x-ray source is usually fairly immobile, the calibrated couch to which the patient is attached is moved so that the desired target within his or her head coincides with the isocentre<sup>§</sup> of the x-ray delivery system. Irradiation is then given according to the individually calculated treatment plan. Two systems are routinely used to deliver stereotactic radiosurgery or radiotherapy. The first, the Cobalt-60 'gamma knife' is a dedicated stereotactic radiotherapy treatment system, consisting of many (typically 180 to over 200) small Cobalt-60 sources positioned radially around a hemisphere; the emitted gamma rays are focused by individual collimator tubes to the machine's isocentre. It was developed by a group, including Lars Leksell, and first used in Stockholm in 1968.<sup>60</sup> While allowing the foundations of stereotactic neuro radiosurgery to be laid, the gamma knife remains prohibitively expensive to install and maintain, and is only in use in a handful of centres worldwide. An emerging alternative is to modify and use a conventional modern radiotherapy x-ray linear accelerator (linac). This was first proposed in 1983 by Heifetz *et al.*,<sup>38</sup> and put into practice by 1985 by Colombo *et al.*<sup>22</sup> and Hartmann *et al.*<sup>36</sup> Linacs already are used in radiotherapy departments in a large number of hospitals, and so modifying one would be relatively cheap, not requiring a new installation, and the linac also could be used in its usual mode when not required for radiosurgery. The linear accelerator is usually mounted on a gantry which can rotate through 360° around a couch, upon which the patient lies for treatment. If the target point is set to the isocentre of the linac, then the rotation of the gantry, coupled with rotation of the couch, allows the x-ray beam to be incident upon the head over a wide range of

---

<sup>§</sup>the focal point in space around which all the axes of rotation and x-ray beam delivery, of the treatment device rotate.

### **3. Neurosurgical Stereotactic Techniques**

---

angles, imitating the gamma knife. If the linac is continuously irradiating while the gantry or the couch is moving, then an arc is irradiated, producing a more uniform result than irradiating from a finite number of fixed angles. Additional collimation of the x-ray beam results in a x-ray beam profile at least as good as that produced by a gamma knife. An error associated with linacs which is potentially larger than that on a gamma knife is the change in position of the centre of the x-ray beam as the gantry, weighing several tens of thousands of Newtons, sags as it rotates through large angles. However, after adjustments to compensate for errors, a modern linac should be able to irradiate a volume from a wide range of angles while confining the centre of the x-ray beam to less than two millimetres.

Stereotactic radiosurgery lends itself to a number of new treatments. Small brain tumours are particularly suitable for this technique, as the more accurate localization of the target, compared with traditional methods for head and neck radiotherapy, allow a smaller margin to be added for positional uncertainty and a higher radiation dose to be given, as less surrounding healthy tissue will be irradiated to a high dose, resulting in a lower probability of morbidity. The smaller high dose volume will reduce effects from any necrosis within, and it is also easier to achieve a more uniform and well defined high dose volume with radiation beams of smaller size. An emerging important use of stereotactic radiosurgery is in the treatment of arteriovenous malformations (AVM's), an abnormal growth of weak blood vessels in the brain between the arterial supply and venous drainage. While 'short circuiting' the full blood supply to parts of the brain may cause problems, the major risk from an AVM is of it haemorrhaging. AVM's may be treated using stereotactic radiosurgery, with a lower radiation dose than that given to tumours, in a single-shot treatment. Although irradiation causes only slow occlusion of the feeding vessels and fistula (a late effect of radiation damage) over a few years, it can be used to treat AVM's in locations which would be impossible to treat surgically. It also has a very small mortality rate, unlike surgery to place a clip to seal the AVM. As the surrounding brain is healthy, to minimize morbidity, it is crucial to accurately treat as small a volume as possible. With the larger errors associated with traditional radiotherapy, over a centimetre in

### 3. Neurosurgical Stereotactic Techniques

---

margin would have to be added to the dimensions of the target volume, resulting in an unacceptably large volume of healthy brain being destroyed, along with the associated morbidity due to the large volume of necrosed tissue. Combined with excellent long term results and multi-modal imaging for planning, radiosurgery is becoming the treatment of choice for management of AVM's.

#### 3.4 The BRW and CRW Stereotactic Systems

A modified form of the BRW system is currently in use in Nottingham. Imaging and neurosurgical biopsies are performed at the Queen's Medical Centre (QMC — the University Hospital in Nottingham). Radiosurgery of small tumours and AVM's, using a modified linac, is undertaken in conjunction with the City Hospital in Nottingham, where the radiotherapy department is based. The work in this thesis relating to stereotaxis is based around the use of the BRW system, which is described below. The BRW and CRW stereotactic systems are produced by Radionics (Burlington MA, USA).

The Brown-Robert-Wells stereotactic system, first introduced in 1979<sup>12,13</sup> and currently in use in Nottingham, consists of a head ring, various fiducial frames for imaging, and a surgical treatment jig. The head ring, approximately 30 cm in diameter and 2×2 cm thick, is first attached to the patient, who may be under a general anaesthetic, or just locally anaesthetized at the points where the ring is attached to the head. It is placed around the patient's head so that its axis of circular symmetry is parallel to the inferior-superior<sup>¶</sup> axis of the patient, at a level near to the height of the patient's mouth. This low placement is one advantage of the BRW head ring over many of its competitors, as it allows clearer access to the top of the head during treatment. The ring is rigidly attached to the patient's skull by means of three upright posts. These are attached to the head ring at one end, and have threaded holes at the other. Each hole takes a pin, which is screwed through the post and into the patient's head, forcing its way a few millimetres into the skull. This results in the head ring being rigidly attached to the head. It remains in place throughout the procedure, providing a

---

<sup>¶</sup>that is, feet-to-head. See Figure 2.18.

### 3. Neurosurgical Stereotactic Techniques

---

fixed reference plane relative to the skull and, it is assumed, the brain. The ring is surprisingly well tolerated by non-anaesthetized patients, and it may have to be 'worn' for up to twelve hours. See Figure 3.1.

To allow treatment planning, the patient must then be diagnostically imaged using one or more modalities. During each imaging session, an appropriate fiducial system must be fitted over the patient's head and rigidly attached to the head ring. Markers on this fiducial frame must be visible on the resultant images, while not obscuring too much anatomy. As their position relative to the head ring is already known, they are used to calculate the target coordinate(s) relative to the head ring. The fiducial system must have been designed to allow scaling, rotation, and translation transformations of the image to be performed. During imaging, the patient should not move, and to ensure this, is often attached to the couch upon which he or she lies while being imaged. The BRW system was primarily designed to be used with CT imaging. The cylindrical BRW CT-compatible fiducial frame, shown in Figure 3.2, consists of three sets of three rods. Each set of rods is arranged so that two are perpendicular to the head ring, and the third rod runs diagonally in between, forming a 'N' configuration. This is attached to the patient's head ring, Figure 3.3. He or she is then placed into a CT scanner, as shown in Figure 3.4. The transverse<sup>ll</sup> images acquired by the CT scanner will 'cut' the rods, which then appear on each image as nine high-density points around the head (see Figure 3.5 for a typical example). Knowing the true dimensions of the fiducial rods, and by a consideration of similar triangles, three dimensional coordinates can be calculated for each of the diagonal rods (see Chapter 5) in known units. The coordinates of the three diagonal rods define the plane of the image slice (assumed to be flat) relative to the head ring, allowing any other point in the image to be transformed from a two dimensional coordinate in pixels, to a three dimensional point relative to the head ring. During the planning of the treatment, points such as the centre and extremities of the target volume, may be transformed in this way. This is a straightforward technique using a computer and appropriate software to identify the rod positions, select the target pixel coordinates and calculate the transformation, although it

---

<sup>ll</sup>that is, perpendicular to the inferior-superior axis of the patient. See Figure 2.18



**Figure 3.1** BRW stereotactic head ring attached to patient's skull by upright posts and pins. All photographs taken after obtaining the patient's informed consent.



**Figure 3.2** BRW CT compatible fiducial frame.

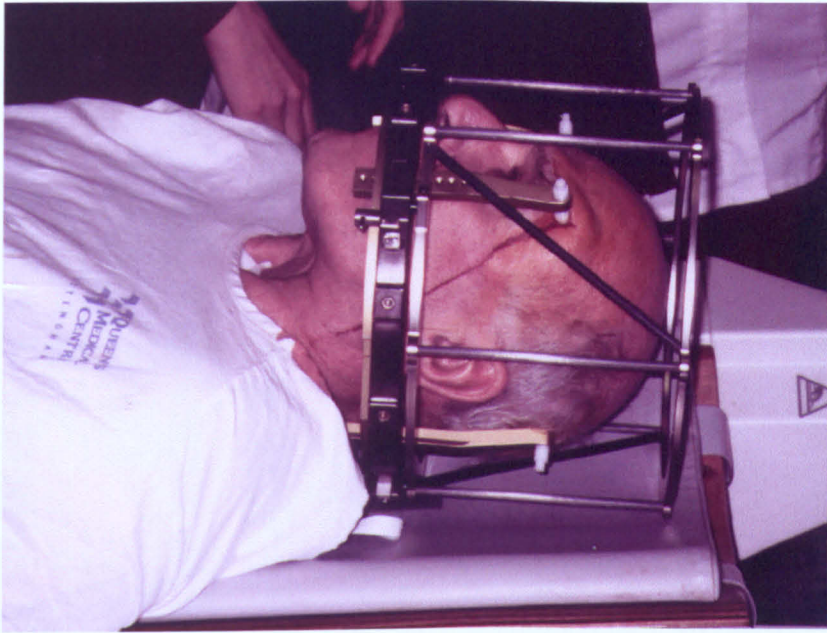


**Figure 3.3** BRW CT compatible fiducial frame and head ring attached to patient.



**Figure 3.3** Typical unenhanced CT image. The nine fiducial rods of the BRW frame, the four weight points, and central target volume, are visible (cf. figure 3.33).

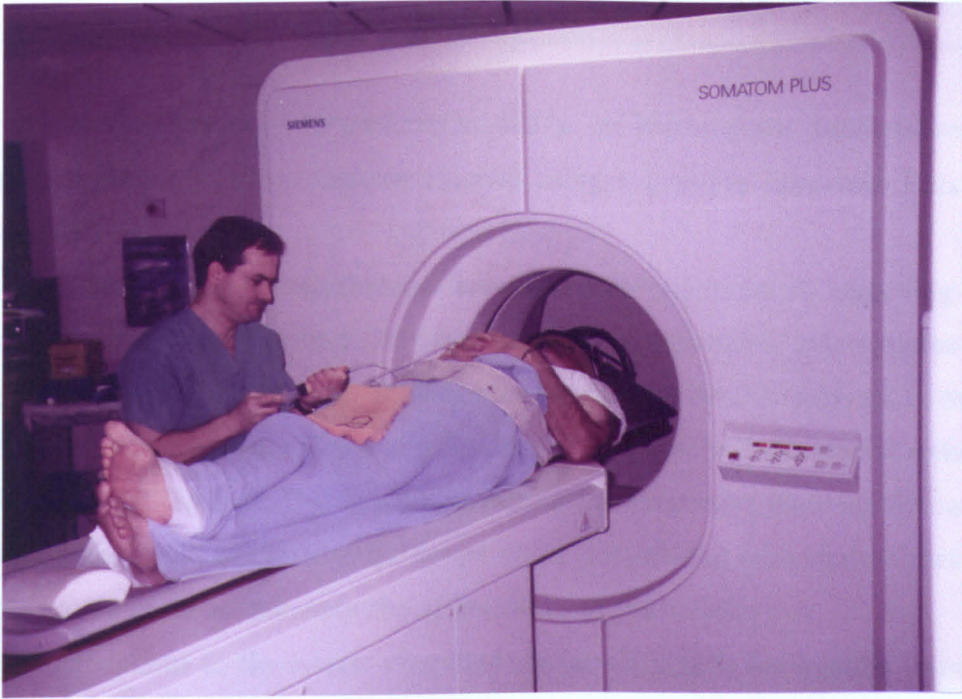


**Figure 3.4** Stereotactic patient prior to contrast enhanced CT scan.

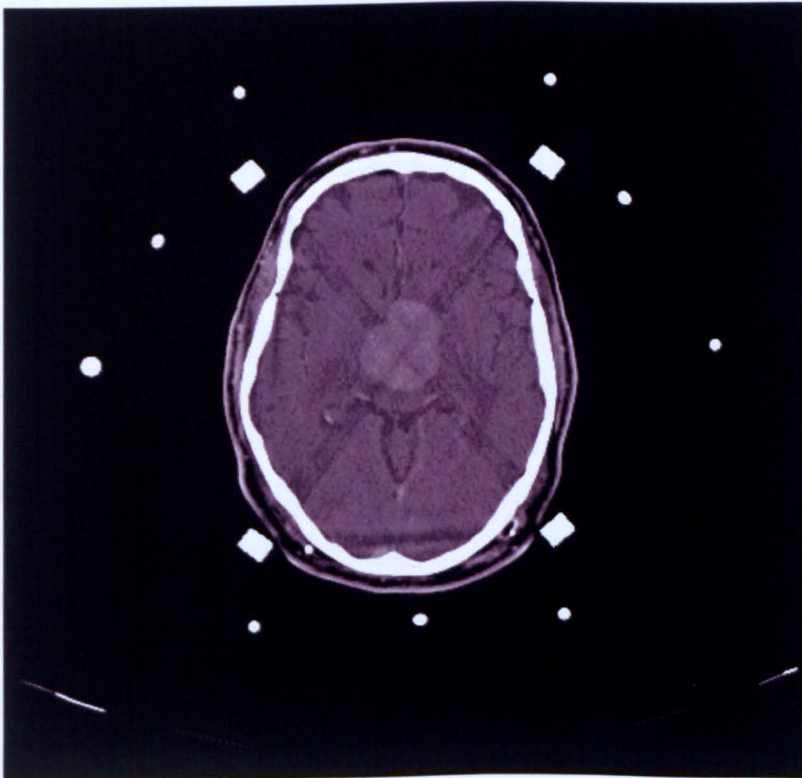


**Figure 3.5** Typical transaxial CT image. The nine fiducial rods of the BRW frame, the four upright posts, and central target volume, are visible (*c.f.* figure 3.13).

### 3. Neurosurgical Stereotactic Techniques

---

would be very laborious to perform manually. In Nottingham, patients undergoing stereotactic techniques are scanned using a Siemens Somatom Plus CT scanner.

Neurosurgery and radiotherapy have different requirements regarding the range of CT images acquired. Minimal neurosurgical planning only requires images through the target lesion. Radiosurgery requires images throughout as much of the head as possible, limited only by the requirement that all fiducial rods are present in each image. This is because during the treatment planning for radiotherapy, the depth of tissue to the target point is needed at many points through each arc, in order to calculate the attenuation of the x-rays.

Modifications to the system described above will usually be required to make it compatible with other imaging modalities. For planar x-ray angiography, a different fiducial system is used with the BRW system. Angiography involves imaging the vascular system; using x-ray, this is usually done by injecting a radio-opaque dye (contrast agent) into an artery *via* a catheter. This is particularly useful for visualizing AVM's, and there is a wealth of experience of diagnostically interpreting x-ray angiograms of them. With the increasing use of accurate and relatively quick digital subtraction angiography, where a radiograph taken when no contrast agent is present is subtracted from a radiograph taken when contrast is present, in order to improve the contrast of the blood vessels, angiography continues to play an important role in stereotactic planning. The fiducial system consists of a rectangular Perspex frame which attaches to the head ring. On each of the anterior, posterior, and both lateral\*\* faces, four dots, identified by letters, are marked with a radio-opaque material. Plane lateral and anterior-posterior radiographs are taken, usually, but not necessarily, orthogonal to each other, so that eight dots (four on the near face, four on the far face) are visible on each angiographic image. These allow the same target points, identified in both angiograms, to be transformed to three dimensional coordinates relative to the head ring, corrected for magnification, rotation, translation, and divergence of the x-ray beam. Again, although the BRW angiographic system allows these images to be easily obtained, the transformation can only be routinely performed

---

\*\*that is, front, back, and sides respectively. See Figure 2.18

### **3. Neurosurgical Stereotactic Techniques**

---

using a computer system.<sup>112</sup>

Once the images have been acquired, the treatment planning is undertaken. All fiducial rods are identified, allowing a computer to transform any point within the image to a three dimensional coordinate relative to the head ring. For neurosurgery, the surgeon may just require the target point to be converted to the appropriate coordinates to 'dial up' on the treatment jig. In this case, one image may be selected as containing the centre of the lesion to be treated. Using the computer controlling the CT scanner, the coordinates of the fiducial rods are found, using the basic imaging processing software that is delivered with all CT scanners. The pixel coordinate of the target point is also found. These are entered into a small, separate, dedicated computer, similar to a modern day programmable desk-top calculator, which performs the numerical coordinate transform. Alternatively, the surgeon may wish to plan the surgery visually using dedicated software on a computer, using the images transferred from the scanner, in order to select not only the target, but the most appropriate path of approach to the target, avoiding the most sensitive regions within the brain. The program then calculates a further transformation of the target coordinates to the system used to directly specify the coordinate on the treatment jig. Radiosurgery treatment planning may only be performed with the extensive use of a computer running dedicated software, and requires all the images acquired. The target volume, as well as other radiosensitive structures, is outlined on each image in which they appear, as well as the skin surface. The application of the arcs of radiation can then be modelled on the computer, taking into account the measured characteristics of the radiation beam at the collimator field size selected, and the particular depth in the head for each portion of the arc that the beam has to traverse to reach the target. A map of the radiation dose throughout the target and head can then be constructed, and parameters of the arcs varied until the most uniform high dose volume covers the target volume, while minimizing 'hot spots' of radiation dose elsewhere. This solution is then transformed into the coordinate system used by the treatment linear accelerator.

Once the treatment has been planned, the patient is then moved to a treatment room. Neurosurgery takes place in an operating theatre. The patient is

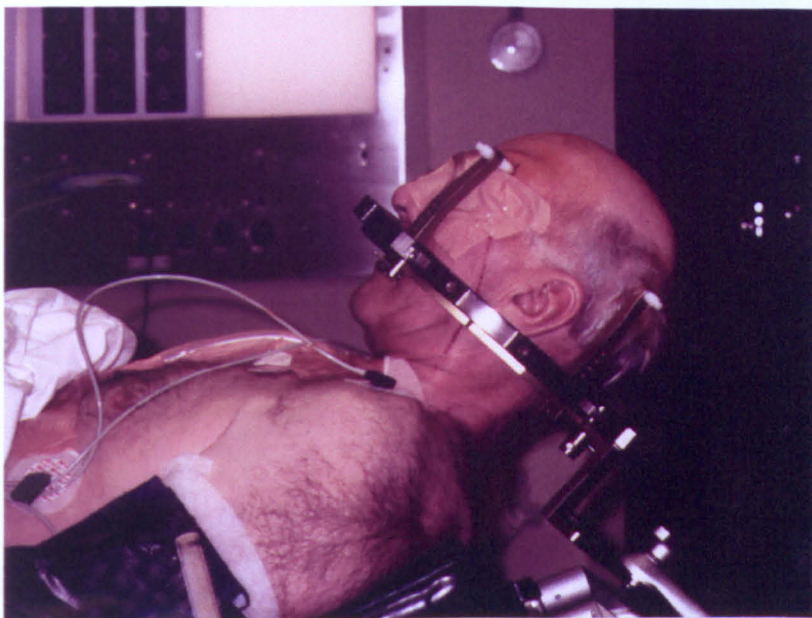
### 3. Neurosurgical Stereotactic Techniques

---

fixed to the operating table *via* the head ring, onto which the biopsy treatment jig is attached, see Figure 3.6. This calibrated jig allows the target point to be 'dialled up' using the previously calculated coordinates, so that the needle passes through the desired entry point, to the target point. The jig works according to a polar coordinate system; the two arcs are set, and the needle advanced along a radius until it reaches the desired pre-calculated depth. The initial BRW jig, shown in Figure 3.7, was not terribly convenient to use in theatre. It was later modified, and this new Cosman-Roberts-Wells (CRW) biopsy jig greatly simplifies the setting of target coordinates, and use in theatre (see Figure 3.8). Its use in determining the target during a craniotomy is shown in Figure 3.9. For radiosurgery, the patient is attached to the calibrated treatment couch in the linac bunker. Extensive routine quality control tests will have been performed to ensure that the axes of rotation, collimation, and radiation output fall within predefined tolerances. The couch and linac gantry are moved to the starting position of the first arc. From outside the bunker, irradiation and movement of the gantry through the pre-planned arc are initiated. For the usual multi-arc treatment, the new starting positions of the couch and gantry are set before initiating the each arc.

When treatment has been completed, the frame is removed quickly. In the case of radiotherapy, where it is desirable to perform fractionated treatment over at least a week, an alternative head ring is available for use with the BRW system — the Gill-Thomas-Cosman (GTC) head ring. A dental impression of the patient's teeth and roof of the mouth is taken while biting. This mouth bite is rigidly attached to the head ring, which is held at the back of the head by an individually moulded silicon pad placed over the occiput; straps over the top of the head complete the fastenings. With practice, the GTC head ring may be repeatably attached to a cooperative patient's head with quoted variation of about 1 mm, which would be suitable for fractionated treatment.

The BRW, and more recently the CRW, systems have been used in the Queen's Medical Centre in Nottingham for many years for performing stereotactic biopsies and directing craniotomies. These are planned using CT images and carried out at the rate of about one per week. Stereotactic radiotherapy of



a.



b.

**Figure 3.6** Anaesthetized patient being prepared for neurosurgery. In Figure 3.6b, the CRW biopsy jig has been attached to the BRW head ring.

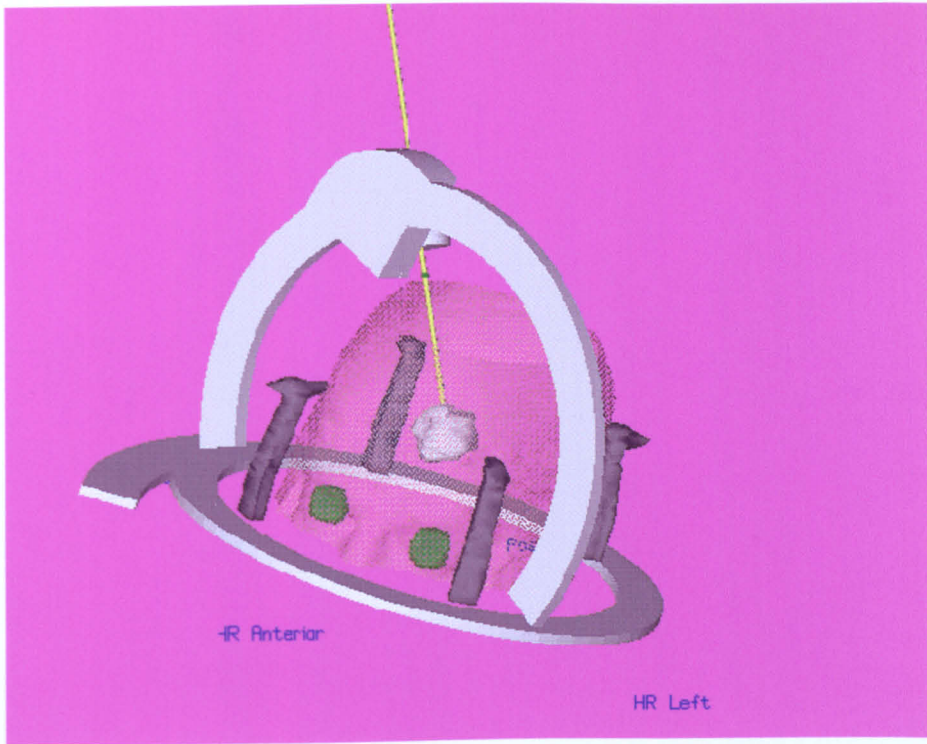


**Figure 3.7** BRW biopsy jig (from StereoPlan software).

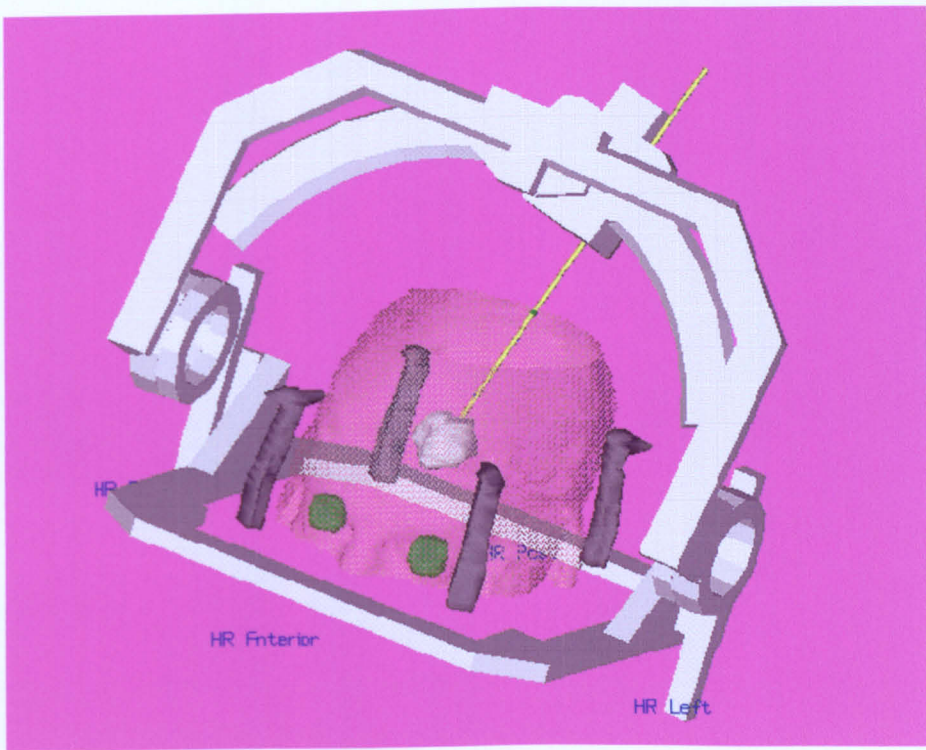
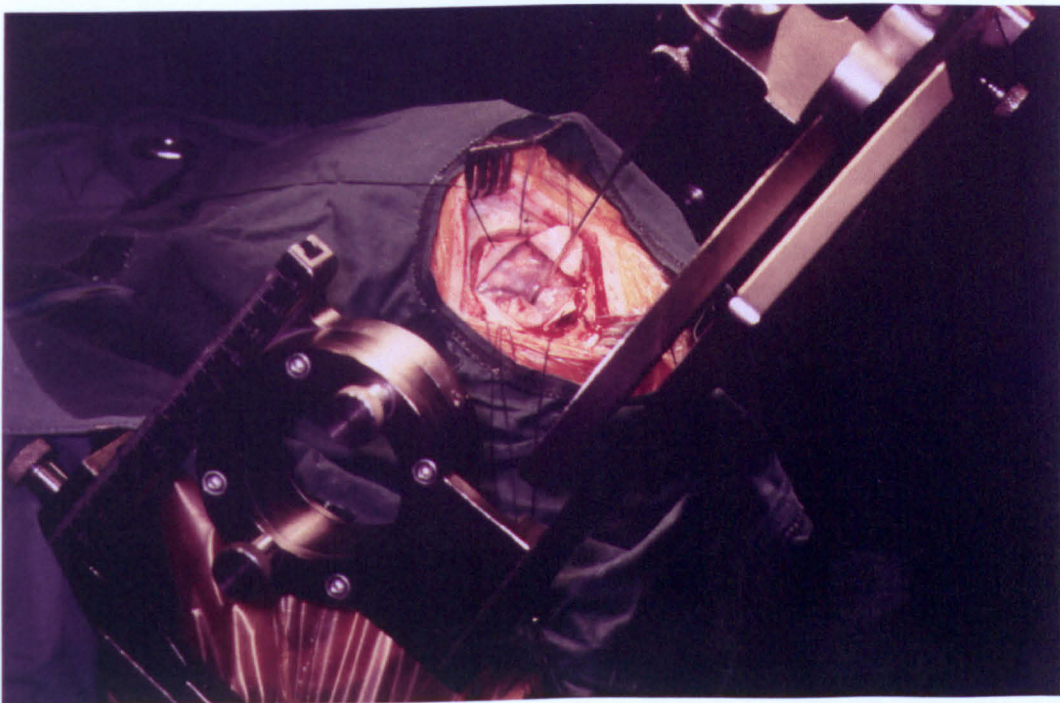


**Figure 3.8** CRW biopsy jig (from StereoPlan software).



a.



b.

**Figure 3.9** Three dimensional localization of a tumour with the CRW biopsy jig during a craniotomy. Target coordinate chosen from CT and MR images.

### **3. Neurosurgical Stereotactic Techniques**

---

small tumours was first undertaken in 1995, with the head ring being fitted, and patient CT scanned, at the QMC, while the radiotherapy occurred later that day at the Nottingham City Hospital. For radiosurgery of AVM's, planar x-ray angiography was also performed and used to aid the treatment planning. Image based treatment planning is performed using the StereoPlan and XKnife programs supplied by RSA (Burlington MA, USA), running on a Hewlett Packard 715/75 workstation. For neurosurgical planning, where just the target coordinate in one slice is required quickly, a SCS1 computer system is used. While the GTC head ring was successfully used on a few patients, its success depended on the cooperation of the patient, who had to understand exactly what was required of him or her, so far as maintaining a constant bite on the mouth bite. As the normal BRW surgical head ring was found to be so well tolerated, and fractionated stereotactic radiotherapy is not offered, the GTC head ring is not currently in routine use.

### **3.5 Application of MRI to the BRW System**

The modification of the BRW system to allow the inclusion of MR images for treatment planning is not so straightforward as for other imaging modalities. Historically, most components of stereotactic systems have been constructed from steel or other ferromagnetic materials. Placing these within the uniform high static magnetic field of a MR imager results in them becoming magnetized leading to distortion of the main uniform field. The inhomogeneities cause spatial distortion in any images acquired, as described in Chapters 2 and 4. Large amounts of ferromagnetic materials may also cause physical danger to the patient, staff, and equipment due to the large forces they experience within the high magnetic field. Conducting materials may also distort the main magnetic field if they are constructed so that they contain loops, which may allow induced eddy currents to circulate, resulting in the generation of a localized magnetic field. A further constraint is that it is highly preferable if the MR compatible fiducial system fits within the head RF coil inside the MR scanner, resulting in an image with a larger signal to noise ratio compared to larger diameter RF coils, such as a whole body coil. Head coils have a typical internal diameter of less

### 3. Neurosurgical Stereotactic Techniques

---

than 30 cm. Thus, a complete re-design of the stereotactic system is required to make it MR compatible.

The MRI compatible BRW system uses a different head ring, separate from the usual CT compatible head ring. It is made of aluminium, 'broken' twice into two semicircles and re-joined with a non-conducting material insulating the two halves to block the flow of the majority of eddy currents (see Figure 3.10). It is attached to the patient using four up-right posts, with the pins that screw into the patient's skull being made of aluminium coated with plastic, in a similar fashion to the BRW head ring attachment. Onto this fits a fiducial frame made of Perspex and containing straight tubes, in 'N' configurations, which may be filled with distilled water<sup>††</sup>, to provide a NMR signal during imaging. Whereas raw CT images may only be acquired as transverse sections, or slices at an angle to transverse of no more than about 20°, MR images may be acquired at any orientation relative to the patient. The MR compatible fiducials allow for sagittal and coronal images, as well as transverse, by modifying the 'N' configuration of the fiducial rods, by adding two extra rods to cross the open ends of the 'N', creating a square of rods, cut by a diagonal rod, from corner to corner. By placing sets of this boxed 'N' configuration on the anterior, posterior, laterals, and superior faces of the fiducial frame, any image acquired parallel to one of the transverse, sagittal, or coronal planes, or at not a large angle to one of them, will contain enough rods to allow the plane of that image to be defined. This MR compatible fiducial frame is called the Universal Compact Localizing Frame (UCLF), and shown in Figure 3.11.

Both the MR compatible head ring and the fiducial system will fit within the head RF coil of the MR scanners used for imaging, which allows greater flexibility of patient position within the head coil (see Figure 3.12). A typical MR image acquired of a patient undergoing stereotactic planning is shown in Figure 3.13. However, with the low fitting of the head ring, level with the patient's mouth, it is not necessary to place the head ring within the coil, as in the vast majority of cases, the target volume will be over 5 cm superior to the head ring. If

---

<sup>††</sup>or, if a shorter  $T_1$  is required, a solution of copper sulphate and distilled water, or just tap water.



**Figure 3.10** MR compatible BRW head ring.

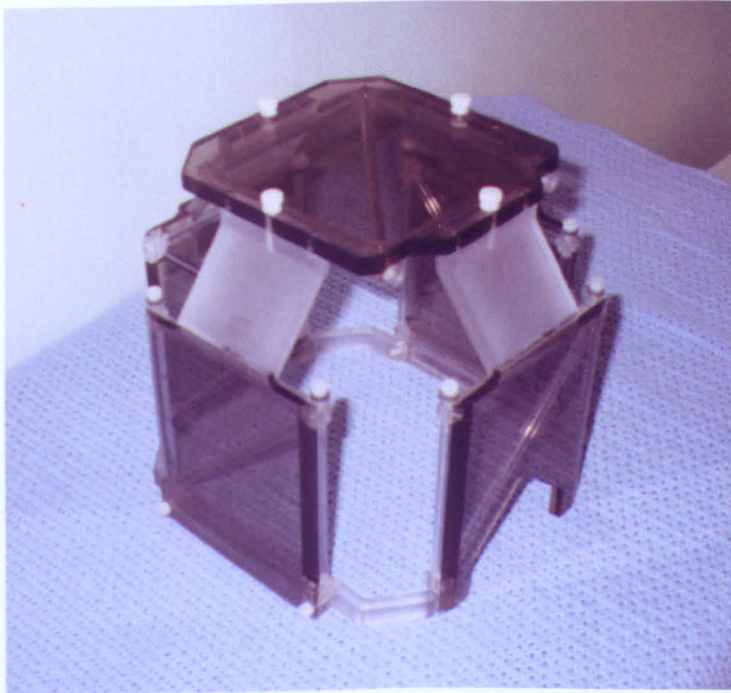


**Figure 3.11** MR compatible fiducial frame (UCLF).



**Figure 3.12** Patient, with MR compatible BRW stereotactic system attached, positioned in opened RF head coil prior to MR scan.

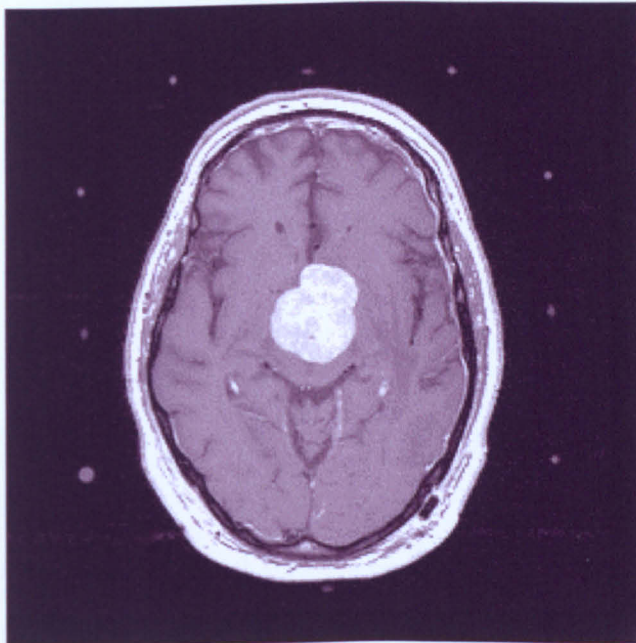


**Figure 3.13** Typical transaxial MR image. The nine fiducial rods and central target are visible (*c.f.* Figure 3.5). The posterior rod is used for sagittal images only.

### **3. Neurosurgical Stereotactic Techniques**

---

the head ring is butted up against the outside of the head coil, this is a large enough distance to allow the target volume to be in a region of uniform RF field, resulting in normal MR images. A larger diameter head ring, such as the BRW CT compatible head ring, is tolerated much better by patients than a relatively smaller, tight, BRW MR compatible head ring, and hence can be worn for a longer time by the patient, allowing more imaging modalities to be used, and more thorough treatment planning to take place.

The BRW MR compatible head ring is designed to allow the traditional BRW CT compatible head ring to be fitted over the top of it, and rigidly attached together (see Figure 3.1). From then on, the head ring system behaves as if it was the usual BRW CT compatible head ring. Fiducial systems for CT and x-ray planar angiography may be fitted directly to the CT compatible head ring, which in turn will locate to the same fastenings on the couch in the operating theatre for biopsies, and the linac couch.

In Nottingham, both the StereoPlan and XKnife image based treatment planning systems, and the SCS1 computer, accept MR images containing fiducial rods as positioned in the UCLF. Coordinates in these images are transformed to the same coordinate system as points from CT images acquired with the BRW fiducial system attached. Hence the StereoPlan and XKnife programs can register CT and MR image sets and display the result, allowing the neurosurgeon to use information from both imaging modalities simultaneously while planning the treatment.

### **3.6 Discussion of Advantages and Disadvantages of Using MRI for Stereotactic Treatment Planning**

The potential gain in using MR images to aid planning of stereotactic procedures is vast. Contrast in diagnostic x-ray images is purely due to different densities within the object, and hence only anatomy with contrasting densities is visible. However, depending on the imaging sequence used, MR images may show not only water density contrast, but contrast between regions with equal water

### 3. Neurosurgical Stereotactic Techniques

---

densities containing different chemical environments, *via*  $T_1$  and  $T_2$  relaxation time weightings. Other MR imaging sequences can exploit or suppress other contrast mechanisms, described in Chapter 2; in particular, MR angiographic images are most informative regarding the location of AVM's. Use of the correct MR imaging sequence results in the lesion to be targeted being highly visible in MR images, compared to its visibility in CT images, if, indeed, it is visible in a CT image at all. The extra physiological information contained in MR images, from  $T_1$  and  $T_2$  effects, allow the boundary of the lesion to be defined more precisely, especially when it is surrounded by pathological tissues which are not to be treated, *e.g.*, the feeding vessels surrounding the nidus of an AVM. The ability to directly acquire images in planes other than transaxial is another advantage of using MRI; many lesions are more easily located and defined in non-transverse planes. Also, MR image sets may be acquired as a volume, with voxels isotropic in dimension with no artefacts due to 'cross-talk' between individual slices. This provides a consistent data set which may be sampled in different planes during post-processing, to allow the lesion or anatomy to be shown more clearly.

The main disadvantage in using MR images for stereotactic planning is the inherent spatial distortion present in images acquired using contemporary techniques. This is mainly caused by inhomogeneities in the magnetic field, and is described in Chapter 4. It would be expected that the placement of the additional apparatus required for stereotaxis, as described earlier in this chapter, close to the region being imaged, could lead to a further increase in the inhomogeneity of the magnetic field. The problems caused by distortion for stereotactic planning based on MR images can be categorized into two groups. Firstly, distortion may cause problems for the clinician in determining the size and position of the lesion, as its shape may be distorted, and the distortion may have led to regions of false contrast enhancements or signal loss. Secondly, distortion, not only of the target point, but also of the fiducial rods, will lead to incorrect pixel coordinates being used in the stereotactic transform to three dimensional coordinates, and hence to an incorrect final target point. As the stereotactic system is being applied in order to improve the accuracy of locating the final target coordinate, the application of MR, with its potential spatial uncertainties may appear to be counter

### 3. Neurosurgical Stereotactic Techniques

---

intuitive. However, keen to utilize the advantages of MR over CT, as described above, research has been undertaken in many centres over the past decade to try to judge the suitability of using MR images for neurosurgical stereotactic planning. This is described more fully in Chapter 5. This work has concentrated on both correcting any distortion present in the MR images prior to their use for stereotactic planning, and quantifying the distortion present in order to judge whether it is acceptable. However, despite the positive conclusions of most of these works, it is still considered 'received wisdom', especially among clinicians, that spatial distortion in MR images invalidates the use of this modality for stereotactic treatment planning.

To try to get what is seen as the best of both worlds, many centres acquire both CT and MR images of stereotactic patients, and use both to plan the treatment. However, this leads to a rather unscientific state of affairs. If the target coordinates calculated from the two modalities agree, then it would seem unnecessary to perform both scans, except for research purposes. If the target coordinate from MR differs greatly from that obtained from CT, the CT target coordinate is usually taken as the final coordinate, not least because of the concern that the difference may be due to spatial distortion in the MR image. Both these scenarios suggest that the extra effort in performing a MR scan, in terms of scanning time, prolonging the duration for which the patient must 'wear' the stereotactic head ring, and effort in modifying the stereotactic system to make it MR compatible, is not worthwhile or clinically useful. However, another possibility to account for the different target coordinates calculated from CT and MR images is that the two modalities are highlighting clinically useful different aspects of the target, rather than spatial distortion. If this is the case, then application of MR imaging will prove to be most valuable in precisely defining the target. Before this can be evaluated, the amount of spatial distortion present must be known, in order to allow any real spatial difference between anatomical structures to be appreciated. Furthermore, it would seem reasonable to conclude that if the spatial errors in MR images due to distortion are too great, then MRI should not be used routinely in stereotactic treatment planning<sup>‡‡</sup> as information

---

<sup>‡‡</sup>although this does not, of course, invalidate its use in diagnosis

### **3. Neurosurgical Stereotactic Techniques**

---

calculated from MR images would not be trusted or used. However, if the spatial errors are acceptable, then the target calculated from MR images is to be trusted, and so it is unnecessary to perform CT imaging for surgical planning purposes at all. CT still may be necessary for the planning of radiosurgery, as it is possible to convert the pixel intensity in a CT image to a physical density. At the x-ray energies used for radiotherapy, the Compton effect dominates the interactions between photons and atoms, and the resulting attenuation is proportional to density.<sup>51</sup> Treatment planning programs may use this information to correct their radiation dose calculations for various densities throughout the head.

Although CT images are generally assumed to be free from spatial distortion, they do suffer from their own artefacts. In particular, reconstruction 'streak' artefacts, caused by high density objects (such as the metal apparatus used for the BRW stereotactic head ring and fiducial frame) may overlay and obscure regions within the image, or cause regions to appear with incorrect contrast (this effect is present to a small degree in Figure 3.5 as a darker cross between the four posts). Although x-rays travel in straight lines, the finite collimation required of the beam and x-ray detectors, as well as finite mechanical tolerances, mean that CT images themselves may exhibit small amounts of spatial distortion. Despite this uncertainty, CT images are usually taken as the undistorted 'golden standard' against which potentially distorted MR images are compared.

### **3.7 Conclusion**

This chapter has outlined the continuing importance of neurosurgical stereotactic techniques. The practical aspects of a stereotactic procedure have been described with reference to the BRW system. The superior contrast of anatomy and pathology available in MR images, relative to CT, has made its application to stereotactic treatment planning an important area of research. Spatial distortion of the MR images is the main drawback of this application of MRI. In order to judge the suitability of using MR images for neurosurgical stereotactic planning, any distortion must be measured and quantified. However, this distortion is not the error in the final stereotactic coordinate, as distortion in the image affects both the target pixel coordinate and the fiducial rods' pixel coordinates,

### **3. Neurosurgical Stereotactic Techniques**

---

and both are combined to calculate the final three dimensional coordinate. Previous work mainly has considered the distortion present in MR images in order to judge its suitability for use in stereotactic treatment planning. Less attention has been given to considering the effect this distortion will have on the final three dimensional coordinate. The work presented in this thesis aims to provide a more comprehensive quantification of distortion in MR images and its effect on and relationship to the final three dimensional stereotactic coordinate. Sources of error, other than distortion in MR images, will be included from previously published work. An appreciation of what error is acceptable will be derived from calculation of what error is already being accepted by default, from standard CT planned stereotactic procedures. This will allow a more thorough evaluation of the suitability of the use of MR images in neurosurgical stereotactic treatment planning.

# Chapter 4

## Spatial Distortion in MRI

### 4.1 Introduction

The work presented in this thesis was undertaken with the aim of being able to quantify the effect of distortion in MR images in stereotactic neurosurgical procedures, and to correct this distortion where possible. Before considering the particular case of the effects of MR image distortion in stereotaxis, it is necessary and enlightening to consider the subject of distortion in MR images more generally, as well as methods for its correction.

This chapter presents a more thorough analysis of distortion in MR images, followed by reviews of previously published methods for its correction. As will be seen, inherent in any correction method lies quantification of the original distortion, and so a correction method serves the dual purpose of producing a corrected image and the production of a spatially localized map of the original distortion across the image. One of these correction methods, devised by Chang & Fitzpatrick<sup>17</sup> was implemented as part of the current work and used to correct distortion in single slice MR images, acquired using both spin warp and EPI acquisitions, as well as to quantify the initial distortion. This was performed on MR images of both phantoms and human subjects.

With application to distortion in frame-based stereotaxis, an obvious potential source of distortion in MR images would be the aluminium head ring used, as described in Chapter 3. The correction method was used to quantify any dif-

## 4. Spatial Distortion in MRI

---

ference in distortion in images of a phantom with and without the local presence of the head ring in the MR scanner.

While the work presented in this chapter was being performed, the chance arose to compare Chang & Fitzpatrick's correction method with another method for correcting distortion in MR images based on phase evolution, described below. The results of this comparison are presented here briefly, as they provide validation of the local implementation of Chang & Fitzpatrick's correction method as well as highlighting some limits and restrictions in the method.

Although the work presented in this thesis is primarily concerned with distortion in MR images with application to stereotaxis, the problem of MR image distortion is present in many other fields of MRI. The application of the implemented distortion correction method to two other wide-spread contemporary uses of EPI also is presented.

Finally, the method of correcting the distortion present in multislice volume acquisitions presented by Chang & Fitzpatrick is implemented and explored more fully. Theoretical modifications to their method are presented, implemented, and evaluated.

### 4.2 Sources and Description of Spatial Distortion in MRI

As described in Chapter 2, the process of constructing a magnetic resonance image requires a known one-to-one relationship between the frequency of the nuclear magnetic resonance signal and the spatial position of its source. The presence of an unknown inhomogeneous magnetic field in the imaged volume results in the actual relationship deviating from the assumed relationship by an unknown amount. As the reconstruction of the image follows the assumed relationship, distortions of space and intensity in the final image result. Magnetic resonance imaging is usually performed using imaging systems that are designed to have a main static uniform magnetic field, onto which is superimposed spatially varying linear magnetic field gradients. These linear conditions are assumed to be true when constructing the image from the acquired NMR signal. However, in practice, these fields are not homogeneous; spatial magnetic field inhomogeneous.

## 4. Spatial Distortion in MRI

---

ogeneities are introduced by the design and construction of the sources of the main magnetic field and gradient sets, and from local magnetic fields caused by differences in magnetic susceptibility between various objects in the imaged volumes.<sup>62</sup> A MR image acquired in the presence of an inhomogeneous magnetic field, but reconstructed assuming a homogeneous field, will exhibit geometrical and intensity distortions.<sup>17, 62</sup>

These magnetic field inhomogeneities may be classified in to two categories; static and time dependent. Time dependent inhomogeneous magnetic fields vary throughout the MR image acquisition, and are typically caused by the decay of short lived eddy currents, induced into the magnet by the switching of the magnetic gradients. They, and their effect on the resulting MR image, are difficult to model, and are ignored in the work in this thesis. Only static magnetic field inhomogeneities, which remain constant throughout the image acquisition, are considered.

### 4.2.1 Spatial Distortion in Spin Warp Acquisitions

The effects of a static magnetic field inhomogeneity on a MR image can be modelled mathematically.<sup>17</sup> As shown in Chapter 2, the detected NMR signal,  $S$ , from a thin slice located at  $z=z_1$  as a function of time,  $t$  (or  $k$ ), for a traditional spin echo spin warp imaging sequence, in homogeneous magnetic fields and ignoring  $T_2$  and  $T_2^*$  decay, can be written as

$$S(k_x, k_y, z_1) \propto \iiint \rho(x, y, z) \delta(z - z_1) e^{ik_x x} e^{ik_y y} dx dy dz \quad (4.1)$$

If the frequency encoded and phase encoded axes are along  $x$  and  $y$  respectively, then

$$k_x = \gamma \int_{-\frac{t_{fe}}{2}}^t G_x(t') dt' \quad \text{and} \quad k_y = \gamma \int_0^{t_{pe}} G_y(t') dt' \quad (4.2)$$

where  $t_{fe}$  is the time for which the NMR signal is sampled, while the readout gradient,  $G_x(t)$  is applied. The origin of  $t$  is taken at the centre of the echo, which is also set to the centre of the sampling window.  $t_{pe}$  is the duration for which the phase encoded gradient,  $G_y(t)$ , is applied, prior to the readout gradient. In order to elucidate the equations, it is usual to replace the integrals in Equation 4.2

#### 4. Spatial Distortion in MRI

with the product of time and the mean gradient over that duration. So, if

$$G_x = \frac{1}{t_{fe}} \int_{-\frac{t_{fe}}{2}}^{\frac{t_{fe}}{2}} G_x(t') dt' \quad \text{and} \quad G_y = \frac{1}{t_{pe}} \int_0^{t_{pe}} G_y(t') dt' \quad (4.3)$$

then  $k_x = \gamma G_x t$  and  $k_y = \gamma G_y t_{pe}$ . In practice, the NMR signal is usually acquired in the presence of a constant gradient.

A thin slice has been selected along the  $z$  axis at  $z=z_1$  away from the magnet's isocentre, represented in Equation 4.1 by a Dirac delta function. In the absence of any magnetic field gradients (or at the magnet's isocentre) the angular Larmor frequency is given by  $\omega_0 = \gamma B_0$  where  $\gamma$  is the gyromagnetic ratio of the nucleus of interest. With the application of a linear slice selection gradient,  $G_z$ , the nuclei located at a distance  $z_1$  away from the isocentre will spin with frequency  $\omega_1 = \gamma (B_0 + G_z z_1)$ . Hence the slice at  $z_1$  will be excited by application of radiowaves with central angular frequency  $\omega_1$  where

$$z_1 = \frac{\omega_1 - \omega_0}{\gamma G_z} \quad (4.4)$$

A static magnetic field inhomogeneity\* can be described by a function  $B_e(x, y, z)$  where  $B_e$  is the deviation from the main static homogeneous magnetic field  $B_0$ .  $(x, y, z)$  represents the actual coordinate system in space, regardless of any spatial distortion that may be introduced by  $B_e$ . In the slice select direction, this will have the effect of modifying Equation 4.4. If radiowaves are applied at a general frequency  $\omega$ , then a slice,  $z'$ , will be excited, where

$$\omega = \gamma (B_0 + B_e(x, y, z) + G_z z') \quad (4.5)$$

As  $B_e$  is a function of  $x, y$ , &  $z$ , then  $z'$  also is a function of position. During image acquisition, Equation 4.4 is expected to hold, and so radiowaves of frequency  $\omega_1$  are applied, with the expectation of exciting a slice at  $z_1$ . However, with the presence of  $B_e$ , a slice  $z'_1$  will be excited, which from Equations 4.4 and 4.5 is described by

$$z'_1(x, y, z) = z_1 - \frac{B_e(x, y, z)}{G_z} \quad (4.6)$$

---

\* $B_e$  is also commonly referred to as  $\Delta B_0$  in the literature

#### 4. Spatial Distortion in MRI

---

This results in a different slice being excited than would have been in the absence of  $B_e$ . If the MR image is calculated without consideration of  $B_e$ , then the signal which has come from slice  $z'_1$  will be 'labelled' as coming from  $z_1$ . This can be viewed as signal actually originating from slice  $z'_1$  being spatially distorted to slice  $z_1$ . Hence, to take account of  $B_e$ , the argument of the delta function in Equation 4.1 must be replaced by the  $(z - z'_1)$ , or  $\left(z - \left(z_1 - \frac{B_e(x,y,z)}{G_z}\right)\right)$ .

The presence of  $B_e(x, y, z)$  in addition to  $B_0$  will result in the nuclei at any point precessing with frequency  $\omega(x, y, z) = \gamma(B_0 + B_e(x, y, z))$ , according to Larmor's equation. After the radiowave excitation pulse, this will result in an accumulation of phase of the NMR signal with time, relative to the NMR signal in the absence of  $B_e$ . This results in an additional term in Equation 4.1 of  $\exp(i\gamma B_e(x, y, z)t)$ . From general analysis of Fourier transform pairs, it can be shown that a spatial shift in one function of the pair results in a phase shift in the other function.<sup>3</sup> As the MR image is obtained by performing a Fourier transform on  $S$ , it might be expected that a phase change in  $S$  would result in a spatial shift in the MR image. For spin warp imaging, the duration of the phase encoding gradient ( $t_{pe}$ ) is kept constant, and the amplitude of  $G_y$  is varied with subsequent excitations to acquire different lines of  $k$  space. Although  $B_e$  will result in a different phase of the spins during the application of the phase encoding gradient, this phase will be the same for each phase encoded line of  $k$  space, as the phase encoding gradient is applied for the same duration and at the same time, after each RF excitation. Hence, the difference in phase between adjacent lines of  $k$  space, for a particular  $k_x$ , will not be affected by the addition of  $B_e$ , and so  $B_e$  will not affect the MR image in the phase encoded direction. This has been observed empirically by Sumanaweera *et al.*<sup>108</sup>

Rewriting Equation 4.1 to include the effects of  $B_e$  gives

$$\begin{aligned}
 S_1(k_x, k_y, z_1) &\propto \iiint \rho(x, y, z) \delta\left(z + \frac{B_e(x, y, z)}{G_z} - z_1\right) e^{ik_x x} e^{ik_y y} e^{i\gamma B_e(x, y, z)t} dx dy dz \\
 &\propto \iiint \rho(x, y, z) \delta\left(z + \frac{B_e(x, y, z)}{G_z} - z_1\right) e^{ik_x \left(x + \frac{B_e(x, y, z)}{G_x}\right)} e^{ik_y y} dx dy dz
 \end{aligned}
 \tag{4.7}$$

It can be seen that the addition of  $B_e$  has caused a shift in the signal along the  $x$  and  $z$  axes of  $\frac{B_e(x, y, z)}{G_x}$  and  $\frac{B_e(x, y, z)}{G_z}$  respectively. It is useful to make the

#### 4. Spatial Distortion in MRI

---

following change of variables reflecting this spatial distortion, in order to derive the effect the distortion has on the final MR image.  $(x, y, z)$  represent the source of the NMR signal and  $(x_1, y_1, z_1)$  represents the position to which that signal is assigned in the final MR image.  $y_1$  is included for generality, and  $z'$  as a dummy variable for integration.

$$\begin{aligned} x_1 &= x + \frac{B_e(x, y, z)}{G_x} \\ y_1 &= y \\ z' &= z + \frac{B_e(x, y, z)}{G_z} \end{aligned} \quad (4.8)$$

which, substituting into Equation 4.7, along with Equation 4.6, gives

$$\begin{aligned} S_1(k_x, k_y, z_1) &\propto \iiint \rho(x(x_1, y_1, z'), y(x_1, y_1, z'), z(x_1, y_1, z')) \\ &\quad \delta(z' - z_1) e^{ik_x x_1} e^{ik_y y_1} \left[ J \left( \frac{x_1, y_1, z'}{x, y, z} \right) \right]^{-1} dx_1 dy_1 dz' \end{aligned} \quad (4.9)$$

where  $J \left( \frac{x_1, y_1, z'}{x, y, z} \right)$  is the Jacobian of the transformation between the  $(x_1, y_1, z')$  and  $(x, y, z)$  coordinate systems. The Jacobian is assumed to be non-zero and finite; this is discussed further below. It is given as

$$\begin{aligned} J \left( \frac{x_1, y_1, z_1}{x, y, z} \right) &= \begin{vmatrix} \frac{\partial x_1}{\partial x} & \frac{\partial x_1}{\partial y} & \frac{\partial x_1}{\partial z} \\ \frac{\partial y_1}{\partial x} & \frac{\partial y_1}{\partial y} & \frac{\partial y_1}{\partial z} \\ \frac{\partial z_1}{\partial x} & \frac{\partial z_1}{\partial y} & \frac{\partial z_1}{\partial z} \end{vmatrix} \\ &= 1 + \frac{1}{G_x} \frac{\partial B_e(x, y, z)}{\partial x} + \frac{1}{G_z} \frac{\partial B_e(x, y, z)}{\partial z} \end{aligned} \quad (4.10)$$

Integrating over  $dz'$  gives

$$\begin{aligned} S_1(k_x, k_y, z_1) &\propto \iint \rho(x(x_1, y_1, z_1), y(x_1, y_1, z_1), z(x_1, y_1, z_1)) \\ &\quad e^{ik_x x_1} e^{ik_y y_1} \left[ J \left( \frac{x_1, y_1, z_1}{x, y, z} \right) \right]^{-1} dx_1 dy_1 \end{aligned} \quad (4.11)$$

Now the slice selection integral has been performed, Equation 4.6 can be rewritten consistently as

$$z_1 = z + \frac{B_e(x, y, z)}{G_z} \quad (4.12)$$

## 4. Spatial Distortion in MRI

---

where  $z$  is the actual source of  $S_1$  and  $z_1$  is where it appears to be from in the presence of  $B_e$ .

A two dimensional Fourier transform of  $S_1$  over  $k_x$  and  $k_y$  yields the MR image,  $i_1$ , exhibiting any effects of  $B_e$ . Likewise,  $i$  is the Fourier transform of  $S$ , the NMR signal in the absence of  $B_e$ . They are given as

$$\begin{aligned} i_1(x_1, y_1, z_1) &= A \iint S_1(k_x, k_y, z_1) e^{-ik_x x_1} e^{-ik_y y_1} dk_x dk_y \\ &= \frac{A \rho(x, y, z)}{J\left(\begin{smallmatrix} x_1, y_1, z_1 \\ x, y, z \end{smallmatrix}\right)} \end{aligned} \quad (4.13)$$

$$\begin{aligned} \text{and } i(x, y, z) &= A \iint S(k_x, k_y, z) e^{-ik_x x} e^{-ik_y y} dk_x dk_y \\ &= A \rho(x, y, z) \end{aligned} \quad (4.14)$$

where  $A$  is a constant. Substituting Equation 4.14 into Equation 4.13 to eliminate  $\rho(x, y, z)$  gives

$$i_1(x_1, y_1, z_1) = \frac{i(x, y, z)}{J\left(\begin{smallmatrix} x_1, y_1, z_1 \\ x, y, z \end{smallmatrix}\right)} \quad (4.15)$$

The above analysis of the effect of the addition of a spatially varying magnetic field inhomogeneity,  $B_e$ , over the object being imaged by a spin warp acquisition, highlights two effects of the same distortion. One is the spatial shift of signal along the  $x$  and  $z$  axes, described by Equations 4.8 and 4.12, and the second is the effect that this has on the intensities in the spatially distorted image, shown by Equation 4.15. The latter effect causes a 'piling up' of image intensity due to non-linear spatial distortion.

### 4.2.2 Spatial Distortion in EPI Acquisitions

A similar analysis can be performed for other imaging sequences. For a slice selective full Fourier EPI sequence, where all the required region of  $k$  space is sampled after one RF excitation, the phase accumulation caused by  $B_e$  is not 'reset' between subsequent acquisitions of frequency encoded lines of  $k$  space by another RF pulse, as it is for spin warp imaging, but evolves throughout the whole acquisition. Echoes refocus the phase of the spinning nuclei at the centre of  $k$  space, and this point is taken as the origin of time. Each frequency

#### 4. Spatial Distortion in MRI

---

encoded gradient, along the readout  $x$  switched axis, also causes a subsequent gradient echo; the NMR signal is refocused once per image in the broadening phase encoded direction, and once per line of  $k$  space in the readout frequency encoded direction. Once again, the mean magnetic gradient strengths along the  $x$  and  $y$  axes are used, given by

$$G_x = \frac{1}{t_{fe}} \int_{-\frac{t_{fe}}{2}}^{\frac{t_{fe}}{2}} G_x(t') dt' \quad \text{and} \quad G_y = \frac{1}{t_{pe}} \int_{-\frac{t_{pe}}{2}}^{\frac{t_{pe}}{2}} G_y(t') dt' \quad (4.16)$$

$t_{fe}$  is the duration of one sweep of  $k$  space in the frequency encoded switched direction, and  $t_{pe}$  spans the total time over which the broadening gradient is applied. For a typical EPI acquisition,  $t_{pe}$  is the duration of the whole acquisition of  $k$  space, and  $t_{fe}$  is  $\frac{t_{pe}}{N_{pe}}$  where  $N_{pe}$  is the number of frequency encoded lines of  $k$  space acquired, *i.e.*, the number of steps along the  $k_y$  direction. Then  $k_x = \gamma G_x t$  and  $k_y = \gamma G_y t$ . The integrals in Equation 4.16 give the area under the broadening gradient, regardless of whether a blipped or constant broadening gradient is used for phase encoding, and the area under the readout gradient, whether it is trapezoidal or sinusoidal. The analogous equation to Equation 4.7 for a single slice EP image then becomes

$$\begin{aligned} S_1(k_x, k_y, z_s) &\propto \iiint \rho(x, y, z) \delta\left(z + \frac{B_e(x, y, z)}{G_z} - z_1\right) e^{ik_x x} e^{ik_y y} e^{i\gamma B_e(x, y, z)t} dx dy dz \\ &\propto \iiint \rho(x, y, z) \delta\left(z + \frac{B_e(x, y, z)}{G_z} - z_1\right) e^{ik_x \left(x + \frac{B_e(x, y, z)}{G_x}\right)} \\ &\quad e^{ik_y \left(y + \frac{B_e(x, y, z)}{G_y}\right)} dx dy dz \end{aligned} \quad (4.17)$$

By making the following substitutions,

$$\begin{aligned} x_1 &= x + \frac{B_e(x, y, z)}{G_x} \\ y_1 &= y + \frac{B_e(x, y, z)}{G_y} \\ z' &= z + \frac{B_e(x, y, z)}{G_z} \end{aligned} \quad (4.18)$$

and

$$J\left(\frac{x_1, y_1, z_1}{x, y, z}\right) = 1 + \frac{1}{G_x} \frac{\partial B_e(x, y, z)}{\partial x} + \frac{1}{G_y} \frac{\partial B_e(x, y, z)}{\partial y} + \frac{1}{G_z} \frac{\partial B_e(x, y, z)}{\partial z} \quad (4.19)$$

#### 4. Spatial Distortion in MRI

---

Equation 4.9 is obtained and the analysis proceeds as above. Spatial distortion is present along all three axes.

The distortion in EP images can be compared to the distortion in conventional spin warp images, assuming both are acquired with the same field of view. In the latter case, the NMR signal for each frequency encoded line of  $k$  space is typically acquired for 5 to 10 ms; for EPI it is typically a tenth of this duration which requires a magnetic gradient in the frequency encoded direction of ten times the magnitude. From consideration of Equations 4.8 (for spin warp imaging) and 4.18 (for EPI) it can be seen that this will result in the spatial distortion along the frequency encoded axis of an EP image being one tenth of that in a spin warp image. However, in the phase encoded direction, where there is no spatial distortion in a spin warp image, in EPI the phase encoding magnetic gradient is effectively applied throughout the image acquisition. For an EP image composed from  $N_{pe}$  (typically 128) frequency encoded lines of  $k$  space, this gradient would be affecting the phase of the spins for  $N_{pe}$  times the duration of the frequency encoded gradient. For an image containing isotropic pixels, its magnitude would be  $\frac{1}{N_{pe}}$  <sup>th</sup> of that of the readout magnetic gradient, and thus the spatial distortion  $N_{pe}$  times worse along the phase encoded axis than along the frequency encoded axis. As will be seen later in this chapter, spatial distortion in a spin warp image is typically 1 mm along the frequency encoded axis. For a typical EP image acquired with the same field of view, the spatial distortion along the frequency encoded axis would be 0.1 mm and 13 mm along the phase encoded axis. The spatial distortion in EP images is dominated by that along the phase encoded axis, and that along the frequency encoded axis is usually considered to be insignificant by comparison. Hence spatial distortion in the image plane is usually considered to be one dimensional under both imaging regimes; along the frequency encoded readout axis in a spin warp image and along the phase encoded broadening axis in a EP image.

As can be seen from Equation 4.8, the distortion along the frequency encoded  $x$  axis depends on  $G_x$ . The choice of the value of  $G_x$  determines the extent to which  $k$  space is traversed along the  $k_x$  axis (see Section 2.4.1). The maximum excursion along this axis is  $k_{x_{max}} = \frac{1}{2}\gamma G_x t_{fe}$ , for the symmetric imaging experi-

#### 4. Spatial Distortion in MRI

---

ment considered above. In order to generate a MR image using a discrete Fourier transform (FT), the NMR signal must be digitized, in  $N$  points for a duration of  $t_{fe}$ . The properties of the subsequent discrete FT<sup>91</sup> result in the final image possessing a pixel resolution of  $\frac{1}{2k_{x,max}}$  and total width (*i.e.*, field of view) of  $\frac{N}{2k_{x,max}}$ . Hence, to maintain a fixed field-of-view (and pixel size), the product of  $G_x$  and  $t_{fe}$  must be constant. However, as  $G_x$  may vary, so long as  $t_{fe}$  compensates, it is possible to acquire an image with the same pixel size and field-of-view, but varying amounts of spatial distortion. It is more usual and convenient, to express this in terms of bandwidth per pixel (or frequency per point) along an axis, *i.e.*,  $\frac{1}{t_{fe}}$ . This is the range of frequencies which contribute to the signal intensity in any one pixel in the MR image (assuming linear magnetic gradients are used during image acquisition). Spatial distortion due to  $B_e$  may now be presented in an alternative formalism: the addition of  $B_e$  causes nuclei to precess with an additional frequency of  $\gamma B_e$  and hence signal intensity in the MR image will be misplaced by  $\gamma B_e t_{fe}$  pixels. In the style of Equation 4.8 this is

$$X_1 = X + \gamma B_e(x, y, z)t_{fe} \quad (4.20)$$

where  $X_1$  and  $X$  are in units of pixels. This can be a more useful form of Equation 4.8 in an empirical setting as it is usually easier to measure  $t_{fe}$  than  $G_x$ . Hence, if the actual distortion caused by  $B_e$  can be measured in the MR image, in the arbitrary units of pixels, then a value of  $B_e$  at that point may be calculated.

For both the spin warp and EP images considered above, the spatial distortion along the slice selected axis is the same. As can be seen from Equation 4.8, the larger the slice select magnetic gradient, the smaller the spatial distortion along the slice axis. For RF pulses of constant bandwidth, this is the same as saying that thinner slices result in less through-slice spatial distortion. For single slice MR images, the slice thickness is usually a few times larger than the in-image-plane pixel size. For a spin warp image on a modern MR scanner with an in-plane pixel size of 1 mm and slice thickness of 3 mm, the slice select gradient is typically three times the strength of the frequency encoded gradient, hence the spatial distortion along the slice select axis will be one third of that along the frequency encoded axis.

## 4. Spatial Distortion in MRI

---

This section has outlined a mathematical description of the distorting effect that the addition of a static magnetic field inhomogeneity has on a MR image acquired in its presence. In the following sections, this description will be used to formulate schemes which attempt to correct the image distortion.

### 4.3 Methods for the Correction of Spatial Distortion

A number of methods have been proposed to correct the spatial distortion in MR images caused by the addition of an inhomogeneous static magnetic field,  $B_e$ . If  $B_e$  could be determined, then its effect could be removed from Equation 4.7 and an image free from its distorting effects constructed. Methods for correcting spatial distortion therefore revolve around determining  $B_e$ , either directly or indirectly. As mentioned above,  $B_e$  may be composed of magnetic fields originating from many sources. Modern MR scanners can be shimmed to give a high level of uniformity over the imaging volume, leaving the magnetic field caused by magnetic susceptibility differences within the object being imaged to contribute significantly towards  $B_e$ . As the distribution of regions of differing magnetic susceptibility varies between patients, or between phantoms, the correction needs to be performed for each object being imaged in order to obtain distortion-free images.<sup>29</sup>

The majority of methods for correcting spatial distortion in MR images fall into two categories; those which calculate  $B_e$  by determining the extra accumulation of phase in the NMR signal in  $k$  space due to  $B_e$ , and those which calculate  $B_e$  by determining the spatial shift in intensity seen in the final image. Both methods require the acquisition of additional information, on an object by object basis, in order for the correction to be performed. They will be termed the phase map correction method and the reversed gradient correction method, and are described below.

In Section 4.2 above, it was mentioned that the slice selective magnetic gradient usually has a larger magnitude than either the phase or frequency encode gradients, for single slice acquisitions. From consideration of Equations 4.8, 4.10, 4.18, or 4.19, it can be seen that this will result in a smaller distorting effect

## 4. Spatial Distortion in MRI

---

along the slice selected axis than along an axis in the image plane. Spatial distortion may then be considered to occur predominantly along only one axis in the plane of the image. The problem of correcting spatial distortion then reduces to correcting each one dimensional line in the image, along the axis exhibiting distortion.

In a typical MRI acquisition, the NMR signal consists of contributions from the hydrogen nuclei present in both water and fat. There is a chemical shift in Larmor frequency between these nuclei, described in Chapter 2, which in a MR image may result in the fat image appearing shifted relative to the water image, along the same axes experiencing spatial distortion due to  $B_e$ . This introduces added complications for both distortion correction methods described below, and so it is assumed that no chemical shift effects are seen in the images prior to correction. This can be ensured by either imaging fat-free phantoms or acquiring a MR image in such a way that the NMR signal from hydrogen nuclei in fat does not contribute to the detected NMR signal.

### 4.3.1 Phase Map Correction Method

As was seen in Section 4.2 above, the addition of  $B_e$  results in an accumulation of phase in the NMR signal, compared to that which would be obtained in the absence of  $B_e$ . If this additional phase can be measured and removed from the NMR signals used to map  $k$  space, then the resulting image will be free from the distorting effects of  $B_e$ . A relatively quick and straightforward method for measuring the accumulation of phase (and hence  $B_e$ ) on a pixel-by-pixel basis, for a spin warp imaging acquisition was proposed by Sekihara *et al.*<sup>103</sup> This was applied to the correction of spin warp images by Sekihara *et al.*<sup>102,104</sup> and Prammer *et al.*,<sup>90</sup> and is described below.

A typical spin echo MRI acquisition of one frequency encoded line of  $k_x$  space consists of a  $90^\circ$  RF excitation pulse followed by a  $180^\circ$  RF pulse, separated by a time  $\frac{1}{2}TE$ . The  $180^\circ$  RF pulse refocuses the spinning nuclei into an echo, the centre of which forms after a further time  $\frac{1}{2}TE$  after the  $180^\circ$  pulse. The frequency encoded readout gradient is applied throughout the spin echo while the NMR signal is being sampled. As the application of the frequency encoded

#### 4. Spatial Distortion in MRI

---

gradient causes the spinning nuclei to dephase (resulting in a loss of the NMR signal), another gradient is applied along the frequency encoded axis prior to the readout gradient of opposite effective sign. The dephasing caused by this earlier gradient is refocused by the readout gradient to cause a gradient echo. The spin and gradient echoes are usually arranged to coincide in time, resulting in the maximum and most coherent NMR signal being formed at the centre of this echo. For spin warp imaging, this process is repeated with different levels of phase encoding occurring along an orthogonal axis to build up a map covering  $k$  space. In the presence of  $B_e$  it is not known whether phase changes across  $k$  space are due to evolution under the applied gradients or the effect of  $B_e$ .

If the spin warp MR imaging described above is repeated, but with an additional time delay,  $\frac{\tau}{2}$ , inserted between the  $90^\circ$  and  $180^\circ$  RF pulses, the spin echo will occur at a time  $TE + \tau$  after the excitation RF pulse, while the gradient echo will still occur at a time of  $TE$  at centre of  $k_x$  space. This second image has effectively been acquired with an offset of  $\tau$  in the time variable,  $t$ , in Equation 4.7. From Fourier theory,<sup>3,91</sup> a shift in one variable results in a phase shift in the related variable in the Fourier transform pair. Hence, the first image,  $i_0$ , will be modulated by  $\exp(i\gamma B_e(x, y, z)t)$  while the second image,  $i_\tau$ , will be modulated by  $\exp(i\gamma B_e(x, y, z)(t + \tau))$ . The result of the Fourier transform of  $k$  space to calculate  $i_0$  and  $i_1$  is complex<sup>†</sup>. The argument of each complex point in the image,  $\phi$ , where

$$\phi(x, y, z) = \arctan \left( \frac{\Im(i(x, y, z))}{\Re(i(x, y, z))} \right) \quad (4.21)$$

yields the phase accumulation at that point.<sup>29</sup> If  $\phi_0(x_1, y_1, z_1)$  is the phase at each point throughout  $i_0$  and  $\phi_\tau(x_1, y_1, z_1)$  the phase at each point throughout  $i_\tau$ , and as the duration of the acquisition of the NMR signal the same for both  $i_0$  and  $i_\tau$ , then

$$\begin{aligned} \phi_\tau(x_1, y_1, z_1) - \phi_0(x_1, y_1, z_1) &= \gamma B_e(x_1, y_1, z_1)(t + \tau) - \gamma B_e(x_1, y_1, z_1)t \\ &= \gamma B_e(x_1, y_1, z_1)\tau \end{aligned} \quad (4.22)$$

---

<sup>†</sup>For a hypothetically perfect MRI acquisition, as  $\rho(x, y, z)$  is real, so would be the calculated image. However, imperfections in a real imaging acquisition, such as timing offsets or imperfect RF pulses, result in a MR image being complex.

#### 4. Spatial Distortion in MRI

---

As the images are acquired in the presence of  $B_e$ , they exhibit the spatial distortion caused by  $B_e$ , and hence are referenced by the distorted coordinates  $(x_1, y_1, z_1)$ . Unlike in the general analysis of spatial distortion presented in Section 4.2 above,  $B_e$  is referenced by distorted coordinates as well, and is given by

$$B_e(x_1, y_1, z_1) = \frac{\phi_\tau - \phi_0}{\gamma\tau} \quad (4.23)$$

Once  $B_e$  is known, a corrected image may be produced as follows. For a spin warp MR image acquisition, from Equation 4.8,

$$\begin{aligned} x_1 &= x + \frac{B_e(x_1, y_1, z_1)}{G_x} \\ y_1 &= y \\ z_1 &= z + \frac{B_e(x_1, y_1, z_1)}{G_z} \end{aligned} \quad (4.24)$$

In Equation 4.24 above,  $B_e(x_1, y_1, z_1) \equiv B_e(x, y, z)$  as  $(x, y, z)$  and  $(x_1, y_1, z_1)$  describe the same point in the object; it is just referenced by either correct or distorted coordinates.

The Jacobian of the coordinate transform, in this case, is

$$\begin{aligned} J \left( \begin{array}{c} x, y, z \\ x_1, y_1, z_1 \end{array} \right) &= \begin{vmatrix} \frac{\partial x}{\partial x_1} & \frac{\partial x}{\partial y_1} & \frac{\partial x}{\partial z_1} \\ \frac{\partial y}{\partial x_1} & \frac{\partial y}{\partial y_1} & \frac{\partial y}{\partial z_1} \\ \frac{\partial z}{\partial x_1} & \frac{\partial z}{\partial y_1} & \frac{\partial z}{\partial z_1} \end{vmatrix} \\ &= 1 - \frac{1}{G_x} \frac{\partial B_e(x_1, y_1, z_1)}{\partial x_1} - \frac{1}{G_z} \frac{\partial B_e(x_1, y_1, z_1)}{\partial z_1} \end{aligned} \quad (4.25)$$

As mentioned in Section 4.2 above, in a typical single slice MR imaging acquisition, the slice selective magnetic gradient is usually considerably larger than either the frequency or phase encoding magnetic gradient. Hence, from a consideration of Equations 4.24, the majority of the distortion can be seen to occur along the frequency encoded axis, for a spin warp acquisition. It is common practice to ignore the distortion along the slice selected axis and just consider the distortion along one axis, especially if the distortion in single slices is being corrected.

In order to perform the correction, Equations 4.24 are used to calculate the spatial distortion at each point through the modulus image  $i_0$  and the Jacobian

#### 4. Spatial Distortion in MRI

---

calculated for each distorted image point. The correct image is then given, from Equation 4.15, as

$$i(x, y, z) = \frac{i_0(x_1, y_1, z_1)}{J\left(\frac{x, y, z}{x_1, y_1, z_1}\right)} \quad (4.26)$$

Interpolation will have to be performed in order to map the discrete points  $(x_1, y_1, z_1)$  to  $(x, y, z)$ .

In order for the corrected modulus image,  $i(x, y, z)$ , to be meaningful, it must not contain any negative numbers or singularities. Hence,  $J\left(\frac{x, y, z}{x_1, y_1, z_1}\right)$  must be greater than zero, *i.e.*,

$$\begin{aligned} G_x &> \frac{\partial B_e(x_1, y_1, z_1)}{\partial x_1} \quad \text{when } G_x > 0 \quad \text{and} \\ G_x &< \frac{\partial B_e(x_1, y_1, z_1)}{\partial x_1} \quad \text{when } G_x < 0 \quad \text{for all } x_1 \end{aligned} \quad (4.27)$$

in distorted coordinates. If the Jacobian in Equation 4.10 could be used<sup>‡</sup>, along with Equation 4.15, the condition in Equation 4.27 may be stated in undistorted coordinates as

$$\begin{aligned} G_x &> - \frac{\partial B_e(x, y, z)}{\partial x} \quad \text{when } G_x > 0 \quad \text{and} \\ G_x &< - \frac{\partial B_e(x, y, z)}{\partial x} \quad \text{when } G_x < 0 \quad \text{for all } x \end{aligned} \quad (4.28)$$

Generally,  $B_e$  could be of either sign across the image, especially if it results from local differences in magnetic susceptibility rather than poor shimming. In order for this correction to produce meaningful results in practice, the effective imaging gradient along the axis experiencing distortion must be greater than any opposing gradient caused by  $B_e$ , *i.e.*, the total gradient must be either continuously rising or continuously falling. This is the same as stating that, for correction to be performed, the distortion may cause the image to be stretched and shifted, but no pixel must be shifted so much that it 'piles up' or 'piles over' adjacent pixels.<sup>62</sup>

The phase correction method also has been applied to EP images<sup>49, 82, 116</sup> by noting that in EP images, the majority of in-plane distortion occurs along the phase encoded axis, compared with the frequency encoded axis in spin warp MR

---

<sup>‡</sup>it could be used here theoretically, but it is more straightforward numerically to use Equations 4.25 and 4.26 in this correction method.

## 4. Spatial Distortion in MRI

---

imaging (see Section 4.2 above). One dimensional phase correction is performed along the phase encoded axis rather than the frequency encoded axis; all other steps in the phase correction process remain the same.

The phase correction method generally performs well in the correction of one dimensional spatial distortion. However, it suffers from two problems related to phase wrapping and unconnected objects within an image.

When the phase at each point in the distorted images is calculated using Equation 4.21, it always lies within the range  $-180^\circ < \phi \leq 180^\circ$ ; no distinction can be made between phase angles which differ by multiples of  $360^\circ$ . If the phase across the images does vary by more than  $360^\circ$ , a crude phase calculation would result in an incorrect phase at those points, and so those pixels will be erroneously corrected. This may be overcome by using a number of algorithms,<sup>82</sup> e.g., by following lines out from the centre of the phase maps and assuming any large discontinuity in the value of phase represents the phase crossing a  $360^\circ$  boundary;  $360^\circ$  may then be added to the radial phase values (“unwrapping the phase”). The phase also must not have wrapped between the images acquired with differing values of  $\tau$ , else incorrect phase value will be used in Equation 4.23. Hence,  $\tau$  must be small enough to ensure that this condition is met. However, this requires that an estimate of  $B_e$  be known before the images are acquired, in order to choose an appropriate value for  $\tau$ .

The second problem is more relevant to the application of the phase correction method to the correction of spatial distortion in MR images of the stereotactic apparatus (described in Section 3.5). It is that to ensure that phase wrapping has not occurred, all points in the image of the object must be connected. In order for the phase to be calculated at any particular pixel, it requires that there is some intensity present in that pixel; phase values calculated in the background noise are meaningless (and must be masked out so as not to take part in the phase correction method). In an image containing stereotactic fiducial rods, the rods are spatially separate from the object they surround and so the phase of the pixels representing the rods can not be stated with certainty. Sumanaweera *et al.*<sup>107</sup> believe that this problem may be overcome by acquiring a third image with  $\tau = 1$  ms “during which time no phase-wraps are typically expected”, however it

## 4. Spatial Distortion in MRI

---

is felt that this reasoning does not offer a general approach. Despite the success of the phase correction method in correcting spatial distortion, it is felt that the problems it suffers regarding unconnected objects in the MR image makes it unsuitable for general application of the characterization of spatial distortion in MR images used for stereotaxis.

### 4.3.2 Reversed Gradient Correction Method

A different approach to distortion correction in spin warp MR images has been taken by Chang & Fitzpatrick.<sup>17</sup> They noted that if a second acquisition is performed, identical to the first with the exception that the frequency encoded gradient is reversed in sign, then the effect of  $B_e$  differs between the two images. For a modulus MR image,  $i_{1n}$ , acquired in the normal way, Equation 4.8 is restated as

$$x_{1n} = x + \frac{B_e(x, y, z)}{|G_x|} \quad (4.29)$$

whereas for the modulus image acquired with the sign of the frequency encoded gradient reversed,  $i_{1r}$ , Equation 4.8 becomes

$$x_{1r} = x - \frac{B_e(x, y, z)}{|G_x|} \quad (4.30)$$

$x$ ,  $x_{1n}$ , and  $x_{1r}$  all reference the same actual point in the object, even though it could appear at a different pixel locations within the images. The subscript  $n$  relates to an image acquired with 'normal' gradient polarity; the subscript  $r$  to an image acquired with gradients with reversed polarity compared to 'normal'. A relationship between the distorted coordinates and the undistorted coordinate can be obtained by eliminating  $\frac{B_e(x, y, z)}{|G_x|}$  from Equations 4.29 and 4.30 to give

$$x = \frac{x_{1n} + x_{1r}}{2} \quad (4.31)$$

If the distortion is considered to be only one dimensional, along the frequency encoded axis, then the Jacobian of Equation 4.10 may be written as

$$J \left( \frac{x_1, y_1, z_1}{x, y, z} \right) = \frac{dx_1}{dx} \quad (4.32)$$

#### 4. Spatial Distortion in MRI

---

where  $x_1$  could be either  $x_{1_n}$  or  $x_{1_r}$ . The corrected image,  $i$ , would then be given by Equation 4.15 as

$$i(x, y, z) = i_{1_n}(x_{1_n}, y_1, z_1) \frac{dx_{1_n}}{dx} = i_{1_r}(x_{1_r}, y_1, z_1) \frac{dx_{1_r}}{dx} \quad (4.33)$$

In order to perform this correction, corresponding pairs of  $x_{1_n}$  and  $x_{1_r}$  must be identified. Integrating and rearranging Equation 4.33 gives

$$\int i_{1_n}(x_{1_n}, y_1, z_1) dx_{1_n} = \int i_{1_r}(x_{1_r}, y_1, z_1) dx_{1_r} \quad (4.34)$$

This equation defines a relationship between  $x_{1_n}$  and  $x_{1_r}$ . The limits of the integrals in Equation 4.34 must be chosen carefully. The edges of the object in the images  $i_{1_n}$  and  $i_{1_r}$  along each line of the  $x_1$  axis provide corresponding points which should satisfy Equation 4.34 and these are taken as the limits of integration. This allows pairs of  $x_{1_n}$  and  $x_{1_r}$ , and hence  $x$ , to be identified, from which the pixel shift due to distortion and the corresponding Jacobian can be calculated. Hence a corrected image may be produced using Equation 4.33 by correcting each frequency encoded line in turn. Corrected images may be calculated from both  $i_{1_n}$  and  $i_{1_r}$  and may be combined as follows. Differentiating Equation 4.31 with respect to  $x$  gives

$$2 = \frac{dx_{1_n}}{dx} + \frac{dx_{1_r}}{dx} \quad (4.35)$$

and substituting from Equation 4.33 to eliminate the differentials in Equation 4.35 gives

$$i(x, y, z) = \frac{2 i_{1_n}(x_{1_n}, y_1, z_1) i_{1_r}(x_{1_r}, y_1, z_1)}{i_{1_n}(x_{1_n}, y_1, z_1) + i_{1_r}(x_{1_r}, y_1, z_1)} \quad (4.36)$$

This has the advantage of increasing the SNR in the corrected image by a factor approaching  $\sqrt{2}$  compared to one uncorrected image.

The reversed gradient correction method suffers from a different set of limitations than the phase correction method, described in Section 4.3.1. So long as the edges of the objects in the image are correctly identified, the correction can be performed independently for each object in the image, thereby overcoming the limitation of the phase correction method requiring one connected object. However, incorrect identification of the edges of the object may introduce an

#### 4. Spatial Distortion in MRI

---

artefact in the corrected image not seen with the phase correction method. If edges are incorrectly identified, an offset will appear on one side of Equation 4.34, including either the integral of a region of background noise or ignoring some image intensity within the object. This offset will affect all pairs of  $x_{1_n}$  and  $x_{1_r}$  calculated along that line and can therefore potentially introduce artefacts at any point along that line. Artefact would be expected to be more evident in regions of low image intensity within the object as that is where a small offset in Equation 4.34 would cause the largest error in the pairing of  $x_{1_n}$  and  $x_{1_r}$ , *i.e.*, a large change in  $x_1$  is required to produce the small change in the integral of image intensity needed to balance the erroneous offset. A more complete analysis of this effect is presented in Chang & Fitzpatrick's paper.<sup>17</sup> This effect would also be expected, to a lesser degree, in a corrected image produced from two noisy images; noise results in incorrect pairings of  $x_{1_n}$  and  $x_{1_r}$ , leading to a blurring of the corrected image. It is also worth noting that for the reversed gradient correction method to work, valid edges of the object must be present in both  $i_{1_n}$  and  $i_{1_r}$ .

As for the phase correction method, in order for the reversed gradient correction method to produce a meaningful corrected image, the Jacobian term must be greater than zero. However, this condition must hold for both  $i_{1_n}$  and  $i_{1_r}$ , regardless of the sign of  $G_x$ . Hence, the condition for a meaningful correction with the reversed gradient method is

$$\begin{aligned} G_x &> \frac{\partial B_e(x, y, z)}{\partial x} \quad \text{when } G_x > 0 \quad \text{and} \\ G_x &< -\frac{\partial B_e(x, y, z)}{\partial x} \quad \text{when } G_x < 0 \quad \text{for all } x \end{aligned} \quad (4.37)$$

If the main source of  $B_e$  is from magnetic susceptibility mismatches within the object, which may result in  $B_e$  of either sign, then this condition is effectively the same as for the phase correction method, *i.e.*, that the effective imaging gradient along the axis experiencing distortion must be greater than any opposing gradient caused by  $B_e$ . However, if the main contribution to  $B_e$  is from external magnetic fields, *e.g.*, due to poor shimming, then it may be that  $B_e$  is predominately one sign or the other. This would make no difference to Equation 4.37, but with previous knowledge of the sign of  $B_e$ , the sign of the frequency encoding

## 4. Spatial Distortion in MRI

---

gradient used for the phase correction method could be chosen to favour the first inequality in Equation 4.28. This would allow  $B_e$  inhomogeneities of larger magnitude to be corrected than would be possible using the reversed gradient method.

In MRI, the NMR signal is acquired in the presence of a linear frequency encoding gradient. For a typical MRI acquisition, this gradient remains at a constant level while the NMR signal is acquired. Any static nonlinearities in the gradient will cause spatial distortion and may be considered as a component of  $B_e$ . Gradient inhomogeneities of this type will be corrected by the phase map method as all NMR acquisitions are acquired in the presence of a gradient of the same sign and amplitude. However, this is not the case for the reversed gradient correction method. This method only can correct for a  $B_e$  which remains invariant when the polarity of the frequency encoding gradient is reversed; if the gradient nonlinearity is reversed with the gradient it will not be corrected. However, both correction methods will correct for invariant gradient offsets.

The reversed gradient correction method, described above for spin warp MR imaging, also may be applied to EP imaging.<sup>8</sup> As shown in Section 4.2, the distortion present in EP images along the phase encoded axis is analogous to distortion along the frequency encoded axis in spin warp images. However, due to the low bandwidth per point in EP images compared with spin warp imaging, the spatial distortion appears to be much worse in EP images. Therefore, Equation 4.37 will fail to be satisfied for much lower values of  $B_e$ .

Theoretically, Chang & Fitzpatrick's reversed gradient distortion correction method may easily be extended from the correction of distortion along one axis to the correction of distortion along two or three axes.<sup>17</sup> In this case, a contiguous volume of MR multislice images is required, spanning the object. The case for correction of spatial distortion along all three axes is described below, as would be found in a contiguous multislice EPI acquisition. The analysis may easily be reduced to distortion along two axes, such as would be found in a contiguous multislice spin warp acquisition.

Equations 4.18 may be expressed in vector notation as

$$\mathbf{r}_1 = \mathbf{r} + B_e(\mathbf{r})\mathbf{g} \quad (4.38)$$

## 4. Spatial Distortion in MRI

---

where

$$\begin{aligned}\mathbf{r} &= (x, y, z) \\ \mathbf{r}_1 &= (x_1, y_1, z_1) \\ \mathbf{g} &= \left( \frac{1}{G_x}, \frac{1}{G_y}, \frac{1}{G_z} \right)\end{aligned}\quad (4.39)$$

As  $B_e$  is a scalar, it can be seen that all the distortion term vectors,  $B_e(\mathbf{r})\mathbf{g}$ , are parallel throughout the image volume, *i.e.*, the distortion acts in one fixed direction throughout the volume. A new coordinate system may be defined,  $(x_r, y_r, z_r)$ , where the  $x_r$  axis is parallel to  $\mathbf{g}$ . The rotation of the  $y_r$ - $z_r$  plane around  $x_r$  may be chosen arbitrarily. Hence, all the spatial distortion caused by  $B_e$  appears to be acting along  $x_r$ , *i.e.*, distortion which was present along all three of the MR scanner's axes of acquisition has been reduced to distortion in one dimension, along  $x_r$ . The magnitude of the effective gradient along  $x_r$  is given by

$$\frac{1}{G} = |\mathbf{g}| = \sqrt{\frac{1}{G_x^2} + \frac{1}{G_y^2} + \frac{1}{G_z^2}} \quad (4.40)$$

Hence, the spatial distortion along the  $x_r$  axis is

$$x_{r1} = x_r + \frac{B_e(x_r, y_r, z_r)}{G} \quad (4.41)$$

To perform this one dimensional correction in the rotated coordinate space, two image volumes are needed. In order to reverse the sign of the effective gradient,  $G$ , along  $x_r$ , a second image volume must be acquired with the signs of  $G_x$ ,  $G_y$ , and  $G_z$  reversed. Both image volumes must be rotated so that  $x_r$  lies along  $\mathbf{g}$ , and one dimensional correction may then be performed along  $x_r$ . The corrected image volume may then be rotated back from  $(x_r, y_r, z_r)$  to  $(x, y, z)$  to produce an image volume corrected for spatial distortion along all three axes.

In order to study spatial distortion present in MR images used for planning stereotactic neurosurgery, it was decided to implement Chang & Fitzpatrick's reversed gradient correction method.

### 4.3.3 Implementation of Reversed Gradient Correction Method

The implementation of Chang & Fitzpatrick's reversed gradient distortion correction method involves two stages. Firstly, acquiring two MR images at each slice

## 4. Spatial Distortion in MRI

---

position, the second image with gradient(s) of reversed polarity. These images must then be post-processed to produce one corrected image per slice.

The reversed gradient method can only correct for magnetic field inhomogeneities which are invariant with gradient reversal, as described in Section 4.3.2 above. The polarity of the gradients may be reversed in the imaging sequence prior to amplification. However, this will not reverse any offsets or non-linearities which are introduced by the gradient amplifiers, and hence it will not be possible to separate these effects from inhomogeneities within the magnetic field itself. If the required gradients were reversed by physically swapping the cables carrying current into the gradient set, any effects of the gradient amplifiers also would be reversed; the distortion corrected and measured would be that due to inhomogeneities within the magnetic field in the environment of the object being imaged only. The latter option is not practical. Both normal and reversed gradient images should be acquired with as little delay between them to reduce the chance of patient movement. Also, physically reversing the gradient connections results in all gradients along a particular axis being reversed; it will be seen later that in some cases (e.g., diffusion weighted imaging) it is necessary only to reverse the gradients used for image acquisition. As a compromise, gross gradient offsets should be removed by careful calibration of the MR scanner prior to image acquisition. The sign of a gradient then may easily be reversed within the sequence code.

It was decided to implement the post-processing in a general, interactive, and easy to use fashion, so that it could be applied to a variety of MR imaging projects. The program was written in C, under the UNIX operating system, with the user interface and image display portions making use of XView and X Windows functions. This interface allowed quick and relatively easy post-processing, allowing interactive setting of a variety of parameters. All reference to frequency and phase encoded axes refer to the spin-warp case where distortion occurs along the frequency encoded axis. This axis is assumed to be horizontal (*i.e.*, parallel to the lines in an image, as opposed to the columns).

## 4. Spatial Distortion in MRI

---

### Edge Detection

In a practical setting, the reversed gradient correction method relies on the detection of the object's edges in the image. Although elaborate edge detection algorithms exist, it was felt that their use lay beyond the scope of this thesis, and so a thresholding method was used. A threshold value could be selected as a percentage of either the mean or maximum pixel intensity within an image. Scanning along each line of the image, an edge was assumed when the pixel intensity crossed this value. The same absolute threshold value was applied to both pairs of distorted images. An attempt was made to correct for false edges by ensuring that if an edge was detected along any particular line of the image, it was not too distant from detected edges in lines above and below it. Both left and right edges of the object in the image were detected. Due to artefacts which are often present at the edges of MR images, such as ghosts, spikes from an external radiofrequency source, or reconstruction artefacts, it was found that the success rate of the edge detection was improved by searching for edges from the centre of the images outwards rather than from the edges in. However, for images containing several spatially separate objects, this algorithm may mismatch the pairs of edges to their associated objects, and so in this case, edge detection from the edges inwards was allowed. Experimentation was performed in constructing various gradient maps of the MR images, and then performing a thresholding edge detection on the gradient maps. While this technique was successful, it did not perform so well as thresholding on the image itself, particularly when multiple objects existed within an image. When a multislice image set was available, the absolute threshold value was fixed for all images to try to ensure the same edge was detected throughout the volume. Also, the option was given to scan through the image to find single pixels which were considerably larger than their immediate neighbours; these 'spike' pixels could then be replaced by the mean of their neighbours, thus removing the possibility that they may be mistaken for an edge. While the methods described here improved the detection of edges and hence the efficacy of distortion correction, the detection of the same pairs of edges in the pair of distorted images remains a weakness of this implementation.

## 4. Spatial Distortion in MRI

---

### Image Correction

Once the edges of the object(s) in both distorted images had been identified, the line integrals along each line, between each left and right edge pair were normalized to their geometric mean. Ideally, the signal intensity, excluding noise, should not change between the acquisitions of pairs of images, however this normalization ensures that the line integrals between the same lines in the pair of images are consistent. This may introduce a bias in particularly noisy images, but in this case, the correction is likely to be poor anyway.

The distortion correction could now be performed between pairs of edges. Throughout the distortion correction process, images are considered in terms of unit pixels. The dimensions of the pixels are not necessary for the implementation of the single slice correction method; where necessary for volume correction, they are always kept as scaling factors of unit voxels. In implementation, it was felt to be most straightforward to step through each pixel in the corrected image matrix, giving  $x$ . The problem is then to determine values of  $x_{1_n}$  and  $x_{1_r}$ , which satisfy Equation 4.31. This was done by first producing an array indexing corresponding pairs of  $x_{1_n}$  by  $x_{1_r}$ , by considering equal values of the line integral<sup>§</sup> and then searching this array until Equation 4.31 was satisfied. This involved interpolation, as generally, an integral value of  $x$  gives rise to non-integer values of  $x_{1_n}$  and  $x_{1_r}$ . Linear interpolation was used. Once a triad of  $x$ ,  $x_{1_n}$ , and  $x_{1_r}$  were known, the corrected image intensity could be calculated using Equation 4.36. This was repeated until the entire corrected image had been constructed.

It has been shown that linear interpolation of MR images introduces errors; these may be avoided by using an interpolation method where the interpolated point is the sum of surrounding pixels weighted by a sinc function.<sup>34</sup> This method was implemented as an option for post-processing, typically calculated over a range of eight pixels in each dimension. However, it was not used routinely as no visible improvement in the results was seen while the increase in post-processing

---

<sup>§</sup>by stepping through  $x_{1_r}$  and asking, "What value of  $x_{1_n}$  is required so that

$$\int_{x_{1_r(\text{edge})}}^{x_{1_r}} i_{1_r}(x'_{1_r}, y_1, z_1) dx'_{1_r} = \int_{x_{1_n(\text{edge})}}^{x_{1_n}} i_{1_n}(x'_{1_n}, y_1, z_1) dx'_{1_n} \quad (4.42)$$

"

## 4. Spatial Distortion in MRI

---

time was significant.

### Distortion Map

Once a corrected image had been produced, it was possible to produce an additional image mapping the spatial distortion which had been corrected, on a pixel by pixel basis. This was optionally converted to a field map using Equation 4.20. As the main use of the reversed gradient correction method in this thesis is to quantify the spatial distortion present in MR images used for planning stereotactic procedures, an automatic algorithm was implemented to segment the map of pixel distortions into regions containing individual stereotactic fiducial rods, as well as the main object. Statistics could then be calculated for each region (*i.e.*, each fiducial rod) independently. The measures chosen were the mean of the absolute distortion, and the standard deviation of the signed distortion, both taken over all the pixels within the chosen region which were considered to be in the object, as defined by the edge detection.

### Three Dimensional Volume Correction

The implementation of the three dimensional version of Chang & Fitzpatrick's correction method proved to be computationally complicated. The angle of the vector  $g$  was calculated from the appropriate gradient strengths according to Equation 4.39. This was viewed as remapping the distorted volumes onto a rotated matrix volume, rotated by the same angle as  $g$ . Each point in the rotated matrix volume was stepped through, and its position in the unrotated distorted volume calculated. Interpolation was performed to find the pixel intensity at this point; the option of linear or sinc interpolation was given. The standard single slice distortion correction was then performed on each of the slices in the rotated volume; the corrected volume was then rotated back to the original image orientation.

For the single slice version of Chang & Fitzpatrick's correction, the actual sign of the frequency encoding gradient was not required to enable the correction to be performed, so long as it could be reversed. However, for the volume correction method, the relative sense of the sign of both the frequency encoded

#### 4. Spatial Distortion in MRI

---

and slice selected gradients is required. If the sense is incorrect,  $g$  would be calculated in the wrong quadrant and hence the volume rotated the wrong way (or resampled along the wrong direction). Hence, the rotation of the volume would not have brought the actual total distortion (along the real  $g$ ) into the resampled images, resulting in incomplete distortion correction. In order to define a consistent relative sign between the frequency encoded and slice selective axes, the following experiment was performed. Imaging was performed in the presence of an obvious  $B_e$  magnetic field (produced by a coin positioned beneath one end of the RF head coil, containing a spherical phantom). Three multislice volume sets were obtained; the first with normal gradient, the second with the frequency encoded gradient reversed, and the third with slice selective gradient only reversed. Considering the first two volume sets, a positive frequency encoding gradient was designated as resulting in distortion shifting the image to the right. The second and third sets were resliced along the frequency encoded axis so that each new image contained the slice selective and phase encoded axes (*i.e.*, the volume was rotated by  $90^\circ$  around the phase encoded axis). This allowed the distortion along the slice selective axis to be visualized. A positive slice selecting gradient was considered to be one that resulted in distortion causing shifts to the right of these resampled images. The functions in the computer program which calculated the rotations and resamplings required for Chang & Fitzpatrick's volume correction method were then adjusted to correctly process image volumes which were orientated according to this convention. In the case of the uniform, spherical phantom in the presence of a large, local,  $B_e$ , it was visually easy to see whether the signs of the gradients (and image orientation) was correct relative to each other, during the slice by slice correction in the rotated image space; in images of human subjects this was not so noticeable.

The volume correction method performs the correction along an axis at an angle (defined by  $g$ ) relative to the primary imaging axes. The distortion map is also initially calculated along  $g$ . It is more useful to know the distortion in the coordinate frame of the imaging axes. In order to do this, the volume distortion map must be resampled along the original imaging axes, along with the corrected image volume. However, the values of distortion in this map are still parallel to

## 4. Spatial Distortion in MRI

---

$\mathbf{g}$ , and so the distortion map must be resolved into separate distortion along the frequency encoding and slice selective axes, on a pixel by pixel basis. These maps may then be characterized and compared by the same methods as distortion maps produced by single slice correction methods.

Care must also be taken when dealing with non-cubic voxels, which is the usual case. It is computationally easier to consider the multislice image volume as being made up of cubic voxels; this was especially so for the algorithms concerned with the rotation of, and interpolation into, the image volume. For this implementation, parameters were scaled before and after the correction to allow for non-cubic voxels, but the rotation and correction themselves were performed assuming cubic voxels. In particular, the angle of rotation of the volume, to align with  $\mathbf{g}$  becomes  $\theta$  assuming all voxels are cubic, where

$$\theta = \arctan \left( \frac{G_x v_x}{G_z v_z} \right) \quad (4.43)$$

where  $v_x$  and  $v_z$  are the voxel dimensions along the frequency encoding and slice selective axes respectively.

### 4.3.4 Results and Discussion of Reversed Gradient Correction Method (single slice)

In order to test the implementation of the reversed gradient method, a number of MR images were acquired in which spatial distortion was deliberately introduced, either by offsetting one of the shims of the main magnetic field, the addition of a paramagnetic object close to the object being imaged (e.g., a coin), or by imaging a phantom containing adjacent regions of differing magnetic susceptibility. These three cases are presented below to demonstrate the validity of the correction.

#### EPI on 0.5 T system

Coronal (*i.e.*, horizontal, see Figure 2.18) MR images were acquired through a phantom using the 0.5 T magnet located in the Magnetic Resonance Centre at the University of Nottingham. The phantom consisted of a two litre glass beaker of tap water (with a diameter of 100 mm), in the centre of which a sealed vertical plastic tube (diameter 20 mm) of water doped with medical gadolinium

## 4. Spatial Distortion in MRI

---

contrast agent was rigidly placed. A spin echo full Fourier EPI acquisition was used with 128 echoes. The voxel size was  $1 \times 1 \times 2$  mm. The magnet's shims and other imaging parameters had been manually adjusted for the best practically achievable performance. Figure 4.1 shows the MR image obtained (the average of ten acquisitions) with normal imaging parameters, the MR image obtained with a phase encoding blipped gradient of reversed polarity, the corrected image produced, and the calculated map of pixel shifts. The phase encoded axis is aligned horizontally. The circular tube appears distorted into an 'arrow-head' shape, as expected for this configuration.<sup>62</sup> The addition of gadolinium to the water in the central tube has reduced the  $T_2$  of the solution such that no signal is present in these inherently  $T_2$  weighted EP images.

The correction performs well; the circular shape of both the beaker and tube is restored. However, the distortion map shows a typical artefact of the gradient reversal method, namely the erroneous shifting of pixel intensity into the central region of low pixel intensity. This is due to either an error in the edge detection or the effect of noise in the line integrals of intensity. However, the actual amount of image intensity shifted into the low intensity region is itself small, as reported elsewhere,<sup>17</sup> and so this artefact does not visibly manifest itself in the corrected image. By selecting the post-processing option to detect more than one pair of edges along each line, the artefact is removed as no correction occurs within the central region; see Figure 4.2.

### EPI on 3 T system

EP images of a structured phantom also were obtained using the 3 T magnet located in the Magnetic Resonance Centre at the University of Nottingham. Again, a spin echo full Fourier EPI acquisition was used with 128 echoes. The voxel size was  $1.6 \times 1.6 \times 2$  mm. The long axis of the cylindrical phantom was aligned parallel to the  $z$  axis of the magnet and transaxial images were obtained. The  $x^2-y^2$  shim was deliberately offset to provide a global  $B_e$  field. The images acquired, along with the corrected image and distortion map, are shown in Figure 4.3. The gross distortion is corrected well, and the distortion map shows the characteristics expected from the  $x^2-y^2$  shim. The images were orientated so that the phase

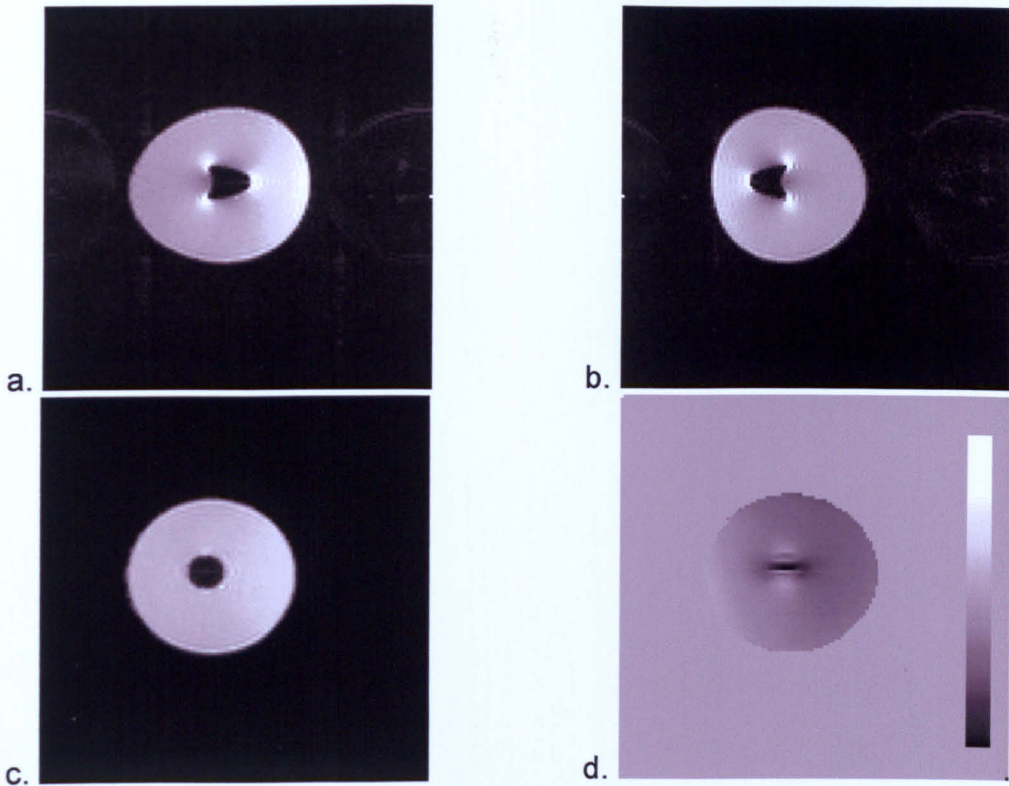


**Figure 4.1** Coronal EP images of a beaker of water containing an upright cylinder. Acquired using the 0.5 T MRI system.

- a) Image acquired under normal conditions.
- b) Image acquired with reversed phase encoding blipped gradient (horizontal axis in images).
- c) Corrected image, using the reversed gradient method. One pair of left and right edges has been detected per line.
- d) Distortion map. Note that some intensity has been misregistered into the central region of the phantom. Scale bar represents distortion from -10 to 10 mm.

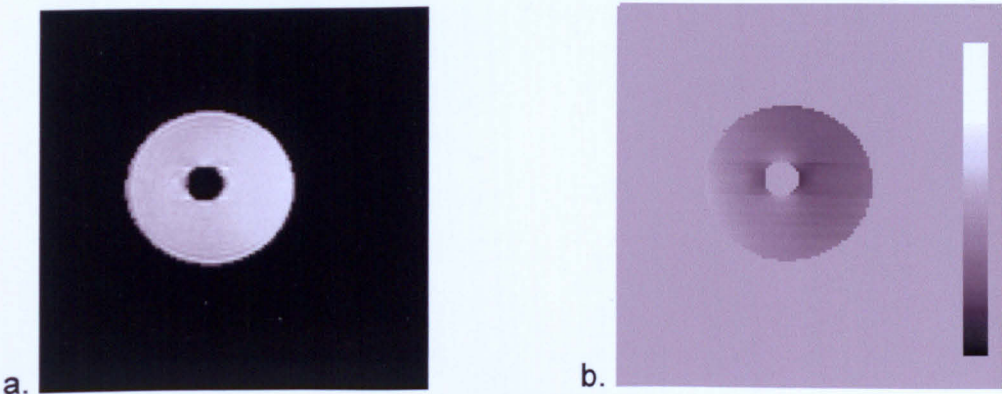


**Figure 4.2**

- a) Corrected image with edge detection capable of finding multiple edge-pairs per line.
- b) Distortion map. Scale bar represents  $\pm 10$  mm.

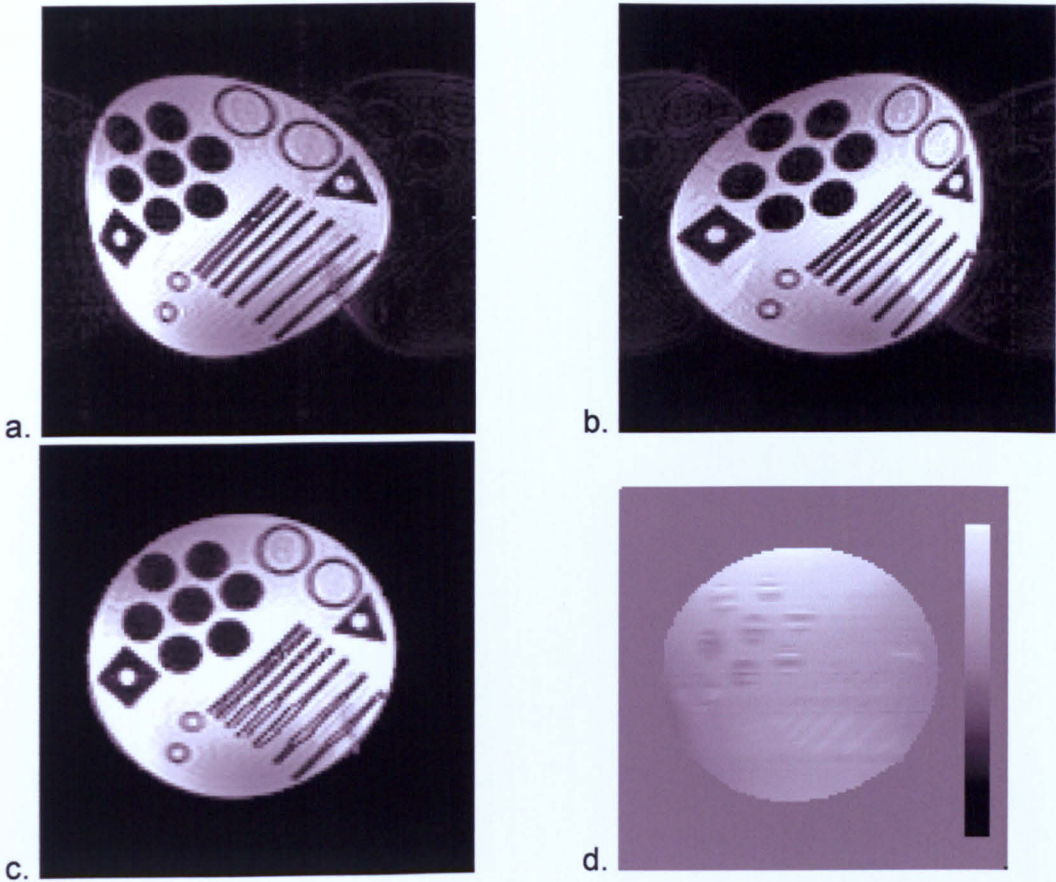


**Figure 4.3** EP images of a phantom acquired using the 3 T MRI system. The  $x^2-y^2$  shim was deliberately offset to cause distortion.  $128 \times 128$  matrix. Full Fourier spin echo MBEST EPI.

Voxel dimensions were  $1.6 \times 1.6 \times 2.0$  mm

- a) Image acquired under normal conditions.
- b) Image acquired with reversed phase encoding blipped gradient (horizontal axis in images).
- c) Corrected image, using the reversed gradient method. One pair of left and right edges has been detected per line. Note misregistered signal in the centre of the diagonal stripes.
- d) Distortion map. Scale bar represents  $\pm 25$  mm.

#### 4. Spatial Distortion in MRI

---

encoded axis was horizontal. Single pairs of edges were detected along each line. Artefact is seen in the phantom's internal regions of low image intensity. Attempting to use detection of multiple edge pairs fails with these images due to non-corresponding pairs of edges being detected in the two distorted images.

Having shown the potential of the correction method, a volunteer's head was imaged using the 3 T magnet. The magnet's shims and gradient strengths were adjusted previously, while imaging a phantom, to produce an image containing isotropic pixels and exhibiting as little spatial distortion as possible; this corresponds to a normal setting for the scanner prior to routine use. A spin echo full Fourier EPI acquisition was used with 64 echoes. The dimensions of a voxel were  $3.5 \times 3.5 \times 2$  mm. The transaxial images obtained with normal and reversed phase encoding gradients are shown in Figure 4.4 as well as the corrected image produced using the reversed gradient correction method. Successful correction occurs.

#### Spin Warp on 1.5 T system

Transaxial spin-warp images of a water phantom were acquired using the 1.5 T Vision scanner in the Imaging Centre of the Queen's Medical Centre. The results are shown in Figure 4.5 in the same format as for the EP images presented above. In this case, the images are orientated so that the frequency encoding gradient is horizontal. A magnetic field offset,  $B_e$ , was generated by rigidly fixing a small coin to the phantom approximately 10 cm out of the plane of the image. The correction performs well and the spatial variation of  $B_e$  is seen clearly in the distortion map. A typical  $T_1$  weighted spin-echo spin warp imaging sequence<sup>†</sup> was used to acquire these images. The 1.5 T Vision MR scanner performs a number of automatic adjustments at the beginning of each image acquisition, such as shimming and transmitter and receiver gains. In order for these adjustments not to change between acquiring an image with normal gradients and an image with reversed gradients, these adjustments were inhibited after acquisition of the first image, resulting in the values optimized for the first image being used for all

---

<sup>†</sup>se\_12b130.wkc TE=15 ms TR=300 ms voxel size  $1.17 \times 1.17 \times 5$  mm on  $256 \times 256$  matrix. Bandwidth per point of 130 Hz along the frequency encoding axis.

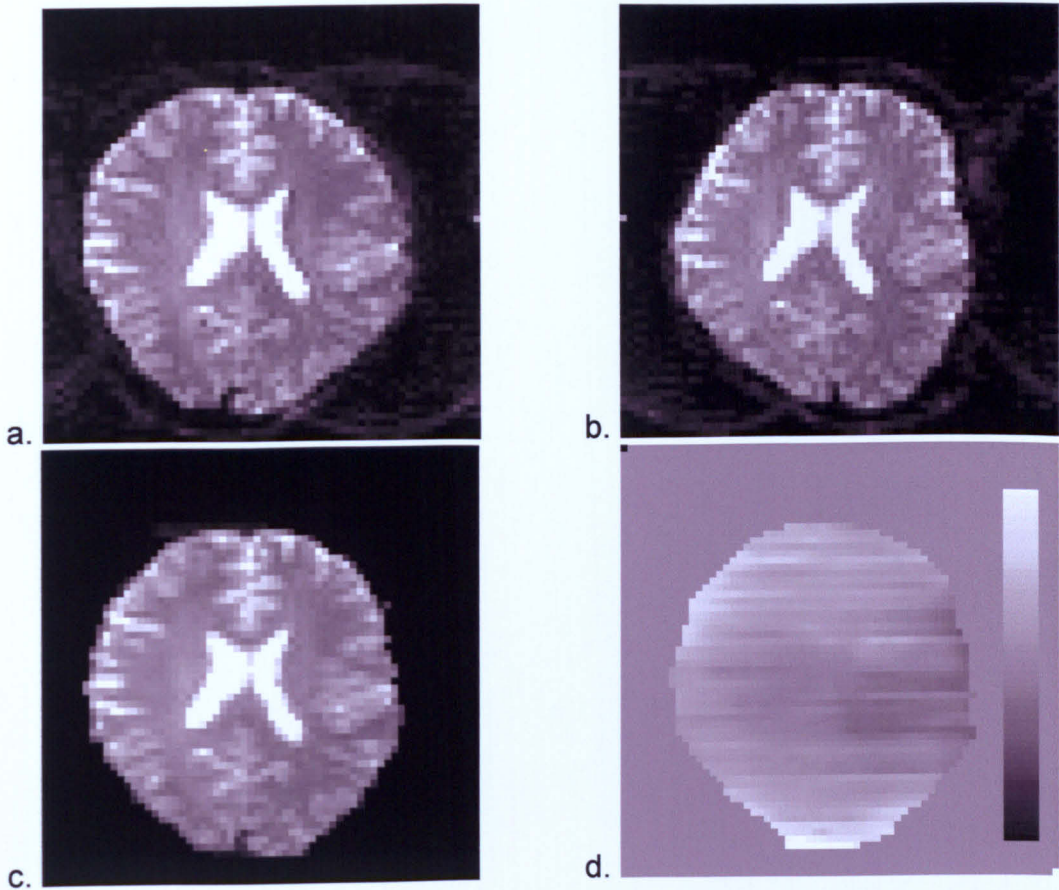


**Figure 4.4** EP images of a volunteer's head acquired using the 3 T MRI system. No offset of the shims was introduced. Full Fourier spin echo MBEST EPI. Voxel dimensions were  $3.5 \times 3.5 \times 2.0$  mm.  $64 \times 64$  matrix. [a-d] as in Figure 4.3. Scale bar in distortion map represents  $\pm 10$  mm but note that the extreme distortion values are in the posterior streak artefact caused by an erroneous edge being found in the skin.

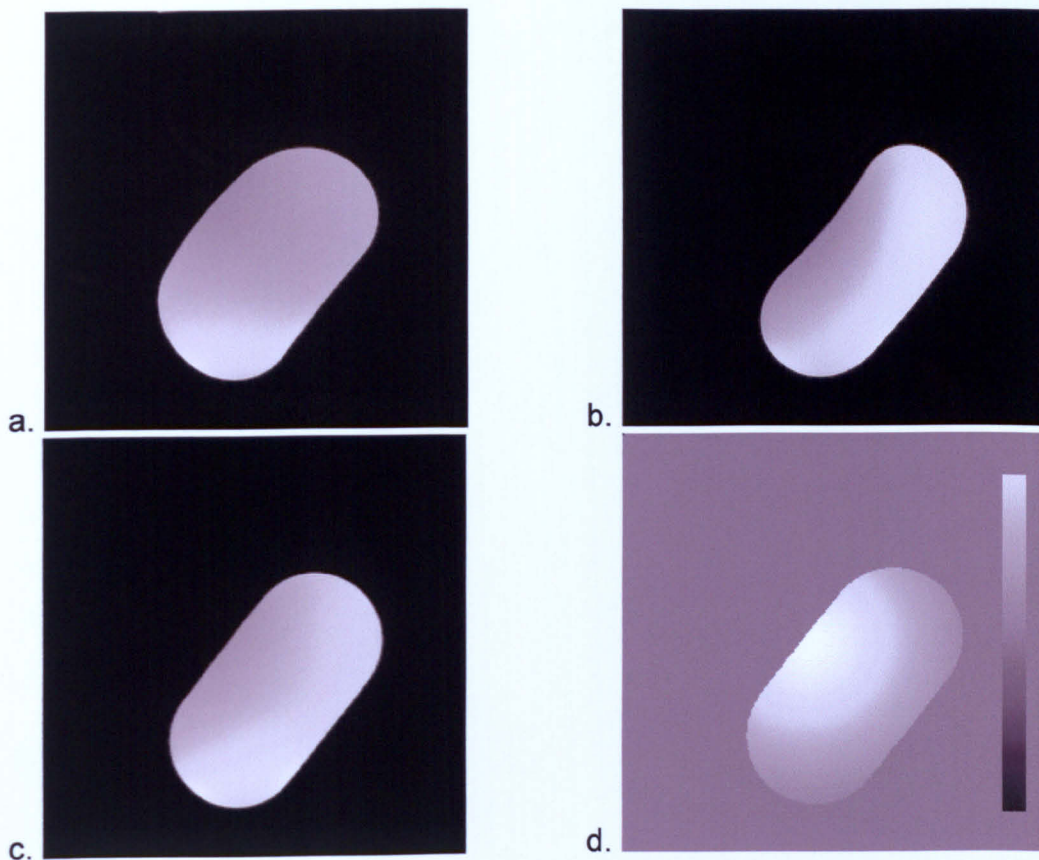


**Figure 4.5** Full Fourier spin echo, spin warp images of a phantom acquired using the 1.5 T Vision MRI system. Distortion caused by a coin. Voxel dimensions were  $1.2 \times 1.2 \times 5.0$  mm.

- a) Image acquired under normal conditions.
- b) Image acquired with reversed frequency encoding gradient (horizontal axis in images).
- c) Corrected image, using the reversed gradient method.
- d) Distortion map. Scale bar represents distortion from  $-14$  to  $14$  mm.

## 4. Spatial Distortion in MRI

---

subsequent images. However, the automatic adjustment had to be enabled for the first acquisition of a particular sequence type to allow the MR scanner to correctly set RF pulse flip angles, gradient calibrations, and amplifier gains.

The above experiment was repeated using a volunteer, with the coin attached to his chin. The same imaging parameters were used. Distortion of several centimetres is seen, in Figure 4.6. This is extremely well corrected, and again, the pattern of the  $B_e$  field variation is clearly seen in the distortion map. No artefact is visible in the corrected image despite regions of low signal intensity in the skull and ventricles. The high SNR present in these images facilitates accurate edge detection and reduction of noise induced errors in the line integrals of intensity.

### 4.3.5 Results and Discussion of Reversed Gradient Correction Method (volume)

The 3D reversed gradient correction method was applied to multislice spin echo spin warp image acquisitions, acquired on the Vision MR scanner. 64 contiguous slices of  $256 \times 256$  pixels were acquired. Initial phantom experiments showed that the mean pixel intensity varied between adjacent slices if the volume was acquired in one multislice acquisition ( $TR=1410$  ms). This appeared to be due to 'cross-talk' between adjacent slices. Even though an interleaved slice excitation ordering scheme was used, the TR set was of the order of 1500 ms – too short to allow full longitudinal relaxation to occur. Longer TR's would have lead to long imaging times, and so each volume was acquired as two interleaved sets, where each set had a slice separation (centre to centre) equal to its slice width. This method of acquisition did not significantly add to the total imaging acquisition time, as with only 32 slices per set, the TR could be nearly halved. This also gave the additional benefit of increasing the  $T_1$  weighting to that which is more usual in clinical imaging. Images in each volume could be reordered correctly during post-processing.

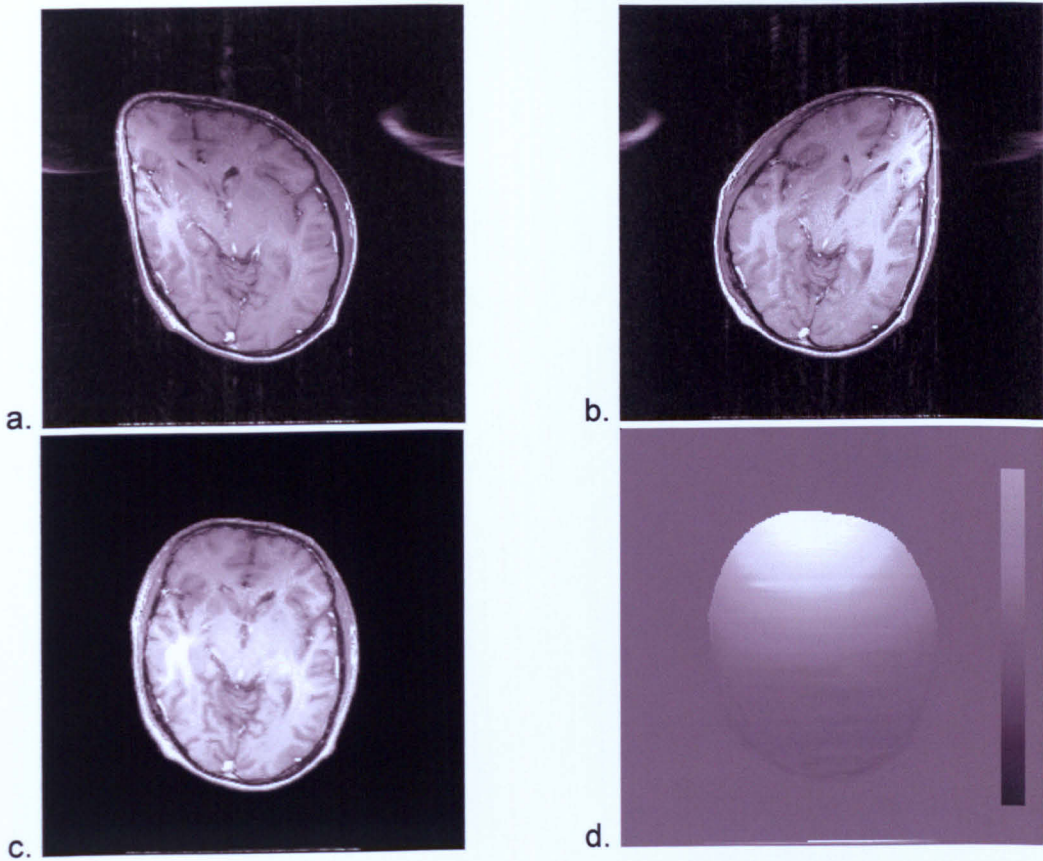


**Figure 4.6** Full Fourier spin echo, spin warp transverse images of a volunteer's head acquired using the 1.5 T Vision MRI system. Distortion caused by a coin taped to the volunteer's chin. Voxel dimensions were  $1.2 \times 1.2 \times 5.0$  mm.

- a) Image acquired under normal conditions.
- b) Image acquired with reversed frequency encoding gradient (horizontal axis in images).
- c) Corrected image, using the reversed gradient method.
- d) Distortion map. Scale bar represents distortion from  $-18$  to  $18$  mm.

## 4. Spatial Distortion in MRI

---

### Volume Correction of Phantom

The volume reversed gradient correction method was first applied to a spherical water filled phantom, imaged in the head coil using the same spin-echo spin warp imaging sequence as before. (se\_12b130.wkc, TE=12 ms, TR=800 ms, voxel size  $1 \times 1 \times 3$  mm on a  $256 \times 256$  matrix.  $G_x=3.059$  mTm<sup>-1</sup> and  $G_z=8.000$  mTm<sup>-1</sup>, as quoted by the scanner.) A copy of the sequence was modified to reverse the polarity of the frequency encoding and slice selective gradients. A third volume was acquired with just the frequency encoding gradient reversed, to allow single slice correction to be performed on all slices, for comparison. A coin was placed under the RF head coil to create a  $B_e$  which caused a distortion of several pixels at most. Transaxial images were obtained. The results are shown in Figures 4.7, 4.8, and 4.9 using the central slice of the volume as an example of the entire volume. Figure 4.7 shows the single slice reversed gradient correction. The volume correction first requires that both distorted volumes are rotated and re-sampled along  $g$ . This corresponded to rotation through an angle of  $20.92^\circ$ . Distorted images, in the rotated frame, are shown in Figure 4.8, along with the corrected image in this frame. Finally, the corrected images (and distortion map) are rotated back into the original acquisition plane, as shown in Figure 4.9.

The volume correction on the spherical phantom appears to work well. Figure 4.10 shows how the measured distortion varies with slice position, for both single slice and volume correction. The effect of the coin can be seen with increasing distortion towards the superior side of the phantom (low  $z$  values) where the coin was placed. For the results from the volume correction, distortion along both the frequency encoding and slice selective directions may be calculated from the distortion map, per slice. It would be expected that the ratio of the distortion along these two axes would be in the ratio of their respective magnetic gradient field strengths, and this is observed. Figure 4.10c shows a direct comparison of distortion along the frequency encoded axis as calculated from the single slice and volume correction methods, on the same graph. This shows that the volume correction appears to be correcting more distortion along this axis than the single slice correction, although both curves follow a similar trend. This might be expected, as the volume correction method is attempting

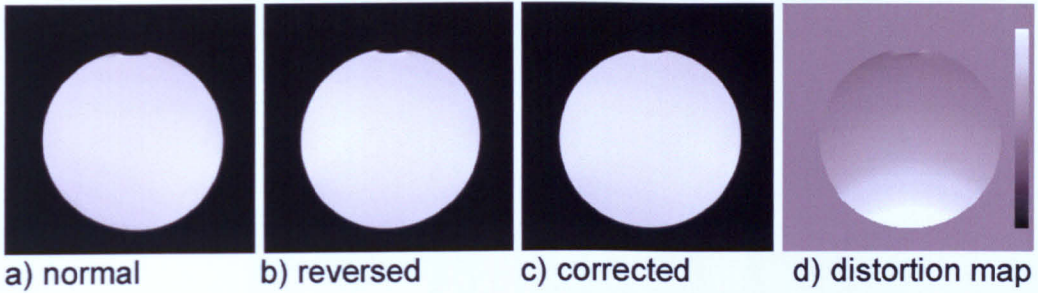


**Figure 4.7** Single slice reversed gradient correction on multislice volume. Example of an image through a water filled spherical phantom. A coin placed under the RF head coil can be seen to have caused distortion. The frequency encoding gradient of this spin echo spin warp sequence was horizontal. The distortion map shows larger pixel shifts as bright or darker relative to the background (zero shift). The scale bar represents  $\pm 3$  mm.

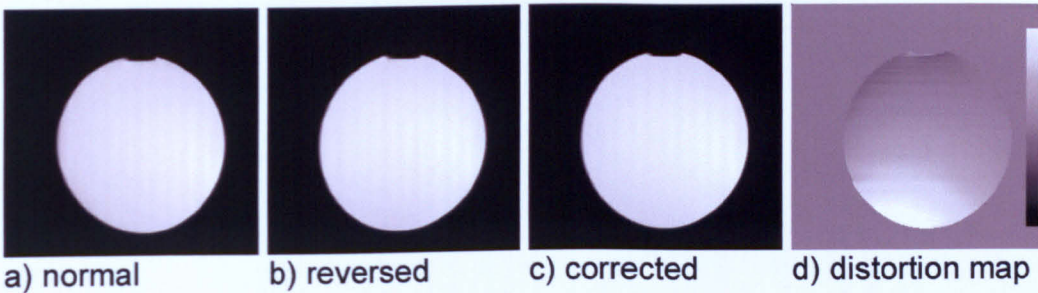


**Figure 4.8** Volume reversed gradient correction method. An example of correction of a slice after rotation around the phase encoding axis by the angle of vector  $\mathbf{g}$ .

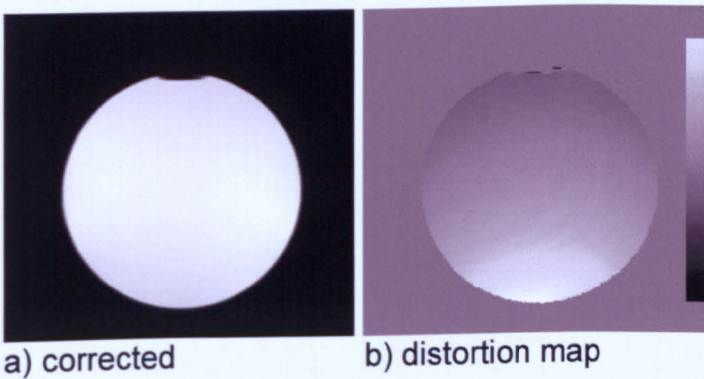


**Figure 4.9** Volume reversed gradient correction method. Example of corrected slice rotated back into the original volume orientation.

**Figure 4.10** Mean absolute distortion per slice, measured using reversed gradient method. 'Error bars' represent the spread of distortion throughout that slice. Transaxial slices through a spherical water phantom. A coin was placed under the RF head coil to create additional distortion, seen in the slices with lower z values. Acquired on the Vision MR scanner. Spin echo, spin warp sequence, 130 Hz per pixel.

**Figure 4.10a**

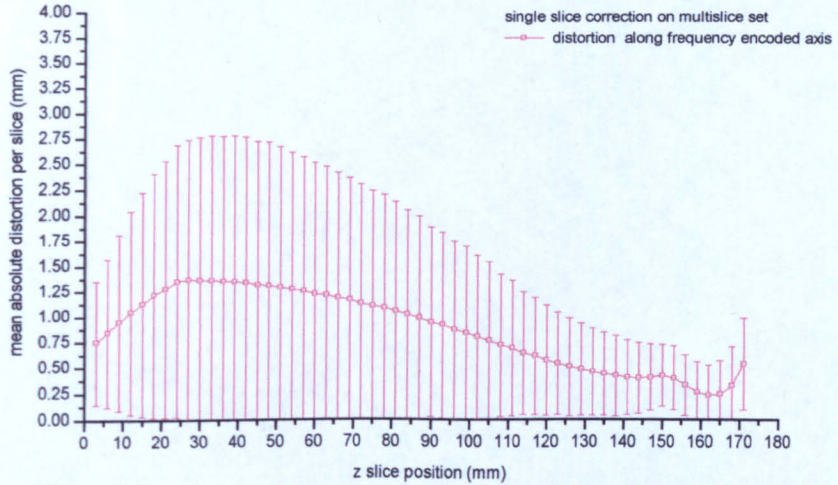


**Figure 4.10b**

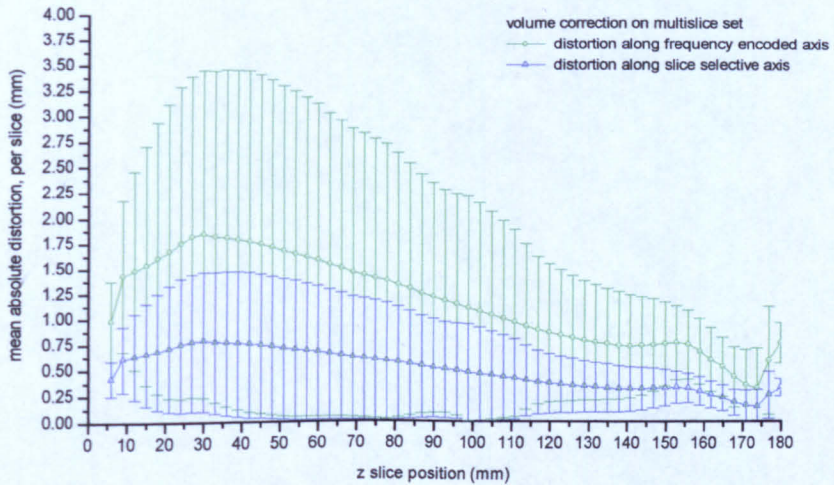
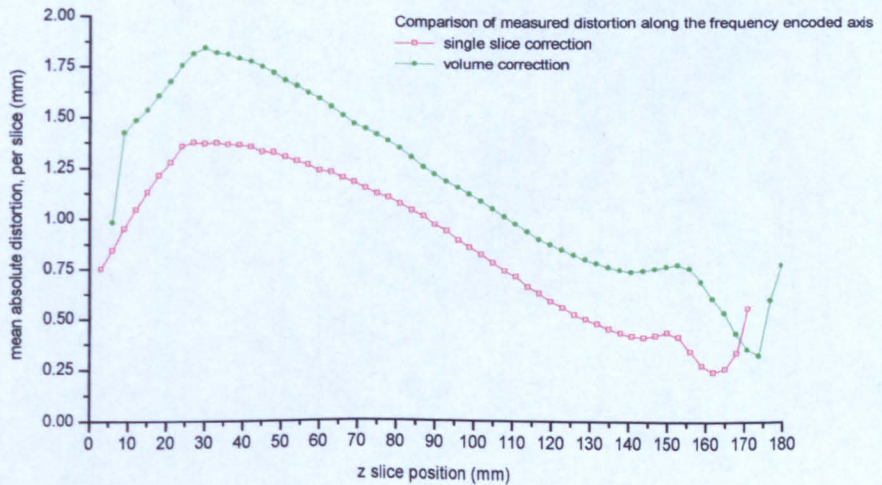


**Figure 4.10c**



## 4. Spatial Distortion in MRI

---

to correct for the distortion along the slice selective and frequency encoded axes and hence is correcting 'more' of the total distortion.

The effect of noise in the MR image on the correction of distortion throughout an image volume was studied briefly using this experimental set-up. After all image acquisitions had been completed, a final multislice image volume was acquired with normal polarity magnetic gradients. This was then substituted as a multislice volume with inverted frequency encoded gradient for the single slice correction on all slices in the volume. The other image volume used for the correction was the multislice set acquired with normal gradients at the beginning of the experiment. The coin, causing measurable distortion, was left in place under the RF head coil. The only difference between the two volumes used for this correction should be noise. The results are presented in Figure 4.10d, along with the actual distortion measured when the second multislice volume used for correction actually did have the frequency encoding gradient inverted during acquisition. This shows a background offset in the mean absolute distortion over a slice of about 0.1 mm. The increase in the standard deviation of the distortion throughout each slice, which occurs in the centre of the volume, corresponds to slices containing the water meniscus within the phantom, which interferes with the edge detection.

### Volume Correction of Head

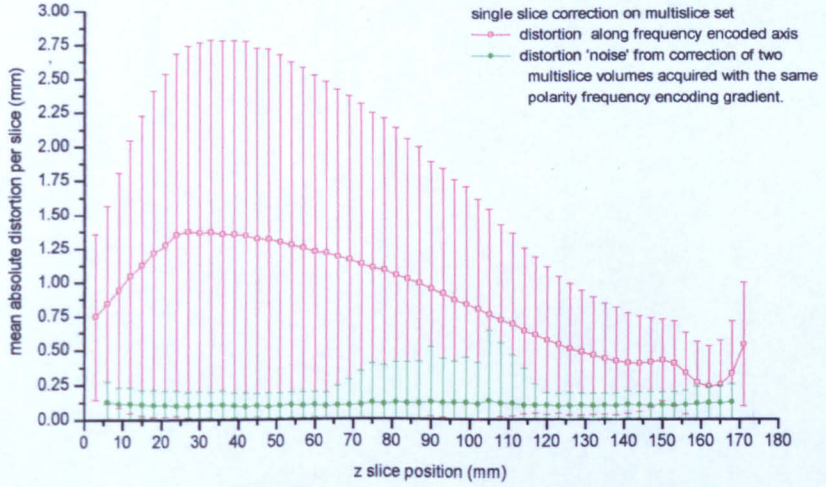
The volume reversed gradient correction method was then applied to images of a volunteer's head. Unlike for a phantom, which may be totally spanned by the imaged volume, a person will always have part of his or her anatomy leaving the volume. As the reversed gradient correction method requires the same edges to be found in pairs of images along the frequency encoding and slice selective axes, these axes must be orientated so that the head is covered by the volume in these directions. Therefore the phase encoding axis must be aligned in the direction of the anatomy which leaves the volume. In the case of a head, the phase encoding axis must be parallel to the inferior-superior direction. This is unfortunate, as in many cases it is preferable not to align the phase encoding axis in this direction as it is likely that signal from the anatomy outside the volume will 'wrap' into

**Figure 4.10d** Comparison of the mean absolute distortion per slice and noise, produced by the reversed gradient method.

'Error bars' represent the spread of distortion throughout that slice.

Transaxial slices through a spherical water phantom. A coin was placed under the RF head coil to create additional distortion, seen in the slices with lower z values.

Acquired on the Vision MR scanner. Spin echo, spin warp sequence, 130 Hz per pixel.



## 4. Spatial Distortion in MRI

---

the images. However, in the case of the head RF coil, this does not occur as the NMR signal from structures outside of the coil diminishes rapidly with distance outside of the coil, resulting in no visible 'wrap' of signal.

Sagittal image orientation was chosen for acquisition of the MR image volumes through the head, with the same imaging parameters as those used for the acquisitions of the spherical phantom. The phase encoding gradient was aligned parallel to the inferior-superior axis. The results are shown in Figures 4.11, 4.12, and 4.13. The distortion caused by the coin under the RF coil is clearly visible at the back of the head. Correction using the single slice reversed gradient correction method is shown in Figure 4.11. Correction in the brain appears good; however artefacts are seen lower in the head, around the tongue, and in the air spaces behind the nose. Distorted images, in the rotated frame, are shown in Figure 4.12, along with the corrected image in this frame. Finally, the corrected images (and distortion map) are rotated back into the original acquisition plane, shown in Figure 4.13. While the gross shape of the head is correct, and the distortion caused by the coin is corrected and identified in the final distortion map, the final corrected images are blurred, compared to the initial images, and contain artefacts. Consequently, the data set is of a poorer diagnostic quality than the initial images. As the artefacts are more prominent in the corrected images of the head than the phantom, it is felt that the source of the artefacts results from the rotation and interpolation of the image volume.

Figure 4.14 shows how the measured distortion varies with slice position, for both single slice and volume correction. The effect of the coin is not so obvious in these graphs, compared to the results from the spherical phantom, because mean absolute distortion over a sagittal slice does not highlight variations in distortion between the inferior and superior regions. Despite the poor quality of the final corrected image, both single slice and volume correction methods identify similar amounts of distortion in the frequency encoding direction.

### 4.3.6 Validity of Reversed Gradient Correction Method

The results presented in this section are similar to those presented elsewhere.<sup>8,17</sup> Chang & Fitzpatrick's single slice distortion correction method appears to have

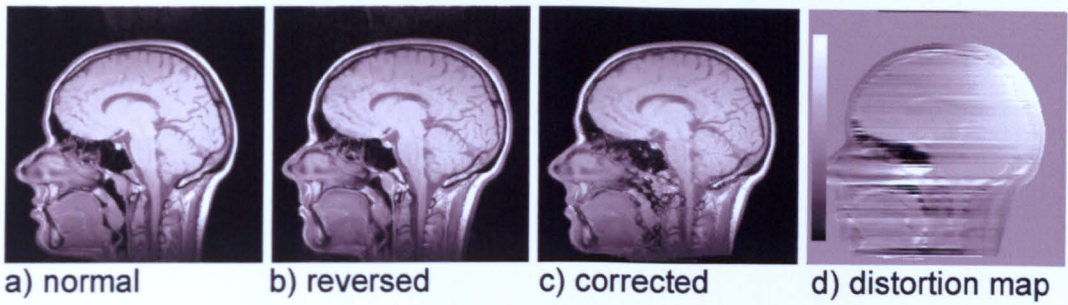


**Figure 4.11** Single slice reversed gradient correction on multislice volume. The central image of a multislice volume through a volunteer's head is shown as an example. A coin placed under the RF head coil can be seen to have caused distortion at the back of the head. The frequency encoding gradient of this spin echo spin warp sequence was anterior-posterior. The distortion map show larger pixel shifts as bright or darker relative to the background (zero shift); the scale bar covers a range of  $\pm 7$  mm.

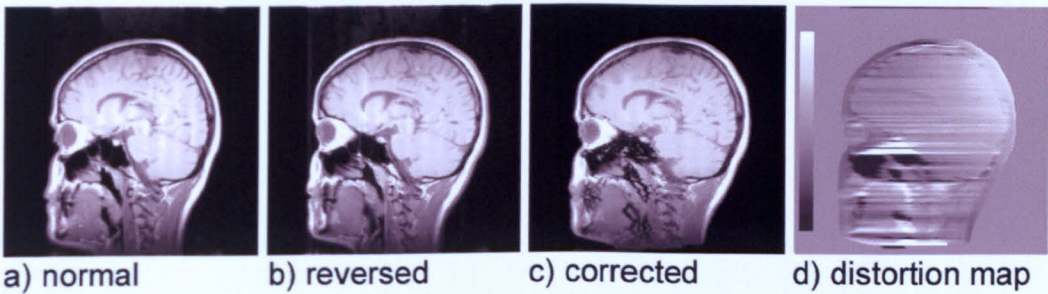


**Figure 4.12** Volume reversed gradient correction method. The correction of the central slice of the volume is shown after rotation around the phase encoding axis by the angle of vector  $\mathbf{g}$ .

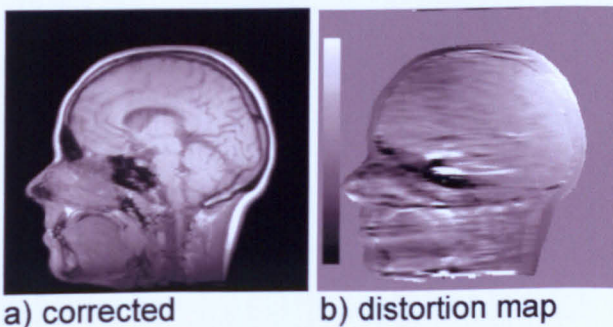


**Figure 4.13** Volume reversed gradient correction method. The central slice of volume rotated back into the original volume orientation.

**Figure 4.14** Mean absolute distortion per slice, measured using reversed gradient method. 'Error bars' represent the spread of distortion throughout that slice. Sagittal slices through a volunteer's head. A coin was placed under the RF head coil to create additional distortion. Acquired on the Vision MR scanner. Spin echo, spin warp sequence, 130 Hz per pixel.

**Figure 4.14a**

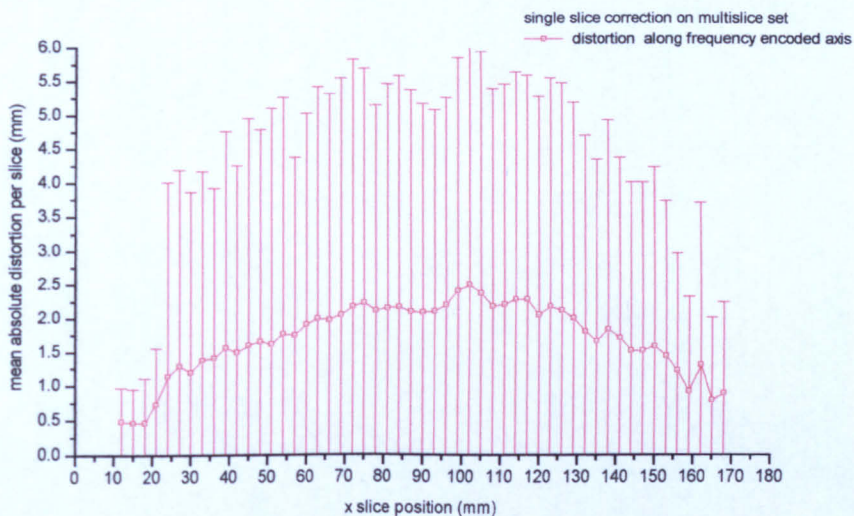


**Figure 4.14b**

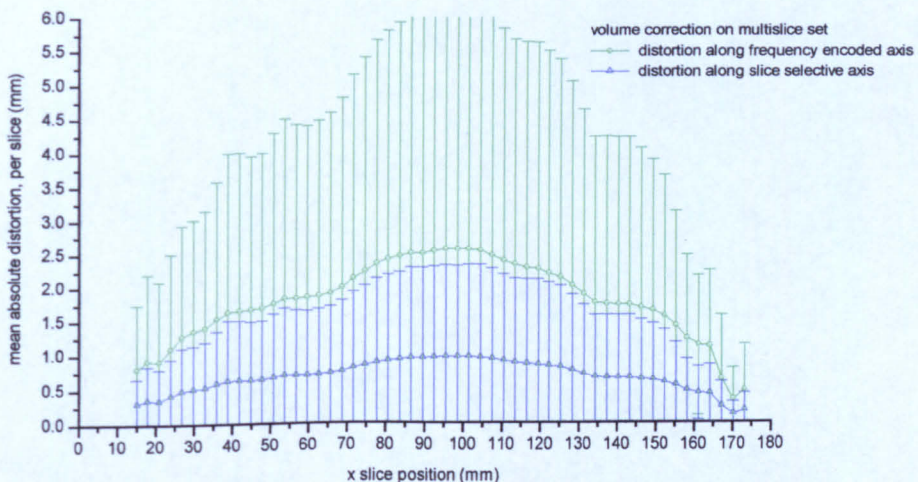
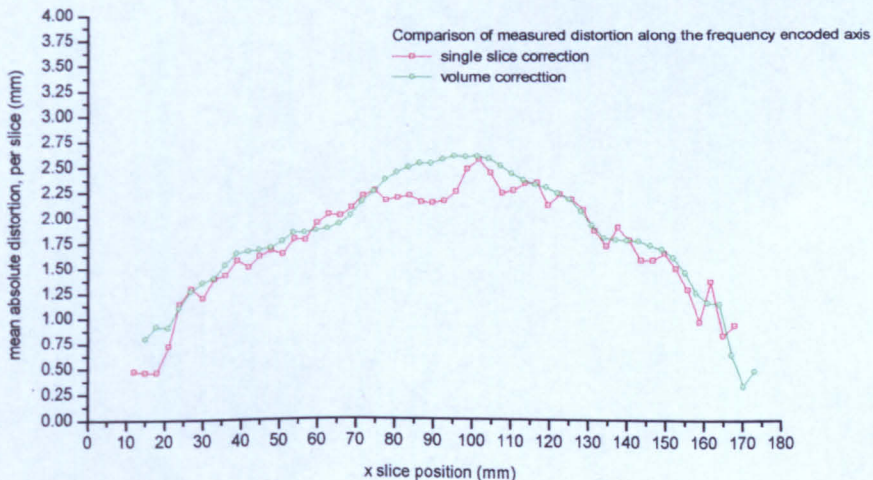


**Figure 4.14c**



## 4. Spatial Distortion in MRI

---

been implemented correctly, and works for both spin warp and EPI acquisitions. The volumetric correction has also been implemented and appears to work correctly. However, the corrected images produced by the volumetric correction appear to be of a poorer quality than the raw distorted images, both as a result of blurring and the addition of artefacts. The majority of the spatial distortion occurs along the frequency encoded direction, and this is identified in both methods. Therefore, it is felt that as the volume correction method provides little extra information compared with the single slice method, and introduces more artefact, that it will not be used further in this work.

The application of the single slice reversed gradient correction method to MR images of stereotactic apparatus would appear to be valid as no visible artefact is seen in the spin warp images of the brain. However, some artefact is observed in the corrected images in regions outside the brain (Figure 4.11), and this is a cause for concern. The multiple edge detection per frequency encoding line works, and should detect and correct the spatially separate fiducial rods as well as the main object. Its application to EP images also appears to be valid, although more prone to artefacts. Displacement maps (and  $B_e$  field maps) have been successfully produced from the correction method on a pixel-by-pixel basis.

### 4.4 Comparison of Correction Methods

During the course of the work presented here using the reversed gradient correction method, a chance arose to compare the efficacy of this correction with the phase map correction technique. The comparison has been presented in full elsewhere;<sup>78,82,83</sup> a summary is given here.

#### 4.4.1 Method for Comparison

In order to compare the reversed gradient correction method with the phase map correction method, a computer simulation of an EPI acquisition was constructed. This allowed various parameters which might affect the distortion correction method to be varied independently. From a simulated circular cross section through a cylindrical structured phantom, a matrix of  $k$  space was calculated by numerically calculating an equation similar to Equation 4.17. The

#### 4. Spatial Distortion in MRI

---

main static magnetic field was aligned perpendicular to this cross-section. A two dimensional fast Fourier transform was used to calculate the image. Static and dynamic inhomogeneous magnetic fields,  $B_e$ , could be added to the simulation, which produced the input data required by both correction methods. For the comparisons, acquisition parameters were chosen to be similar to those used on the 3 T magnet, such as a  $128 \times 128$  matrix with a 200 mm field of view, a frequency encoding gradient strength of  $35 \text{ mTm}^{-1}$  applied for 0.5 ms per line of  $k$  space, and an effective phase encoding gradient of  $2 \text{ mTm}^{-1}$ . The  $T_2$  and  $T_2^*$  values used for the phantom were 100 ms and 60 ms respectively. Distortion effects along the slice selected direction were not modelled. The number of isochromat points used in the calculation of the matrix of  $k$  space was limited by computer processing time; a value of 256 per pixel resulted in reasonable calculation times.

In order to compare the corrected images produced by both methods, four factors were considered: the effect of EP imaging sequence, various levels of signal to noise ratios, various levels of static field inhomogeneities, and the effect of time varying magnetic field inhomogeneities such as might be produced by eddy currents.

A problem which was considered throughout this work was how to quantify the success of the distortion correction, or alternatively, how to quantify the amount of distortion which has been corrected. In the case of real MR images, it is very difficult to do this as the undistorted image is not known. In the case of a computer generated simulation of a MRI acquisition, however, it would be expected that quantitative measures of the success of a distortion correction algorithm and implementation could be constructed. Unfortunately, no suitable quantification method could be found. Quantification of simple subtraction images (of the image calculated by the distortion correction method and an image produced without the influence of  $B_e$ ) failed to produce a reliable score, *i.e.*, one that agreed with the visual impression of the success of the correction. In the field of image registration of images acquired using different image modalities, or exploiting different NMR contrast mechanisms, various measures of the success of image registration have been constructed. As a well corrected image should

## 4. Spatial Distortion in MRI

---

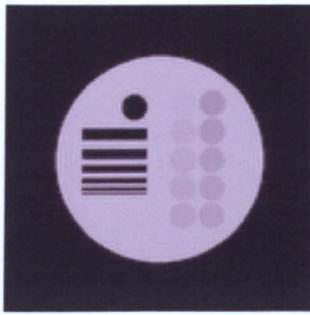
be in good registration with an image produced without the presence of  $B_e$ , it was felt that one of these measures could be applicable in this case. A method used by Studholme *et al.*<sup>106</sup> was implemented; this involved the calculation of a “feature space” between the two images, which could then be quantified by its third moment. It failed to show any correlation with an overall visual impression when used to compare corrected images with undistorted images, or when comparing images corrected with the two different methods. The score seemed to be similarly affected by small differences between the images, possibly due to edge detection or interpolation algorithms, and more gross differences between images. For the comparison presented here, an overall visual inspection of the corrected images produced by the two methods was found to be adequate to judge the success of each method. Further work to quantify the success, or otherwise, of a correction algorithm under a certain set of imaging parameters would be most useful, however, it is felt that this lies in the field of image registration and so outside the scope of this thesis.

### 4.4.2 Results and Discussion of Comparison

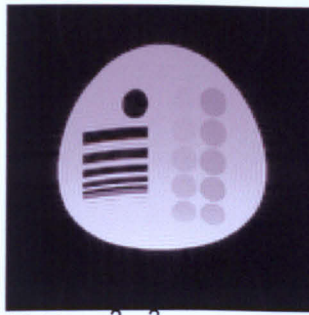
An example of an undistorted image produced by the simulation program is presented in Figure 4.15a. Regions of varying contrast, as well as lines of decreasing separation, are visible. An inhomogeneous field of the form  $x^2-y^2$  was used to produce spatial distortion, and a typical example of its effect on an image is shown in Figure 4.15b. In order to study the effects of different EPI sequences on the correction, the simulation program produced images acquired with and without a  $180^\circ$  spin echo refocusing RF pulse, and acquired with full, or reduced, coverage of  $k$  space in the phase encoding direction.

#### EPI Sequence

For reduced  $k$  space acquisitions, 8 echoes were acquired before the centre of  $k$  space and 64 echoes after. Margosian partial Fourier image reconstruction was performed;<sup>67</sup> this effectively uses the central 16 echoes to construct a phase map of a low resolution image (in the phase encoded direction) which is used to phase correct a full resolution image constructed by the half Fourier technique



a)  $B_e=0$



b)  $B_e=x^2-y^2$

**Figure 4.15** Computer simulated phantom. a) is the EP image with no inhomogeneous magnetic field present, b) is the EP image in the presence of a simulated mis-adjusted  $x^2-y^2$  shim.

**Comparison of corrected images produced by both distortion correction methods.**

**Distorted images were of the form of figure 4.15b.**



a) reversed gradient

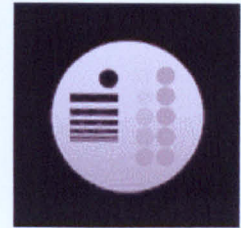


b) phase map

**Figure 4.16** Corrected from full Fourier spin echo EPI.



a) reversed gradient



b) phase map

**Figure 4.17** Corrected from full Fourier gradient echo EPI.

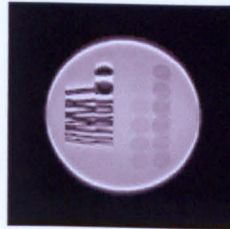


a) reversed gradient

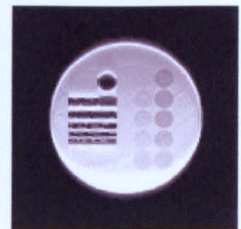


b) phase map

**Figure 4.18** Corrected from half Fourier spin echo EPI.



a) reversed gradient



b) phase map

**Figure 4.19** Corrected from half Fourier gradient echo EPI.

Apart from the full Fourier spin echo EP acquisition, the phase map correction method produces better corrected images than the reversed gradient method. Both methods show increased artefacts for half Fourier acquisitions.

#### 4. Spatial Distortion in MRI

---

(described in Section 2.3.3).

Both methods corrected the distorted simulated images acquired with a spin echo full Fourier technique, as shown in Figure 4.16. However, the reversed gradient correction method introduced severe artefacts in the 'corrected' images that it produced, for all other imaging schemes. The phase map method corrected gradient echo full Fourier images well. It performed less well on the half Fourier images, although considerably better than the reversed gradient method in the same cases. The results of these corrections are shown in Figures 4.17, 4.18, and 4.19.

The reversed gradient method performs poorly in these comparisons, with the exception of a full Fourier spin echo acquisition. It is believed that the poor performance of the reversed gradient method is due to signal loss in the distorted images in all cases apart from the full Fourier spin echo acquisition. As mentioned previously in this chapter, the reversed gradient method relies on the calculation of correct line integrals of intensity across the image. Anything which interferes with this integral will affect the correction along the entire line. Using the phase map correction method, an incorrect pixel value only affects the correction of that pixel. A gradient echo full Fourier MR acquisition does not refocus all the NMR signal; the resulting dephasing leads to signal loss in the MR image. A half Fourier reconstruction relies on a crude phase map to correct the entire image. In regions of rapidly changing phase, e.g., the edges of an object, incorrect values of phase will be assigned to pixels, resulting in incorrect pixel intensities. Both of these processes will interfere with the reversed gradient correction method more severely than the phase map correction method, as the effects of incorrect pixel intensities anywhere along a line will be felt along that entire line. Artefacts in images produced by Chang & Fitzpatrick's correction method using images acquired with gradient echo sequences have been noted by some other researchers and recently a method to reduce their effect has been reported,<sup>52</sup> based on dynamic time warping. Unfortunately, it has not been possible to implement this method to see whether it improves the correction of the images used for this comparison.

## 4. Spatial Distortion in MRI

---

### Noise

The effect of various levels of signal to noise ratios on the two correction methods were studied by adding various amounts of Gaussian noise to the  $k$  space data prior to image construction. An example of a noisy spin echo full Fourier distorted image is shown in Figure 4.20. Both methods corrected noisy images extremely well down to very low signal to noise ratios. The corrected image produced by the reversed gradient method had a higher SNR than that produced by the phase map correction method as it was the combination of both distorted images. The expected improvement of about  $\sqrt{2}$  in SNR was seen in the reversed gradient corrected image compared to one distorted image. Combination of the images used to perform the phase map correction method was not performed as each image acquired with a different  $\tau$  would have slightly different  $T_2$  weighting. The decrease in SNR finally affects both correction schemes: in the reversed gradient correction method, significant noise in the intensity line integrals results in misplaced intensity in the corrected image, as described in Sections 4.3.3 and 4.3.4; in the phase map correction method, the increase in noise increases the error in the phase value calculated for each pixel, which results in that pixel being poorly corrected.

### Level of $B_e$

The sensitivity of the correction methods to increasing static magnetic field inhomogeneities was studied by the addition in the simulation of a  $B_e$  field which would be caused by a sphere with different magnetic susceptibility to the rest of the phantom, placed within the simulated phantom but out of the imaged slice. This resulted in a local magnetic field inhomogeneity of the form described by Lüdeke *et al.*<sup>62</sup> Full Fourier spin echo EPI acquisitions were simulated. Both methods corrected this distortion until the maximum strength of the inhomogeneous magnetic gradient equalled or surpassed that of the effective phase encoding gradient, as expected from Equations 4.28 and 4.37. Simulating an inhomogeneous magnetic field in this fashion introduces both positive and negative inhomogeneous gradients, and it is felt that this is a valid simulation of inhomogeneities that would be found in, *e.g.*, a human head. Simulations were

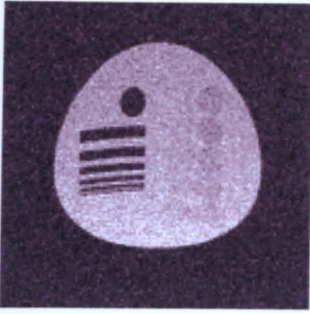


**Figure 4.20** Example of a distorted computer simulated EP image. A large amount of Gaussian noise was added to the simulated  $k$  space prior to image construction.



a) reversed gradient



b) phase map

**Figure 4.21** Comparison of corrected images from both methods. Full Fourier spin echo EP acquisitions were modelled. In addition to the  $x^2-y^2$  static inhomogeneity, a time varying inhomogeneity was also simulated in  $k$  space, to simulate the effect of an eddy current. Although both corrected images show artefacts, in this case the reversed gradient method performs better than the phase map correction.

## 4. Spatial Distortion in MRI

---

also performed by applying  $B_e$  in the form of a linear magnetic gradient along the phase encoding axis;<sup>82</sup> this inhomogeneity may be more of the form that would be encountered from non-optimally adjusted magnetic shims. It was observed that if  $B_e$  was applied with the same polarity as the effective phase encoded gradient, then the phase map correction method continued to correct the distortion even when the gradient caused by  $B_e$  exceeded the effective phase encoding gradient. However, if  $B_e$  is applied with opposing polarity to the phase encoding gradient, phase map correction fails when the gradient caused by  $B_e$  equals or exceeds the magnitude of the phase encoding gradient. This follows from Equation 4.28. However, as the reversed gradient method requires two images acquired with opposing polarities of phase encoding gradient, then one of these images will be acquired when the phase encoding gradient is 'overcome' by the gradient caused by  $B_e$ . This 'piling-over' of image signal intensity causes both correction methods to fail; however with prior knowledge of the polarity of the gradient caused by  $B_e$ , the polarity of the phase encoding gradient used to acquire images for the phase map correction method may be chosen to avoid this 'piling-over' of signal and hence allow success distortion correction even in regions of large  $B_e$  inhomogeneities.

### Eddy Currents

Finally, the effect of time dependent inhomogeneous magnetic fields, such as might be produced by the effects of eddy currents, were studied. The simulation modelled the effect of the exponential decay of a  $x^2-y^2$  inhomogeneity throughout the full Fourier spin echo EPI acquisition, with the amplitude of  $B_e$  falling by 35% throughout the acquisition of the NMR signal. The conjugate symmetry of  $k$  space is broken by the evolving  $B_e$  throughout the image acquisition. This results in some visible signal loss at the edges of the distorted image, which in turn causes some artefacts in the corrected image produced by the reversed gradient correction method, see Figure 4.21a. The phase map correction method also suffers; the corrected images it produces, while an improvement on the distorted image, do not restore the full gross dimensions, or fine detail, of the original phantom; Figure 4.21b.

## 4. Spatial Distortion in MRI

---

### Summary of Comparisons

This section has briefly outlined a simple comparison between the reversed gradient and phase map methods for correcting spatial distortion in modulus MR images. Of the parameters considered, the most important would appear to be that of imaging sequence, in this case the choice of spin or gradient echoes and full or partial Fourier acquisitions. This suggests that if the reversed gradient distortion correction method is to be used, it must be applied to full Fourier spin echo MR acquisitions only. The phase map correction method may be successfully applied to a wider range of imaging regimes, although partial Fourier techniques result in decreased performance. In the other situations considered, there was less of a difference between the corrected images produced by either method. So long as full Fourier spin echo MR acquisitions are performed, the reversed gradient correction method produced very similar results to the phase map correction method. However, for general use, the phase map correction method would appear to provide a far more robust correction.

### 4.5 Distortion Caused by Stereotactic Apparatus

In the previous sections of this chapter, the theory, implementation, and validation of Chang & Fitzpatrick's reversed gradient distortion correction method has been described. This section outlines the application of this technique to the measurement of any additional distortion caused by the introduction of specific items of stereotactic apparatus into the volume being imaged. The application of the reversed gradient correction to more realistic and complete stereotactic set-ups is described in Chapter 5.

Two particular items used in routine stereotaxis were studied; the aluminium MR compatible GTC head ring and the aluminium pins used to attach the CRW MR compatible head ring directly to the patient's skull. Their use in stereotaxis is described in Chapter 3. They are the only two metal stereotactic items that would be placed close to the patient's head during MR scanning. In both cases, a long uniform rectilinear water filled Perspex phantom, with rounded corners, was placed in the RF coil. Transaxial multislice image volumes were obtained

#### 4. Spatial Distortion in MRI

---

throughout the useful range of the head coil, using the 1.5 T Vision MR scanner. The spin echo, spin warp image acquisition was the same as described in Section 4.3.4. The single slice reversed gradient correction method was applied to each slice in turn. The mean absolute distortion per slice was calculated as was the standard deviation of the distortion over each slice. This was used to characterize the distortion throughout the volume.

A pair of multislice volumes was acquired without any stereotactic apparatus present, the second volume with frequency encoding gradient reversed relative to the first. A further pair was acquired with the GTC head ring positioned abutting the inferior border of the RF head coil; the position it would be in were a patient being scanned. Care was taken not to move the patient bed, phantom, or head coil, during positioning of the GTC head ring. Both pairs of volumes were processed using the reversed gradient method. No additional distortion was visually observed between both corrected volumes. The results are plotted in Figure 4.22. The origin of the  $z$  slice selective axis is taken as the magnet's isocentre. This coincided with the centre of the RF head coil. The comparison between the distortion per slice is shown in Figure 4.22c. Throughout most of the volume, there is no significant difference between the images acquired with, and those acquired without, the GTC head ring present. Distortion increased with increasing distance from the isocentre in both  $z$  directions, as would be expected. However, at the inferior section of the phantom (negative  $z$  values; closer to the GTC head ring) a separation is seen between the two curves, with slightly more distortion being observed in the images acquired in the presence of the GTC head ring. It would seem reasonable that this small increase in distortion in the phantom is due to the presence of the GTC head ring.

This experiment was repeated (on a different occasion) except that instead of placing the GTC head ring close to the phantom, an aluminium pin was taped to the centre of the phantom with its tip pointing into the phantom, as if inserted into a skull. The pin was attached to the phantom close to the magnet's isocentre. In this case, distortion was visible on a few images in the volume. An example is shown in Figure 4.23. A large amount of distortion is seen close to the tip of the pin, but it falls to background noise levels very

**Figure 4.22** Effect of the GTC head ring on distortion.

Mean absolute distortion per slice, measured using reversed gradient method.

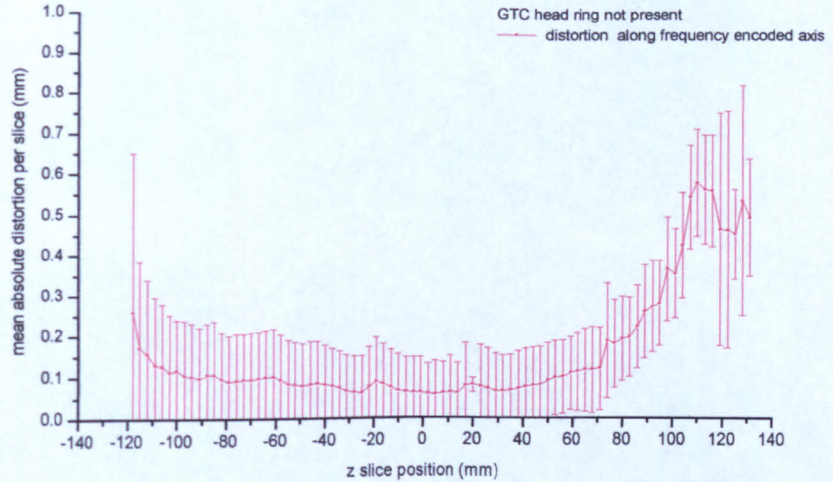
'Error bars' represent the spread of distortion throughout that slice.

Transaxial slices through a long water phantom.

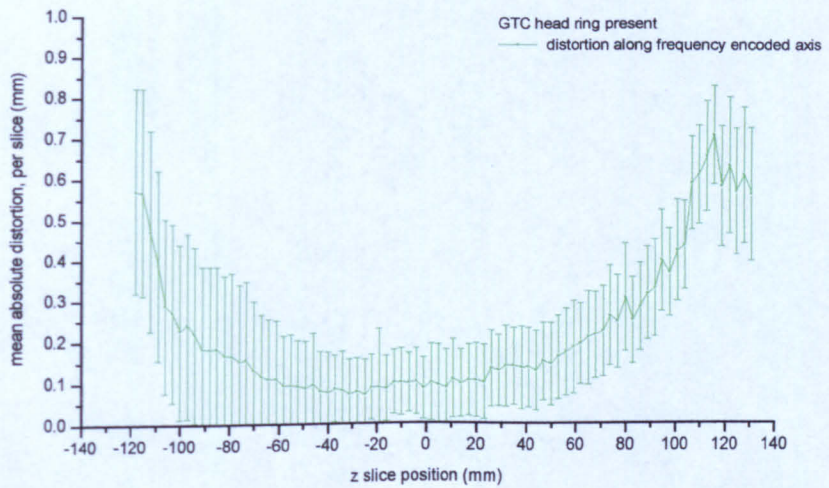
The GTC head ring was placed outside the RF head coil between about  $z=-140$  and  $z=-150$  mm.

Acquired on the Vision MR scanner. Spin echo, spin warp sequence, 130 Hz per pixel.

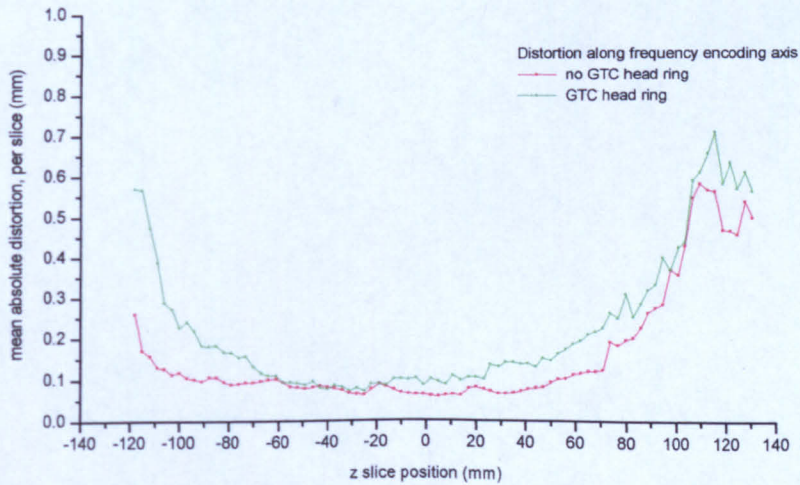
**Figure 4.22a**

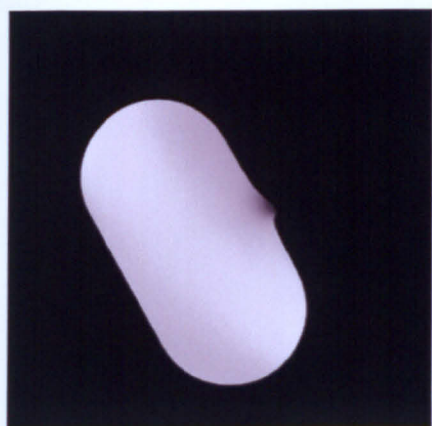


**Figure 4.22b**



**Figure 4.22c**





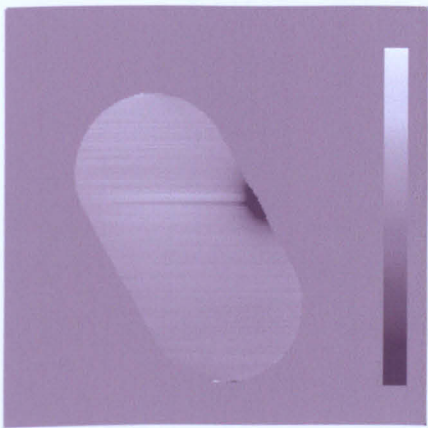
a) normal gradient



b) inverted gradient



c) corrected



d) distortion map

**Figure 4.23** The distortive effect of aluminium pins used to attach the MR compatible CRW head ring to a patient. High amounts of distortion are seen local to the pin's tip, which was placed against the water phantom, but the distortion falls to background levels within a short distance from the pin.

- a) Image acquired with normal frequency encoding gradient.
- b) Image acquired with reversed frequency encoding gradient.
- c) Corrected image
- d) Distortion map. Bright and dark points represent positive and negative shifts away from the grey uniform background, which represents no shift. The scale bar represents  $\pm 2$  mm.

#### 4. Spatial Distortion in MRI

---

rapidly with increasing distance from the pin. It would appear that the local inhomogeneous magnetic field gradient very close to the pin's tip breaks the relationship described in Equation 4.37, as incomplete correction is seen at this point in the corrected image. The results of distortion per slice are presented in Figure 4.24. No significant difference is seen between the mean absolute distortion values between the two corrected volumes, as shown in Figure 4.24c. However, the standard deviation of the distortion increases dramatically for a few images close to the isocentre ( $z=0$ ) which was the location of the pin, as shown in Figure 4.24b. As this increase in standard deviation is not observed in the absence of the pin (Figure 4.24a), it would appear that its local increase is a result of the distortion caused by the pin. This increase in standard deviation but not in mean absolute distortion throughout the slice is consistent with the observation from the distortion map (Figure 4.23d) that the pin causes only local distortion and that the distortion throughout the majority of the phantom remains at background levels.

The investigations performed in this section using the reversed gradient correction method to measure distortion, appear to show a small increase in distortion caused by close proximity of the stereotactic apparatus. However, in the case of the GTC head ring, this additional distortion is small compared to the range of distortion across a slice. However, the measure of distortion used in this section is a mean over the entire slice. This may underestimate the effect of such distortion on the transformation of points to the stereotactic coordinate system by use of the fiducial rods. This is examined in more detail in Chapters 5 and 6. The distortion caused by an aluminium stereotactic pin is considerable larger, but rapidly decreases with increasing distance from the pin. In practical use, the pin is secured into the outer surface of the patient's skull and so is always at least 10 mm away from the brain, and in the vast majority of cases, several centimetres from the target. This is also true of the pin's location in relation to any stereotactic fiducial rods. Therefore, it would seem to be unlikely that the distortion caused by the pin would have any global affect on the stereotactic process.

**Figure 4.24** Effect of MRI compatible stereotactic pin on distortion.

Mean absolute distortion per slice, measured using reversed gradient method.

'Error bars' represent the spread of distortion throughout that slice.

Transaxial slices through a long water phantom. The pin was placed near  $z=0$ .

Acquired on the Vision MR scanner. Spin echo, spin warp sequence, 130 Hz per pixel.

**Figure 4.24a**

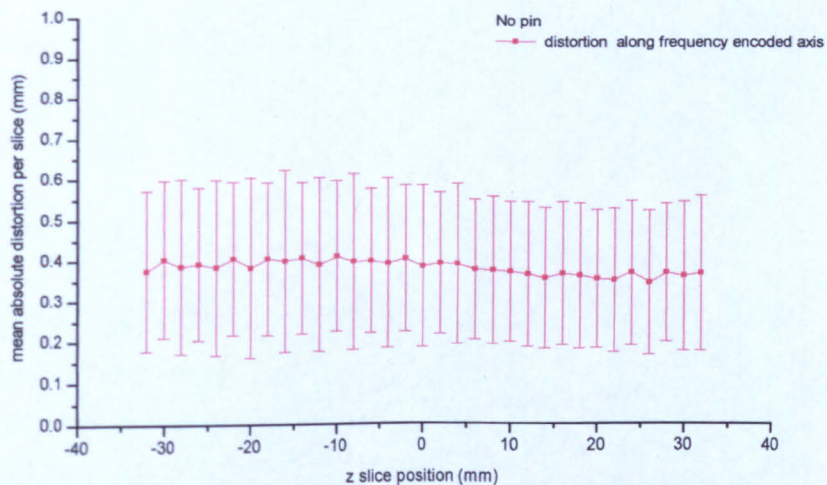


**Figure 4.24b**

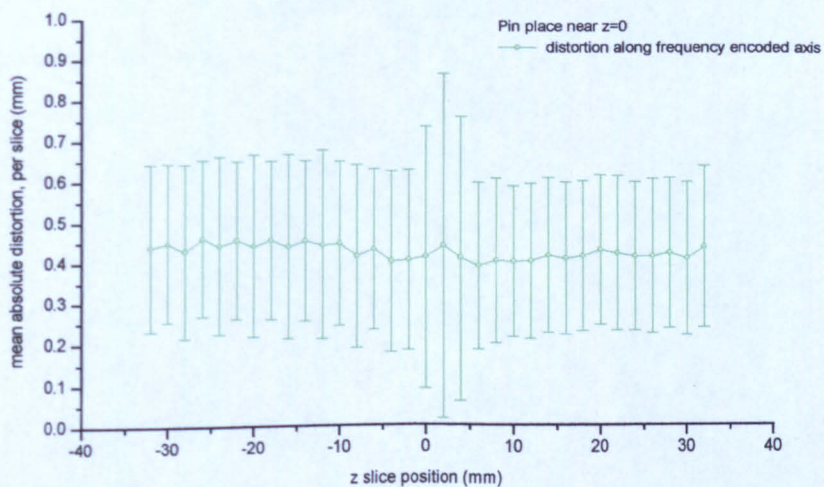
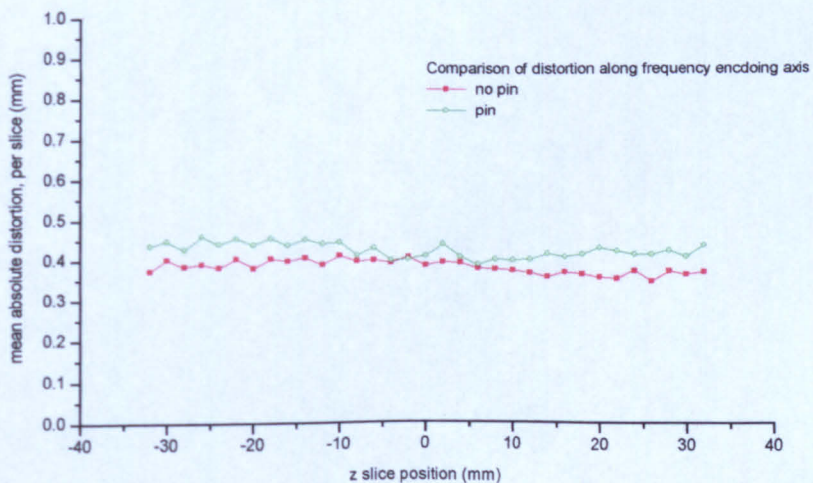


**Figure 4.24c**



### 4.6 Applications of Distortion Correction to Contemporary EPI Techniques

Spatial distortion in MR images affects many other fields of MRI. The application of the reversed gradient distortion correction method to two other wide-spread uses of EPI is presented in this section.

#### 4.6.1 ADC Maps

A MR image acquisition may be sensitized to the effect of the incoherent movement of the nuclei involved in NMR.<sup>101, 110</sup> As it is not the main subject of this thesis, a full description of the processes involved in this movement will not be given; they are described in detail elsewhere.<sup>15</sup> This section will concentrate on the application of the reversed correction method on correction of spatial distortion in the EP acquisitions used to measure this effect.

The incoherent movement of nuclei may be characterized, on a pixel by pixel basis, by the apparent diffusion coefficient (ADC) which represents the effect of all diffusion like processes ongoing throughout a particular pixel.<sup>58</sup> A fast MRI acquisition is desirable to prevent the effects of involuntary patient movements interfering with the calculation of the ADC. As it offers the fastest MR image acquisitions, EPI is ideal for this purpose, and indeed this field is one of the main contemporary applications of EPI to routine clinical MRI. A spin echo EPI sequence may be diffusion weighted with the application of two large and identical diffusion weighting magnetic gradients, one either side of the refocusing RF pulse. Stationary nuclei are dephased by the first diffusion gradient and refocused by the second, thus contributing to the NMR signal. Nuclei which move between the application of the first and second diffusion gradients experience a different rephasing magnetic field under the second gradient than they experienced under the first diffusion gradient, and are not fully rephased. Consequently, they contribute less to the subsequent NMR signal. Hence diffusion weighting has been achieved. In order to affect image contrast enough, large diffusion gradients are required, characterized by their  $b$  value. This may lead to the induction of significant eddy currents in the magnet. The magnetic field caused by these

#### 4. Spatial Distortion in MRI

---

eddy currents may have the effect of destroying the symmetry between the two diffusion gradients, thus incorrectly rephasing nuclei and resulting in false image contrast. If the eddy currents are still present during acquisition of the NMR signal, they also will generate a  $B_e$  magnetic field, potentially causing MR image distortion. If the  $B_e$  caused varies with time throughout the acquisition of the NMR signal, the spatial distortion caused is difficult to correct. However, if the  $B_e$  field caused is slowly varying, it may be considered as static for the duration of the NMR signal acquisition and thus suitable for correction by the reversed gradient method. It has been demonstrated by others<sup>14</sup> that the eddy currents caused by the diffusion gradients on a 1.5 T Siemens Vision MR scanner fall primarily into the latter category. It is assumed that, as the hardware is the same on the Vision MR scanner located in the Queen's Medical Centre as that used by Calamante *et al.*,<sup>14</sup> then the  $B_e$  caused by the diffusion gradients also may be considered to be static on the Vision in the QMC.

In many settings, image maps of ADC values are of more use than the diffusion weighted image alone, *e.g.*, in the ageing of infarcted brain tissue after a person has suffered a occlusive stroke,<sup>114</sup> or characterization of multiple sclerosis.<sup>44</sup> Accurate ADC maps are also required for the construction of the diffusion tensor,<sup>4</sup> which may provide useful information in the characterization of these disease processes.<sup>117</sup>

Diffusion weighted imaging is particularly useful in the acute assessment of stroke patients, as dead brain tissue has been observed to exhibit a lower diffusion coefficient than viable tissue. This contrast mechanism appears to become clearly visible within about thirty minutes of tissue death (as opposed to other NMR contrast mechanisms, particularly  $T_2$ , which only starts to become visible eight to ten hours after infarction<sup>80</sup>). Since an infarct may be clearly visible on a diffusion weighted image, an ADC map is extremely useful in trying to age the event (*i.e.*, is it due to a new stroke or a previous stroke).

In the simplest case, the ADC can be assumed to describe a monoexponential diffusion process within a voxel, given by<sup>101</sup>

$$i_d = i_0 e^{-bD} \quad (4.44)$$

where  $i_d$  is the image signal intensity of a particular pixel in the diffusion weighted

#### 4. Spatial Distortion in MRI

---

image,  $i_0$  is the image signal intensity of the same pixel in a non-diffusion weighted image (*i.e.*, a repeated acquisition with the magnitude of the diffusion weighted gradients set to zero),  $b$  is a constant characterizing the diffusion weighting, and  $D$  is the ADC. A map of  $D$  can be calculated from two images at each location.

Any contribution to  $B_e$  caused by the application of the diffusion gradients will not be present in  $i_0$ , and hence the two images will be differentially distorted, making the identification of the same point in both images difficult, if not impossible. A number of methods have been proposed to reduce the effect of eddy currents caused by the diffusion weighting gradients. 'Navigator' echoes may be added to the image acquisition<sup>50</sup> from which one dimensional field maps may be constructed and used to enable a first order correction to be performed. Alternatively, the whole imaging module may be surrounded with 'dummy' diffusion weighting gradients of opposite polarity, with the aim of inducing eddy currents of the opposite sense. These then will be cancelled by the application of the actual diffusion weighted gradients.<sup>7</sup> A similar effect may be achieved by using bipolar diffusion gradient pulses,<sup>2</sup> although this has the effect of either decreasing the diffusion weighting or increasing the effective echo time of the acquisition, for the same strength gradients.

If it can be assumed that the  $B_e$  field caused by the diffusion weighting gradients is static for the duration of image acquisition, then an alternative approach is to apply the reversed gradient correction method. If it is applied to both diffusion weighted and non-diffusion weighted images, then the corrected images produced should be in registration with each other. Not only will the effects of the diffusion weighting gradients have been removed, but the spatial distortion from other sources of magnetic field inhomogeneities will have been removed as well. This has the advantage of producing spatially correct ADC maps from EP images, allowing more accurate quantification of areas of the maps, as well as increasing the potential of image registration with other images acquired using an acquisition scheme less sensitive to  $B_e$  effects.

The comparison between the reversed gradient correction method and phase map, reported in Section 4.4 highlighted two areas in which the reversed gradient correction method performed well compared to the phase map correction method.

#### 4. Spatial Distortion in MRI

---

These were when using a full Fourier spin echo EP acquisition, such as is used in diffusion weighted sequences, and when image acquisition was performed in the presence of time varying eddy currents. Although it is being assumed that the  $B_e$  caused by eddy currents created by the diffusion weighting gradients is static, it is encouraging to know that any small time varying component is unlikely to greatly affect the reversed gradient correction.

A standard Siemens diffusion weighted sequence<sup>||</sup> was modified on the 1.5 T Vision MR scanner at the Queen's Medical Centre to reverse the polarity of the phase encoding gradients used for imaging. The polarity of the diffusion gradients were not changed so that any  $B_e$  which they caused would act in the same sense for both normal and reversed phase encoding gradients, and hence potentially be correctable. The sequence acquired four images per slice; three diffusion weighted images, one along each primary axis, and one image with no additional diffusion weighting gradients. This was repeated with the reversed phase encoding sequence. The images were transferred from the scanner onto other computers for post-processing, which involved applying the reversed gradient distortion correction to produce four corrected images per slice. Three ADC maps were then calculated, one along each axis, and the mean of these was calculated to produce a map proportional to the trace of the diffusion tensor.<sup>4</sup>

The correction was tested using a phantom. A coronal image was acquired through a water filled phantom containing, among other structures, two adjacent blocks of Balsa wood, which had been in the phantom for several months, allowing water to permeate the fibres of the wood. The voxel size of the images was  $2 \times 2 \times 5$  mm. The results are presented in Figures 4.25, 4.26, 4.27, and 4.28. Typical distortion for EP images is seen along the phase encoding direction (horizontal in the Figure) although the differential bulk shift between images acquired with diffusion weighting gradients along different axes is not immediately visible. The gross correction of the distortion in the phantom after application of the reversed gradient correction method is clear. The direction of the fibres of the water soaked balsa wood (in the lower right of the phantom)

---

<sup>||</sup> ep2d\_se\_1031hd3b1250\_11.ekc with TE=103 ms, TR=5000 ms, and 0.8 ms per frequency encoding line.  $b=1000$  s  $\text{mm}^{-2}$ .  $128 \times 128$  matrix.

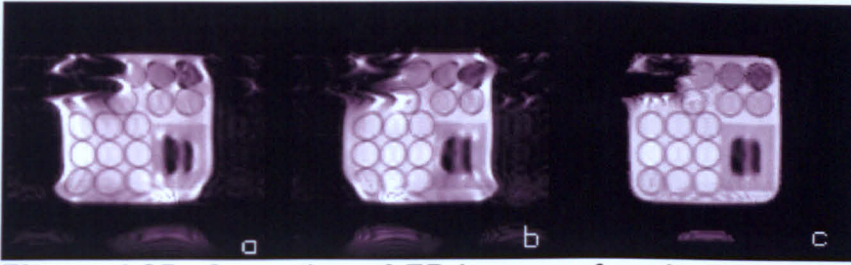


**Figure 4.25** Correction of EP images of a phantom using the reversed gradient correction method. a) is an image acquired with normal gradient polarity, after automatic shimming had taken place. b) is the image acquired with reversed polarity of the phase encoding gradient (horizontal in these images). c) is the corrected image. No diffusion gradients were applied for this acquisition (*i.e.*  $T_2$  weighted EPI).

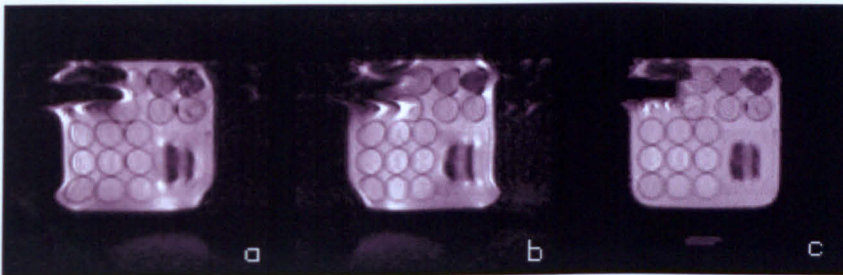


**Figure 4.26** Correction of EP images of phantom using reversed gradient correction method. Diffusion gradients of  $b=1000 \text{ s mm}^{-2}$  applied along the frequency encoding axis (vertical in these images).

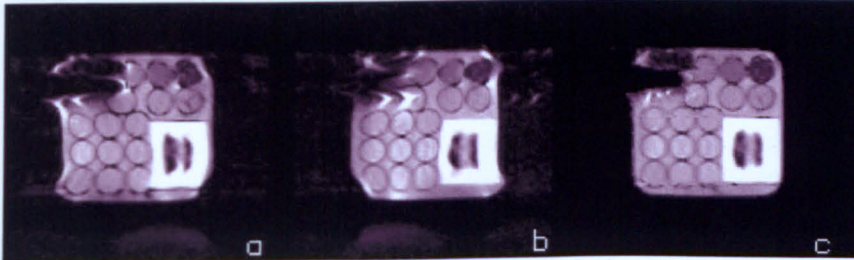


**Figure 4.27** Correction of EP images of phantom using reversed gradient correction method. Diffusion gradients of  $b=1000 \text{ s mm}^{-2}$  applied along the phase encoding axis (vertical in these images). Restricted diffusion can be seen in the two Balsa wood blocks in the lower right of the phantom.

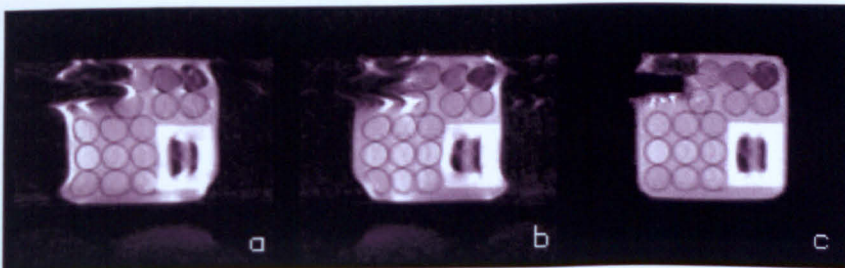


**Figure 4.28** Correction of EP images of phantom using reversed gradient correction method. Diffusion gradients of  $b=1000 \text{ s mm}^{-2}$  applied along the slice selective axis. Restricted diffusion can be seen in the two Balsa wood blocks in the lower right of the phantom.

#### 4. Spatial Distortion in MRI

---

provides excellent diffusion weighting contrast between the images acquired with diffusion weighting gradients along different axes due to the restricted diffusion perpendicular to the wood's fibres.

Figures 4.29 and 4.30 show the result of calculating ADC maps from both the corrected and uncorrected images. The ADC maps produced from the corrected images show improved uniformity across the water (which fills the majority of the phantom), a reduction in the artefact caused by the misregistration of diffusion and non-diffusion weighted images (particularly visible at the edges of objects), and an improvement in gross shape of the image of the phantom.

This experiment was repeated on an acute stroke patient; examples of the results are shown in Figure 4.31. Clear ADC maps are produced. The distorting effect of the directional diffusion gradients is seen more clearly in these raw transaxial images, in particular the image of Figure 4.31c (diffusion gradients applied along the vertical phase encoding axis) is clearly shifted relative to its neighbouring images. This distortion is shown clearly in the ADC maps calculated from the raw images, Figure 4.32, manifesting itself as bright boundary artefact and heterogeneity. By contrast, the ADC maps calculated from corrected images, as shown in Figure 4.33, show little artefact. The trace image shows far more uniform ADC values over healthy white matter, while the individual ADC maps calculated from diffusion weighted gradients along orthogonal axes show varying ADC values due to restricted diffusion along various white matter fibre tracts. Small regions of 25 pixels were selected on the ADC maps, of which the mean and standard deviation of the ADC values were calculated. The value for tap water in the phantom at 20° C was  $2.10 \times 10^{-9} \text{ m}^2\text{s}^{-1} \pm 0.02 \times 10^{-9} \text{ m}^2\text{s}^{-1}$  and for normal appearing white matter in the stroke patient  $0.79 \times 10^{-9} \text{ m}^2\text{s}^{-1} \pm 0.05 \times 10^{-9} \text{ m}^2\text{s}^{-1}$ , which compare well to the values published in the literature.<sup>44,114</sup> Mean absolute distortion values, over an entire slice, of up to 10 mm were observed for some diffusion weighted images.

The reversed gradient distortion correction method may successfully be applied to diffusion weighted EP images used to calculate ADC maps, providing the inhomogeneous magnetic fields present may be considered static throughout the image acquisition. This technique has the advantage of also correcting spatial

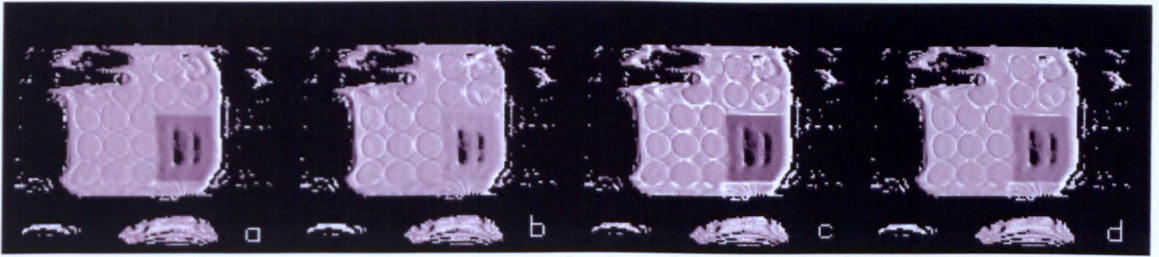


**Figure 4.29** ADC maps of phantom calculated from distorted images. b), c), & d) are the ADC maps in the frequency, phase, and slice directions respectively. a) is the trace of the diffusion tensor. Misregistration artefacts can be seen around the edges of the phantom and around its internal structures.

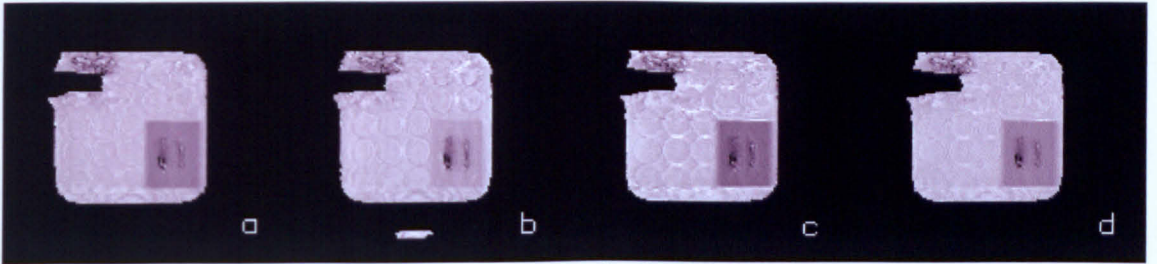


**Figure 4.30** ADC maps of phantom calculated from corrected images. b), c), & d) are the ADC maps in the frequency, phase, and slice directions respectively. a) is the trace of the diffusion tensor. Far fewer misregistration artefacts can be seen compared with the uncorrected maps, and the ADC values are more heterogeneous. Both 'normal' EPI distortion and the differential distorting effects off the diffusion weighting gradients have been corrected.

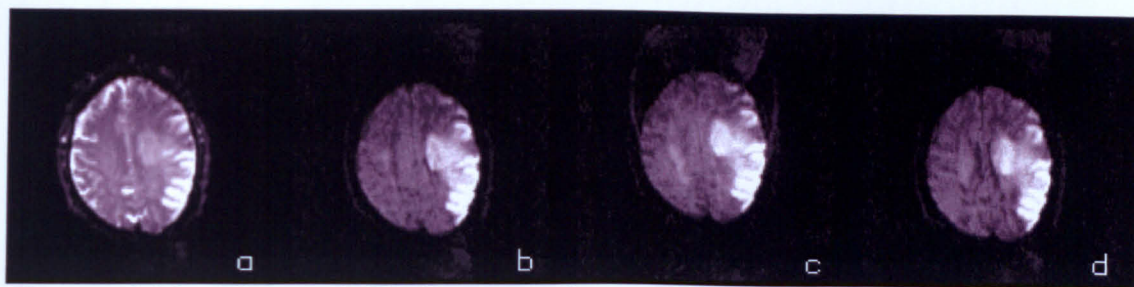


**Figure 4.31** Distorted EP images of an acute stroke patient. a) no diffusion weighting gradients ( $T_2$  weighted). b) diffusion gradients along frequency encoding axis (horizontal in these images). c) diffusion gradients along phase encoding axis. d) diffusion gradients along slice selective axis. All images acquired after automatic shimming had occurred. Differential vertical shifts can be seen with the application of differing directions of diffusion weighting gradients.

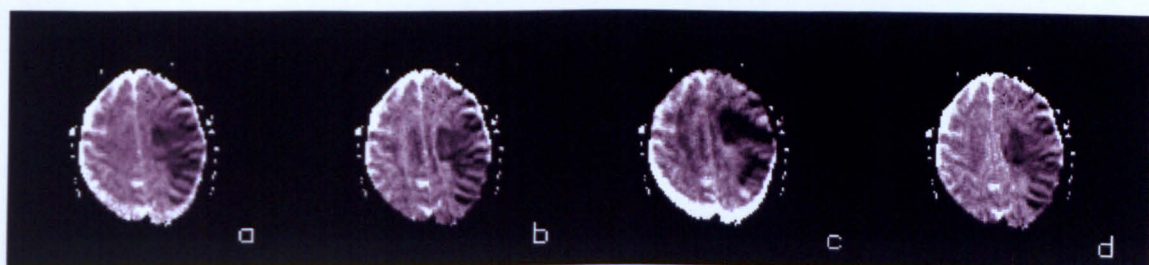


**Figure 4.32** ADC maps produced from uncorrected images above. b), c), & d) are the ADC maps in the frequency, phase, and slice directions respectively. a) is the trace of the diffusion tensor. Misregistration artefacts can be seen around the edges of the brain and around internal structures.

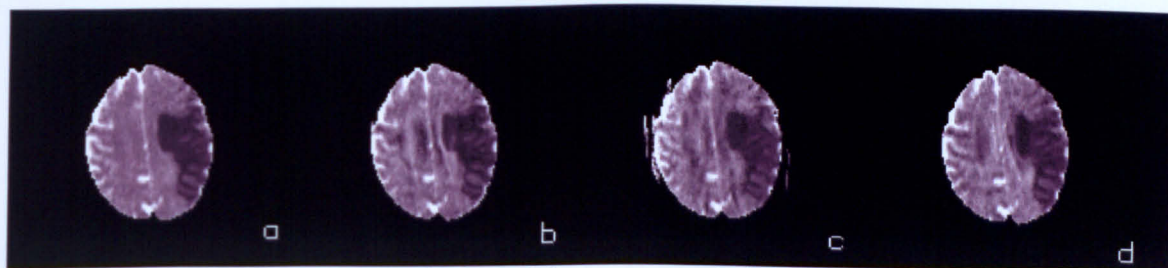


**Figure 4.33** ADC maps calculated from corrected images. b), c), & d) are the ADC maps in the frequency, phase, and slice directions respectively. a) is the trace of the diffusion tensor. Far fewer misregistration artefacts can be seen compared with the uncorrected maps, and the ADC values are more heterogeneous. Both 'normal' EPI distortion and the differential distorting effects off the diffusion weighting gradients have been corrected.

## 4. Spatial Distortion in MRI

---

distortion in the EP images caused by other sources than the diffusion weighting gradients. Disadvantages include doubling the acquisition time, in order to acquire the images with reversed phase encoding gradient, although this results in a  $\sqrt{2}$  improvement in signal to noise in the correct image, compared to a single acquisition. It also does not correct for spatial distortion in the slice selected direction, although as described in Section 4.3.2 this is relatively small in EP images compared with the distortion present along the phase encoding direction. Artefacts will be introduced if the patient moves during image acquisition, and due to poor edge detection. The latter occurs with increased frequency the more inferior the images are acquired in the brain. Hence the application of the reversed gradient correction method has its uses in the correction of distortion in EP images used to construct ADC maps, but must be used with care.

### 4.6.2 BOLD Functional Imaging

One of the more fascinating applications of echo planar imaging over the last decade had been to the area of functional brain imaging. This allows non-invasive identification of active regions of the brain during a particular stimulation or execution of a task. First demonstrated by Kwong *et al.*<sup>10,56</sup> in 1991, it is based on the following effects.<sup>101</sup> Deoxyhaemoglobin in the blood is paramagnetic, while oxyhaemoglobin is weakly diamagnetic. This results in a magnetic susceptibility difference between deoxyhaemoglobin in blood and surrounding tissue, resulting in a shortening of the  $T_2^*$  relaxation time in a region, compared to the  $T_2^*$  that would be obtained in the presence of oxyhaemoglobin. When a region of the brain is active, it is believed that blood flow to that region increases while oxygen consumption there remains constant. Thus the proportion of oxyhaemoglobin in the tissue increases, resulting in an increase in the  $T_2^*$  measured in the region. This is known as the Blood Oxygen Level Dependent (BOLD) effect.<sup>84</sup> The difference between the signal in active and non-active regions increases with main magnetic field strength, and is typically one to five percent in the magnetic field range of 1 T to 3 T.

A simple BOLD functional magnetic resonance imaging (fMRI) experiment would involve continual rapid acquisition of MR images through the brain, while

#### 4. Spatial Distortion in MRI

---

the subject performs an on/off task (or is presented with an on/off stimulus). The active regions of the brain would be expected to respond with the same frequency as the presentation of the task. Pixels following this pattern through time can be identified with post processing, allowing a map of brain function to be constructed. The design and analysis of fMRI experiments can be a complex process, especially if quantitative results are required.

EPI is an ideal MR imaging sequence with which to observe this phenomenon, as it has a fast acquisition time (hence good temporal resolution), large  $T_2^*$  weighting, and high signal to noise ratio. However, it has relatively poor spatial resolution compared with spin warp MRI techniques, making detailed identification of neuro anatomy sometimes difficult. It is often useful to acquire a high resolution spin warp image volume of the brain to provide anatomical detail, onto which the functional map calculated from EP images, may be superimposed. This assumes the EPI and spin warp images are in (or may be put in to) registration with each other. As EP images are usually far more spatially distorted than spin warp images, it is not possible to exactly overlay results from EPI onto spin warp images. Volume registration techniques may help, but can not remove the differing spatial distortion between the different MR acquisition schemes.

The reversed gradient correction method provides a method for correcting spatial distortion in EP images. As the spatial distortion in spin warp images is usually small compared to EPI acquisitions, it may be assumed that the spin warp images contain negligible spatial distortion. Hence, correcting the distortion in the EP images alone should provide an increase in the accuracy of superimposing functional maps onto anatomical images. This was the aim of the work presented in this section. It is not the intention of this work to provide accurate registration between functional maps and anatomical images, but to demonstrate how distortion correction may improve the superposition of functional maps onto anatomical images. This, in turn, should improve the efficacy of any further registration performed.

There are a number of problems in applying the reversed gradient correction method to fMRI. Firstly, for each corrected image, two image acquisitions

#### 4. Spatial Distortion in MRI

---

are needed, the second with reversed phase encoding gradient. This would half the temporal resolution of the experiment, although if this was not important, the experiment would benefit from an improvement in signal to noise as well as correction of distortion. However, the main problem is likely to be the small amount of artefacts introduced into the corrected images, which has been observed throughout this chapter. As the BOLD effect itself is so small, any artefact may mask the BOLD effect entirely, or introduce spurious regions of activation. Therefore, it was felt that the best approach was to correct the distortion after the fMRI processing had been completed, but before superposition of the activation onto a higher resolution spin warp image set.

The following correction scheme was adopted. Immediately prior to the fMRI experiment, a set of spin echo EPI images were acquired in the same position and using the same imaging parameters (except for the  $180^\circ$  RF pulse to form a spin echo rather than the usual gradient echo) as planned for the fMRI experiment. This was repeated with the phase encoding gradient reversed. The fMRI experiment was then performed as usual, followed by the acquisition of a high resolution spin warp image volume. Normal post processing was applied to the fMRI experiment, and a map of activation derived. This activation map will be distorted by the same amount as the raw EP images.

The initial spin echo EP images were processed by the single slice reversed gradient correction method. A corrected image at each slice position was produced by application of Equation 4.36 (where, in the case of EPI,  $x$  refers to the phase encoding gradient). A distortion map was also constructed, in terms of pixel shifts. From this map, or from direct use of Equation 4.33, the Jacobian could be calculated, and saved. The transformation between distorted and undistorted coordinates is now known, and images acquired subsequently may be corrected by application of Equation 4.33 without the acquisition of a second image with reversed phase encoding gradient. There is no mechanism within Equation 4.33 which depends on the image contrast. Hence, so long as the subsequent images are acquired with the same image parameters used in the acquisition of the initial images from which the distortion map was calculated, that the object being imaged has not moved, and  $B_e$  not changed, contrast

#### 4. Spatial Distortion in MRI

---

changes in the subsequent images will not interfere with their correction. Hence the distortion map may be used to correct the activation map. The corrected activation map may now be superimposed on the high resolution spin warp image volume.

The above correction scheme was implemented. Image acquisition was performed on the 1.5 T Vision MR scanner. EP imaging\*\* parameters for the fMRI experiment were a  $64 \times 64$  matrix,  $3 \times 3 \times 3$  mm voxel size,  $TE=60$  ms, with each frequency encoded line of  $k$  space being acquired in 0.600 ms. A volume of 15 contiguous transaxial slices was acquired every two seconds; this was repeated 128 times. The EPI parameters used for the initial spin echo scans from which the distortion map was constructed were the same as above. The TE was chosen as 60 ms as it has been reported that the maximum BOLD contrast at 1.5 T is observed at this value; this allowed adequate time for a refocusing RF pulse to be inserted without having to increase the TE. The reversal of the phase encoding gradient was performed in the sequence code. The high resolution spin warp MR acquisition used was a standard inversion recovery 3D TurboFLASH sequence (3D MP-RAGE) with pixel size  $1 \times 1 \times 1$  mm. This sequence was acquired with a known spatial offset relative to the EP images. A coin was placed under the RF head coil in order to generate a  $B_e$  large enough to cause visible spatial distortion.

A simple fMRI motor paradigm was used, involving gentle right hand finger tapping. The volunteer was verbally instructed when to start and stop. Each cycle consisted of 20 seconds of continuous tapping followed by 20 seconds of no tapping. This was repeated six times. The initial eight image volumes of no tapping were discarded; it was assumed that after this the image contrast had reached a steady state. This resulted in a total of 128 volumes; the maximum allowed on the Vision MR scanner under its present release of software. Post processing was performed using algorithms and software developed at the Magnetic Resonance Centre of the University of Nottingham.<sup>20</sup> This involved calculating the correlation coefficients between the on/off tapping instructions with the time course of each pixel. z scores were calculated from these, and pixels with a high

---

\*\*the EPI sequence used for this experiment was kindly provided by Alistair Howsman, FIL, Queen's Square, London and David Porter, GOS, London.

#### 4. Spatial Distortion in MRI

---

z score were used to form an activation map.

The results from the fMRI experiment are presented in Figure 4.34. This shows the activation, in red and yellow, superimposed on the average of the actual EP images used in the fMRI experiment. The images do not show much contrast due to the use of a TR of two seconds. BOLD activation is seen in the motor cortex in the left hemisphere, which is responsible for the right hand's movement, as expected.

The activation map was interpolated to  $1 \times 1 \times 1$  mm voxels and overlaid onto the appropriate high resolution spin warp images. The registration between the activation map and spin warp images was based entirely on the known three dimensional offset between the two at the time of acquisition. Although more involved methods of image registration are normally used to perform this process, it was felt that the simple method used should highlight any difference between superposition of distorted and corrected activation maps, and it offers a fixed and controlled transformation. Selective slices of the superposition of uncorrected and corrected activation maps are shown in Figures 4.35 and 4.36 respectively. The superposition appears to work well. Little difference is seen visually between the uncorrected and corrected overlays, although on close inspection, the uncorrected activation map is seen to extend outside the brain, and is shifted slightly anterior relative to the corrected activation.

The slice by slice distortion was quantified in the same way as elsewhere in this chapter, and the results shown in Figure 4.37. Examples of the uncorrected and corrected EP images are shown in Figure 4.38. Spatial distortion is clearly seen around the posterior portion of the brain, although little distortion is seen around the region of final activation. This explains why little difference was seen between the corrected and uncorrected activation overlays.

The reversed gradient correction method has been successfully applied to correcting distortion in EP images used for fMRI, potentially allowing more accurate superposition of activation maps on to high resolution anatomical MR images. This suggests that co-registration techniques applied subsequently should benefit from the distortion correction. By only correcting the distortion in a post processed activation map, the effects of correction induced artefacts on the post

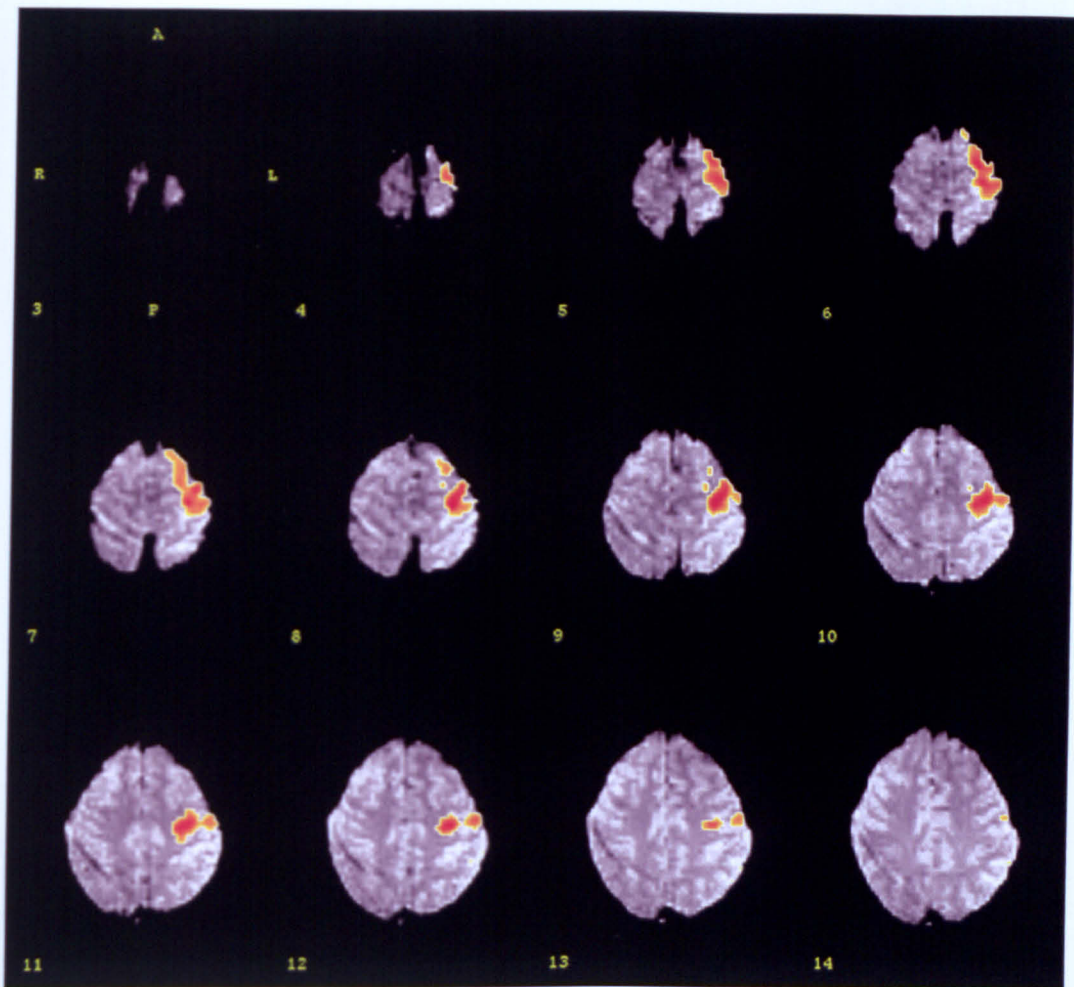


**Figure 4.34** Transaxial BOLD fMRI activation maps (in red and yellow) overlaid on the average of the EPI images used for the fMRI experiment. Activation in the volunteer's left motor cortex is seen from the right hand tapping task performed.

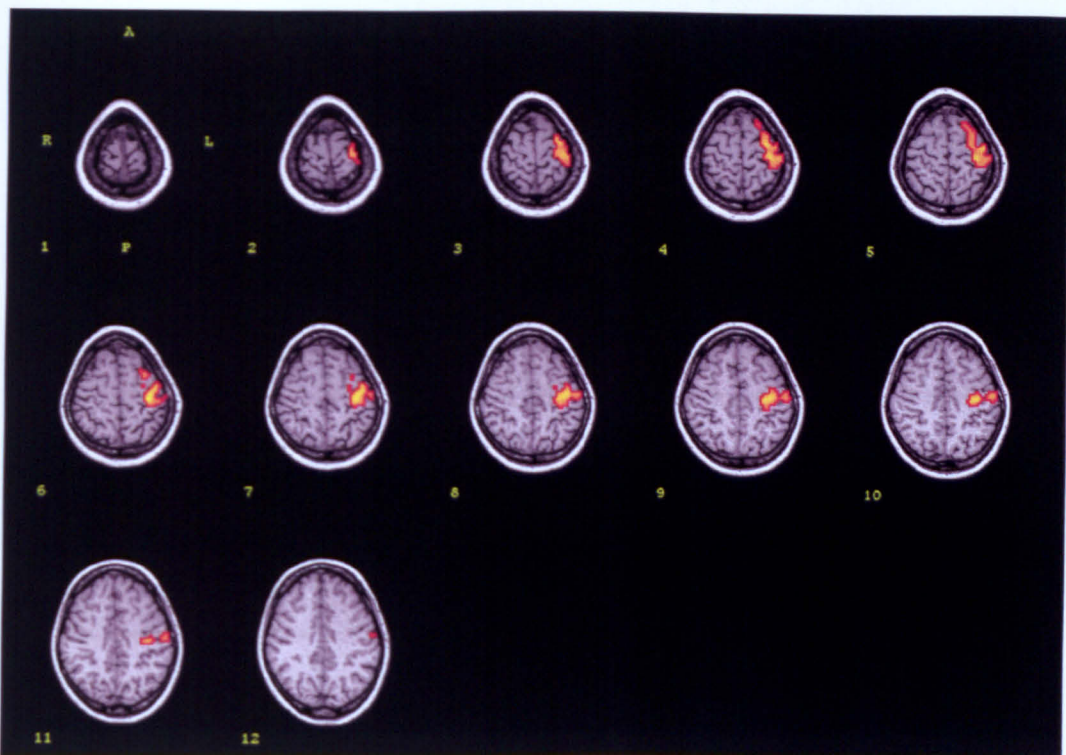


**Figure 4.35** Superposition of the uncorrected BOLD activation maps on high resolution 3D MP-RAGE images.

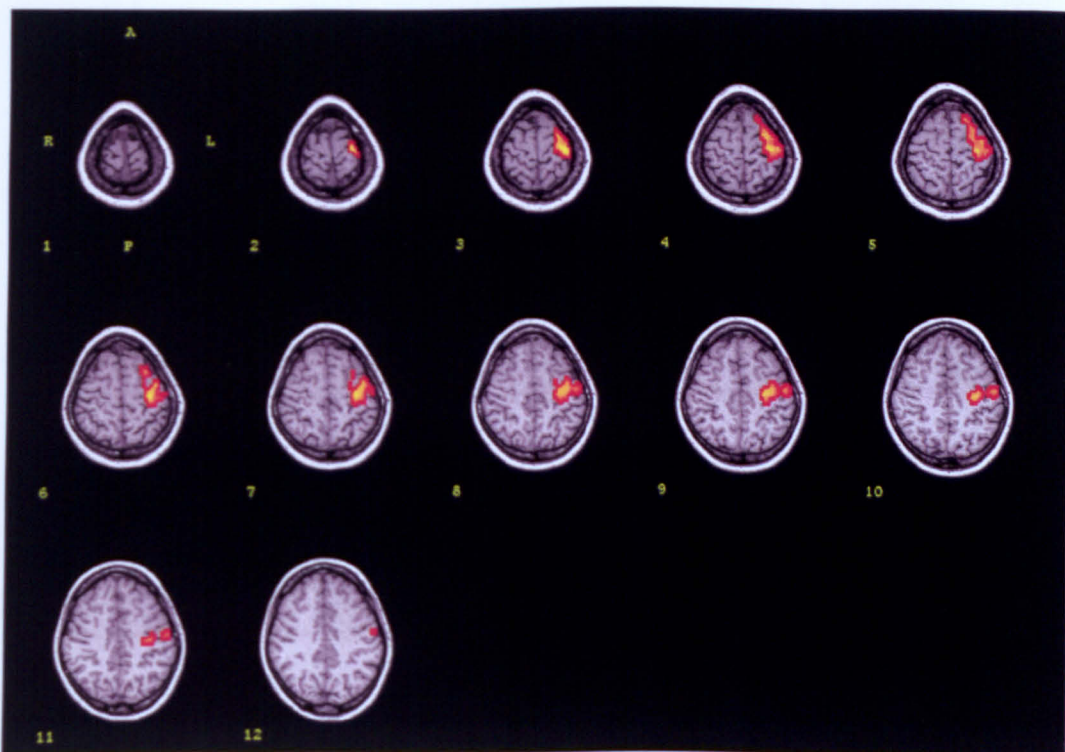


**Figure 4.36** Superposition of BOLD activation maps, corrected with the reversed gradient correction method, on high resolution 3D MP-RAGE images. The corrected activation maps exhibit less 'spill over' outside the brain, and are shifted slightly anterior compared with the uncorrected maps.

**Figure 4.37** Distortion in EP images of fMRI volunteer's brain.

Mean absolute distortion per slice, measured using reversed gradient method.

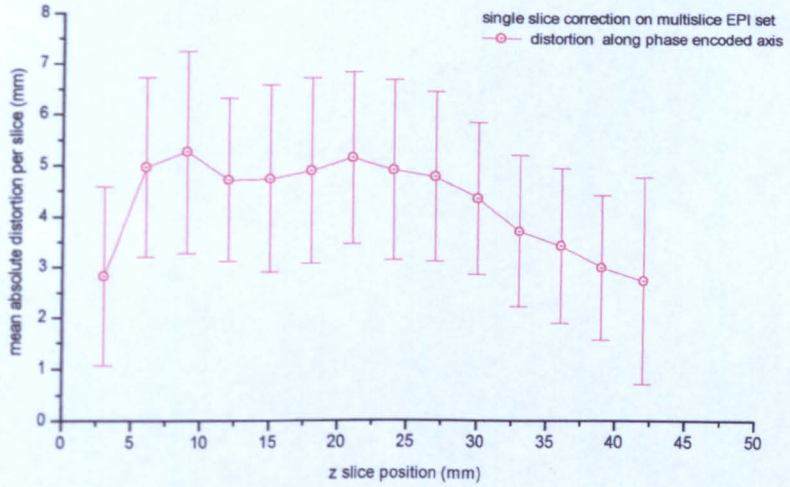
'Error bars' represent the spread of distortion throughout that slice.

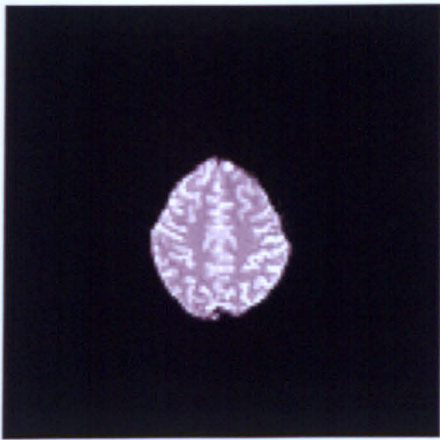
Transaxial slices. A coin was placed under the RF head coil to create additional distortion.

Slices ordered from superior to inferior with increasing z coordinate.

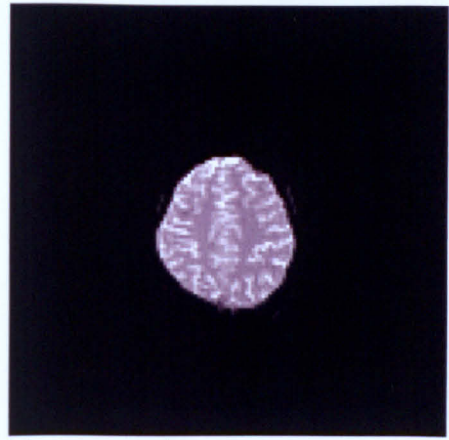
Acquired on the Vision MR scanner.

**Figure 4.37a**

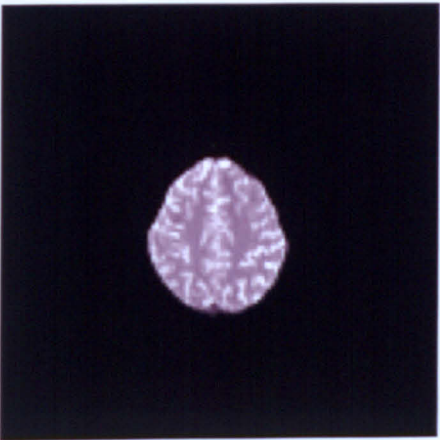




a) normal



b) reversed



d) corrected



e) distortion map

**Figure 4.38** An examples of correction of an initial transaxial spin echo EP images using the reversed gradient method. Spatial distortion is seen in the posterior regions of the brain in a) and b). The phase encoding gradient is aligned parallel to the vertical axis in these images. The calculated distortion map is used to correct the fMRI activation map calculated at this slice position. The distorting affect of a coin placed under the RF head coil can be seen in the posterior portions of the brain. The scale bar represented  $\pm 8$  mm.

## 4. Spatial Distortion in MRI

---

processing are removed. The acquisition of spin echo EP images from which the initial distortion map is produced adds little relative time to the total imaging duration. The correction relies on no movement of the object throughout the imaging process, but this is already an existing requirement of fMRI experiments.

### 4.7 Modifications to Chang & Fitzpatrick's Correction Method

In Section 4.3.2, Chang & Fitzpatrick's reversed gradient method for correction of distortion in both single MR images and MR image volumes was described. Section 4.3.6 concluded that the application of the single slice correction method was preferable to that used for volume correction. In this case, the distortion in the slice selective direction was ignored. However, it still would be preferable to measure and correct the distortion along this axis, even though it is usually less than that along the frequency encoding direction. In the course of this work, two new modifications for correcting the distortion along both the frequency and slice selected axes were devised, implemented, and assessed.

In the usual implementation of Chang & Fitzpatrick's distortion correction method, a corrected image is constructed by the application of Equation 4.36. This avoids the numerical calculation of the differential terms which form the Jacobian. However, if the Jacobian is calculated explicitly, a corrected image may also be produced by application of Equation 4.26. If distortion along the slice selective gradient is ignored, then the Jacobian is of the form of Equation 4.32 and single slice correction is performed. If the Jacobian of Equation 4.25 is used then an image volume is corrected for distortion along both the frequency and slice selective axes. In this case, substituting Equations 4.8 into Equation 4.10 gives the Jacobian term,  $J$ , as

$$J \left( \begin{array}{c} x_1, y_1, z_1 \\ x, y, z \end{array} \right) = \frac{dx_1}{dx} \times \frac{dz_1}{dz} - \frac{dx_1}{dz} \times \frac{dz_1}{dx} \quad (4.45)$$

In order to apply Equation 4.26, and to calculate the required Jacobian term, the pixel by pixel transformation between the distorted space,  $i_1(x_1, y, z_1)$ , and the corrected space,  $i(x, y, z)$ , must be known. From this, the required differentials can be calculated numerically to construct the Jacobian term. The

## 4. Spatial Distortion in MRI

---

new methods presented below use different methods to calculate this transformation;<sup>76</sup> once known, both methods produce corrected image volumes by the same method, by application of Equation 4.26.

### 4.7.1 New Volume Correction Method One

By applying the single slice reversed gradient correction method to each slice in a contiguous multislice volume in turn, a relationship between the distorted coordinate in the frequency encoded direction,  $x_1$ , and the corrected coordinate,  $x$ , is calculated, using Equations 4.34 and 4.31. However, no correction has been made in the slice selective direction,  $z$ , so these corrections apply to a slice at distorted slice position  $z_1$ . The calculated relationship between  $x$  and  $x_1$  therefore should be written as

$$x_1 \equiv X'_1(x, y, z_1) \quad (4.46)$$

because the  $x_1$  that is measured by the single slice correction method is dependent upon the distorted coordinate,  $z_1$ . In order to calculate a spatially correct volume,  $x_1$  is required in terms of  $x$ ,  $y$ , and  $z$  rather than  $x$ ,  $y$ , and  $z_1$ .

An inhomogeneous static magnetic field,  $B_e(x, y, z)$  causes signal in the MR image which actually came from the (correct) coordinate  $(x, y, z)$  to appear at (distorted) coordinate  $(x_1, y, z_1)$ , where the relationship between the correct and distorted coordinates is given by Equation 4.24. By eliminating  $B_e$  from these equations, and substituting for  $x_1$  from Equation 4.46

$$z = z_1 - \frac{G_x}{G_z} (X'_1(x, y, z_1) - x) \quad (4.47)$$

is obtained. This equation gives a relationship between  $z$  and  $z_1$ , where  $z_1$  is in terms of  $x$ ,  $y$ , and  $z_1$ , *i.e.*,

$$z \equiv Z'_1(x, y, z_1) \quad (4.48)$$

In order to produce a corrected volume,  $z_1$  is required in terms of all three undistorted coordinates,  $x$ ,  $y$ , and  $z$ . Equation 4.48 can be inverted numerically to achieve this, resulting in

$$z_1 \equiv Z_1(x, y, z) \quad (4.49)$$

#### 4. Spatial Distortion in MRI

---

In turn, Equation 4.49 can be numerically substituted into Equation 4.46 to eliminate  $z_1$  and gives

$$x_1 \equiv X_1(x, y, z) \quad (4.50)$$

Equations 4.49 and 4.50 give one distorted coordinate in terms of undistorted coordinates only. These may be used to numerically construct the differentials required to calculate the Jacobian term, stated in Equation 4.45, where

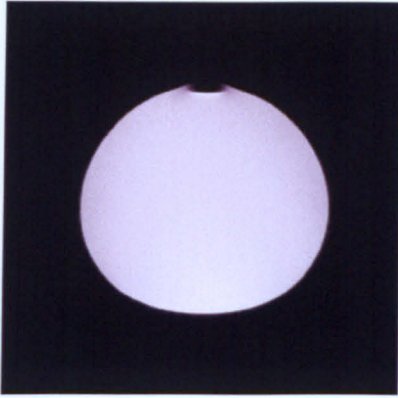
$$J \left( \frac{x_1, y_1, z_1}{x, y, z} \right) = \frac{d}{dx} X_1(x, y, z) \times \frac{d}{dz} Z_1(x, y, z) - \frac{d}{dz} X_1(x, y, z) \times \frac{d}{dx} Z_1(x, y, z) \quad (4.51)$$

using finite differences. The final stage is to construct the corrected volume. This involves stepping through each undistorted point and using Equations 4.49 and 4.50 to calculate the required distorted coordinate before interpolating into the distorted image volume to find the image intensity at that point. The corrected image is then constructed using Equation 4.15.

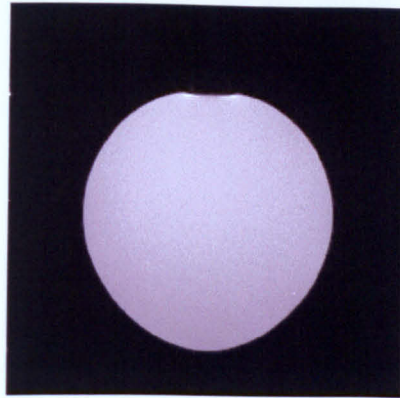
This volume distortion correction method would appear to have a number of advantages over Chang & Fitzpatrick's volume correction method. In particular, because edges of the object in the image volume only need to be found along the frequency encoding direction, the object may extend beyond the imaged volume in the slice selective direction as well as in the phase encoding direction, allowing more flexibility in the set-up of the MRI acquisition.

This new correction method was implemented in the correction computer program. Its implementation involved a considerable amount of interpolation to find values at fractional pixel positions within arrays; a choice of bilinear or sinc interpolation was given. The MR image acquisition time is the same as for either of Chang & Fitzpatrick's correction methods, and the post-processing time similar to their volume correction.

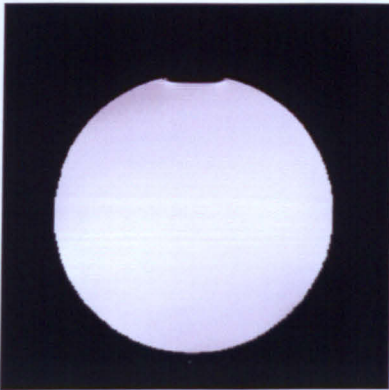
Results from a spherical phantom are presented in Figure 4.39. The same images were used as obtained in Section 4.3.5 above. Graphs showing the calculated mean absolute distortion per slice are shown in Figure 4.40. Good correction is observed. The mean absolute distortion calculated by this method shows good agreement with the distortion calculated by Chang & Fitzpatrick's single slice method.



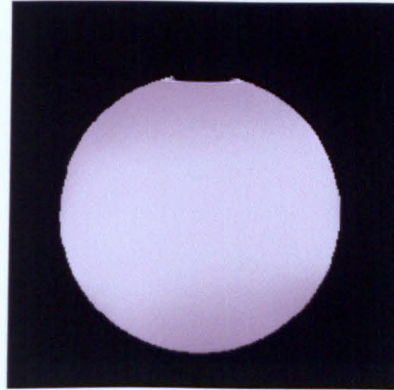
a) normal



b) reversed



c) corrected (method 1)



d) corrected (method 2)

**Figure 4.39** New correction methods applied to a multislice volume. Example of an image through a water filled spherical phantom. A coin placed under the RF head coil can be seen to have caused distortion. The frequency encoding gradient of this spin echo spin warp sequence was vertical. c) shows an image corrected using the first new volume correction method. d) shows an image corrected using the second new volume correction method.

**Figure 4.40** Comparison of the mean absolute distortion per slice measured using various reversed gradient correction methods. 'Error bars' represent the spread of distortion throughout that slice. Transaxial slices through a spherical water phantom. A coin was placed under the RF head coil to create additional distortion. Acquired on the Vision MR scanner. Spin echo, spin warp sequence, 130 Hz per pixel.

**Figure 4.40a**

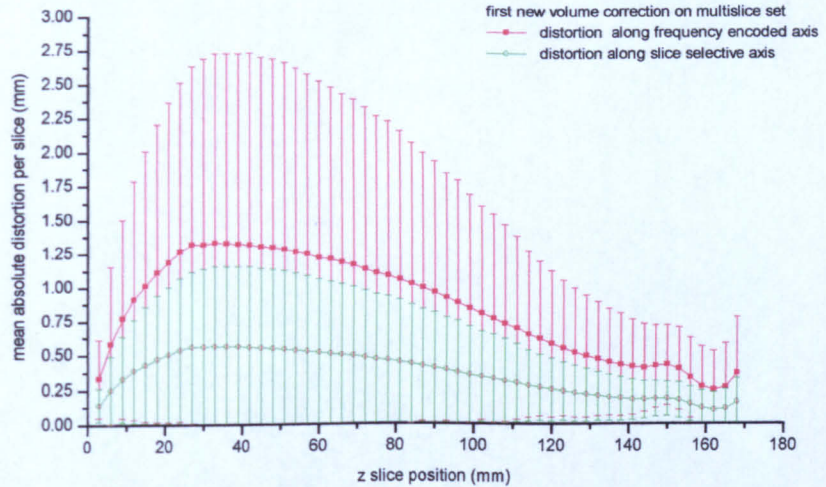


**Figure 4.40b**

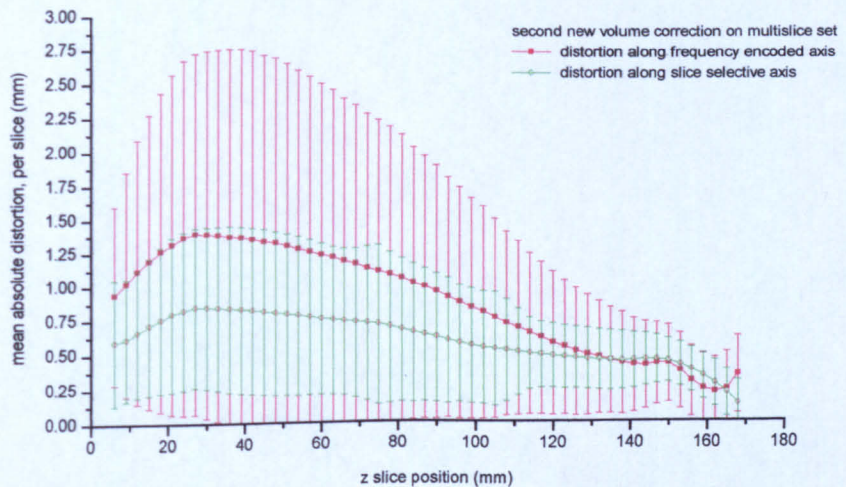
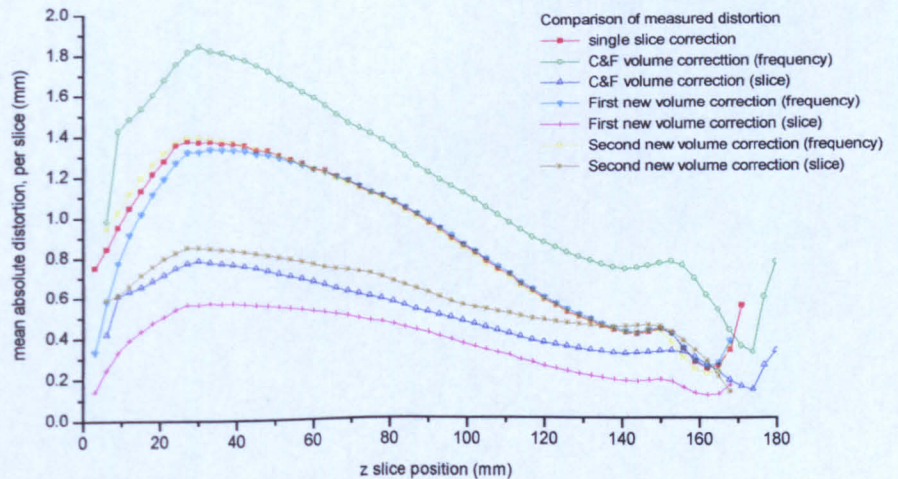


**Figure 4.40c**



## 4. Spatial Distortion in MRI

---

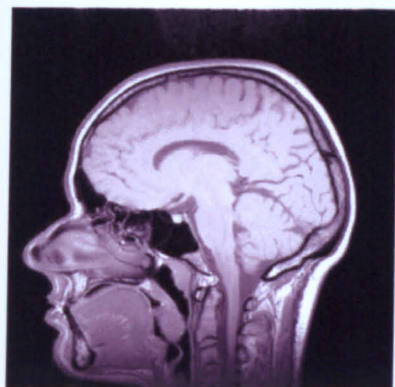
The method also was applied to images of a volunteer's head, again using the same data as in Section 4.3.5. The corrected images are shown in Figure 4.41, and a graph of the mean absolute distortion shown in Figure 4.42. In this case, streaking artefacts are seen in the corrected image, although the gross shape of the head has been corrected. The source of these was not immediately obvious, especially as they were not present in the corrected images of the spherical water phantom. The source of this artefact is explored in the next section (Section 4.7.2).

Although this method appears to be initially attractive from a theoretical point of view, in practice it introduces unacceptable artefacts into the corrected images. However, as discussed in the following section, these artefacts do not affect the calculated values of distortion in either the  $x$  or  $z$  directions, as they do not depend on the differential cross terms of the Jacobian. Its use appears to be valid to calculate the amount of distortion present throughout an image volume.

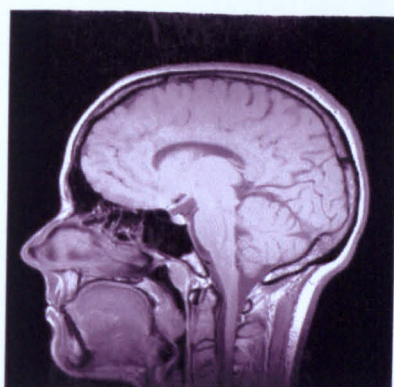
### 4.7.2 New Volume Correction Method Two

As mentioned above, in order to correct a MR image volume, the relationship between the distorted and undistorted coordinates along the frequency encoded and slice selective axes must be found. One new method was outlined in Section 4.7.1 above, which calculated the relationship along the slice selective axis from that measured along the frequency encoded axis. Another approach is to measure both relationships separately, and this is the basis for the second new volume correction method described here.

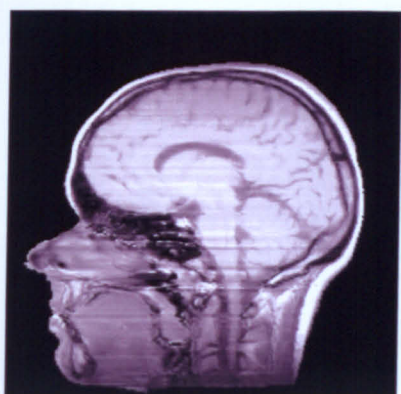
Three contiguous multislice MR image volumes are acquired, the first,  $i_1$ , under normal gradient conditions, the second,  $i_2$ , with the opposite polarity of frequency encoding gradient relative to  $i_1$ , and the third,  $i_3$ , with (just) the opposite polarity of slice selective gradient relative to  $i_1$ . Chang & Fitzpatrick's single slice correction on each slice (in image volumes  $i_1$  and  $i_2$ ) yields the relationship between distorted and undistorted coordinates along the frequency encoded axis. The relationship along the slice selective axis is measured as follows.  $i_1$  and  $i_3$  are re-gridded into new volumes,  $i'_1$  and  $i'_3$ , in which the in-plane axes are the slice



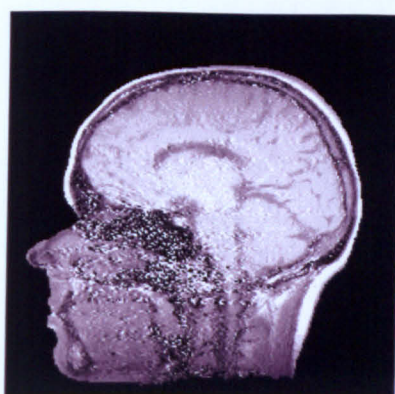
a) normal



b) reversed



c) corrected (method 1)



d) corrected (method 2)

**Figure 4.41** New correction methods applied to multislice volume. Example of an image through a volunteer's head. A coin placed under the RF head coil can be seen to have caused distortion. The frequency encoding gradient of this spin echo spin warp sequence was horizontal. c) shows an image corrected using the first new volume correction method. d) shows an image corrected using the second new volume correction method. Severe artefacts are seen in both corrected images.

**Figure 4.42** Comparison of the mean absolute distortion per slice measured using various reversed gradient correction methods.

'Error bars' represent the spread of distortion throughout that slice.

Sagittal slices through a volunteer's head. A coin was placed under the RF head coil to create additional distortion.

Acquired on the Vision MR scanner. Spin echo, spin warp sequence, 130 Hz per pixel.

**Figure 4.42a**

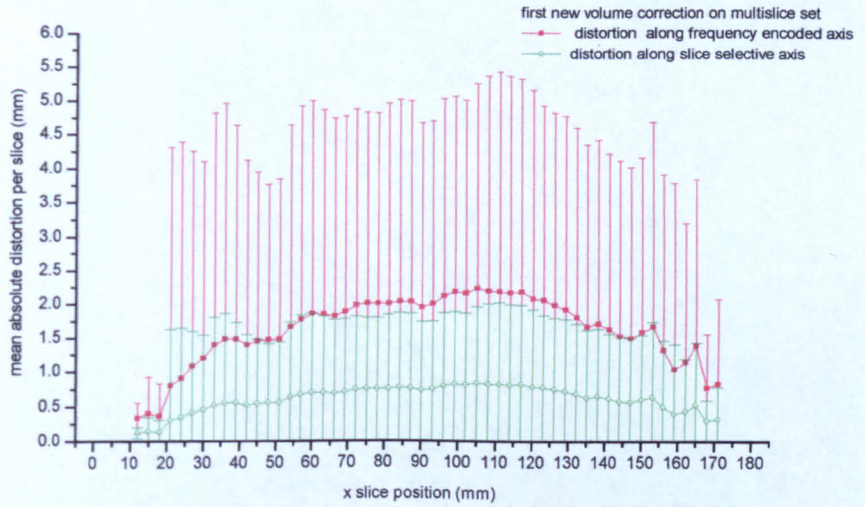


**Figure 4.42b**

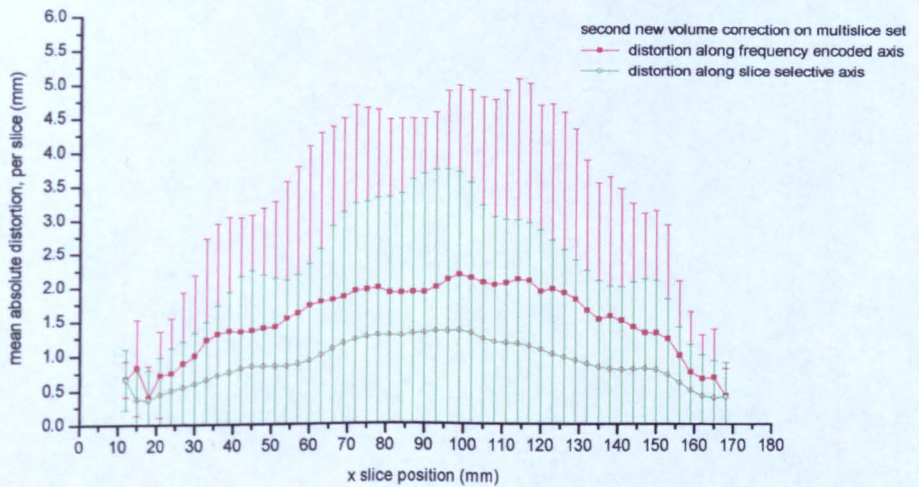
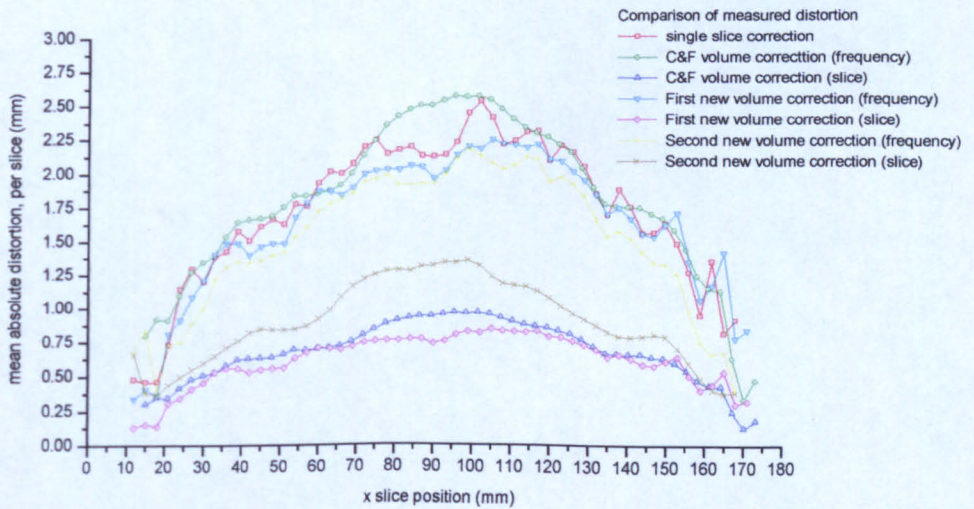


**Figure 4.42c**



#### 4. Spatial Distortion in MRI

---

selective and phase encoding acquisition directions. This may be considered as a rotation of 90° around the phase encoded axis. No interpolation is necessary. Applying Chang & Fitzpatrick's single slice correction to each image in  $i'_1$  and  $i'_3$  along the acquisition slice selective axis (now an in-plane axis in the rotated images), yields the relationship between  $z$  and  $z_1$ .

The two relationships which have been measured are

$$\begin{aligned} x_1 &\equiv X'_1(x, y, z_1) && \text{and} \\ z_1 &\equiv Z'_1(x_1, y, z) \end{aligned} \quad (4.52)$$

as described for the first new volume correction method in Section 4.7.1 above.

However, as for the first new volume correction method, to perform the correction, relationships are required in terms of the undistorted coordinates only, *i.e.*,  $X_1(x, y, z)$  and  $Z_1(x, y, z)$ . Obtaining these from Equation 4.52 is not numerically straightforward. Two methods were implemented, both resulting in the same solution. The first works by assuming  $X_1(x, y, z)$  and  $Z_1(x, y, z)$  are known already, and then using these 'answers' to calculate values of  $X'_1(x, y, z_1)$  and  $Z'_1(x_1, y, z)$ . Equation 4.52 may then be written as

$$x_1 \equiv X'_1(x, y, Z_1(x, y, z)) \quad \text{and} \quad (4.53)$$

$$z_1 \equiv Z'_1(X_1(x, y, z), y, z) \quad (4.54)$$

This describes how to calculate the distorted coordinates if the amount of distortion is known, for each correct coordinate. So long as there is no 'piling over' of signal intensity, there will be a one-to-one mapping between  $(x, y, z)$  and  $(X_1, y, Z_1)$  in Equations 4.53 and 4.54. This can be viewed as, "For a given  $(x, y, z)$ ,  $Z_1(x, y, z)$  will yield  $z_1$  which may be substituted into Equation 4.53 which will yield  $x_1$ . This may be substituted into Equation 4.54, which will yield  $z_1$  which was what we started with." This reasoning can be used to calculate  $X_1(x, y, z)$  and  $Z_1(x, y, z)$  iteratively by inserting starting 'guess' values of  $X_1(x, y, z)$  and  $Z_1(x, y, z)$  into Equalities 4.53 and 4.54 to calculate new estimates of  $X_1(x, y, z)$  and  $Z_1(x, y, z)$ . These are substituted back into Equalities 4.53 and 4.54 until they converge to fixed values. The starting values used in practice were  $x$  and  $z$ . Once the solution has been found for all voxels within

## 4. Spatial Distortion in MRI

---

the image volume, the corrected image maybe be constructed, as described in Section 4.7.1 above.

This new correction method was implemented in the correction computer program. Its implementation involved a considerable amount of interpolation to find values at fractional pixel positions within arrays; a choice of bilinear or sinc interpolation was given. The MR image acquisition time is 1.5 times that for either of Chang & Fitzpatrick's correction methods, and the post-processing time similar to that for their volume correction.

Results from a spherical phantom are presented in Figure 4.39d. Similar images were used as those described in Section 4.3.5 above. Graphs showing the calculated mean absolute distortion per slice are shown in Figure 4.40. Good correction is observed. The mean absolute distortion calculated by this method shows good agreement with the distortion calculated by Chang & Fitzpatrick's single slice method.

Figure 4.40c shows a comparison of the distortion measured by both of Chang & Fitzpatrick's correction methods, and the two new methods proposed here. A difference is seen between the distortion measured in the slice selective direction by this new method, compared to that measured by the first new volume correction method and Chang & Fitzpatrick's volume correction method. This is believed to be due to an offset in all the measured distortion values as is shown in Figure 4.10d. The second new volume correction method measured the  $z$  distortion directly, hence including this offset in an unscaled form. The other methods calculate the  $z$  distortion from the scaling of distortion calculated along other axes, this scaling includes a scaling down of the offset.

The method was also applied to images of a volunteer's head, again using similar acquisitions as in Section 4.3.5. The corrected images are shown in Figure 4.41d, and a graph of the mean absolute distortion shown in Figure 4.42. Again, serious spike artefacts are seen in the corrected image, although the gross shape of the head has been corrected.

A step by step analysis of the numerical calculations of both new correction methods revealed that the artefacts were caused by occasional large values of the Jacobian, and in particular, large values in the  $\frac{dx_1}{dz}$  and  $\frac{dz_1}{dx}$  terms. These

#### 4. Spatial Distortion in MRI

---

	x-1	x	x+1
z-1	121.208900	121.411858	121.614822
z	121.583260	122.119614	122.397278
z+1	94.606422	94.930908	95.524117

Table 4.1: Values of  $X_1$  centred around corrupt point  $x=106, y=106, z=32$

large values occurred mainly around regions of changing contrast in the image. By studying the correction of these regions in particular, it was observed that the large values were due to a misalignment between the calculated  $x_1$  values between adjacent images. When the finite difference between two  $x_1$  values in two adjacent images (*i.e.*, calculating how  $x_1$  varied with  $z$ ) was calculated to evaluate the differential, erroneously large values could occur. This is demonstrated by way of an example from the head data set, centred around an observed spike at  $(x=106, y=106, z=32)$ . Table 4.1 shows calculated values of  $X_1$ .  $\frac{dX_1}{dx}$  gives a reasonable value at  $(106, 106, 32)$ , *i.e.*, of the order of one, as well as at all other coordinates. However,  $\frac{dX_1}{dz}$  has a large absolute value of 13.24. This will result in an intensity artefact in the corrected image. The values of  $X_1$  at the beginning and end of these rows give expected results, (*e.g.*,  $X_1(0, y, z)=0$  and  $X_1(255, y, z)=255$ , for a  $256 \times 256$  image) and the success of the single slice reversed gradient correction on individual images suggests that correct values of  $X_1$  are being calculated, as indexed by  $x$ . The problem appears to lie when comparing values of  $X_1$  between adjacent slices (*i.e.*,  $X_1$  indexed by  $z$ ); at certain positions there is a mismatch, or offset, in  $X_1$  between adjacent slices. This could be caused by an edge detection mismatch between adjacent slices or an accumulated error in the integration from noise which affects different slices differently. This could be due to different structures coming in or out of view as one steps through the slices, or the changing shape of a structure with slice position causing problems (*e.g.*, at the edge of a nasal cavity). Varying the threshold value used for edge detection changes the position of the corrupted points, but does not greatly affect their frequency of occurrence. Errors also may be introduced by the repeated application of interpolation to obtain values at fractional pixel positions in the various arrays. This also explains why there

## 4. Spatial Distortion in MRI

---

does not appear to be any corrupt points in the corrected images of the spherical phantom, produced using both new correction methods, as the phantom contains no structures of varying contrast, nor a rapid change in edge position in any direction.

This artefact is analogous to the mis-translation of intensity to the centre of regions of low signal intensity in the corrected image, as observed in the single slice correction (see Section 4.3.4). The artefact observed in both new methods appears to be a result of the single slice correction artefact occurring in different places in adjacent slices, causing a discontinuity when considering the change in distortion in the  $x$  direction with  $z$ , and *vice versa*. This will be most apparent when calculating the Jacobian term described in Equation 4.51, as this requires calculating changes in  $X_1$  with  $z$ , and  $Z_1$  with  $x$ . No solution could be found to overcome this problem.

The practical application of the second new volume correction method also leads to unacceptable artefacts in the corrected images. Once again, these artefacts are not present in the measured pixel by pixel distortion maps (as these are in terms of  $x_1-x$  and  $z_1-z$ ; no cross-terms are required), and so this method may be used to characterize the spatial distortion along both the frequency and slice selective axes.

## 4.8 Conclusions

The work presented in this chapter has summarized the theoretical background of spatial distortion in MR images. Both the reversed gradient and phase map correction schemes have been described. The single slice and volume reversed gradient correction methods, initially proposed by Chang & Fitzpatrick, have been implemented and verified on phantoms and human volunteers. It was decided that the volume correction introduced unacceptable amounts of artefacts, and would not be used further.

A comparison between the reversed gradient and phase map correction methods was undertaken, using a computer simulation of an EPI acquisition. It concluded that the phase map correction method performed better than the reversed gradient method in cases of partial coverage of  $k$  space and for acquisitions not

#### 4. Spatial Distortion in MRI

---

making use of a spin echo. Both methods performed equally in the case of noisy data, increasing levels of inhomogeneous magnetic field, and in full  $k$  space acquisitions making use of a spin echo. The source and nature of any artefacts seen in the corrected images was explored.

The reversed gradient correction method was used to measure distortion caused by typical MR compatible aluminium apparatus needed when imaging patients undergoing stereotactic neurological procedures. Full Fourier spin echo image acquisitions were used throughout. The advantage of using the reversed gradient correction method is that it may be modified to allow correction of several unconnected objects within an image. This modification was implemented, as it will be required when imaging stereotactic patients, as the fiducial rods are separate from the head. It was found that the presence of the GTC head ring caused a detectable, but small, increase in overall distortion in slices close to it. Pins, which may be used to attach a stereotactic head ring to a patient's skull, were found to cause large amounts of local distortion, but the effect decreased rapidly with increasing distance from the pin. It was concluded that in normal use, the distortion from the pins would not contribute noticeable amounts of distortion to critical structures in the brain or stereotactic fiducial rods.

The reversed gradient correction was applied to EPI, in fields other than imaging for stereotactic planning. Spatial distortion is a particular problem when registration between EP images is required. Two cases which require this are the construction of ADC maps, and BOLD functional MRI. The reversed gradient correction method was successfully applied to the correction of images prior to the construction of ADC maps, which greatly reduced the amount of artefact in the final result, both due to the diffusion weighting gradients and the distortion inherent in EPI. It was also successfully applied to correct the distortion present in the fMRI activation maps, although little spatial difference was observed between the corrected and uncorrected maps.

Two modifications to the reversed gradient correction method were proposed, with the aim of characterizing and correcting distortion in volume MR image sets, but without the problems of Chang & Fitzpatrick's volume correction. While interesting theoretically, when implemented, it was found that neither method

#### **4. Spatial Distortion in MRI**

---

offered any practical advantages over Chang & Fitzpatrick's volume correction, and both introduced severe artefacts.

The reversed gradient correction method has been implemented successfully. Its strengths and weakness have been explored, and its use in characterizing distortion in MR images used for stereotactic planning validated.

# Chapter 5

## Quantification of Errors in Stereotaxis

### 5.1 Introduction

In Chapter 4 the problem of spatial distortion in general MR imaging was stated. This was addressed by use of two methods for correcting this distortion, in order to produce spatially correct images. The reversed gradient and phase map correction methods also could be used to quantify the initial amount of distortion present, on a pixel by pixel basis.

Another method for calculating the spatial distortion at various points across a MR image is by comparing the coordinates of well defined points in the image against their true positions. This has been a popular, and relatively straightforward, method.<sup>17,73,74,100</sup> However, its direct use to state the uncertainty in the final three dimensional stereotactic target coordinate is incorrect. As explained qualitatively in Chapter 3 and quantitatively below, prior to MR imaging of a stereotactic patient, a helmet of fiducial rods arranged in 'N' configurations, is attached to a head ring, which has previously been rigidly attached to the patient's skull. The rods appear in the MR image, and are used to define the plane of the image, relative to the head ring. This allows any two dimensional pixel point within the image to be transformed to a three dimensional point, relative to the head ring. As the positions of both the fiducial rods used to calculate this

## 5. Quantification of Errors in Stereotaxis

---

transform, and any pixel point throughout the image, may be distorted, this could result in an already distorted point being transformed by an erroneous transform. The relationship between spatial distortion of pixels in the MR image, and the error on the final stereotactic target coordinate calculated from this image, is not obvious. Empirical exploration of this relationship is one of the subjects of this chapter.

Once a method to quantify the distortion in the stereotactic MR images has been implemented, it may also be used to identify the source of the distortion observed. This process is performed later in this chapter, to examine the effects of MR scanner, GTC stereotactic head ring, and imaging parameters, on the distortion.

There would appear to be three main methods to quantify distortion in the final stereotactic coordinate: mathematical analysis, use of a phantom of known dimensions, and comparison of points in a patient's head in both MR and CT images, after image registration. The latter method would appear to be the most direct method, as it includes distortions caused by magnetic susceptibility differences within the patient's head, and has been used in by a number of studies.<sup>27,42</sup> However, it depends on being able to identify the same anatomical points in both CT and MR images; the difference in their coordinates after a stereotactic transform, is taken as a measure of distortion at that point. Identification of these points is not trivial, and points taken are typically in the distal portions of the head, or inferior regions of the head.<sup>27,42,75</sup> It is felt that this method, using a number of user defined anatomical points, has a number of weaknesses which make it unsuitable for accurate characterization of spatial distortion. Firstly, it is difficult to find or define anatomical points within the brain which can be located precisely on both CT and MR images. The delineation of the same anatomy in CT and MR images would not necessarily be expected to be in the same spatial location, as contrast in each imaging modality is due to different mechanisms and physical properties. Also, due to repositioning of the patient on each scanner, the images would not be acquired in exactly the same plane or orientation, resulting in partial volume effects, which would introduce errors in identifying points, especially in through-slice dimension. Use of user

## 5. Quantification of Errors in Stereotaxis

defined anatomical volumes, rather than points, circumvents some of the problems mentioned above, but introduces another source of error, as it assumes that the distortion is constant across the defined volume. Another weakness in the method of using anatomical points is that there are few points which may be used in the regions of the brain which contains the vast majority of targets for stereotactic neurosurgery. The distal points used are not only usually located in spatially unrepresentative regions of the brain, but also in regions close to tissue-air boundaries, where local distortions in MR images would be expected to be higher than average, due to the large magnetic susceptibility difference between tissue and air, or bone.

The problems with using anatomical points within a patient's head described above were partially overcome during the course of the work presented in this thesis by Sumanaweera *et al.*<sup>107</sup> Glass tubes filled with a copper sulphate solution were inserted into a cadaver's head to the central region of the brain, onto which a stereotactic head ring and fiducial helmet was attached. This was imaged using CT and MR scanners, and the difference between the centres of the glass tubes in the CT and MR images measured. They found the difference between the final stereotactic target coordinates calculated from MR and CT to lie between 1.5 mm and 2.6 mm for the four tubes used. The MR images were acquired on a 1.5 T MR scanner, although the bandwidths per pixel of the gradient echo sequences used were not quoted. While this is a significant improvement on comparison of the positions of normal anatomical points in MR and CT images, the use of a cadaver is not practical or easy to arrange in most MR scanning centres. Only four tubes were inserted into the brain providing only lines along which the MR distortion could be measured, and the lack of information regarding the bandwidth per pixel used for the MR image acquisition, makes it difficult to compare these results with those obtained on other MR scanners.

The main disadvantage in comparing fixed points within a phantom, between MR and CT images, is that it is not completely representative of a human head, and does not allow the distortion to be calculated on a patient by patient basis. However, there is little difficulty in identifying points within each image, and the design of the phantom can allow these points to be distributed throughout the

## 5. Quantification of Errors in Stereotaxis

---

imaged volume. Although partial volume effects are still present in each image, their influence usually can be removed as the physical shape of the phantom is known.

For the reasons outlined above, a comparison of the location of anatomical points, or landmarks, between MR and CT will not be used in this thesis for quantification of distortion; a rigid phantom will be used instead. The mathematical method will be examined in Chapter 6, and the use of a phantom to characterize distortion is the main subject of this chapter. It falls into two main areas. Firstly, the implementation of a method for quantifying the distortion present in the final stereotactic target coordinate is described and its use demonstrated, and secondly the use of this method in the determination of the main sources of the observed distortion is outlined.

### 5.2 Direct Phantom Measurements

A head sized phantom was designed and constructed specifically for this work. It fits directly on to the MR compatible GTC stereotactic head ring, in place of the patient's mouth bite and occipital pad mounting. The MR compatible UCLF or CT BRW fiducial systems may be attached on to the GTC head ring. The apparatus of phantom, GTC head ring, and UCLF fiducial helmet, was imaged using both CT and MR scanners. Any spatial distortion present in the CT images was assumed to be small compared to distortions present in MR images, and so the CT images were assumed to be a spatially correct representation of the apparatus. All fiducial rods and phantom points were identified and transformed to three dimensional coordinates relative to the head ring, using a purpose written computer program. By comparing the CT coordinates to the MR coordinates of the same point in the phantom, the difference between MR and CT at that point could be calculated. This was taken as a measure of the spatial distortion in the MR image, due to the combination of distortion of the fiducial rods and distortion in the phantom. The phantom was designed to allow distortion along three orthogonal axes to be measured. The use of a phantom to quantify errors in all three dimensions of the stereotactic coordinate is rare; the only known case of doing so was reported briefly by Schad *et al.*,<sup>100</sup> using a Riechert-Mundinger

## **5. Quantification of Errors in Stereotaxis**

---

stereotactic system and a 1.5 T Siemens MR scanner. However, both their method and results are sparsely described and they do not appear to have taken their work further.

This section describes the measurement of distortion in this way. At this stage, no attempt to correct for any distortion was made, to allow any effects due to distortion to be identified, and to quantify the 'worst case' errors. Section 5.3 describes the application of this method to the study of the effect of different MR sequences on the spatial distortion, and the quantification of differences between two MR scanners. These results are used to infer possible sources for the measured distortion.

The validity of the phantom used as a substitute for a human head, in so far as causing distortion in MR images is concerned, is examined by using Chang & Fitzpatrick's distortion correction method, as implemented in Chapter 4. A comparison between distortion measured in the head and that measured in the phantom is performed in Section 5.4. A similarity would suggest that the distortion in the final stereotactic target coordinate measured using the phantom would be generally similar to that expected in the head of a patient undergoing stereotactic neurosurgery. This then allows the results of the distortion in the final stereotactic target coordinate measured using the phantom, with the advantages described above, to be quoted as general expected values of distortion in a patient's head. The effect of correcting the distortion present in the MR images on the error in the final target coordinate is also measured.

### **5.2.1 Materials and Method**

The exterior of the phantom consisted of a hollow Perspex cylinder, with an internal diameter of 170 mm and length of 160 mm. The Perspex was 5 mm thick, and the cylinder closed at both ends. During imaging, the long axis of the cylinder was aligned parallel to the inferior-superior axis of a human head being imaged for stereotactic treatment. The superior disc closing the cylinder was removable, attached *via* nylon screws and a water-tight O ring, and containing two large nylon screws to allow filling of the phantom with water. The inferior disc of the cylinder formed part of a Perspex plate which fitted to the same screw

## 5. Quantification of Errors in Stereotaxis

---

fastenings and locator pins in the GTC head ring as a patient would, *via* their mouth bite and occipital pad mounting.

An insert consisting of an arrangement of rods in known, fixed positions was placed into the hollow cylinder. The insert itself was fixed rigidly to the cylinder *via* Perspex locating pins. The remaining volume inside the cylinder was filled with a saline solution of 9% sodium chloride in distilled water. This models a human head better than just water<sup>79</sup> and facilitates the tuning of the RF coil in the MR scanner, when containing the phantom.

In order to minimize distortions created by the phantom itself, it was necessary to construct the phantom using materials with a small magnetic susceptibility difference compared to saline solution. The material also needed to have a sufficiently different density from water to allow good contrast with saline in CT images. Preliminary experiments were performed on a variety of materials. Cylindrical samples were fixed upright to the base of a large glass beaker filled with saline. This was then imaged on a x-ray machine (a radiotherapy simulator, at the Nottingham City hospital) with 120 kV<sub>p</sub> x-rays, and coronally using an EPI sequence on the 0.5 T MR scanner at the University of Nottingham. The CT scanner at the Queen's Medical Centre University hospital, used for imaging stereotactic patients, uses x-rays with a peak energy of 120 kV. The contrast of each material on the x-ray radiograph was measured using a film densitometer. The materials were ranked for their magnetic susceptibility difference from saline by measuring the amount that each circle distorted into the expected arrowhead shape in the coronal MR images<sup>62</sup> (by measuring the number of pixels between the edge of an overlaid circle and the peak of the arrowhead). Delrin\* was found to exhibit no measurable distortion and had good x-ray contrast, and therefore was used to construct the phantom insert.

To try to simulate the human head, the phantom insert was designed so that the bulk of the phantom volume would be saline. Straight solid rods would provide fixed positions within the phantom, being identified by their lack of signal in MR images. The insert was designed to be imaged by a wide range of MR imaging techniques, including traditional spin warp and EPI techniques. In order

---

\*An acetal resin (DuPont)

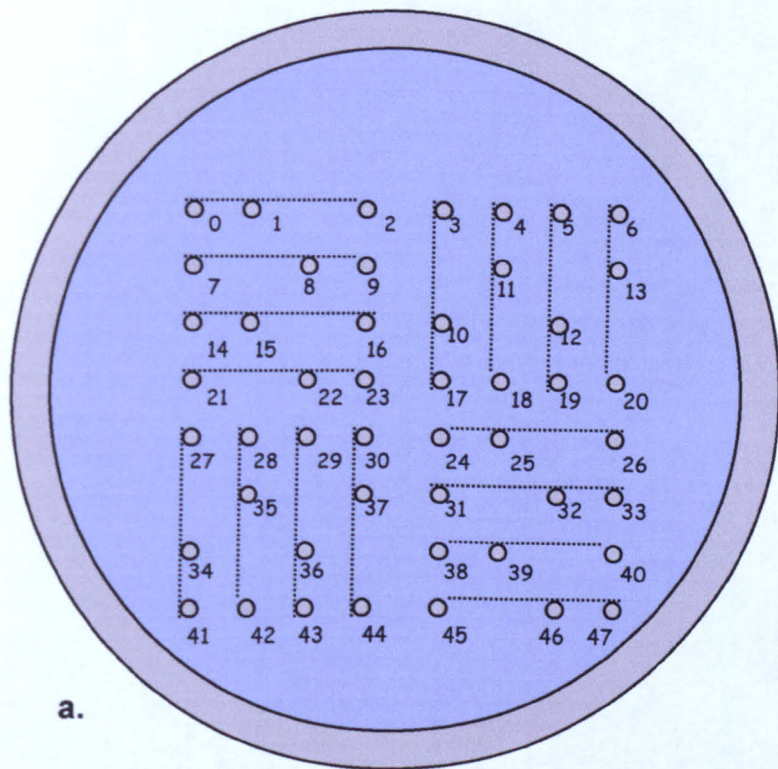
## 5. Quantification of Errors in Stereotaxis

---

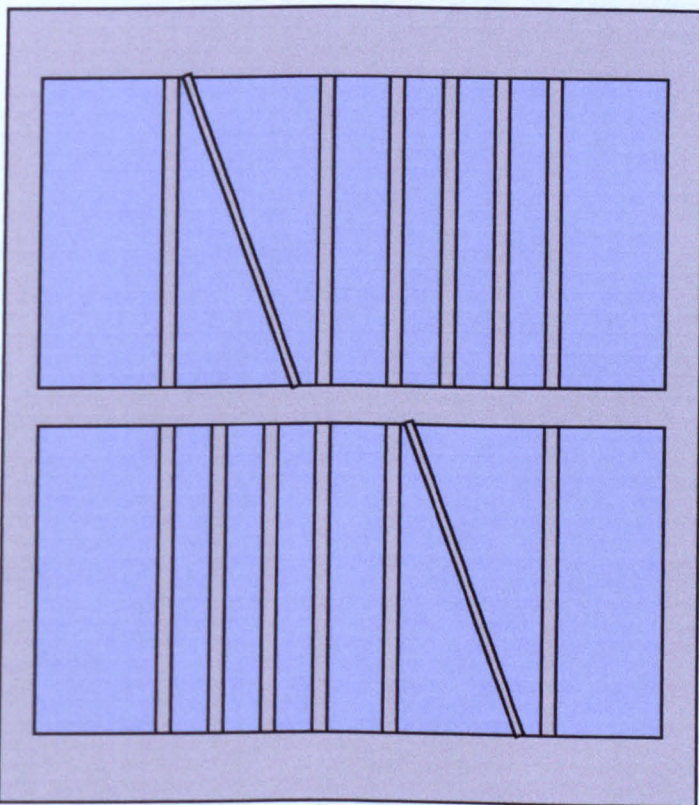
for the rods to be clearly visualized on images acquired at low resolution, 5 mm diameter rods were used. It was assumed that the phantom would be imaged in transverse, or near transverse, sections. In order to measure distortion in the through-slice direction, as well as the in-plane directions, rods were positioned in groups of three, in 'N' configurations, similar to those in the fiducial helmet. The two parallel rods were positioned parallel to the long axis of the cylinder (and hence would be 'cut' perpendicularly by a transverse image slice) with the diagonal rod running in between at an angle of 20° to the parallel rods. This large angle was felt to be necessary in order to allow through-slice differences to be measured to a similar precision to the in-slice differences, even with large pixel sizes. However, in order to span the length of the phantom, while containing as many triads of rods as possible, this required the insert to contain two identical partitions. Each partition spanned a length of 55 mm, the remaining length being filled by the Delrin framework supporting the rods. The triads of rods were arranged across the phantom to try to cover as much of the volume as possible. The phantom is shown schematically in Figure 5.1, and completed in Figure 5.2. It is shown attached to the GTC head ring, to which the UCLF fiducial helmet also is attached, in Figure 5.3. This design is different from many phantoms used to measure distortion in MR images in that it consists mainly of water. Many other phantoms used consist of water filled rods separated by air,<sup>73,100</sup> which would not necessarily mimic a human head as well as the phantom presented here.

The GTC head ring is made from aluminium, and is approximately 245 mm wide and 290 mm high, at its outer perimeter, and made from metal of about 17 mm thickness. Its design includes an anterior section, about 100 mm long, where the metal has been removed and replaced by plastic, to reduce the flow of eddy currents around the entire ring, induced in it by the switching of magnetic field gradients of the MR scanner during image acquisition. The screw threads and screws themselves, for attaching the patient or phantom to the head ring are made from stainless steel. There is no metal in the apparatus apart from that supplied on this head ring.

The UCLF fiducial helmet is attached to the GTC head ring using nylon



a.



b.

**Figure 5.1** (a) End on and (b) plan views of stereotactic phantom. The dotted lines indicate triads of rods, with the central rod being the diagonal one. The rods are numbered 0 to 47. The saline solution is colored blue.



**Figure 5.2** Stereotactic phantom attached to MRI compatible GTC head ring.

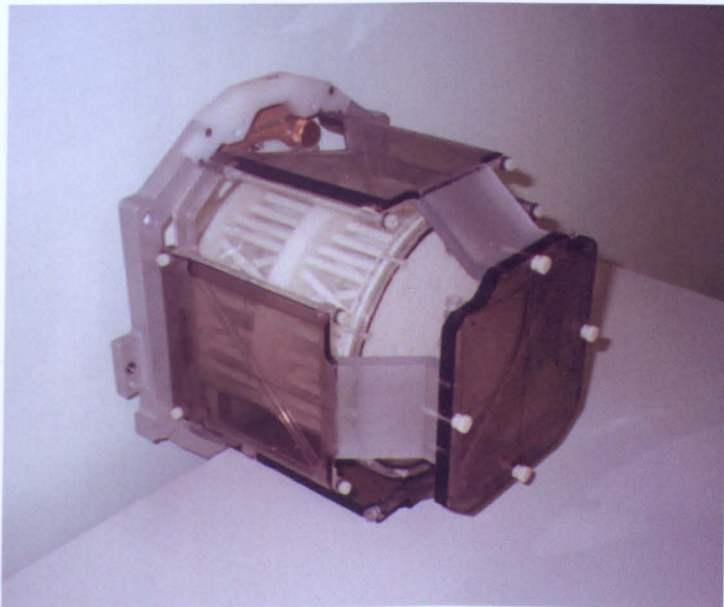


**Figure 5.3** Stereotactic phantom attached to MRI compatible GTC head ring and surrounded by the MRI compatible fiducial system (UCLF).

## 5. Quantification of Errors in Stereotaxis

---

screws. It contains hollow Perspex fiducial rods of 3 mm internal diameter, capped by plastic screws and rubber washers. These were carefully filled prior to imaging by tap water using a syringe and needle. The use of a solution of distilled water and copper sulphate is recommended by the manufacturers, to reduce the  $T_1$  of the solution and hence make it appear brighter on the  $T_1$  weighted images usually acquired for stereotactic planning. However, the  $T_1$  of the hospital's tap water was found to be between 700 ms and 1000 ms at 1.5 T, which resulted in the fiducials appearing with more than adequate contrast in MR images.

The apparatus, consisting of the phantom attached to the GTC head ring, to which the UCLF fiducial helmet was attached, was then imaged. The apparatus was placed on the couch of the CT scanner, or in the quadrature head RF coil of the MR scanner, as if it was a supine patient's head. In the case of the MR scanner, the GTC head ring does not fit within the head coil, and the apparatus was placed inside the head coil as far as possible, with the head ring butted up against the head coil. Transverse image slices were acquired from both modalities. The images covered the apparatus over the length of the fiducial rods in the UCLF; there was no point acquiring images outside this range as pixels in an image could only be transformed to a three dimensional point relative to the head ring if all nine fiducial rods were visible in the image. The apparatus was firmly attached to the scanners' couches by Velcro straps or pads.

The CRW stereotactic system defines an origin in space, being 80 mm superior of the top surface of whichever head ring is used, and in the centre of the head ring (and fiducial helmets) in the lateral and anterior-posterior directions. Unless indicated, this origin was used for all data analysis and for presentation of results below. The CRW origin (marked on the UCLF) was positioned visually, using lasers or focused lights, mounted on the MR scanners, to align with the magnet's isocentre.

CT images were sequentially acquired on a Siemens Somatom Plus scanner at the Queen's Medical Centre, the University hospital in Nottingham, with 120 kV<sub>p</sub> x-rays. They were reconstructed on a 512×512 pixel image matrix by the scanner, which quoted a voxel size of 0.72×0.72×3.00 mm.

MR images were acquired on a Siemens Magnetom Vision 1.5 T scanner using

## 5. Quantification of Errors in Stereotaxis

---

the quadrature head RF coil. A standard full-Fourier spin warp, spin echo imaging sequence was used (using Siemens sequence `se_12b130.wkc`) on a  $256 \times 256$  matrix, with quoted voxel size of  $1.0 \times 1.0 \times 3.0$  mm. The echo time was 12 ms and repetition time 1000 ms; 33 interleaved multisliced images were obtained. This required frequency and maximum phase encoded gradients of  $3.059 \text{ mTm}^{-1}$  and a slice select gradient of  $8.000 \text{ mTm}^{-1}$ . A gap of 0.6 mm (20% of slice thickness) was set between consecutive slices to reduce effects of 'cross talk', the effects of which were observed with smaller slice gaps. The frequency encoded direction was left to right, along  $x$  and the phase encoded direction was parallel to  $y$ . These are typical parameters used to scan patients for neurosurgical stereotaxis, with the exception of the slice gap, which is set to zero.

Images were transferred from both CT and MR scanners to a Hewlett Packard 715/75 Unix workstation via a Siemens' PACSNET and Merge computer, where they arrived encoded in ACR/NEMA version 2.0 image file format.<sup>1</sup> These images were then processed and analysed as described below.

### 5.2.2 Theory and Implementation

In order to calculate the effect of any distortion in the MR images, points throughout the phantom must be identified and transformed from two dimensional pixel coordinates to three dimensional coordinates relative to the head ring, in known units. This must be done for both CT and MR images. A computer program was written to allow semi-automatic user identification of all required points in the images, calculate and perform the transformation, and to calculate the differences in the final three dimensional coordinates, between MR and CT.

All rods appeared in the images as circular or elliptical shapes, depending on their orientation to the imaged slice and contained many pixels. As it was image distortion which was to be measured, it was necessary to reduce as much as possible, or eliminate, any errors associated with identification of the centre of the rod. It is this point which is taken as the position of the rod. If the centre of a rod was chosen by hand, its position could only be selected in units of the dimensions of a pixel, as the centre could be chosen as one pixel, or the next. If the rod is defined in the image by more than one pixel, along each axis, then

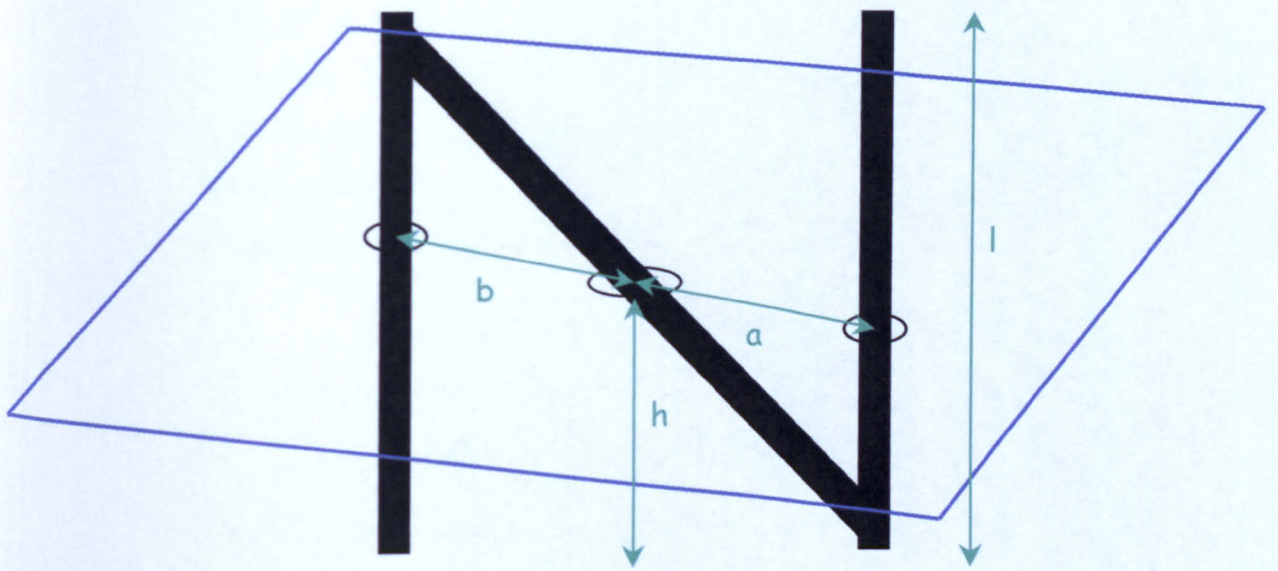
## 5. Quantification of Errors in Stereotaxis

---

a more precise estimate of the centre of the rod may be calculated, by finding its centre of mass (COM).<sup>63</sup> The user's initial estimate of the centre of the particular rod was used to define a square region on the image, large enough to cover a typical rod, but small enough not to include pixels covering adjacent rods. The centre of mass was calculated over this region, using a pixel's intensity as its 'mass', for both in-slice axes. In the MR images of the phantom, rods within the phantom are defined by their lack of signal compared to the surrounding saline; in this case, the pixel intensities within the region were inverted before calculation of the centre of mass. Practically, the centre of mass calculation worked much better if only pixels above a threshold value were included, removing effects of background noise. A level of 10% of the difference between the minimum and maximum pixel values with the region, was used. This is a common technique for identification of fiducial rods in modern stereotactic analysis.<sup>63,69</sup> Assuming no noise or distortion, the centre of mass method will identify the centre of the rod exactly, so long as it is defined by at least two pixels along each axis; even with the addition of noise to the pixel intensities, the centre is still found with an error of much less than a pixel's dimensions. The accuracy of this method is studied in more detail in Chapter 6.

Once the centres of all rods have been identified in an image, the fiducial rods are used to define the plane of the slice, and to construct a transformation matrix to transform any two dimensional pixel within that image to a three dimensional coordinate relative to a fixed origin. The following analysis, based on that described by Lemieux & Wootton,<sup>112</sup> assumes no distortion in the images, allowing the full effects of any distortion in the MR images to be observed.

A rigid body transform must be constructed for each image slice, which will take account of linear scaling, translation, and rotation. As only linear transformations will be considered, three three dimensional points are required to define the plane of the image slice. These are the positions of the three diagonal fiducial rods, one in each triad. The height of a diagonal rod from the base of the fiducial system can be calculated from a consideration of Figure 5.4, regardless of the orientation of the image slice (so long as all fiducial rods are



$$h = \frac{a}{a+b} \times l$$

**Figure 5.4** Calculation of the height of the intersection of a diagonal fiducial rod and the plane of an image by similar triangles. Fiducial rods are black, the image plane is blue, and construction lines are green.

## 5. Quantification of Errors in Stereotaxis

---

completely visualized in the image). That is,

$$h = \frac{a}{a+b} \times l \quad (5.1)$$

from similar triangles. Once the height of the image slice cutting the diagonal rod is known, the in-slice coordinates of that rod can be calculated from a look-up table, or further equations, as the position of all fiducial rods is known. The positions of the fiducial rods in the UCLF, used for these experiments, relative to the CRW origin, are given in millimetres by Equations 5.2. With reference to Figure 5.5, the fiducial rods are numbered clockwise from the lower left, where the rod with the largest diameter is the first rod. Only the diagonal rods are numbered. In each case,  $h_n$  is the height of the  $n^{\text{th}}$  diagonal rod from the base of the fiducial system, calculated using Equation 5.1.

$$\begin{aligned} x_1 &= -100 & y_1 &= -58.5 + h_1 & z_1 &= h_1 - 55 \\ x_2 &= -60 + h_2 & y_2 &= -108.5 & z_2 &= h_2 - 55 \\ x_3 &= 100 & y_3 &= 61.5 + h_3 & z_3 &= h_3 - 55 \end{aligned} \quad (5.2)$$

The three points defining the plane of the image slice are now known. If the in-slice pixel coordinates of the  $n^{\text{th}}$  diagonal rod are  $(X_n, Y_n)$  with corresponding real coordinates, in known units, of  $(x_n, y_n, z_n)$  then the problem is to find the slice transform matrix (STM),  $F$ , where if

$$A = \begin{pmatrix} X_1 & X_2 & X_3 \\ Y_1 & Y_2 & Y_3 \\ 1 & 1 & 1 \end{pmatrix}, \quad \text{and} \quad B = \begin{pmatrix} x_1 & x_2 & x_3 \\ y_1 & y_2 & y_3 \\ z_1 & z_2 & z_3 \end{pmatrix} \quad (5.3)$$

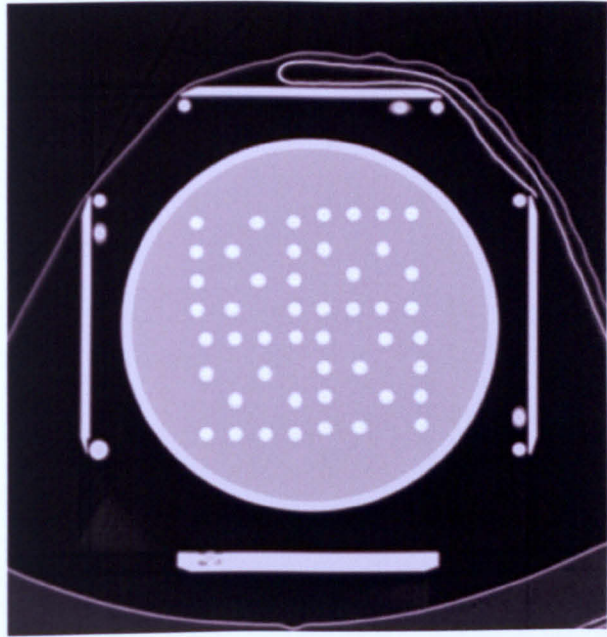
then

$$B = FA \quad (5.4)$$

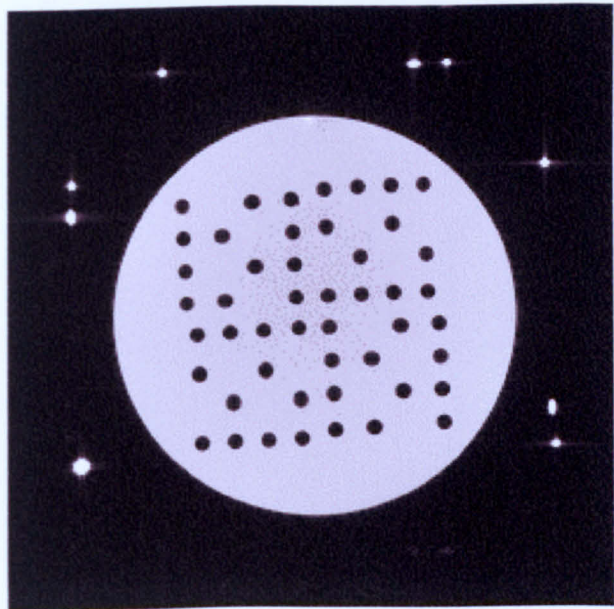
and so

$$F = BA^{-1} \quad (5.5)$$

This gives an exact geometric solution for  $F$ , assuming that  $A$  is non-singular. However, the positions of the two fiducial rods, parallel to each other in each triad, have only been used to find the height of the central diagonal rod. They



a.



b.

**Figure 5.5** Typical (a) CT and (b) MR transverse images of the stereotactic phantom.

## 5. Quantification of Errors in Stereotaxis

---

may also be used to over-determine Equation 5.5; a robust solution may be found using singular value decomposition.<sup>112</sup> These methods have been compared by Lemieux & Jagoe<sup>61</sup> who quantified the reduction in the error in the final coordinate by over-determining Equation 5.5. Their results showed that while the overdetermined STM gave a slightly smaller error on the final target coordinate than the STM calculated from just three fiducial rods, the difference was not statistically significant. For the work presented in this thesis, the method giving an exact solution for F was used, as it is simpler to implement, and should result in a 'worst case' error in the final coordinate. Both methods should be sensitive to the effects of spatial distortion.

The three dimensional coordinates of the position of all rods in the phantom can now be calculated, for both CT and MR images, using the STM. It is highly unlikely that the image slices acquired by CT will exactly overlay those acquired by MR, especially in the through-slice direction. However, as all rods are straight, and it is assumed that there is no distortion in the CT images, then linear interpolation may be used to calculate the coordinate of a CT rod at any particular MR slice position. It is assumed, for ease of the following explanation only, that the  $(x,y,z)$  axes are roughly aligned to the pixel axes  $(X,Y)$  and through-slice axis, and that the parallel rods in the phantom are roughly aligned parallel to the  $z$  axis. Practically, with the GTC head ring butted up against the RF head coil, this was always the case. For any parallel rod, its  $(x_{MR}, y_{MR}, z_{MR})$  coordinate was calculated from MR images. The same rod was identified in two CT images with the closest  $z_{CT}$  to the  $z_{MR}$  in question, and using linear interpolation (or extrapolation if appropriate),  $x_{CT}$  and  $y_{CT}$  calculated at  $z_{MR}$ . The distortion of the rod in the MR image at that point, after stereotactic transform, could then be quantified as  $x_{CT}-x_{MR}$  and  $y_{CT}-y_{MR}$  in millimetres. This was calculated for all 32 parallel rods in the phantom, and used to define the in-slice MR distortion, after stereotactic transform.

The 16 diagonal rods in the phantom were used to calculate the through-slice distortion in a MR image after stereotactic transform, as follows. The equation of a straight line along the diagonal rod was calculated from coordinates from the two CT images used above, giving  $z$  as a function of the ratio of the distance of

## 5. Quantification of Errors in Stereotaxis

---

the diagonal rod between the two surrounding parallel rods in the  $x$ - $y$  plane. This is similar to constructing a calibrated Equation 5.1 for the diagonal phantom rod. The ratio of the distance of the diagonal rod between the two parallel rods from the MR image can then be used in this equation to calculate the  $z$  coordinate of the diagonal rod,  $z_h$ , independently of the STM for the MR image. The difference between this value and the  $z$  coordinate of the diagonal rod calculated using the STM for that MR slice,  $z_{MR}-z_h$  gives a measure of through-slice distortion in the MR image.

As a check of the above process, the mean voxel sizes of both MR and CT images were calculated, using the pixel coordinates and actual coordinates of a number of rods in the phantom, and compared to the voxel size quoted by both scanners. Agreement was to within 1% (where quoted to that precision by the scanner), suggesting that the STM's for all images had been calculated correctly.

For each triad of rods in the phantom, the distortion, relative to CT, could be calculated along three orthogonal directions, allowing a map of the distortion to be constructed throughout the phantom. In order to interpret the large number of results, they were combined in various ways. Each combination attempted to highlight the parameter being measured. It was wished to quantify how the distortion in the final stereotactic target coordinate varied throughout the phantom. There are two sets of axes along which the distortion may be quantified; the physical MR scanner axes  $X$ ,  $Y$ , and  $Z$ , or the axes defined by the head ring,  $x$ ,  $y$ ,  $z$ . By varying the orientation of these axes to each other the major source of distortion may be revealed. If the major source of distortion lies with the head ring and associated apparatus, then imaging it at different locations within the scanner should result in patterns of distortion which move with the apparatus. If the major source of distortion is fixed relative to the scanner with a relatively small contribution from the head ring and apparatus, then imaging the apparatus at different locations should result in distortion patterns which vary with  $X,Y,Z$ , rather than relative to the apparatus.

However, to benefit from this distinction and to allow the sources of distortion to be separated, the apparatus would need to be imaged at different orientations within the scanner. Due to the tight fit of the apparatus in the RF head coil, and

## 5. Quantification of Errors in Stereotaxis

---

its fixed lateral position on the scanner's couch, this is not generally possible. The only direction in which the RF head coil may easily be repositioned is in the through-slice direction. This experiment is performed in Section 5.5, by moving the patient table (onto which the RF head coil containing the phantom apparatus was attached) further in or out of the magnet bore in steps of 50 mm.

As mentioned above, the positioning of the apparatus within the head coil results in the two sets of axes being almost parallel. As such, no distinction will be made between distortion along an axis relative to the scanner, or relative to the head ring. In the following analysis, axes relative to the head ring are used. After being transformed to coordinates relative to the head ring, the data were 're-sliced', or 'binned', into slices orthogonal to the head ring, before being analysed further. This ensured that the analysis was performed with a consistent set of data, although strictly this should not be necessary, as all images were acquired orthogonal to the scanner's axes, *i.e.*, with no tilt.

In order to characterize how the distortion varied along the  $z$  axis, the mean of the absolute value of the distortion for all relevant rods in each slice, was calculated along  $x$ ,  $y$ , and  $z$  axes. To measure the spread of distortion across each slice, the standard deviation of the distribution of the individual distortion of each rod throughout the image was calculated. This gives a measure of the spread of distortion over a slice, and is less affected by rogue points than a consideration of the maximum and minimum distortion would be.

A method for presenting the variation of distortion along the  $x$  and  $y$  axes is not so straightforward, as there are no conveniently defined orthogonal slices (as the transverse images were for the variation along the  $z$  axis) over which the distortion can be averaged. The data were grouped into sagittal and coronal 'slices' according to rod number, and the same analysis was performed to present variations in distortion along the  $x$  and  $y$  axes, as was done for the  $z$  axis above.

### 5.2.3 Results and Discussion

The results were calculated from transverse images acquired on the Siemens Vision MR scanner at the QMC, as described above. Typical transverse CT and MR images acquired of the phantom are shown in Figure 5.5. Figures 5.6, 5.7,

## 5. Quantification of Errors in Stereotaxis

---

and 5.8 show the variation of distortion along all three axes, with  $x$ ,  $y$ , and  $z$  respectively. The origin of the abscissae of the graphs presented in this chapter is that defined by the CRW stereotactic system, defined above. This resulted in the GTC head ring being positioned between  $z=-80$  mm and  $-100$  mm for these three graphs. As the apparatus was prevented from being inserted into the RF head coil beyond a certain distance by the GTC head ring, the centre of the RF head coil was not aligned with the magnetic isocentre, but at  $z=60$  mm.

Figure 5.6 shows the distortion along all three axes, as a function of  $z$  position. Figure 5.6a suggests that the distortion along the  $x$  axis increases with decreasing  $z$  value, *i.e.*, with decreasing distance to the GTC head ring and increasing distance from the magnet's isocentre. The spread of the 'error' bars, representing the range of distortion across each transverse slice, remains fairly constant over the range of  $z$ . This is borne out in Figures 5.6b and 5.6c, which show how the distortion along the  $y$  and  $z$  axes respectively varies along the  $z$  axis. Both graphs are fairly horizontal, suggesting little variation in distortion in the  $y$  and  $z$  directions across the phantom. The absolute values in these last two graphs are smaller than in Figure 5.6a. This correlates with the MR frequency encoded, phase encoded, and slice selected gradients being roughly parallel to the  $x$ ,  $y$ , and  $z$  axes.

Figures 5.7 and 5.8 present the same data as in Figure 5.6, but characterized by variation along the  $y$  and  $x$  directions respectively. All graphs are fairly horizontal, again suggesting that there is little variation in distortion with  $x$  and  $y$  positions within the phantom.

### 5.3 Comparison of MR Sequences and Scanners

In Section 5.2, a method has been presented for measuring and quantifying the distortion in the final three dimensional stereotactic coordinate calculated from MR images, using a phantom. In this section, the method is applied to measurement of the distortion on two MR scanners, both using a variety of MR imaging sequences, and to quantify the differences between these systems.

Two 1.5 T MR scanners are in use at the Queen's Medical Centre in Nottingham, both supplied by Siemens; a Vision, and an older SP model. Their

**Figure 5.6** Variation of distortion in final x, y, & z coordinates along the z axis, calculated from MRI. The absolute difference between CT and MR for each rod in the stereotactic phantom was calculated. The mean for all rods in a transverse slice was calculated and plotted. The error bars are the standard deviation of the distortion across each slice, and are representative of the range of distortion across each slice. The GTC head ring was positioned between z=-80 and -100 mm. Acquired on the Vision MR scanner using sequence *se\_12b130.wkc*

**Figure 5.6a**

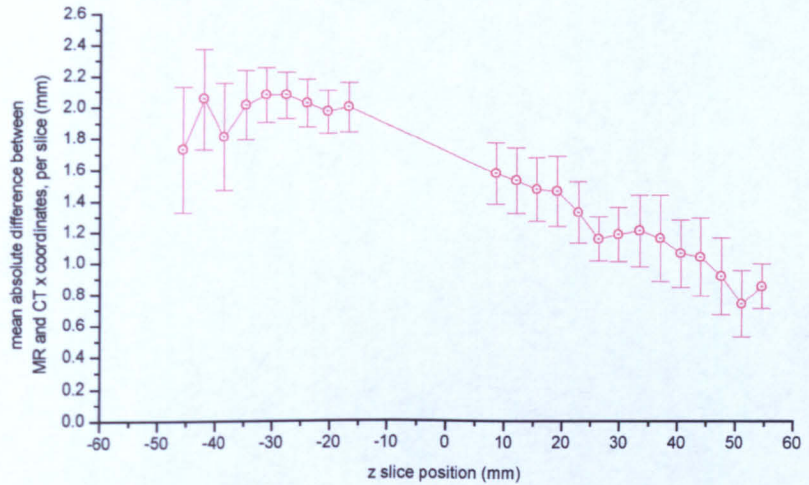


**Figure 5.6b**

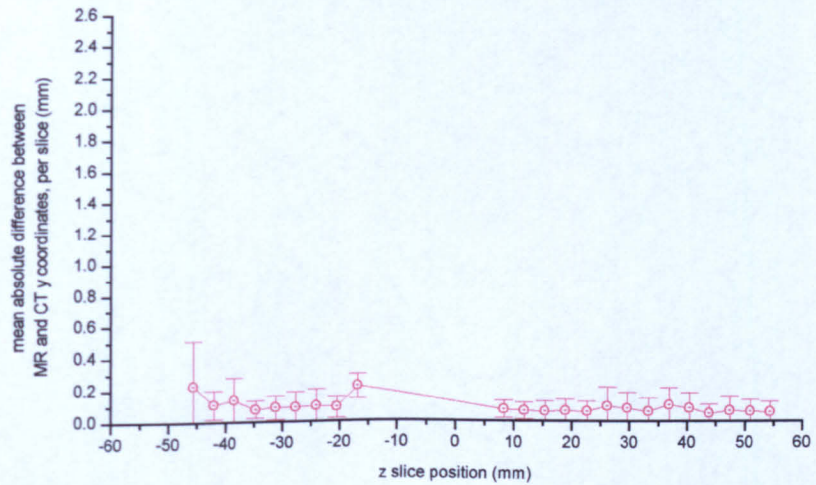


**Figure 5.6c**

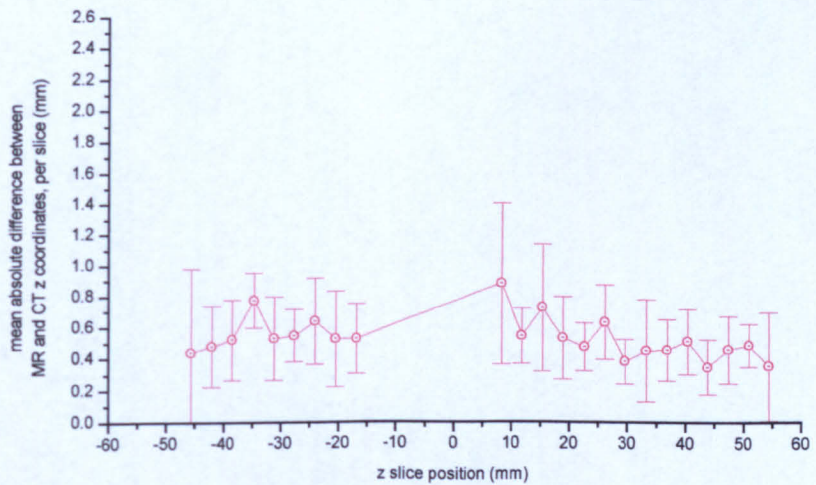


**Figure 5.7** Variation of distortion in final x, y, & z coordinates along the y axis, calculated from MRI.

The absolute difference between CT and MR for each rod in the stereotactic phantom was calculated. The mean for all rods in an interpolated coronal slice was calculated and plotted. The error bars are the standard deviation of the distortion across each slice, and are representative of the range of distortion across each slice.

Acquired on the Vision MR scanner using sequence *se\_12b130.wkc*

**Figure 5.7a**

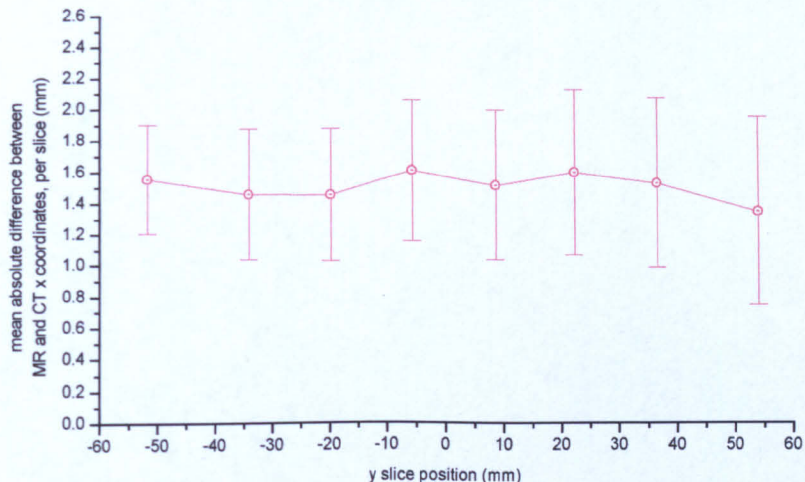


**Figure 5.7b**

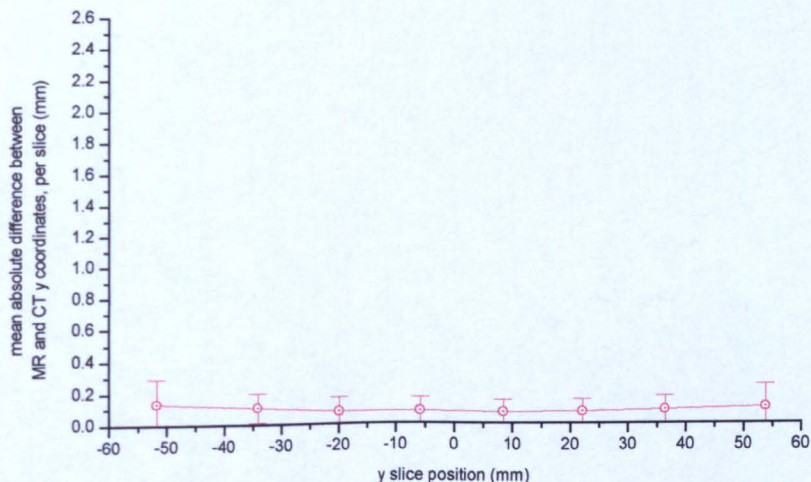


**Figure 5.7c**

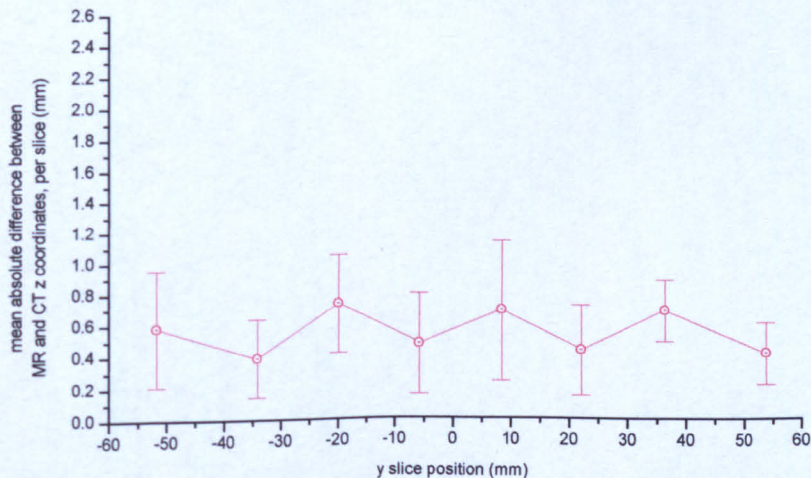


**Figure 5.8** Variation of distortion in final x, y, & z coordinates along the x axis, calculated from MRI. The absolute difference between CT and MR for each rod in the stereotactic phantom was calculated. The mean for all rods in an interpolated sagittal slice was calculated and plotted. The error bars are the standard deviation of the distortion across each slice, and are representative of the range of distortion across each slice. Acquired on the Vision MR scanner using sequence *se\_12b130.wkc*

**Figure 5.8a**

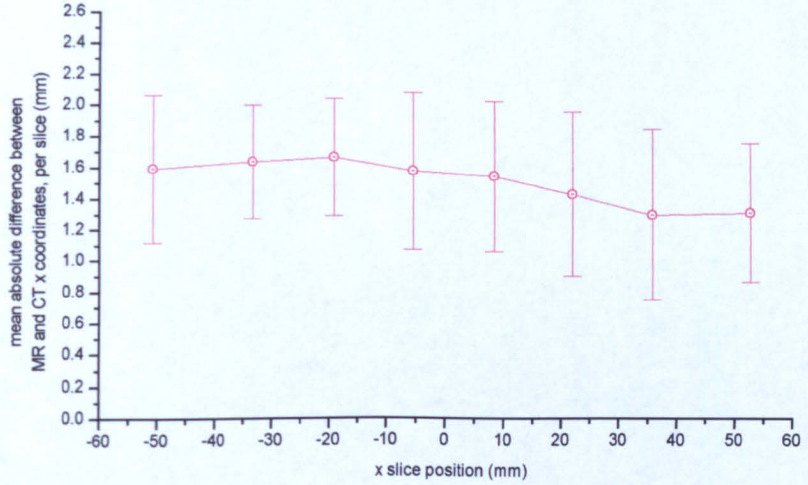


**Figure 5.8b**

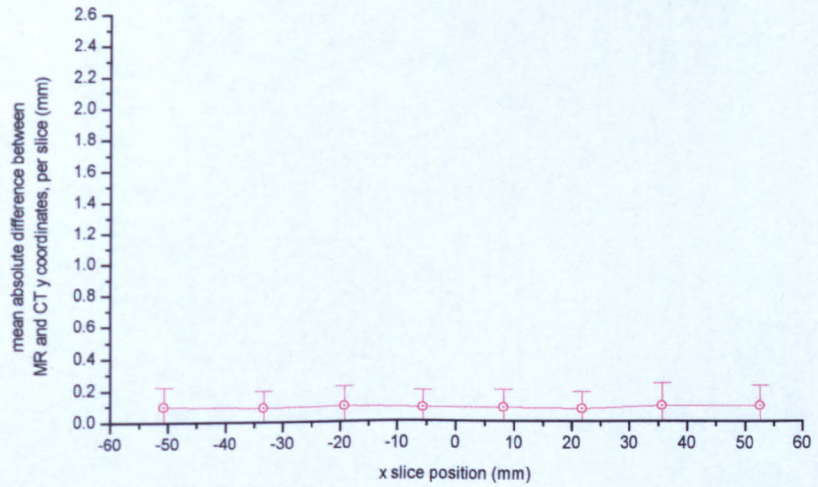
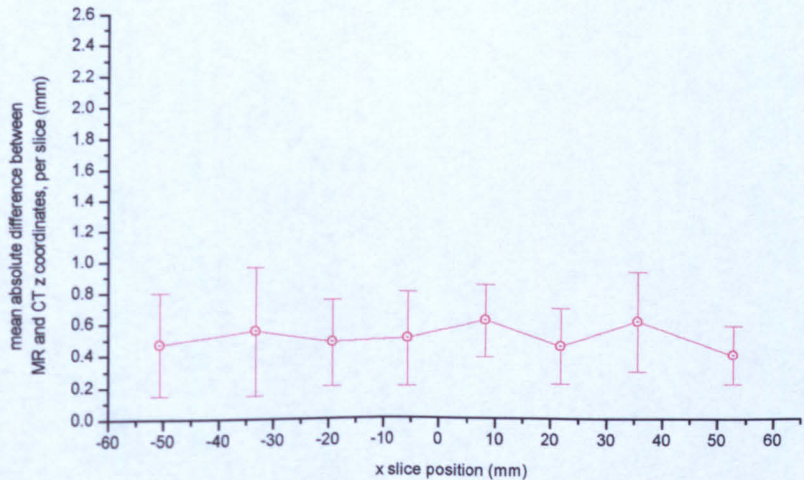


**Figure 5.8c**



## 5. Quantification of Errors in Stereotaxis

---

specifications are briefly described in Section 2.5. At the same magnetic field strength, it would be expected that the amount of distortion caused by magnetic susceptibility mismatches in the subject would be the same, whereas the amount of distortion caused by magnetic field inhomogeneities, and possibly eddy currents, would be scanner dependent.

A variety of scanning sequences are available on both scanners, the details of which are described in Chapter 2. It would be expected that for the same applied magnetic field gradients, and the same bandwidth per pixel, different sequences should cause the same amount of distortion. It also would be expected that the amount distortion would vary with the bandwidth per pixel, as described in Chapter 2, with the regions with highest distortion also expected to show the largest variation with changing bandwidth.

Where appropriate, the use of the results to identify or eliminate possible sources of the observed distortion is discussed.

### 5.3.1 Method

The imaging parameters used for both scanners are as described in Section 5.2.1 above. On the newer Vision scanner the actual gradient strengths are quoted, but the older SP does not provide this information readily. However, from analysis of comparable spin echo sequences available on both scanners (using the same selective RF pulses), it appeared that the same slice select magnetic field gradient was used to obtain the same slice thickness. By selecting the same slice thickness, pixel size, and matrix dimensions, for all the sequences used, it was assumed that the frequency encoded and slice select magnetic gradients should be the same for a fixed bandwidth per pixel, and hence their influence on distortion should be the same. As the apparatus fits tightly into the head RF coil, it can be positioned fairly reproducibly from experiment to experiment; the same is true for patients. Hence the same small field of view can be used for all experiments centred at the  $x$ - $y$  isocentre. In this chapter, the same field of view and image matrix size was used throughout, and no need was seen to characterize the results by varying the field of view with fixed bandwidth per pixel. Transverse images were acquired throughout, relative to the MR scanners' axes.

## 5. Quantification of Errors in Stereotaxis

---

The sequences selected were either multislice two dimensional spin warp, or three dimensional FT variants. In the latter case the entire slab to be imaged was slice selected and phase encoding occurred along both axes perpendicular to the frequency encoded axis. For these sequences, the number of phase encoding steps in the slice select direction was set so that the same number of partitions as there was slices in the multislice case was obtained. Obviously, in this case, there was no slice gap, and the partition thickness was set to be 3.6 mm.

A large number of imaging sequences were pre-installed on the MR scanners by Siemens. Two bandwidths per pixel are common in these; 130 Hz and 195 Hz. For the comparison between sequences and scanners, the choice of sequence was restricted to those with one of these two bandwidths. This limited the choice of sequences to the standard spin echo, FLASH, and FISP for two dimensional multislicing, and FLASH, FISP, and inversion recovery TurboFLASH (denoted 3D MP-RAGE by Siemens) for three dimensional imaging. On the Vision, additional sequences were available, and have been included for comparison with other Vision sequences only, as their counterparts were not generally available on the SP scanner. These included Turbo Spin Echo, TurboFLASH<sup>†</sup>, EPI, GRASE, and HASTE as two dimensional sequences, and in three dimensional form, Turbo Spin Echo, CISS, and DESS. These are described in Chapter 2.

For the comparison between sequences of different bandwidths per pixel, a standard spin warp, spin echo sequence was used on the Vision. Sequences were available with bandwidths of 56 Hz, 65 Hz, 89 Hz, 130 Hz, and 150 Hz, and all of these were used.

The results are presented graphically on the following pages, in the same format as the results presented in Section 5.2.3 above. Only the graphs which show variation of distortion with  $z$  have been included, as from the discussion in Section 5.2.3, it would appear that they are the most representative of the results. The 'error' bars, representing the spread of distortion throughout each slice, have been removed from most of the graphs to aid clarity; they were all of similar magnitude to those in the graphs which do contain the bars.

---

<sup>†</sup>TSE and TurboFLASH sequences were available on the SP scanner, but not with comparable parameters with those available on the Vision

## 5. Quantification of Errors in Stereotaxis

---

Obviously, only images in which all nine fiducial rods were visible could be processed and included in the following results. Their visibility varied between sequences and scanners. Also, due to the design of the phantom, images exhibiting partial volume effects between the saline solution and either the ends of the phantom or the structure supporting the rods, were clearly identifiable. These images were excluded from the following results, as they could result in a rod within the phantom being assigned a misleading position.

A subset of these results were presented at the fifth annual meeting of the International Society for Magnetic Resonance in Medicine in 1997.<sup>77</sup>

### 5.3.2 Results from Bandwidth Comparison and Discussion

The results of the comparison between bandwidths on the Vision is shown in Figure 5.9. The curves are identified by the name of the spin echo sequence used, using Siemens nomenclature. The first few letters represent the sequence type (in this case, se for spin echo) followed by the minimum echo time in milliseconds, then b for bandwidth, followed by the bandwidth per pixel in Hertz. As expected, the sequences with larger bandwidth per pixel result in less distortion. As the distortion increases, with decreasing  $z$ , the difference in distortion between the sequences with difference bandwidth also increases. Although not a strictly valid comparison, as the graphs show the distortion in the final stereotactic coordinate rather than the actual distortion in the MR image, it is interesting to note that for slice position, say  $z = -30$  mm, the ratio of distortion between sequences with bandwidths of 130 Hz and 65 Hz is 1.92, compared with the ratio of their bandwidths which is 2. The relationship between bandwidth per point and spatial distortion is described in Section 4.2. The measured distortion in the  $z$  direction, relative to the distortion in the  $x$  frequency encoded axis, also may be compared to that expected from theory. For the gradient strengths used, it would be expected that the distortion along the  $z$  axis would be  $\frac{3.059}{8.000} = 0.382$  times that along the  $x$  axis, and this also compares well to typical values measured from Figure 5.9.

**Figure 5.9** Variation of distortion in final x, y, & z coordinates along the z axis, with bandwidth per pixel. Comparison between spin echo sequences. Final number in sequence name is the bandwidth per point in Hertz. Acquired on the Vision MR scanner.

**Figure 5.9a**

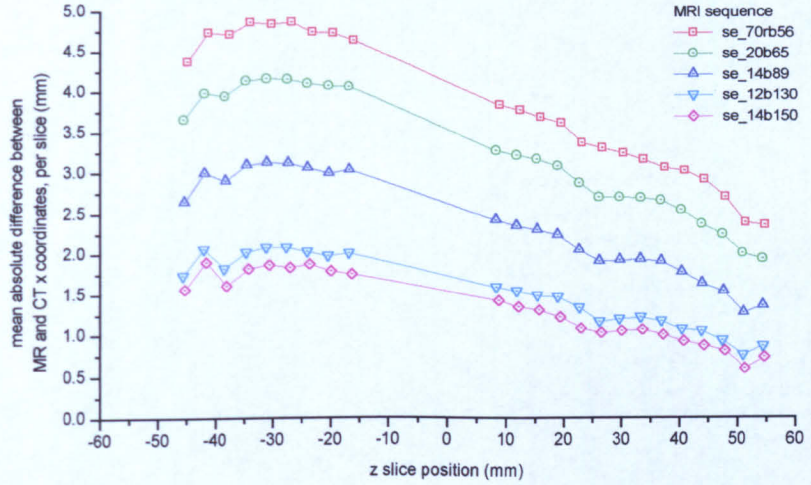


**Figure 5.9b**

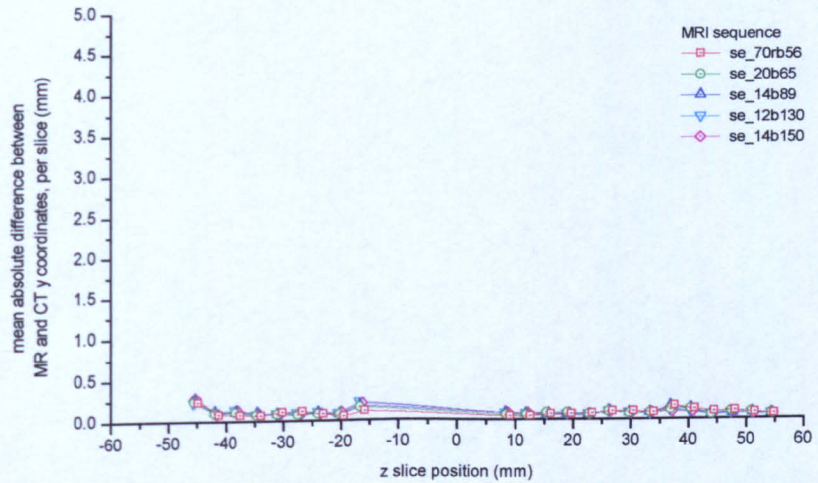
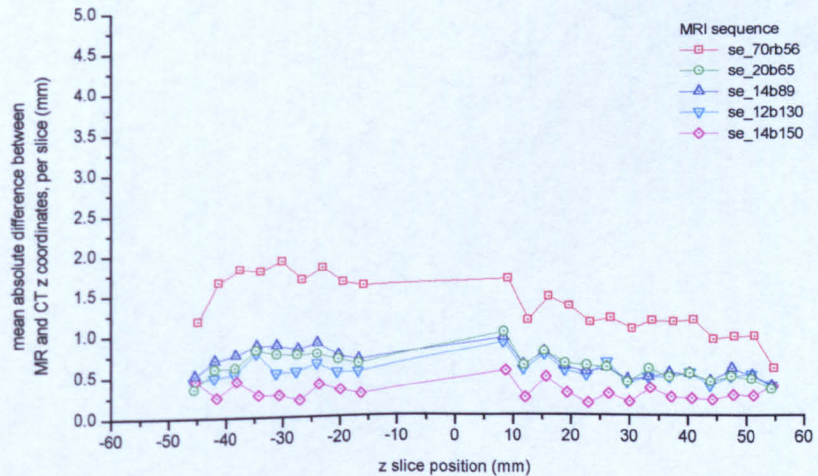


**Figure 5.9c**



### 5.3.3 Results from Scanner Comparison and Discussion

The results of the comparison between the Vision and SP MR scanners is shown directly in Figure 5.10. Similar, standard spin echo, spin warp sequences on both scanners were used for this comparison, with a bandwidth per point of 130 Hz. The 'error' bars on this graph represent the range of distortion values present across the slice.

The results from both scanners appear very similar. For the Vision, the distortion along the  $x$  frequency encoded direction is larger than for the SP, but this is reversed when considering distortion along the  $y$  phase encoded direction. This difference could be due to slightly different rotational alignment between the phantom apparatus in each scanner. Figure 5.11 shows the result of combining the measured distortion in the  $x$  and  $y$  directions, before finding the absolute mean for each slice, by Pythagorus. The results from both scanners now do not appear to be significantly different from each other. This is reasonable, as both scanners operate at the same nominal main static field strength, and with the same field of views set for image acquisition, the same gradient strengths should have been applied.

Both the main magnets, shims, and gradient coils, are of different designs in the two scanners, with the Vision's main magnet being actively shielded with extra active shims, and different cryogen design, as well as a redesigned gradient set, compared to the unshielded main magnet of the SP, and older shim and gradient technology, resulting in wider tolerances on its magnetic field homogeneity. If the cause of the measured distortion were scanner related magnetic field inhomogeneities or eddy currents, then one would expect a difference between the measured distortion for the Vision and the SP, with the SP probably giving rise to the worst distortion. The similarity between the curves in Figure 5.11 suggests that the main causes of observed distortion are not eddy currents or magnetic field inhomogeneities due to the MR scanner. It would suggest that the sources of distortion lie with the apparatus itself, and further confirmation of this is given by the observation that the distortion increases as the distance to the head ring decreases.

It is also worth noting that both scanners have different RF systems. The

**Figure 5.10** Variation of distortion in final x, y, & z coordinates along the z axis. Comparison between Vision and SP MR scanners. The error bars are the standard deviation of the distortion across each slice, and are representative of the range of distortion across each slice. GTC head ring positioned between z=-80 and -100 mm. Acquired using spin echo, spin warp sequences with 130 Hertz per pixel bandwidth.

**Figure 5.10a**

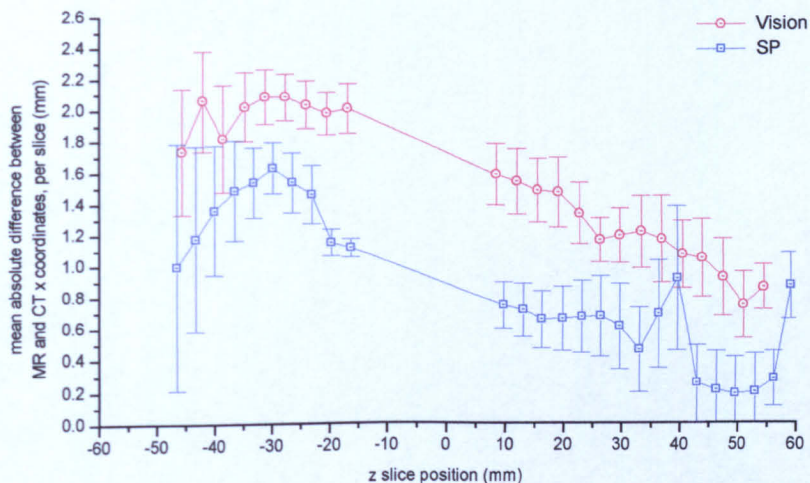


**Figure 5.10b**

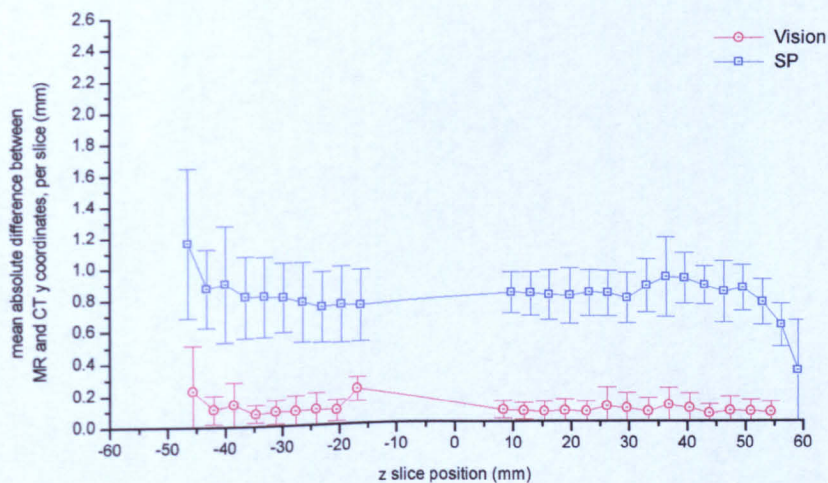


**Figure 5.10c**

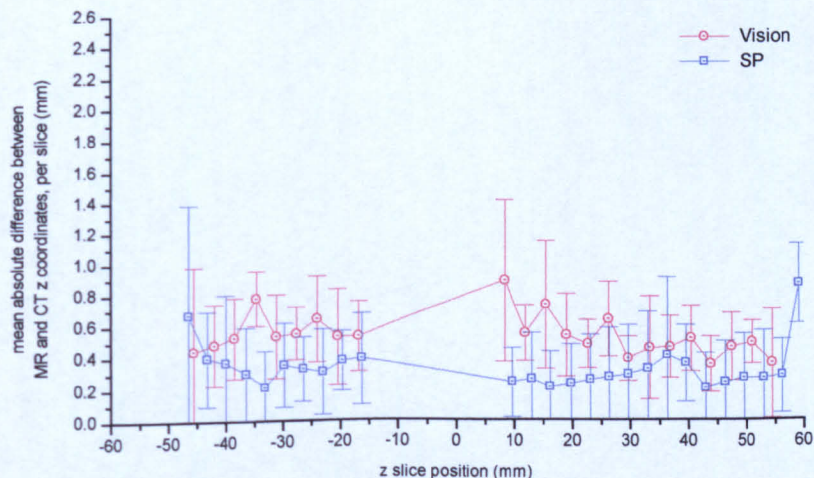


**Figure 5.10** Variation of distortion in final x, y, & z coordinates along the z axis.

Comparison between Vision and SP MR scanners.

The error bars are the standard deviation of the distortion across each slice, and are representative of the range of distortion across each slice.

GTC head ring positioned between z=-80 and -100 mm.

Acquired using spin echo, spin warp sequences with 130 Hertz per pixel bandwidth.

**Figure 5.10a**

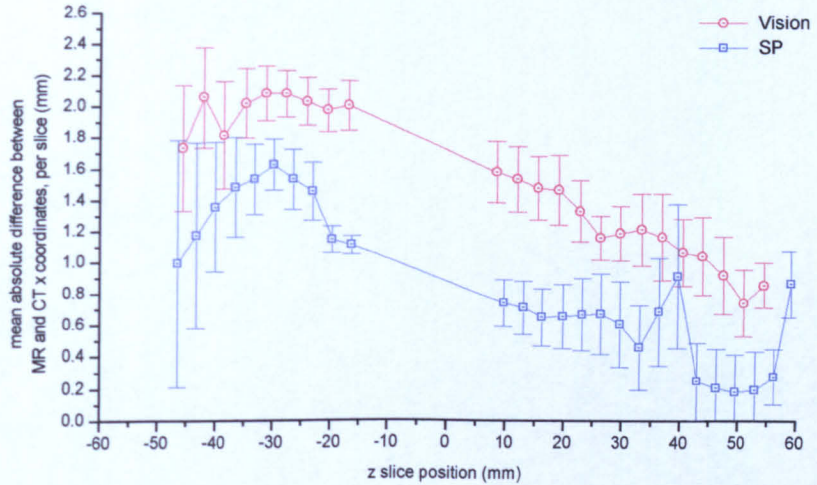


**Figure 5.10b**

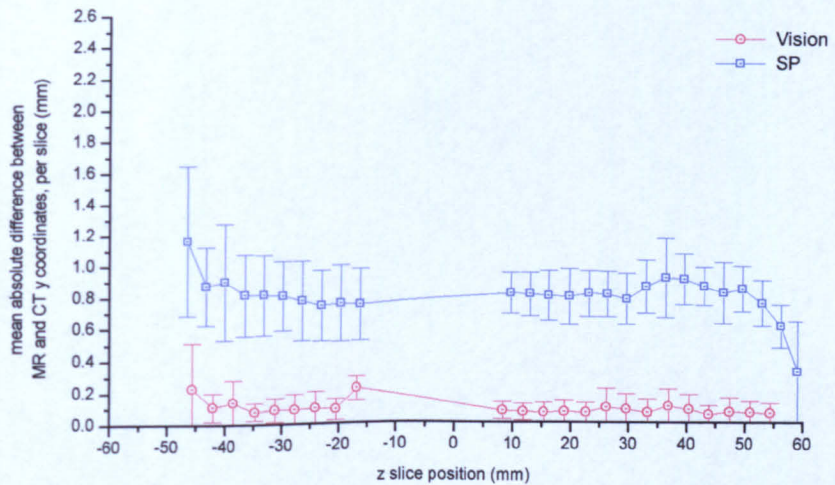


**Figure 5.10c**

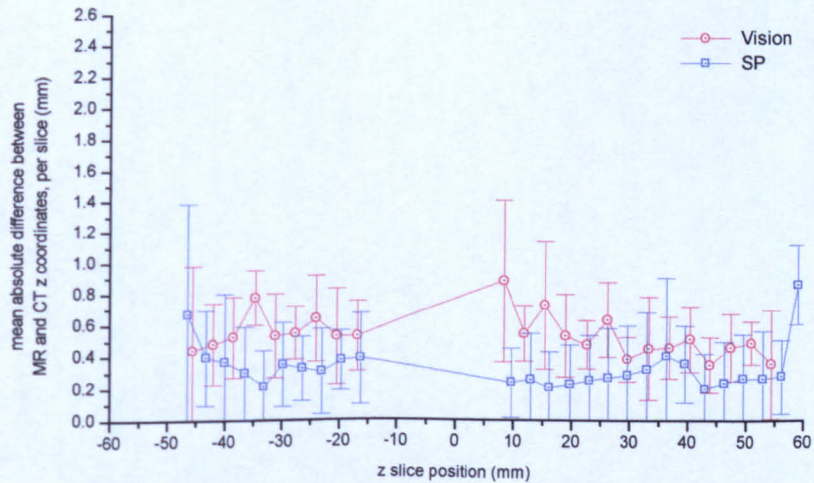
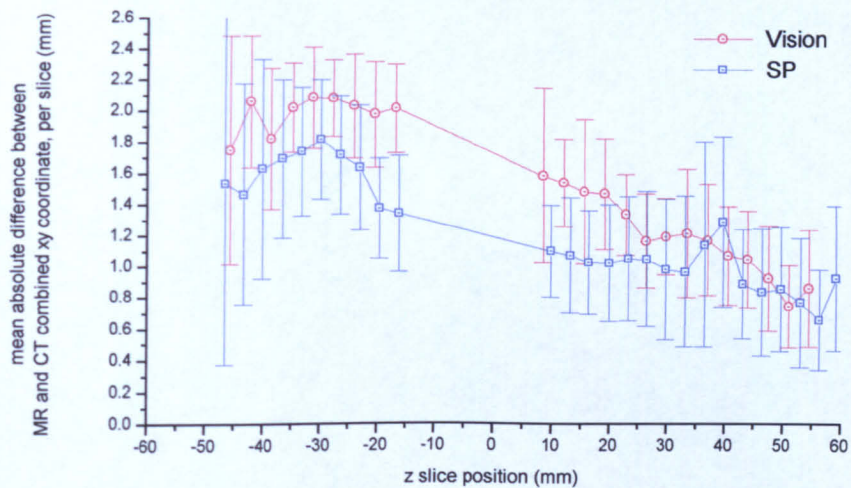


**Figure 5.11** Variation of distortion in final combined xy coordinate along the z axis. Comparison between Vision and SP MR scanners. The error bars are the standard deviation of the distortion across each slice, and are representative of the range of distortion across each slice. GTC head ring positioned between z=-80 and -100 mm. Acquired using spin echo sequences with 130 Hertz per pixel bandwidth.



## 5. Quantification of Errors in Stereotaxis

---

increased distortion with decreasing  $z$  correlates with decreasing distance to the edge of the RF head coil used. It could be argued that the observed increase in distortion depends primarily on this. However, if this were the case, then by the same argument as above, one would expect the different systems to result in differing amount of distortion; this is not seen. In the images acquired on the Vision, no qualitative change in image quality, nor significant quantitative change in SNR, was seen throughout the volume spanned by the fiducial helmet. On the SP, image quality deteriorated more rapidly, to the extent that all nine fiducial rods could not be identified on the few images closest to the edge of the RF coil (and head ring). This shows a clear difference between the RF systems on the two scanners, which is not reflected in difference in the curves in Figure 5.11, suggesting that the position within the RF coil is not a major influence on the distortion being observed.

### 5.3.4 Results from Sequence Comparison and Discussion

The results of the comparison between distortion in images acquired using different sequences on the Vision is shown in Figures 5.12 and 5.13 for sequences with 130 Hz and 195 Hz bandwidth per pixel respectively. The corresponding results from the SP scanner are shown in Figures 5.14 and 5.15 respectively. The curves are identified by the name of the Siemens sequence used. The calculated distortion appears to be fairly independent of the sequence used to acquire it, which is as expected. The effect of bandwidth, and the difference between scanners is therefore the same as discussed in previous two sections, 5.3.2 and 5.3.3. This has an implication for the sequence used to acquire images for stereotactic planning of patients. It appears to be a generally held view among clinicians that more distortion is present in  $T_2$  weighted images than in  $T_1$  weighted images, and hence the former should not be used for stereotactic planning. Many lesions show greater contrast to surrounding tissue in  $T_2$  weighted images than in  $T_1$  weighted images, and so  $T_2$  weighted images would be preferable. From these results, it appears that there is no difference in distortion between  $T_1$  and  $T_2$  weighted images, with the same bandwidth per pixel. The idea that distortion is worse in  $T_2$  weighted images could be due to typical  $T_2$  weighted sequences

**Figure 5.12** Variation of distortion in final x, y, & z coordinates along the z axis, with MR sequence, at constant bandwidth per point. All sequence have 130 Hertz per pixel bandwidth. Acquired on the Vision MR scanner.

**Figure 5.12a**

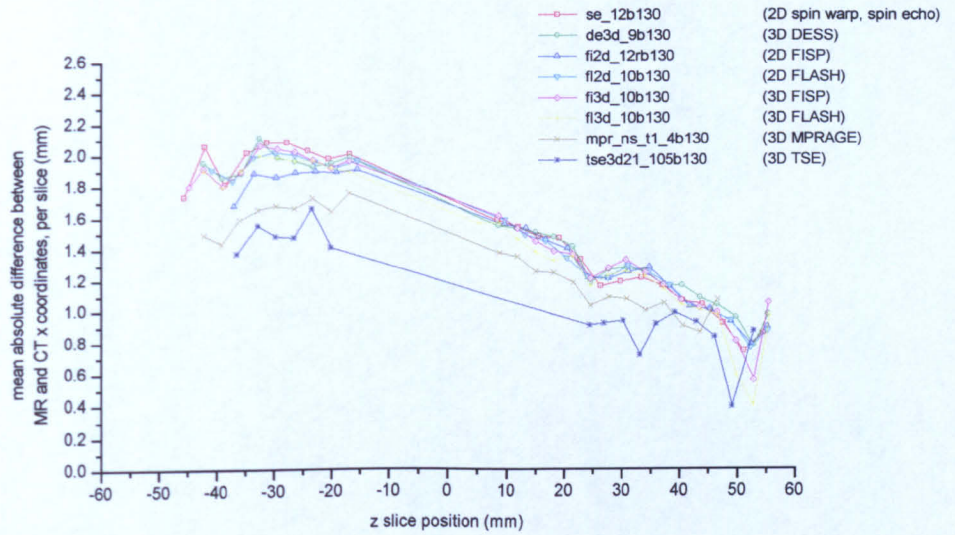


**Figure 5.12b**

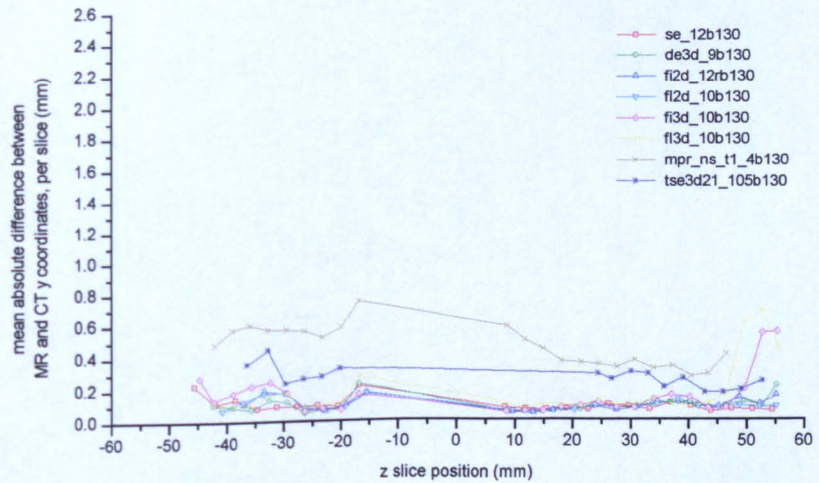


**Figure 5.12c**

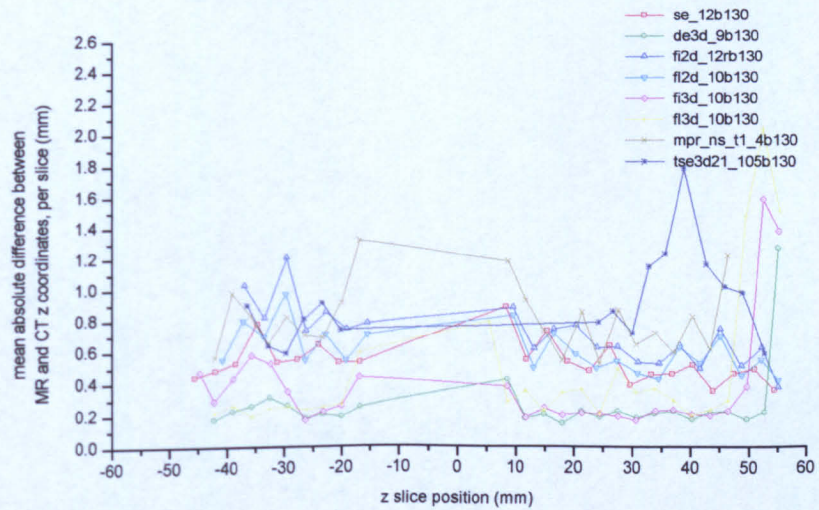


**Figure 5.13** Variation of distortion in final x, y, & z coordinates along the z axis, with MR sequence, at constant bandwidth per point. All sequences have 195 Hz per pixel bandwidth. Acquired on the Vision MR scanner.

**Figure 5.15a**

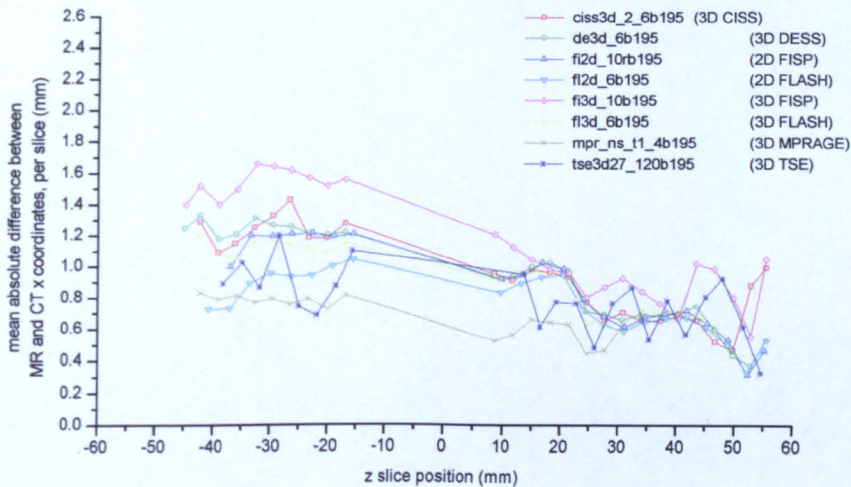


**Figure 5.13b**

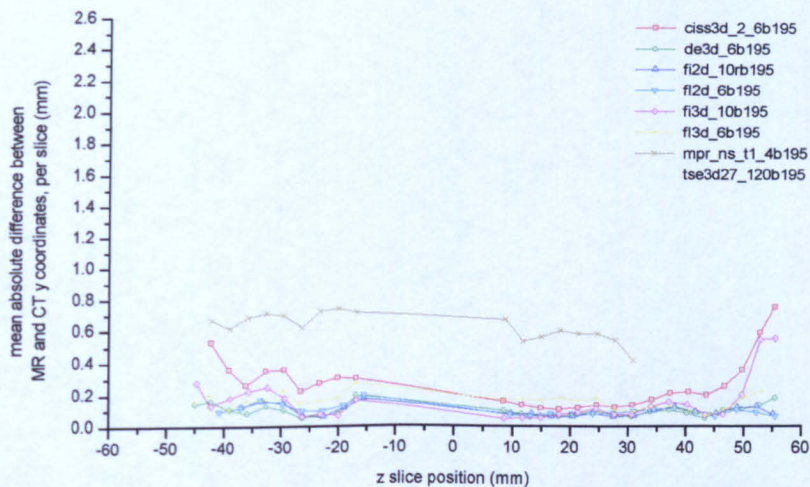


**Figure 5.13c**

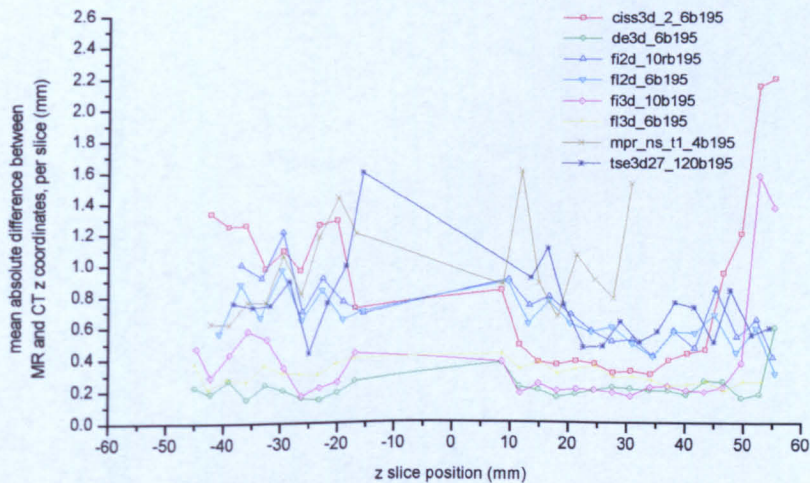


**Figure 5.14** Variation of distortion in final x, y, & z coordinates along the z axis, with MR sequence, at constant bandwidth per point. All sequence have 130 Hertz per pixel bandwidth. Acquired on the SP MR scanner.

**Figure 5.14a**

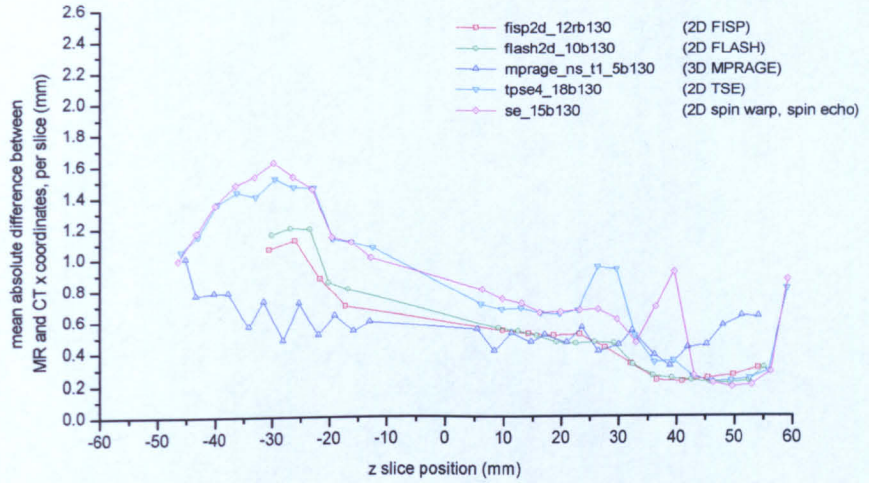


**Figure 5.14b**

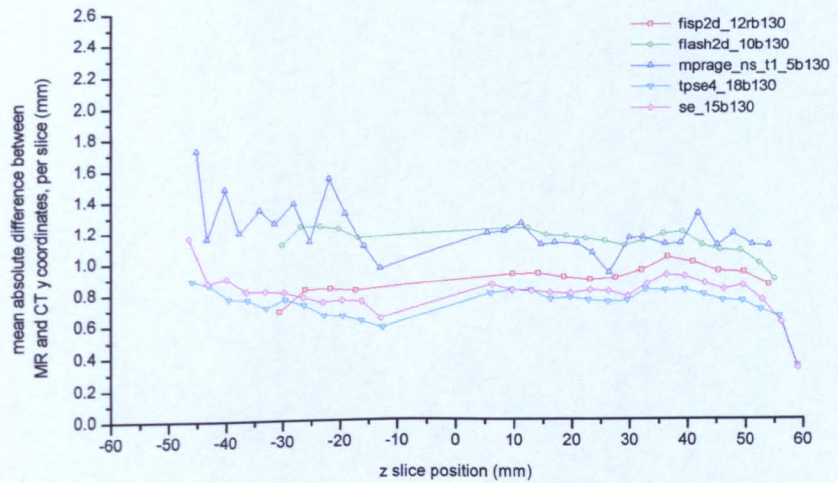


**Figure 5.14c**

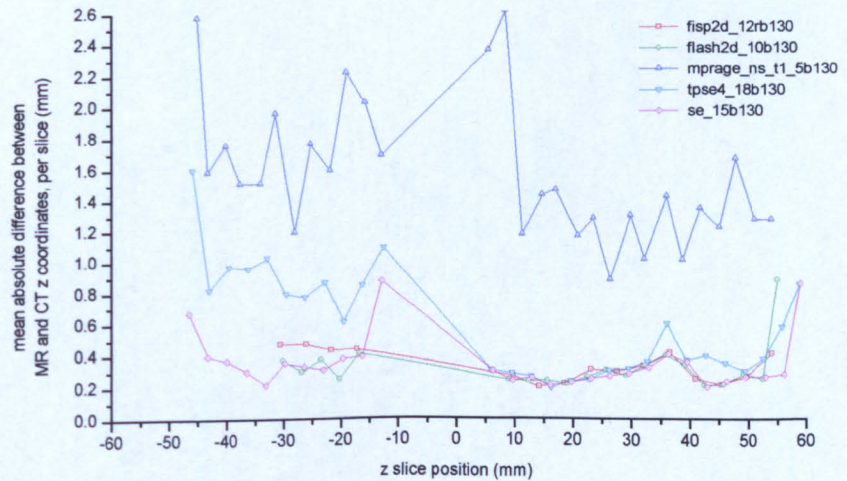


**Figure 5.15** Variation of distortion in final x, y, & z coordinates along the z axis, with MR sequence, at constant bandwidth per point. All sequence have 195 Hertz per pixel bandwidth. Acquired on the SP MR scanner.

**Figure 5.15a**

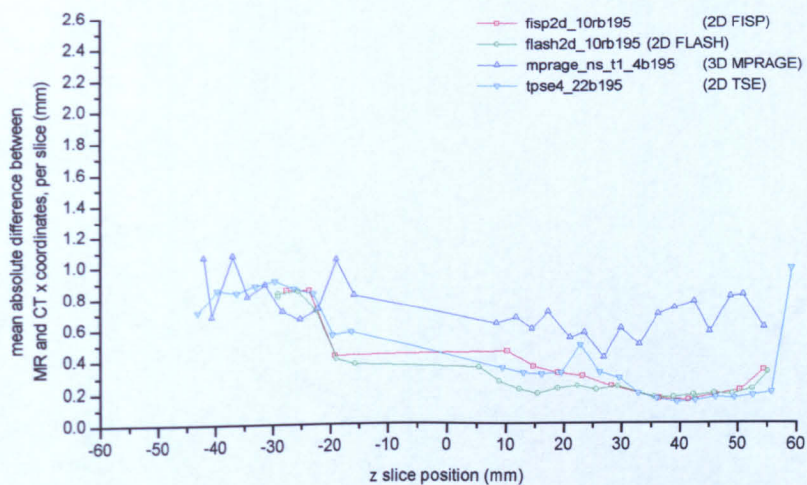


**Figure 5.15b**

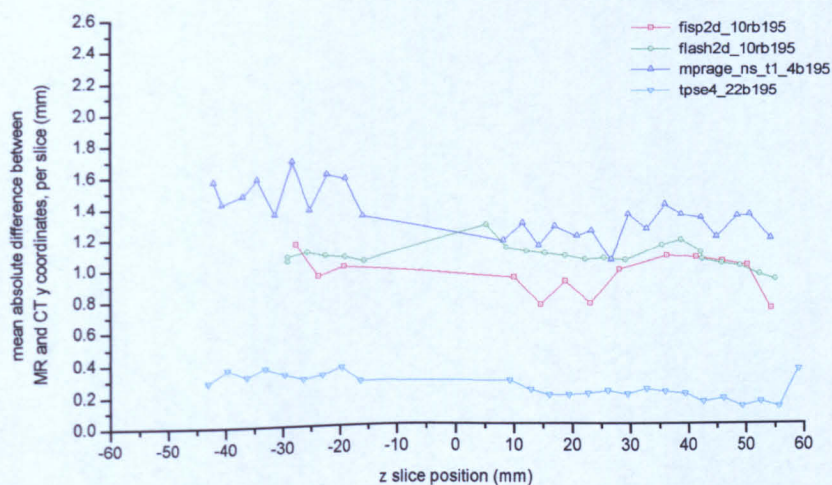
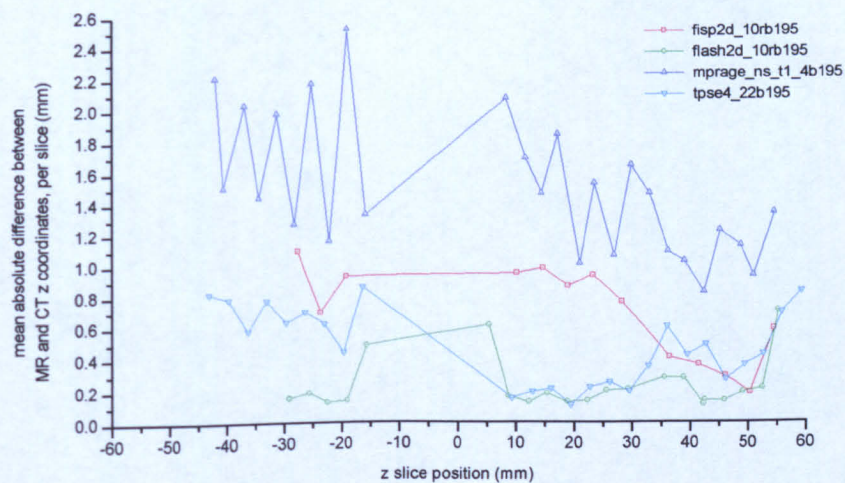


**Figure 5.15c**



## 5. Quantification of Errors in Stereotaxis

---

having a smaller bandwidth per point than  $T_1$  weighted sequences. The longer echo time required for  $T_2$  weighted images allows the NMR signal to be sampled for a longer time, increasing signal to noise while decreasing the bandwidth per point.

The only sequences showing a difference from the norm was the three dimensional TurboFLASH (3D MPRAGE) on the SP, which resulted in a larger distortion along the  $z$  axis, for both bandwidths. This difference was not seen on the similar sequence on the Vision, nor in any other three dimensional sequences. The cause of this is not clear, however, the spread of results over each slice for this MPRAGE sequence was also greater than for the other sequences, and so this difference is not as significant as it first appears. The hardware on the SP is not as advanced as that on the Vision scanner, and it could be that its less than ideal response introduces artefacts in more demanding and sensitive sequence, such as a 3D MPRAGE.

The images acquired from a number of sequences on both scanners were not good enough to be included in these results, due in all cases to some or all of the nine fiducial rods not being visible. These included TurboFLASH and TSE sequences on the SP, and HASTE, GRASE, and EPI sequences on the Vision. The lose of signal from the fiducials is not surprising for the sequences containing gradient echoes and short acquisition times, due to dephasing effects from the rods/air boundary and a lower SNR. Nor is it surprising for the TSE sequence on the SP in which ghosts from the interleaved multiple echo trains are clearly visible, suggesting either a poorly optimized sequence or hardware instabilities. The failure of the HASTE sequence on the Vision to visualize the fiducial rods is somewhat surprising, although it could be due to the lack of correction for phase and amplitude evolution throughout the multiple echoes of the 128 echoes in the echo train. By contrast, the fast spin echo sequence on the Vision (with between 20 and 30 echoes per echo train) includes a pre-scan to attempt to correct for this effect. This correction is absent on the fast spin echo sequences on the SP and this could be one reason for the failure of the sequence on the SP, but not on the Vision.

### 5.4 Application of Distortion Correction to Stereotaxis

In the previous sections of this chapter, a phantom has been used to quantify the distortion present in the final stereotactic target coordinate calculated from MR images. In Chapter 4, Chang & Fitzpatrick's distortion correction method was implemented and used both to correct distortion in MR images and to quantify the distortion present. In this section, Chang & Fitzpatrick's correction method is used to attempt to correct distortion present in MR images of the apparatus used in this chapter. The spatial distortion throughout the phantom and the fiducial rods is quantified. This is required for the analysis presented in Chapter 6.

As mentioned in the introduction to this chapter, one problem with using a phantom for distortion measurements is that it may not simulate the distortion present in a human head. Chang & Fitzpatrick's correction method is used to measure distortion in MR images of the head of a patient undergoing stereotactic neurosurgery. The distortion measured throughout the head is compared to the distortion measured throughout the phantom to demonstrate its validity. If the distortion measured in the phantom is similar to the distortion measured in a head, both of which are surrounded by the head ring and fiducial helmet, then the distortion measured in the final stereotactic target coordinate using the phantom will be comparable to that which would be seen in a human head.

#### 5.4.1 Method

Images of both the phantom and the patient were obtained using a standard spin echo, spin warp sequence (se\_12b130.wkc, TE=12 ms, TR=800 ms, voxel size  $1 \times 1 \times 3$  mm on a  $256 \times 256$  matrix.  $G_x = 3.059 \text{ mTm}^{-1}$  and  $G_z = 8.000 \text{ mTm}^{-1}$ , as quoted by the scanner. The slices were separated by 3 mm to reduce effects from 'cross-talk'; the 'missing' slices were acquired by a second acquisition). A modified version of the sequence was produced with all the imaging gradients applied along the frequency encoded direction having their values negated. Chang & Fitzpatrick's correction method was applied to these images to produce corrected images and pixel by pixel distortion maps. In addition, stereotactic tar-

## 5. Quantification of Errors in Stereotaxis

---

get coordinates were calculated from the corrected images of the phantom, and these were compared with CT coordinates, using the same method as described in Section 5.2 above. Any effect of distortion correction on distortion in the final stereotactic target coordinate could then be seen.

As implemented in Chapter 4, Chang & Fitzpatrick's correction method was not suitable for direct application to MR images containing the fiducial rods. As detailed in Chapter 4, edge detection of the object in the MR image is required, to reduce noise artefacts in the corrected image. Stereotactic images contain a number of separate objects, in particular, the patient's head (or phantom) and the fiducial rods. The edge detection algorithm was modified to find pairs of edges along each line in the frequency encoded direction. Correction was only performed between pairs of edges. This method relies heavily on finding the same pair of edges in the two images used for correction; if this does not happen, streak artefacts will be present in the corrected image. However, using multiple edge detection allows the distortion to be calculated in separate objects within the same image. In Chapter 4, other distortion correction algorithms were mentioned, including a method which relies on the construction of a phase map throughout objects within an image. This can only straightforwardly be performed on connected objects, since an unknown phase wrap of multiples of  $2\pi$  may occur between unconnected objects. This problem may be overcome by assuming a worst possible distortion, and then acquiring images with appropriate parameters (small enough  $\tau$  to ensure no phase wrapping for distortion smaller than the assumed maximum, as described in Chapter 4) from which a phase map of unconnected objects can be constructed.<sup>107</sup> No assumptions of this kind are required for the application of Chang & Fitzpatrick's distortion correction method.

### 5.4.2 Results from Phantom and Discussion

The results of applying the distortion correction on the phantom are presented in Figure 5.16. Figures 5.16a and 5.16b are two typical transverse image slices through the phantom, the first acquired with the frequency encoded gradient applied as normal, and the second acquired with the sign of the frequency encoded

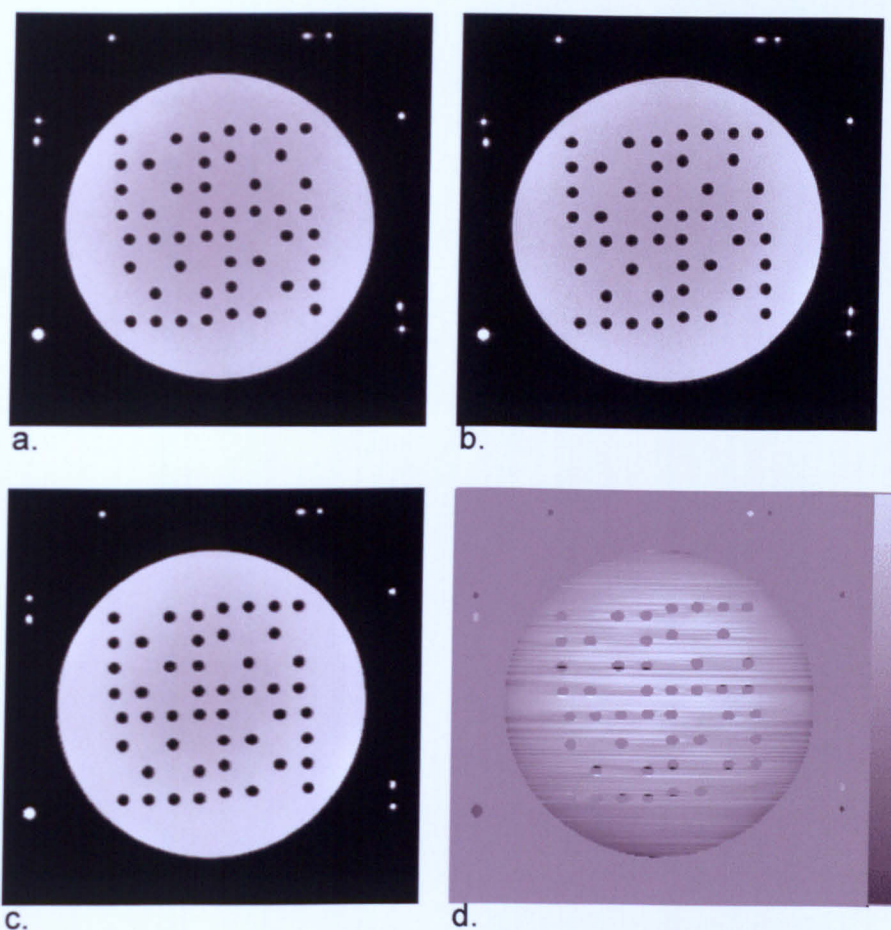


**Figure 5.16** Correction of distortion in the stereotactic phantom using the reversed gradient correction method. Multiple edge pairs could be detected along each row to allow the stereotactic fiducial rods to be corrected in isolation. Full Fourier spin echo, spin warp images acquired using the 1.5 T Vision MRI system.

Voxel dimensions were  $1 \times 1 \times 3$  mm.

a. Image acquired under normal conditions.

b. Image acquired with reversed frequency encoding gradient (horizontal axis in images).

c. Corrected image, using the reversed gradient method.

d. Distortion map. Scale bar represents distortion from  $-1$  to  $1$  mm.

## 5. Quantification of Errors in Stereotaxis

---

gradient reversed. The frequency encoded gradient is oriented parallel to the horizontal  $x$  axis, and differential distortion of the two vertically running diagonal fiducial rods can be seen between these two images.

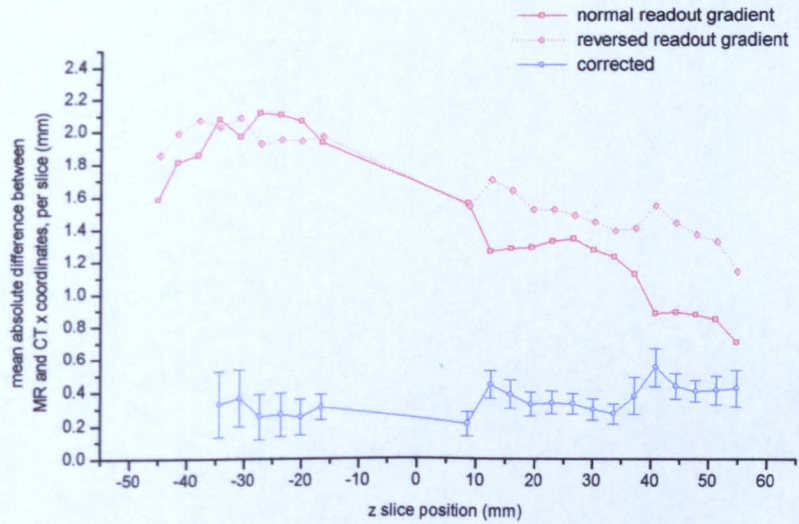
The corrected image produced by Chang & Fitzpatrick's correction method is shown in Figure 5.16c, and the distortion map produced from this correction shown in Figure 5.16d. The correction map image contains both positive and negative values, depending on whether a particular pixel has been distorted to the left (darker) or to the right (lighter). The uniform grey level value seen in the background represents no distortion; this may change from distortion map to map as the contrast has been adjusted to show the range of distortion present in the object. The success of the multiple edge detection can be seen; the fiducial rods have been separated from the main phantom. However, adjustment of the threshold value used for the multiple edge pair detection method was far more critical than for the single edge pair detection, to ensure successful edge detection. As described in Chapter 4, the streaking effect seen here is due to a mismatch between the detected position of the same edges in both images. Streaks between unconnected objects in the distortion map indicate the failure of the multiple edge detection method to correctly identify the same pairs of edges in both images.

Figure 5.17 shows the effect of applying the correction to the MR images before calculating the final  $x$  stereotactic target coordinate. Points calculated from the corrected image show less distortion than those calculated from the raw MR image. The reduction is largest in the regions of greatest distortion. The variation of distortion along the  $x$  axis calculated from the corrected images is fairly uniform along the  $z$  axis, suggesting that the majority of the distortion has been corrected.

Figure 5.18 shows the mean absolute distortion calculated from the correction algorithm. The program performing the correction was modified to automatically classify the distortion of each fiducial rod separately from the distortion in the main phantom. Data from the most inferior slices is not presented, as the multiple edge detection clearly failed to distinguish the fiducials from the main phantom in this slices. Most of the fiducial rods exhibit more distortion than the centrally

**Figure 5.17** Variation of distortion in final x, y, & z coordinates along the z axis, calculated from MRI. The effect of distortion correction on the final 3D stereotactic coordinate. 'Error bars' are shown for the corrected data; the 'error bars' for the uncorrected data are shown in Figure 5.6. Acquired on the Vision MR scanner using sequence *se\_12b130.wkc*

**Figure 5.17a**



**Figure 5.17b**

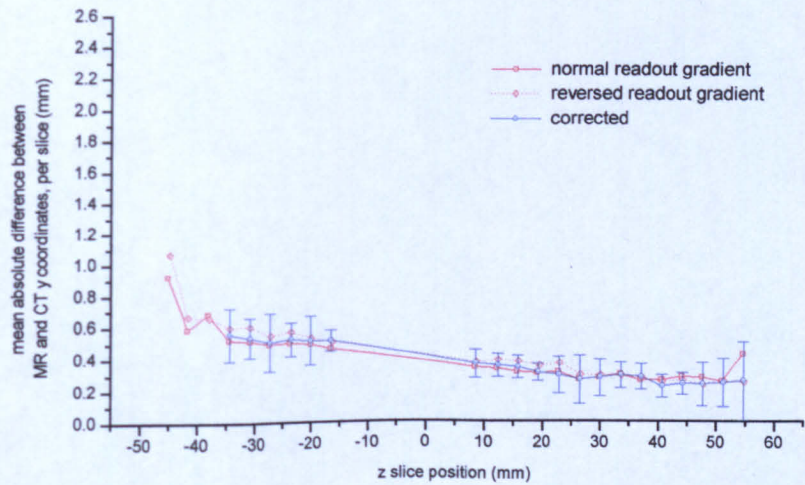


**Figure 5.17c**

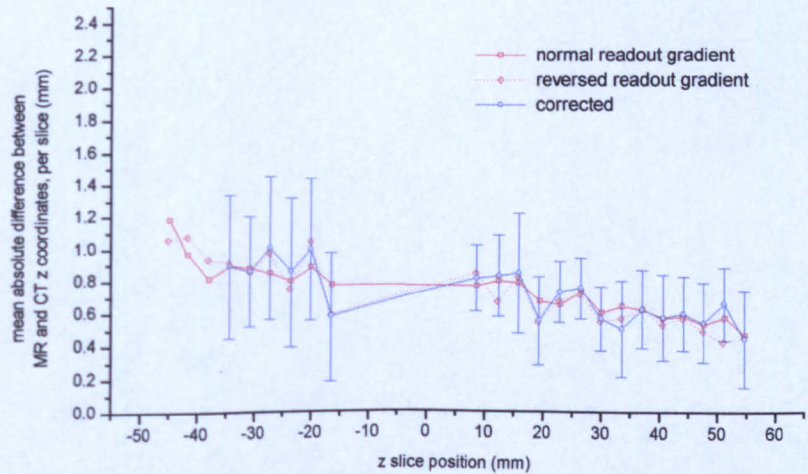


**Figure 5.18** Actual distortion for each fiducial rod and the main phantom.  
 Measured using reversed gradient distortion correction method.  
 GTC head ring positioned between  $x=-80$  and  $-100$  mm.  
 Acquired on the Vision MR scanner using sequence *se\_12b130.wkc*

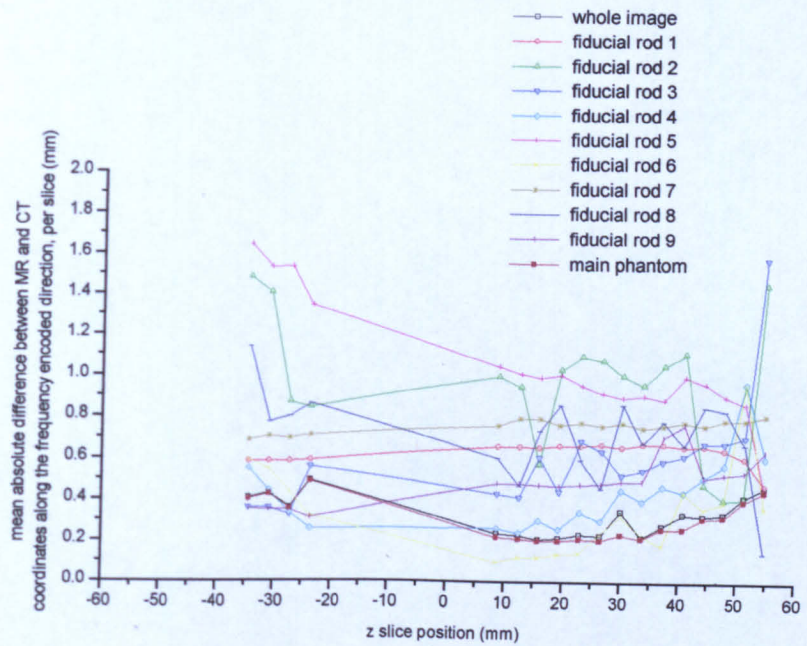
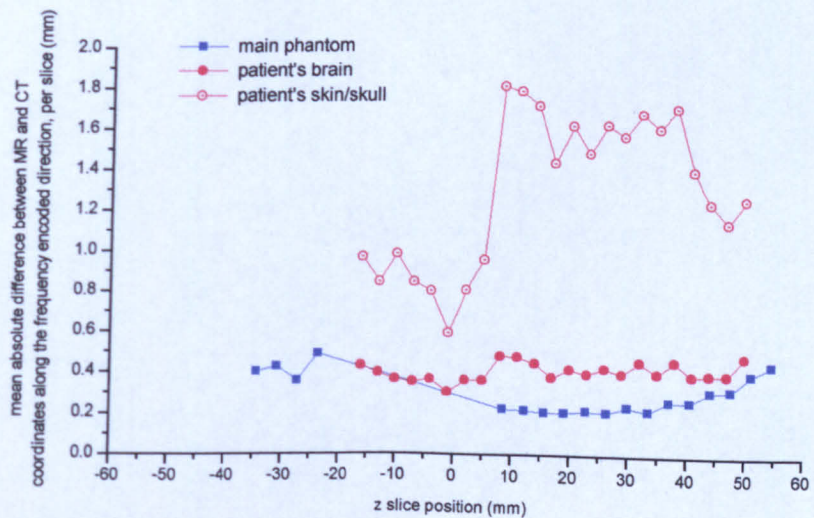


**Figure 5.20** Comparison of the actual distortion between the main phantom and a patient's head.  
 Measured using reversed gradient distortion correction method.  
 Head ring positioned between  $z=-80$  and  $-100$  mm.  
 Acquired on the Vision MR scanner using sequence *se\_12b130.wkc*



## 5. Quantification of Errors in Stereotaxis

---

placed main phantom. As discussed in the introduction to this chapter, it would be expected that the combination of distortion of the fiducial rods, as well as of the phantom (or patient's head) would combine to result in a greater distortion being seen in the final stereotactic coordinate, than just the actual distortion within the phantom. This would appear to be borne out in these results, when compared with those presented in Section 5.2.3.

It is interesting to note that the effect of distortion correction is seen mainly along the  $x$  axis, which is aligned parallel to the frequency encoded axis. While this would be expected for the actual distortion in the phantom, it is not obvious that the same effect would be seen in the distortion in the final stereotactic coordinate, after it has been transformed by Equation 5.5.

The results presented here also are discussed in Chapter 6.

### 5.4.3 Results from Patient and Discussion

The result of the application of Chang & Fitzpatrick's distortion correction method to images of a patient is presented in Figure 5.19. The frequency encoded gradient was applied parallel to the vertical axis of the images. The patient was undergoing a stereotactic biopsy of a suspected brain tumour and was imaged on both CT and Vision MR scanners. Figure 5.19a and 5.19b show two potentially distorted images. Differences due to distortion can be seen between these two images around the anterior and posterior bone marrow. Figure 5.19c is the corrected image, and Figure 5.19d is the distortion map. As can be seen, the detection of multiple edges does not work well on patient data. The fiducial rods have been poorly identified, and the three anterior rods have been absorbed into the head, due to incorrect edge detection. Discrete streaks are also seen in the distortion map. This is a result of multiple edges found in the head, especially around the skull. This increases the chance of a mismatch of edge pairs between the two images used in the correction. From visual inspection of the distortion map, the amount of distortion appears fairly constant over the brain. It also appear to be constant around the skin/skull, but of a different magnitude to that in the brain. The mean absolute distortion along the frequency encoded axis over the head is plotted as a function of  $z$  in Figure 5.20 along with the

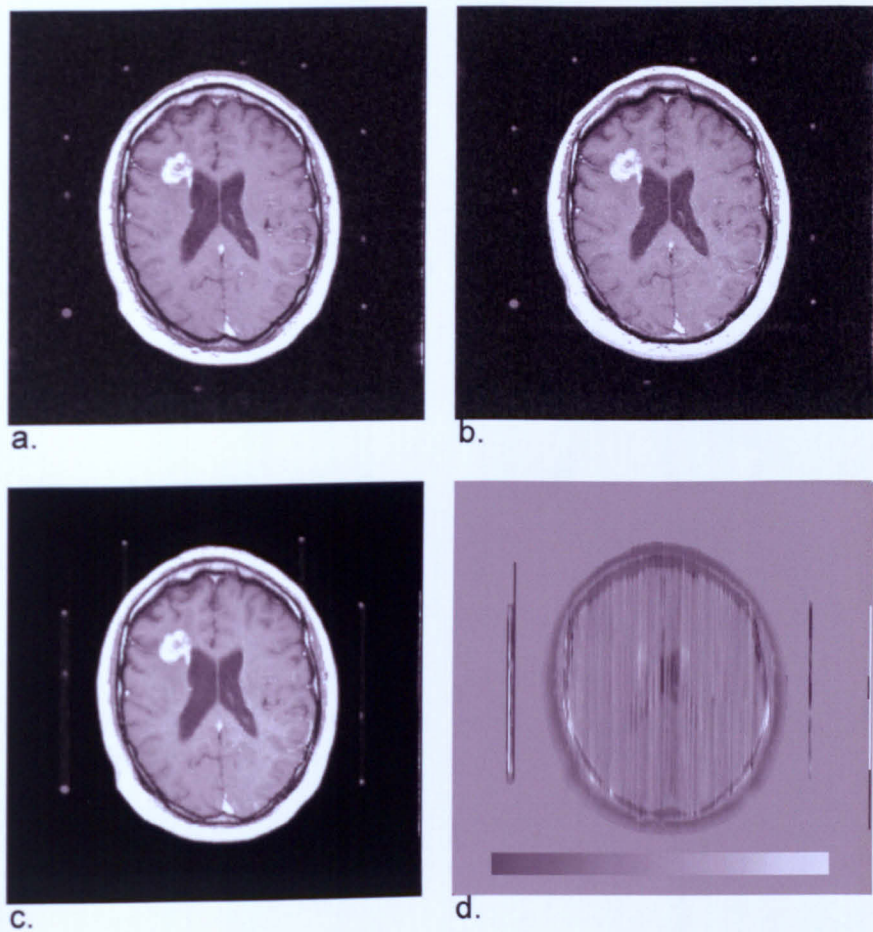


**Figure 5.19** Correction of distortion in a patient's brain using the reversed gradient correction method. Only a single edge pair was sought along each column as multiple edge pair detection found erroneous edges in the patient's skull. Images acquired using the 1.5 T Vision MRI system. Voxel dimensions were  $1 \times 1 \times 3$  mm.

- a. Image acquired under normal conditions.
- b. Image acquired with reversed frequency encoding gradient (vertical axis in images).
- c. Corrected image, using the reversed gradient method.
- d. Distortion map. Scale bar represents distortion from  $-2$  to  $2$  mm.

## 5. Quantification of Errors in Stereotaxis

---

mean absolute distortion over the phantom (as presented in Section 5.4.2) for comparison. The distortion map of the head has been manually segmented into brain and skin/skull regions, which have been plotted separately. The mean distortion measured in the phantom appears to be very similar to that measure in the brain. As all the surgical stereotactic targets lie within the brain, it would seem that distortion measured in the phantom is similar to that measured in the brain. A local increase of distortion in MR images of regions of the brain close to structures such as the sinuses or petrous bone would be expected, and would have to be treated as a special case. However, in general the distortion measured in the final three dimensional stereotactic coordinate calculated from MR images of the phantom will be comparable to that seen in a brain, at a magnetic field strength of 1.5 T. The results obtained in this chapter using the phantom may then be considered valid in the context of a general human stereotactic patient.

The artefacts seen in the image of the patient's head produced using this implementation of the reversed gradient method are concerning. While an occasional artefact may be acceptable and relatively easily interpreted in MR images of a phantom, this is not the case in MR images which will be open to diagnostic interpretation. As noted in Section 4.3.4, Figures 4.1, 4.2, and 4.21, streaks in the distortion map as a result of misregistration of signal intensity across a low signal region do not necessarily introduce visible artefacts in the corrected image, as the misregistered intensity usually has a low value. However, the extent of the artefact would be extremely difficult to quantify and would be expected to vary on an image by image and patient by patient basis. It also is concerning that there appears to be a slight difference, in the form of banding, between adjacent lines in the distortion map. This suggests differing amounts of distortion correction occurring along adjacent lines. The cause of this may be due to a difference in edge detection between adjacent lines, due to a varying intensity around the perimeter of the object or indistinct edges as a result of through-slice partial volume effects. No method to overcome this form of artefact could be devised during the course of this work<sup>†</sup>. Therefore, it is not believed to be wise

---

<sup>†</sup>However, recently Kannengießer *et al.*<sup>52</sup> have applied dynamic time warping to the reversed gradient correction method and they believe this may overcome some of the streak artefacts

## 5. Quantification of Errors in Stereotaxis

---

to use the reversed gradient correction method, as implemented for this work, to directly correct MR images of patients used for stereotactic planning. However, it may still be used to produce distortion maps of the patient's head, from which small regions may be sampled to provide a measure of localized distortion. This information is then available to the clinician for consideration during the selection of the target on the uncorrected MR images. Hence, the reversed gradient correction method may be applied to measure distortion but can not reliably be used to correct it to produce MR images for diagnostic interpretation.

### 5.5 Determination of Sources of Distortion

In the previous section of this chapter, a method of quantifying the distortion in the final stereotactic target coordinate calculated from MR images of a phantom has been presented. While the method to calculate distortions and the results of its use stand in their own right, they may also be used, together with the results from Chapter 4 to gain insight into the causes of the observed distortion. Some information has already been extracted from the previous results in this chapter regarding the source of the observed distortion. Four additional experiments are described in this section to further classify the sources of distortion, and to eliminate other possible sources.

#### 5.5.1 Method

To observe whether the pattern of distortion seen in Section 5.2.3 is caused by a source fixed relative to the phantom or relative to the magnet, multiple MR images sets were acquired with the patient bed (onto which the RF head coil and apparatus were fixed) positioned further in, or out, of the magnet bore. It appears from Section 5.2.3 that the observed distortion varies mainly with position along the  $z$  axis. It is fortunate that this is the one position in which the apparatus may be moved easily. The table was moved in steps of 50 mm, resulting in an overlap between the one partition of the phantom with the other partition, at subsequent table positions.

---

seen here.

## 5. Quantification of Errors in Stereotaxis

---

As the aluminium GTC head ring was thought likely to be the major source of distortion, a non-metallic plate was designed and constructed to replace the GTC head ring, while holding the phantom and UCLF in the same relative positions to each other. The plate, and supporting fixtures, were constructed from Tufnol<sup>§</sup>, Perspex, and nylon. This was then imaged on both CT and MR scanners, as described in Section 5.2.1 and the distortion in the stereotactic coordinates of the phantom rods calculated, as above. The results were then compared to those obtained in the same way, but with the aluminium GTC head ring, as presented in Section 5.2.3. Although the Tufnol plate was carefully constructed to hold the phantom and UCLF in the same relative positions as the GTC head ring, the apparatus containing the Tufnol plate was scanned on the CT scanner as well as the MR scanner. The distortion in the MR images of the apparatus containing the Tufnol plate was calculated by comparison to the CT images obtained with the Tufnol plate, rather than those gathered with the GTC head ring. This should remove the effect of any systematic offsets due to the Tufnol plate not holding the phantom and UCLF in exactly the same relative positions as the GTC head ring. It was also felt to be useful to repeat the experiment described above of moving the patient bed in and out of the magnet bore, with the apparatus containing the Tufnol plate.

All MR images acquired for this chapter were acquired with the frequency encoded gradient applied along the horizontal axis. The effect of swapping the frequency and phase encoded axes on distortion was examined, using the apparatus with the GTC head ring.

As the apparatus was imaged on the various scanners over a number of months, the reproducibility of fitting the various components together was briefly measured by calculating the 'distortion' between two measurements of the same acquisition on different days, instead of between MR and CT. This would give an indication of the amount of measured distortion that might be due to reconstruction of the apparatus between CT and MR imaging sessions.

---

<sup>§</sup>A phenolic resin laminate (Tufnol, Birmingham, England)

### 5.5.2 Results from Tufnol Base Plate and Discussion

The results of the distortion measured when the GTC head ring was replaced by a Tufnol base plate are presented in Figure 5.21. The results from Section 5.2.3 are also plotted for comparison. The results show significantly less distortion along the  $x$  axis in the inferior partition of the phantom with the Tufnol plate present, compared with the distortion with the GTC head ring present. Distortion is also less in the superior partition of the phantom, but not by such a marked amount. No significant difference is seen in distortion in the  $y$  and  $z$  axes. As the GTC head ring is located approximately between  $Z=-80$  mm and  $Z=-100$  mm, it would appear that the GTC head ring is the major source of the observed distortion.

### 5.5.3 Results from Phantom Translation and Discussion

The results of the effect of the table translation on distortion, using the apparatus with the GTC head ring, are plotted in Figure 5.22. The results from images acquired at each table position are displayed in a different colour. Only the graphs of distortion as a function of  $z$  position are presented, since as described in Section 5.2.3, the amount of distortion only varied with  $z$  position, and this was also the case for these results.

It was not possible to acquire images at all desired table positions, as the Vision MR scanner failed on various automatic checks when the apparatus was at particular off-centre locations. These failures related to the calculation of the RF power required for a  $180^\circ$  pulse, or calculation of the attenuation of the RF receiver. While this could have been overridden, it was felt to be too risky on a heavily used clinical MR scanner in case damaged resulted.

As might be expected, the amount of distortion increased at large distances from the magnet's isocentre. The origin of the  $z$  axis is the magnet's isocentre. The most interesting feature of these results is the similarity seen in the distortion pattern at the two table positions with most negative  $z$  position (cyan and blue curves), and to some extent the following table position (green curve), in Figure 5.22a. This suggests that the source of distortion moves with the table, and therefore that the observed distortion is not caused primarily by sources such

**Figure 5.21** Variation of distortion in final x, y, & z coordinates along the z axis, calculated from MRI. Comparison between the aluminium GTC head ring and a Tufnol substitute. The absolute difference between CT and MR for each rod in the stereotactic phantom was calculated. The mean for all rods in a transverse slice was calculated and plotted. The error bars are the standard deviation of the distortion across each slice, and are representative of the range of distortion across each slice. The GTC head ring was positioned between  $z=-80$  and  $-100$  mm. Acquired on the Vision MR scanner using sequence *se\_12b130.wkc*

**Figure 5.21a**

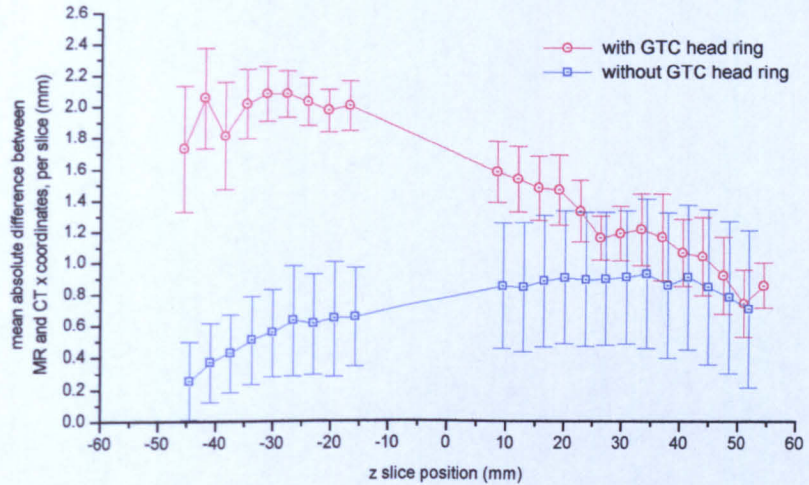


**Figure 5.21b**

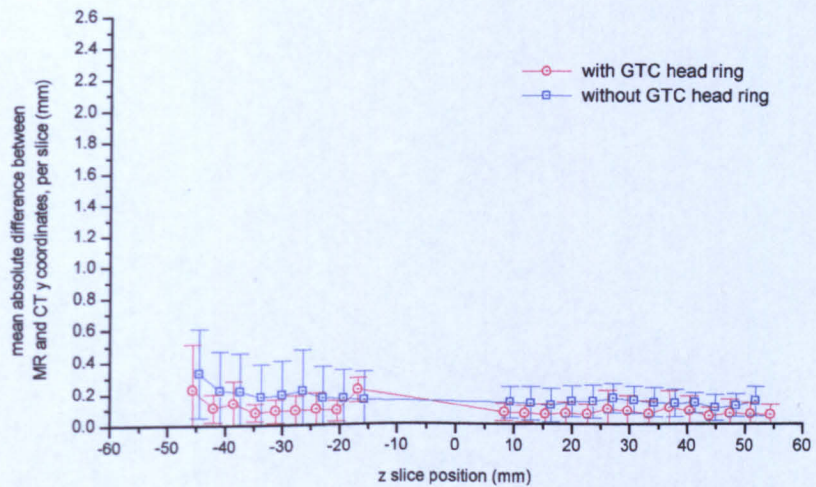


**Figure 5.21c**

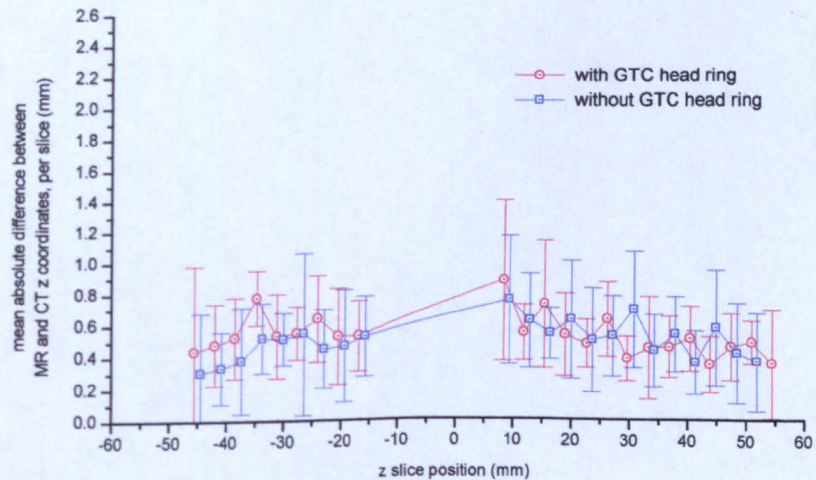


**Figure 5.22** Variation of distortion in final x, y, & z coordinates along the z axis, calculated from MRI. Image acquisition was repeated for different positions of the apparatus along the z axis. Each apparatus position is shown in a different colour. Acquired on the Vision MR scanner using sequence *se\_12b130.wkc*

**Figure 5.22a**

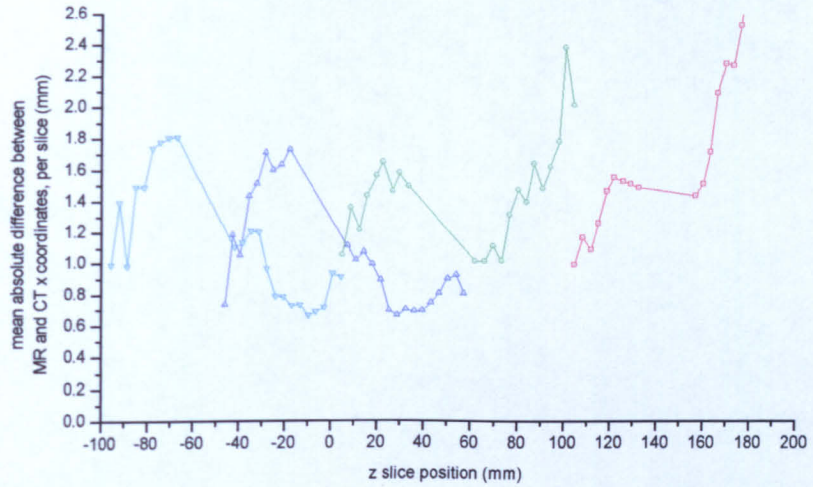


**Figure 5.22b**

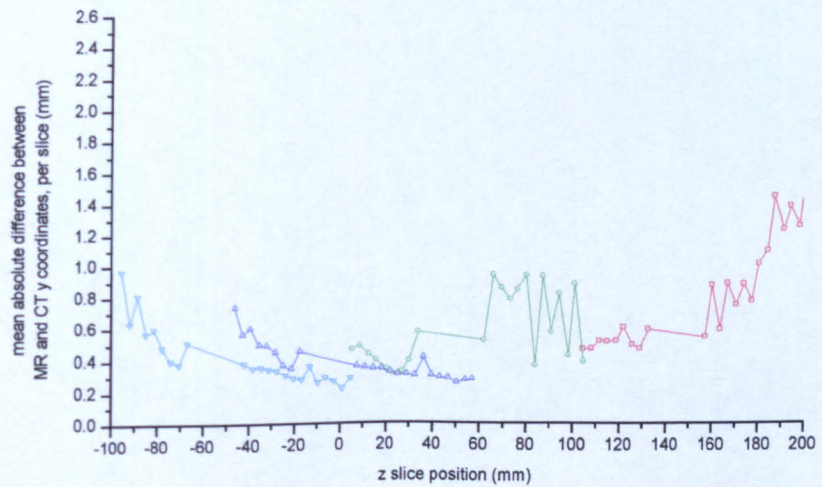
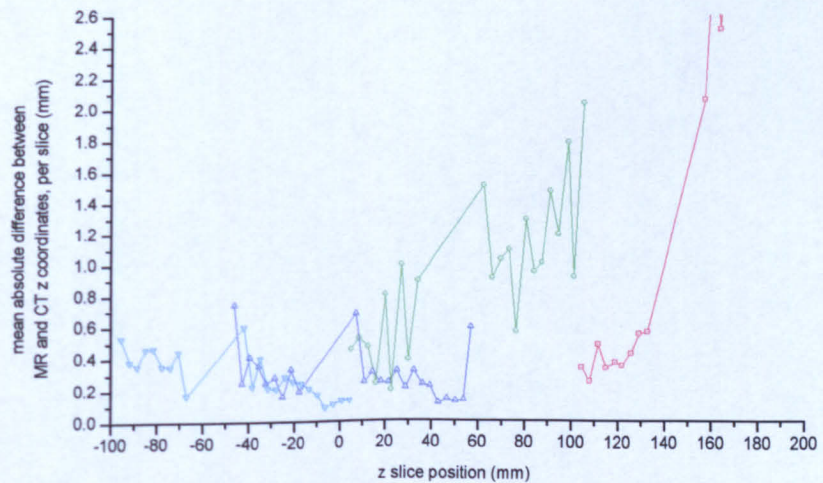


**Figure 5.22c**



## 5. Quantification of Errors in Stereotaxis

---

as inhomogeneities in the main magnetic field, gradients, or eddy currents in the magnet housing. Likely sources of distortion moving with the table would be the RF head coil or apparatus, which includes the aluminium GTC head ring.

Figure 5.23 shows the effect of table translation on distortion, when the GTC head ring has been replaced by the Tufnol base plate. As in Figure 5.21 above, less distortion is seen along the frequency encoded direction, whereas similar amount of distortion are seen along the other axes, compared to the results with the GTC head ring present. Also, the results acquired at different table positions match up more smoothly than those obtained with the GTC head ring present. Although this result may seem to conclusively show that the GTC head ring is the source of the distortion, it is felt that there is some uncertainty as to the rigidity of the apparatus when held together by the Tufnol base plate, compared to the GTC head ring. The difference in distortion in Figure 5.21 is up to 1.5 mm. As presented below in Section 5.5.5, the reconstruction of the apparatus consisting of the GTC head ring may introduction a difference of about 0.2 mm in the final stereotactic coordinate. The construction of the apparatus with the Tufnol base plate does not seem to be so rigid, and so it might be reasonable to assume that its reconstruction would introduction a difference greater than 0.2 mm. Therefore, it would seem to be important to interpret these results in combination with results from other experiments presented in this chapter.

It would appear that there is a baseline distortion of about 0.8 mm along the frequency encoded  $x$  axis which is seen in the superior portion of the phantom, with an additional amount of distortion of about 0.8 mm which is seen in the inferior portion of the phantom when the GTC head ring is present. This is discussed more fully below, in Section 5.5.6.

### 5.5.4 Results from Interchanging Frequency and Phase Encoded Axes and Discussion

The results of the comparison between the amounts of distortion measured in the final coordinates, calculated from images acquired with interchanged frequency and phase encoded axes are presented in Figure 5.24. It is clear that much

**Figure 5.23** Variation of distortion in final x, y, & z coordinates along the z axis, calculated from MRI. Image acquisition was repeated for different positions of the apparatus along the z axis. Each apparatus position is shown in a different colour. Using the Tufnol GTC head ring substitute, instead of the aluminium GTC head ring. Acquired on the Vision MR scanner using sequence *se\_12b130.wkc*

**Figure 5.23a**

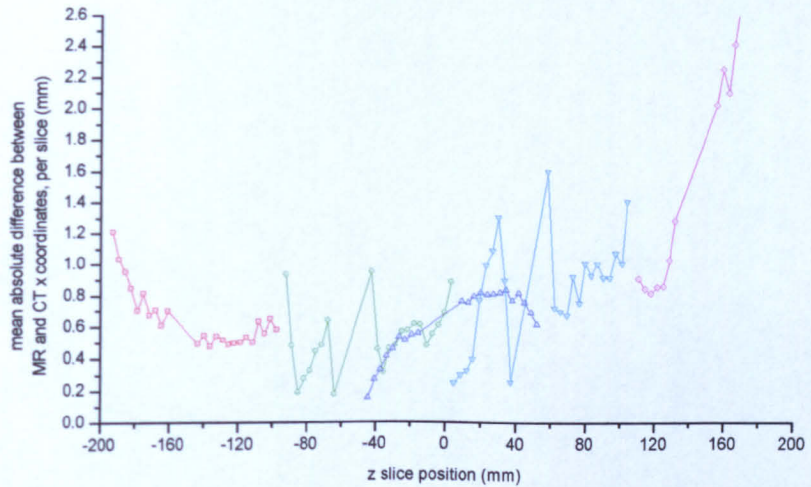


**Figure 5.23b**

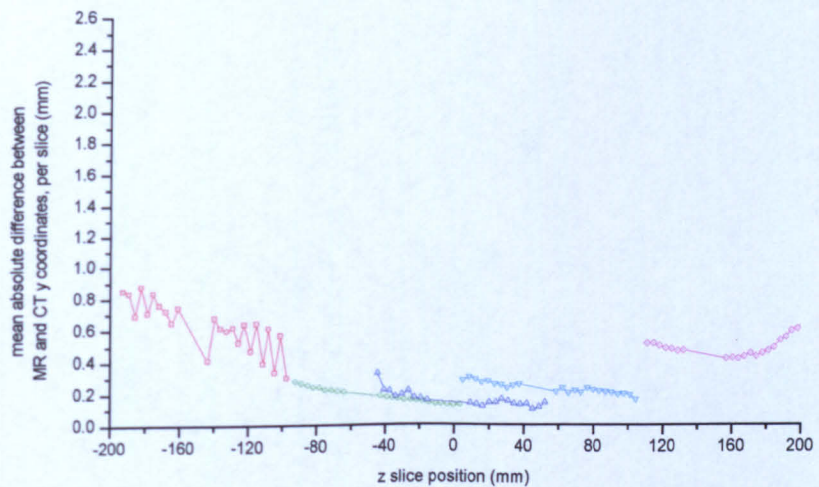


**Figure 5.23c**

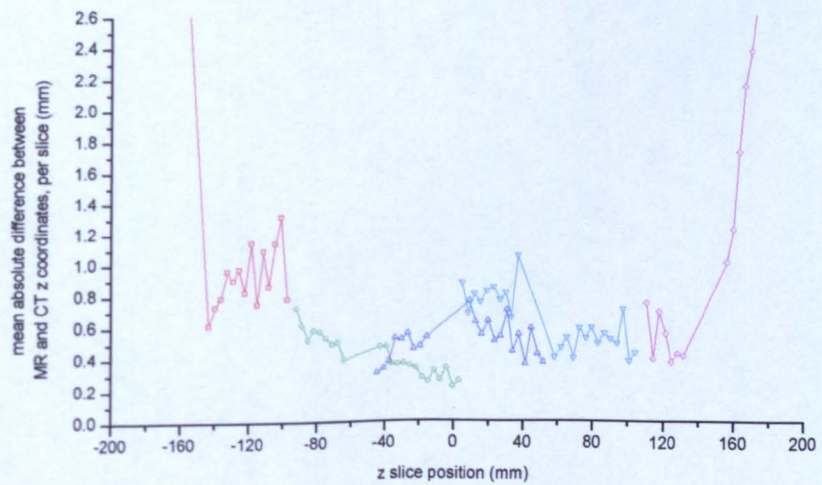


**Figure 5.24** Variation of distortion in final x, y, & z coordinates along the z axis, calculated from MRI. Comparison between images acquired with the frequency encoded gradient along the x axis and along the y axis. GTC head ring positioned between z=-80 and -100 mm. Acquired on the Vision MR scanner using sequence *se\_12b130.wkc*

**Figure 5.24a**

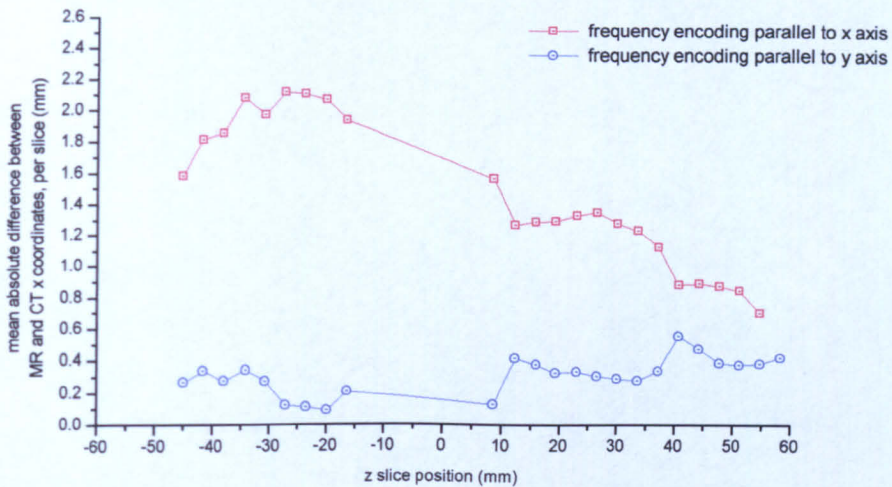


**Figure 5.24b**

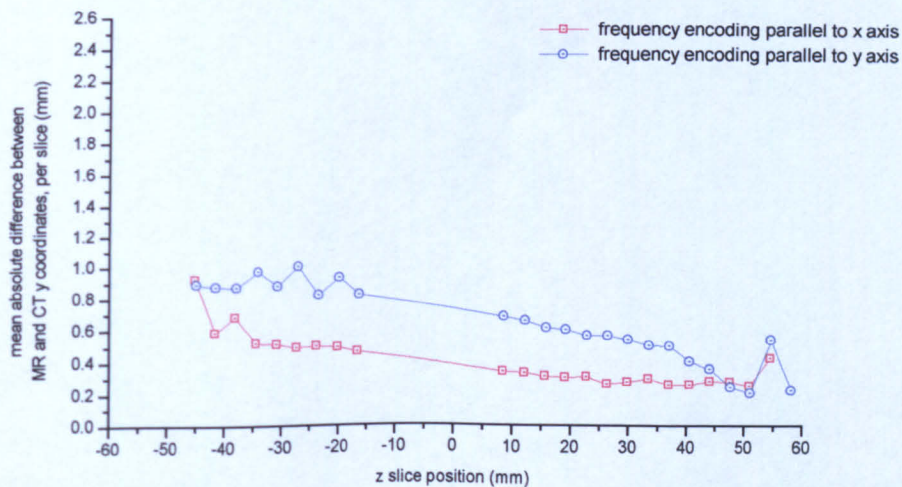
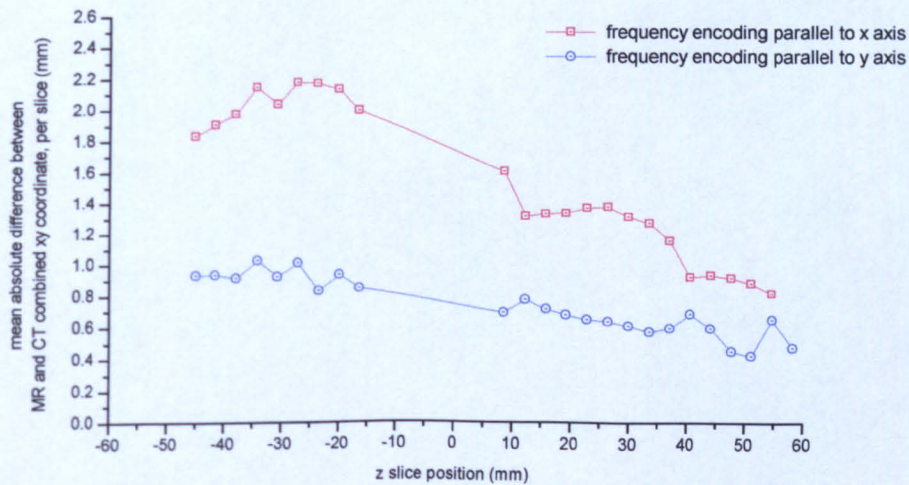


**Figure 5.24c**



## 5. Quantification of Errors in Stereotaxis

---

less distortion is seen in the final coordinate when the frequency encoded axis is aligned parallel to the  $y$  axis than when it is aligned parallel to the  $x$  axis. No difference was seen in distortion in the  $z$  direction, and so Figure 5.24c shows the result of combining the distortion along the  $x$  and  $y$  axes by Pythagoras to calculate the total in-plane distortion. The reason for this difference is not obvious from these results alone. However, it is interesting to note, with reference to Figure 5.5, that the MR compatible fiducial helmet consists of two parallel pairs of triads of rods, with one triad perpendicular to these. It may be that the effect of spatial distortion on the final coordinate is worse if it is parallel to a line joining all three rods in a triad than if it were perpendicular, or *vice versa*. If this is the case, it might be expected that the final distortion would be worse when the orientation of the two parallel triads of rod was such to maximize this effect, as the larger distortion would then be felt by two of the three triads of rods used to calculate the STM. Another reason could be that if the distortion is due primarily to eddy currents induced in the GTC head ring, then it could be conceivable that changing the orientation of the magnetic gradients to the head ring result in differing eddy currents in it. The effect of a shift in the position of a fiducial rod (*i.e.*, spatial distortion) is examined more thoroughly in Chapter 6.

It would seem to be clear that as a practical point, when acquiring MR images of a supine patient fitted with the GTC head ring and UCLF for stereotactic planning, it should be ensured that the frequency encoded axis be orientated vertically, to reduce distortion in the final target coordinate. With reference to Figure 5.10, the distortion in the final coordinate is a factor of approximately three greater if the frequency encoded gradient is parallel to the  $x$  axis than if it is parallel to the vertical  $y$  axis. In the former case, the mean distortion throughout the phantom is 1.5 mm compared to the latter case where it is 0.5 mm. Fortunately, it is common in clinical practice to align the frequency encoded axis vertically for long acquisitions of images of heads, so that potential artefacts caused by eye motion in the phase encoded direction do not overlay the brain.

### 5.5.5 Results from Apparatus Reassembly and Discussion

An indication of the accuracy to which the apparatus could be reproducibly assembled was gained by repeating image acquisition with the same parameters, but on separate days in between which the apparatus had been disassembled and then reassembled. This was performed twice with CT (with the scan dates separated by a year) and three times on the Vision over the same duration. Pairs of image acquisitions on the same modality were then processed as if calculating the distortion between MR and CT. Between all image sets, a constant difference of about 0.2 mm was seen in the in-plane coordinates (the differences along the  $x$  and  $y$  axes combined by Pythagoras) and about 0.2 mm in the  $z$  axis. This was constant throughout the phantom, and so it would seem that there is a constant error of about 0.2 mm introduced into the final coordinate through repeated assembly of the apparatus. It would have been desirable to repeat the measurement more often, to obtain a measure of the application accuracy of the apparatus on the final target coordinate. However, this was not possible due to the restricted access to the busy MR and CT scanners. The total application accuracy of stereotactic frames has been studied in much greater detail by Maciunas *et al.*<sup>63</sup> and their results are considered in more detail in Chapter 6. However, a mean uncertainty of 0.2 mm introduced by repeated assembly of the apparatus is consistent with the reapplication errors measured by Maciunas *et al.* of between 0.1 mm and 0.4 mm.

### 5.5.6 Discussion of Sources of Distortion

Spatial distortion in MR images is due to magnetic field inhomogeneities. This could be due to existing inhomogeneities in the main static magnetic field or the magnetic field gradients, the effect of eddy currents, or differences in magnetic susceptibilities of objects in the magnet bore.

The results in this chapter have been briefly discussed in isolation when they were presented. The results from Section 5.2.3 showed that the in-plane distortion rose from about 1.2 mm in the superior portion of the phantom to about 2.0 mm in the inferior portion of the phantom closest to the GTC head ring. From Section 5.5.3, it was found that this spatial distribution of distortion remained

## 5. Quantification of Errors in Stereotaxis

---

fairly constant, relative to the apparatus, as it was moved in the  $z$  direction. This suggests that the main source of distortion seen in the final stereotactic coordinate is fixed relative to the apparatus. Therefore it would seem unlikely that the main source of distortion lay with inhomogeneities in either the main magnetic field or the gradient magnetic fields, or any other source fixed relative to the magnet, such as eddy currents induced in the magnet's housing. Potential sources of distortion which moved with the apparatus were the RF head coil, the aluminium GTC head ring, the phantom, and the patient bed. It would seem to be unlikely that the fiducial helmet itself would cause significant distortion relative to the other suspect items mentioned. Due to the near symmetry between the inferior and superior partitions of the phantom (see Figure 5.1), it would seem unlikely that one partition caused significantly more distortion than the other.

The results from the direct comparison between the two different 1.5 T MR scanners, presented in Section 5.3.3, suggest that the source of distortion is unlikely to be the RF head coil or patient bed. Both items vary between scanners, as discussed in that section. If the source of distortion lay with these items of different design, it would be expected that a difference would be seen in the distortion results. No significant difference is seen. This also corroborates the conclusion of the previous paragraph suggesting that the cause of distortion does not lie with a source fixed relative to the magnet, as it would be expected that if it were fixed relative to the magnet, then differences would be seen between two different magnets. While it is possible that the cause does lie with the RF coil and patient bed and it is just coincidence that two different designs interact in such a way as to result in the same overall distortion, it is felt that this is very unlikely.

When the GTC head ring was replaced by a non-metal, Tufnol substitute, the results in Section 5.5.3 show little difference between distortion in the superior and inferior partitions of the phantom. This suggests that removal of the GTC head ring removes a major source of distortion.

In Section 4.5, the reversed gradient correction method was used to measure the distortion caused by the GTC head ring and MRI compatible stereotactic

## **5. Quantification of Errors in Stereotaxis**

---

head pins. The presence of the GTC head ring was seen to result in a small increase in the mean distortion in slices within 70 mm of it. The results from Sections 5.5.2 and 5.5.3 agree well with this range; they suggest the GTC head ring causes distortion throughout the inferior portion of the phantom. For the results presented in this chapter, the GTC head ring was located between  $z=-80$  mm and  $-100$  mm and the inferior portion of the phantom ranged between  $z=-55$  mm and  $-15$  mm.

It would therefore seem reasonable to conclude that it is most likely that the source of the observed distortion lies with the GTC head ring.

## **5.6 Conclusions**

In this chapter, a method has been devised and presented to measure the distortion in the final three dimensional stereotactic target coordinate calculated from images of a phantom. Distortion may be quantified along three orthogonal axes. By using a phantom, where all rod centres are automatically identified by their centre of mass, increased precision is expected over the use of user defined anatomical landmarks in patients' heads.

For a standard spin echo MRI sequences on a 1.5 T Vision MR scanner with 130 Hz per pixel bandwidth, using the GTC head ring and UCLF, and with the frequency encoded axis aligned horizontally, the distortion in the final stereotactic coordinate is 2.0 mm between 35 mm and 65 mm from the head ring, and ranging between 1.6 mm and 0.8 mm between 90 mm and 135 mm from the head ring. This is reduced to 0.6 mm and 0.4 mm respectively if the frequency encoded gradient is aligned vertically, as is the normal case for scanning patients' heads. While there are few direct comparisons available in the literature, distortions of between 1.5 mm and 2.6 mm have been reported in the stereotactic coordinate system in cadaver studies on a 1.5 T MRI scanner,<sup>107</sup> which appears to have used the same stereotactic system as was used for the experiments in this chapter. Using a different stereotactic system (a Riechert-Mundiger device), errors in the stereotactic coordinate in a mainly air-filled phantom have been reported of between 1 and 3 mm on a 1.5 T Siemens MRI scanner.<sup>100</sup> Distortion of anatomical landmarks in MR images, also acquired with a 1.5 T scanner, has

## 5. Quantification of Errors in Stereotaxis

---

been quoted as up to 5 mm in the stereotactic coordinate system,<sup>27</sup> but also using a different stereotactic system.

The expected reduction in distortion with an increase in bandwidth per pixel was observed. No significant difference was seen between different MR sequences with the same bandwidth per pixel. Recommendations for MR imaging of patients undergoing stereotactic neurosurgical procedures would be to use any sequence with a bandwidth for pixel of 130 Hz or more, and to align the frequency encoded axis vertically if using the UCLF.

By performing additional experiments, and using the method presented in this chapter for quantifying spatial distortion, an estimate can be made of the major source of the observed distortion. This was found to be the MR compatible GTC head ring. This is not entirely surprising when it is considered that the ring is constructed from aluminium. However, there does not appear to be any other MRI compatible materials from which a rigid frame may be constructed. The manufacturers of the CRW system do not believe that plastic materials are rigid enough, and have encountered difficulties in manufacturing the items using ceramics.

The reversed gradient correction method has been applied to MRI in a stereotactic setting. It has been used to verify the validity of the phantom as a brain phantom, regarding distortion. However, due to the potential of it introducing artefacts in corrected images, as seen in Section 5.4.3 and Chapter 4, it is concluded that it is not wise to allow the corrected images to be interpreted clinically. Therefore, it is suggested that its use be limited to measuring the distortion present rather than for the correction of MR images used for stereotaxis.

# Chapter 6

## Propagation of Errors in Stereotaxis

### 6.1 Introduction

In the previous two chapters, methods for quantifying the distortion present in MR images, and for estimating the error present in the final stereotactic target coordinate calculated from MR images, have been presented, implemented, measured, and discussed. In order to understand further how known spatial distortion in MR images affects the final stereotactic coordinate, it is necessary to consider other components of the stereotactic process which give rise to errors and to estimate their magnitude. The relative importance of each identified source of error may then be assessed.

With the use of MR images in stereotactic treatment planning becoming more desirable, it is important to understand how spatial distortion in MR images affects the total error in a typical stereotactic procedure. Only then may its significance be judged. Previous work has concentrated on measuring the spatial distortion in MR images<sup>17,73,74</sup> or in the final stereotactic coordinate<sup>27,107</sup> as performed in Chapter 5. However, the errors from MRI have not previously been combined with other errors in a stereotactic procedure and hence not viewed from the perspective of the final treatment error.

The accuracy in the final target coordinate in stereotactic neurosurgery using

## 6. Propagation of Errors in Stereotaxis

---

a modern frame and planning from CT images frequently has been quoted as being sub-millimetric.<sup>112</sup> However, more recently, some doubt has been raised over these values; Maciunas *et al.*<sup>63</sup> thoroughly measured the 'total' error in a typical CT planned stereotactic neurosurgical biopsy procedure using the BRW system, including measurements of the effect of parameters such as weight-bearing and reapplication of biopsy arc jigs, and reported typical total 'application accuracies' of between two and three millimetres. The use of MRI for stereotactic treatment planning has often been criticized as it was believed that errors introduced by spatial distortion in the images would result in treatment errors larger than one millimetre. However, if errors from other sources in the stereotactic process are larger than initially expected then the relative contribution of the error from spatial distortion in MRI to the total error may be smaller than expected.

At the end of a stereotactic procedure, the error which is of interest to the clinician is the error relating to the difference between the centre of the planned target coordinate and the actual target in the patient's brain. This will be termed the treatment error. This error may be broken down into errors associated with various sub-processes.

The final treatment error will be considered to be a result of –

1. Mechanical inaccuracies in the fitting of the stereotactic apparatus to the patient and performing the treatment. This may manifest itself at a minimum of four distinct occurrences throughout the stereotactic procedure.
  - (a) Non-rigid attachment of the head ring to the patient. In the BRW system attachment is achieved either by pins attached to the patient's skull or by a mouth bite and occipital pad. In the latter case, the position of the head ring is likely to be affected by the level of cooperation of the patient through time, in particular their ability to maintain a constant pressure on the mouth bite. For patients attached to the head ring *via* pins, as is the preferred method in Nottingham, it has been observed that the MR compatible pins, made of plastic with an aluminium core, have bent under the strain of being forced into the patient's skull. While this deformation is believed only to occur during fixing, there remains a possibility that the head ring may move

## 6. Propagation of Errors in Stereotaxis

---

slightly relative to the patient through time. It is worth noting that it is only movement of the head ring relative to the patient between imaging and treatment that is important.

- (b) Mechanical inaccuracies in the 'helmet' of fiducial rods used, or in the attachment of the fiducial system to the head ring. These could be a result of miscalibration of the apparatus, wear and tear, or small deformations of the apparatus under the weight of the patient. The error could present itself as either a constant offset, or as random errors due to non-rigidity of the apparatus. A constant offset may be considered as spatial distortion of the image. For example, a damaged, bent fiducial rod in an undistorted image is analogous to an undamaged, correctly positioned fiducial rod in an image where the region containing that rod is spatially distorted. These errors will affect the calculation of the target coordinate.
- (c) Mechanical inaccuracies in the treatment apparatus. Whether using a stereotactic biopsy jig or radiotherapy linear accelerator, the target coordinate set on the apparatus may not be the physical target coordinate actually treated. This error could arise in the biopsy system due to stress from the weight of the patient or from the biopsy needle flexing during insertion into the brain. For treatments using a radiotherapy linear accelerator, an error will be introduced from small differences between the centre of the radiation field set in the apparatus and the actual field delivered. To increase the uniformity of the high radiation volume treated and reduce high radiation dose 'hot spots' outside this volume, radiation delivery is usually performed while the linear accelerator's gantry is rotating around the patient; the centre of the radiation field would be expected to shift slightly with gantry angle due to changes in the weight distribution of the gantry. From experience of mechanical calibration of modern linear accelerators, it is highly unlikely that the movement of the centre of the radiation treatment field will be less than one millimetre during rotation of the gantry or the couch. The weight of the patient on the treatment

## 6. Propagation of Errors in Stereotaxis

---

couch and head ring fixation apparatus also may cause small changes in the treatment coordinate.

- (d) Brain deformation. During a stereotactic guided craniotomy, the brain may physically deform once a portion of skull has been removed and no longer supports it. The shape of the brain may also be modified by changes in intracranial pressure from the anaesthetic process, if used. Mean differences of 4.4 mm have been measured between the surface of the brain in images and the surface when exposed during surgery.<sup>43,71</sup> While the error deeper in the brain might be expected to be less than this value, it is unlikely to be negligible. By way of comparison, the displacement of the brain at different head orientations with the skull closed is believed to be less than 1 mm<sup>43</sup> while the brain displacement due to cardiac pulsatility is less than 0.5 mm.<sup>89</sup>

2. Imaging. Two factors which may introduce errors *via* images acquired for planning are distortion and resolution. Distortion can be in the form of spatial shifting or pixel intensity modification. Small distortion of pixel intensity may affect the localization of fiducial rods by methods such as finding their centre of mass, as well as clinical interpretation and target selection. The effects of spatial distortion form the main subject of this thesis. It might be expected that a finite voxel size would limit the final target accuracy. However, in an image with large signal to noise, so long as each fiducial rod spans at least two pixels in both in-plane axes, then its centre of mass will yield its centre to a sub-pixel accuracy. Partial volume effects in the through-slice direction also will not affect the localization of the centre of mass of a fiducial rod so long as it is straight. It would seem that the larger effect of finite voxel size would be on the detection of the target centre. If this is selected on a pixel by pixel basis, then the uncertainty in the target coordinate will be related to the voxel dimensions. However, if a treatment volume is defined over areas in several slices and the target point is taken at the centre of this volume, then its location may be defined to sub-voxel accuracy.<sup>118</sup>

## 6. Propagation of Errors in Stereotaxis

---

3. Treatment planning. Uncertainties are introduced by the clinician during selection of the target point on the images. Unlike the fiducial rods whose centres are usually detected to sub-pixel accuracies by methods such as finding the centre of mass, the treatment target is usually defined qualitatively on a pixel by pixel basis in the images. Repeated selection of the target on different occasions or by different clinicians, may result in a variation of target coordinate, all of which may be clinically acceptable. This error has been estimated to lie between 0.3 mm and 2.4 mm for various well defined, near-point sized anatomical landmarks in the head.<sup>41,42</sup> It might be expected that this error would be larger when manually choosing the centre of a distributed target.

A number of terms to describe some of these errors have been defined by the group at Vanderbilt University (Nashville, TN, USA)<sup>27,30,69</sup> which includes Fitzpatrick and Maciunas. These are Fiducial Localization Error (*FLE*), which is the error with which the centre of a fiducial rod is found, and Target Registration Error (*TRE*), which is the error in a non-fiducial point in the image after being transformed to stereotactic space under the influence of *FLE*. Hence, the *TRE* is the error in the final quoted target coordinate, and has been referred to as the error in the final target coordinate throughout this thesis. It is not the same as the treatment error ('application error' in Vanderbilt terminology) as it does not incorporate any mechanical errors associated with actual treatment. Another useful term is the Target Localization Error (*TLE*) which measures the error in localizing the centre of the target point in the image set. If the target is defined on a pixel by pixel basis, this will be of the order of the voxel dimensions; if it is defined by a centre of mass (or other geometric) method it is likely to be smaller than a voxel's dimensions.

Many of the separate errors described above have been measured previously. In particular Maciunas *et al.*<sup>63</sup> have considered the errors introduced from sources such as the stereotactic frame, CT imaging protocols, aiming accuracy, and the weight-bearing properties, of a variety of popular stereotactic neurosurgical systems, including the BRW system (which includes the BRW and CRW stereotactic jigs). Previously, it would appear that the accepted view was that the final treat-

## 6. Propagation of Errors in Stereotaxis

---

ment error was a combination of any errors from imaging (in particular image distortion) and the mechanical precision with which the target coordinate could be set on the treatment jig. By this reasoning, the millimetric scales on the treatment jig and sub-millimetre CT pixel sizes suggested localization errors of less than one millimetre. This fostered the view that spatial distortion of the order of a millimetre or two in MR images was unacceptable. Maciunas *et al.*<sup>63</sup> found that a typical patient exerted a weight-bearing force of between 100 N and 250 N; when applied to a phantom, these caused mean errors in treatment position of 0.3 mm and 2.0 mm (worst case errors of 1 mm and 5 mm). Unfortunately, these authors did not investigate the source of this error, and so it is unclear whether additional mechanical adjustments could be introduced to correct it. However, they found no measurable error if the phantom was stressed with less than 50 N, and it is interesting to note that many phantoms used to measure errors in the stereotactic process may weigh less than this. The weight of the phantom used in this thesis was approximately 180 N. Reapplication of a phantom to a treatment jig was found to lead to a mean error of 0.3 mm in the treatment point (worst case error 0.8 mm). They found no significant variation in the treatment error with target position in the image. However, they found what appeared to be a positive linear relationship with treatment error and CT slice thickness, as well as a positive linear relationship with treatment error and the angle to which the CT slice was tilted away from perpendicular to the fiducial system. Extrapolating to zero CT slice thickness (perpendicular to the fiducial system) gave a mean error of 1.6 mm and worst case error of 2.3 mm, which they associate with the mechanical accuracy of the whole stereotactic system.

One of the interesting points raised by their work was the dependence of treatment error on slice thickness and slice angle. As all fiducial rods are straight, and assuming a symmetric image slice profile, the centre of mass method should correctly identify the centre of a fiducial rod regardless of slice thickness or orientation. Mathematically, as described in Chapter 5, the slice transform matrix (STM) does not favour any particular orientation of the image slice relative to the fiducial system (so long as all fiducials may be visualized separately). Hence, the dependence on slice angle is difficult to explain. The dependence on

## 6. Propagation of Errors in Stereotaxis

---

slice thickness could be explained by the size of the target points used in their phantom; these were formed from the tip of a 2 mm diameter rod, tapering to the point over 2 mm. This could not have been identified by a centre of mass method and therefore its TLE would depend on the voxel size.

The work of Maciunas *et al.*<sup>63</sup> would suggest that even with 'perfect' imaging and the use of targets which can be located precisely in the image, typical errors in the final treatment coordinate of 1.6 mm can be expected (up to 2.3 mm in the worst case). They also made the point that from a clinical point of view, it is a 'worst case' error rather than a mean error which is important. The risk of a neurosurgical procedure will depend more on how wrong it could be; it is of no comfort repeating surgery on a patient in the knowledge that the mean target will be closer to the desired target. They chose the 'worst case' error as "the mean error of localization at a confidence interval of 99.9% (a certainty of 999 cases out of 1000)."

The work in this chapter aims to investigate further the relationship between the error in localizing the centre of the fiducial rods and target point on the calculated stereotactic target coordinate, and hence gain an increased understanding of the effects of spatial distortion in MR images on the target coordinate. This has been studied elsewhere by the use of fiducial rod perturbation<sup>30,41,42,61</sup> studies and numerical analysis.<sup>30</sup>

Many studies have considered perturbations in either a generalized fiducial system or in systems developed locally. Lemieux & Jagoe<sup>61</sup> performed numerical perturbation studies of the fiducial rod positions in the BRW system. Their method randomly perturbed the nine fiducial rods in the image plane, with a standard deviation of 1 mm along each axis (the pixel dimensions). The error caused by the resulting STM on unperturbed target points was then calculated for each fiducial perturbation pattern. Fiducial rods were identified using a centre of mass method. They found a *TRE* of 1.6 mm with standard deviation 0.8 mm if the STM was calculated using the three diagonal fiducial rods (the method used in this thesis). If all nine fiducial rods were used, the *TRE* was reduced slightly to  $1.4 \pm 0.8$  mm. Interestingly, they reported that the largest *TRE*'s occurred in fiducial perturbation patterns which mimicked a tilt in the slice plane about the

## 6. Propagation of Errors in Stereotaxis

---

lateral axis. They reported that the  $TRE$  they measured was directly proportional to the in-plane pixel size, however they did not consider slice thickness. The  $TRE$  from the perturbation studies was least at the in-plane centre of the fiducial system and increased with increasing radial distance from this centre. Although not a point considered in this work, they also studied the effect of adding a fourth triad of fiducial rods in a 'N' configuration, and reported that this reduced the  $TRE$  by 40%. This could well be an important design parameter in the design of future stereotactic frames.

Recently, Fitzpatrick *et al.*<sup>30</sup> have produced rigorous expressions relating the  $TRE$  to the  $FLE$ , the number of fixed fiducial points,  $N$ , and number of spatial dimensions in the data set to be registered. For a three dimensional image set, they showed that their general expression reduced to

$$\langle TRE^2(\mathbf{r}) \rangle \approx \frac{\langle FLE^2 \rangle}{N} \left( 1 + \frac{1}{3} \sum_{k=1}^3 \frac{d_k^2}{f_k^2} \right) \quad (6.1)$$

to second order, where  $k$  counts through the three principal axes with the origin at the centre of the fiducial system,  $d_k$  is the distance of the target point along the  $k^{th}$  axis,  $f_k$  is the root mean square distance of the fiducial rods along the  $k^{th}$  axis, and  $\mathbf{r} = d_1\mathbf{i} + d_2\mathbf{j} + d_3\mathbf{k}$ . Equation 6.1 gives an expression, which has been lacking for some time, allowing the error of point based image registration to be calculated for a range of applications, of which stereotaxis is only one. A linear dependence of  $TRE$  on  $N^{-\frac{1}{2}}$  had been observed previously from simulation studies;<sup>41,70</sup> this is borne out in Equation 6.1. Computer simulations were also performed by Fitzpatrick *et al.*<sup>30</sup> to check Equation 6.1 which they found to be extremely accurate. For fiducial rod perturbations of zero mean and a variance of  $\frac{1}{3}$  mm, placed in a configuration similar to a typical stereotactic head fiducial system, they calculated a  $TRE$  of 2.2 mm, using three fiducial rods. This is higher than, although comparable with, the 1.6 mm reported by Lemieux & Jagoe<sup>61</sup> above. A number of inferences were drawn from this equation by Fitzpatrick *et al.* When  $\mathbf{r} = 0$ ,  $\langle TRE^2(\mathbf{r}) \rangle \approx \frac{\langle FLE^2 \rangle}{N}$ , giving the minimum  $TRE$  at the centre of the fiducial system. As  $\mathbf{r}$  increases, the  $TRE$  increases, and approaches a  $r^2$  dependence. An increase in  $TRE$  with increasing  $\mathbf{r}$  has been measured before<sup>61</sup> although it is interesting to note that Maciunas *et al.*<sup>63</sup> did

## 6. Propagation of Errors in Stereotaxis

---

not measure any significant spatial variation in the treatment error. This could suggest that the treatment error they measured does not contain a significant contribution of the  $TRE$ , when using CT images for planning. Sensitivity to the design of the system of fiducials used comes into Equation 6.1 via the variable  $f_k$ . This suggests that the fiducial rods should be placed as far from the centre of the system as possible, as well as away from the principle axes. In practice, the design of the fiducial system is more likely to be limited by the imaging modality, e.g., to be able to be placed within the imaging bore of a CT or MRI scanner. Also, for a fixed matrix size, increasing the field of view to include a larger fiducial system would reduce the resolution of the patient's anatomy.

While the work of Fitzpatrick *et al.*<sup>30</sup> described above shows the relationship between  $FLE$  and  $TRE$ , it does not seek to quantify the size of the initial  $FLE$ ; rather perturbation studies are performed. It would be useful to estimate a typical value for the  $FLE$  and this is done below. Also, while Equation 6.1 shows the effect of an error in the spatial location of the fiducial rods, it does not include any error in the location of the target point,  $\mathbf{r}$ , itself; in MRI, both fiducial rods and chosen target point are likely to be spatially distorted. Calculating the effect on  $TRE$  for an error in  $\mathbf{r}$  (i.e., the  $TLE$ ) as well as the  $FLE$  is not the same as including the effect of an error in  $\mathbf{r}$  in Equation 6.1; doing that would just give information as to how the  $TRE$  varies with  $\mathbf{r}$ . In this thesis, spatial distortion in MR images in both the fiducial rods and points throughout a phantom have been measured using Chang & Fitzpatrick's reversed gradient correction method. An estimate of the  $TRE$  at points throughout the phantom has also been measured in Chapter 5 by calculating the difference between the same target points from CT and MR images. This  $TRE$  includes contributions from spatially distorted fiducial rods and spatially distorted target points in the MR images. This allows the  $TRE$  measured directly to be compared to a  $TRE$  calculated using Equation 6.1 and this is undertaken below.

### 6.2 Estimation of Fiducial Localization Error

Fitzpatrick *et al.*<sup>30</sup> have recently analytically evaluated the relationship between the error in the spatial localization of fiducial points,  $FLE$ , and the resulting error

## 6. Propagation of Errors in Stereotaxis

in the target points calculated from these fiducial points,  $TRE$ . Perturbation studies also have been useful in exploring this relationship. These usually assume that the  $FLE$  is normally distributed with a standard deviation of the order of half a pixel dimension. This would seem reasonable if the centre of the fiducial point could only be identified to the nearest pixel, giving an error of  $(\pm \frac{1}{2} \times \text{pixel dimension})$ . However, contemporary computer planning systems usually identify the centre of the fiducial point by a centre of mass method, or a variation thereof. In this case, the centre of the fiducial point may be localized to sub-pixel accuracy, resulting in a correspondingly smaller  $FLE$ .

Figure 6.1 shows a representation of a  $M \times M$  pixel portion of an image,  $I(x, y)$ , containing a single contrast object of which the centre of mass of intensity is required. The object is spanned by more than one pixel in each direction. If this were not the case and the object only contributed to intensity in one pixel, then its centre could not be localized any more precisely than to  $(\pm \frac{1}{2} \times \text{pixel dimension})$ . The sum,  $A$ , of intensities over the portion of the image will be

$$A = \sum_{i=1}^M \sum_{j=1}^M I(i, j) \quad (6.2)$$

and along the  $x$  axis, the centre of mass,  $COM_x$ , will be

$$COM_x = \frac{1}{A} \sum_{i=1}^M i \sum_{j=1}^M I(i, j) \quad (6.3)$$

If random noise is superimposed on the intensities in the entire grid with a mean of zero and variance  $\sigma^2$ , then the error in  $A$  will result from the addition of  $M \times M$  intensities values, hence

$$\sigma_A^2 = \sum_{k=1}^{M^2} \sigma^2 = M^2 \sigma^2 \quad (6.4)$$

If Equation 6.3 is rewritten as

$$COM_x = \frac{C}{A} \quad (6.5)$$

where

$$C = \sum_{i=1}^M i B_i \quad \text{and} \quad B_i = \sum_{j=1}^M I(i, j) \quad (6.6)$$

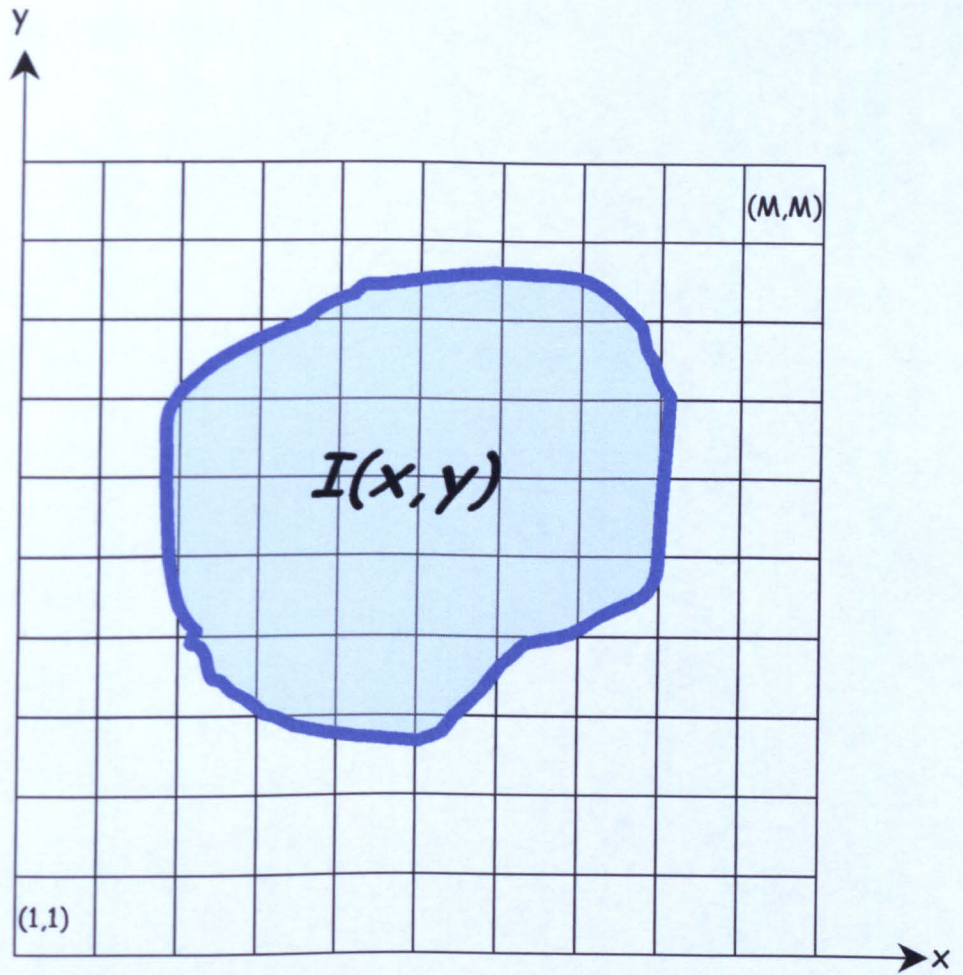


**Figure 6.1** Portion of image containing an object represented by intensity distribution  $I(x,y)$ . The centre of mass of the intensity values, is calculated over the square from pixel coordinate (1,1) to (M,M), relative to the portion of the image chosen.

## 6. Propagation of Errors in Stereotaxis

---

then, as for the error in  $A$ ,

$$\sigma_B^2 = \sum_{j=1}^M \sigma^2 = M\sigma^2 \quad (6.7)$$

and\*

$$\begin{aligned} \sigma_C^2 &= \sum_{i=1}^M i^2 \sigma_B^2 \\ &= M\sigma^2 \sum_{i=1}^M i^2 \\ &= \frac{1}{6} M^2 (M+1)(2M+1) \sigma^2 \end{aligned} \quad (6.8)$$

From Equation 6.5

$$\begin{aligned} \sigma_{COM_x}^2 &= \frac{C^2}{A^2} \left( \frac{\sigma_C^2}{C^2} + \frac{\sigma_A^2}{A^2} \right) \\ &= (COM_x)^2 \left( \frac{1}{C^2} \left( \frac{1}{6} M^2 (M+1)(2M+1) \right) + \frac{1}{A^2} N^2 \sigma^2 \right) \\ &= (COM_x)^2 M^2 \sigma^2 \left( \frac{(M+1)(2M+1)}{6 \left( \sum_{i=1}^M i \sum_{j=1}^M I(i,j) \right)^2} + \frac{1}{\left( \sum_{i=1}^M \sum_{j=1}^M I(i,j) \right)^2} \right) \end{aligned} \quad (6.9)$$

Equation 6.9 gives an expression for the error in the calculated centre of mass of a spatially undistorted object in an image under the influence of noise, along the  $x$  axis.  $\sigma_{COM_x}^2$  varies with the level of noise, and strongly depends on  $M^2$ . A similar expression (with the indices  $i$  and  $j$  reversed) will give the error along the  $y$  axis. For a fiducial rod in an image detected by the centre of mass method

$$FLE^2 = \sigma_{COM_x}^2 + \sigma_{COM_y}^2 \quad (6.10)$$

CT images were acquired of the stereotactic phantom for the work presented in Chapter 5 using a Siemens Somatom Plus CT scanner. The voxel size was  $0.72 \times 0.72 \times 3.00$  mm. From regions placed over areas of water in the phantom, a typical intensity was 1035 with variance of 30. A typical intensity of a fiducial rod was 1500 and the rod diameter was 7 pixels. The expression derived above

---

\*from the relationship that if  $w = xy$  then  $\sigma_w^2 = \sigma_x^2 \left( \frac{\partial w}{\partial x} \right)^2 + \sigma_y^2 \left( \frac{\partial w}{\partial y} \right)^2$

## 6. Propagation of Errors in Stereotaxis

---

was included in the section of the computer program written to analyse the stereotactic images in Chapter 5 and when applied to fiducial rods with CT imaging parameters as described above, resulted in typical values for the  $FLE$  of  $6.3 \mu\text{m}$ . The value of  $M$  used was 15, and the positioning of the grid over each fiducial rod was performed manually. In order to allow a large value of  $M$  (to reduce the chance of missing pixels contributing to the fiducial rod) while reducing the effect of large  $M$  in Equation 6.9, a threshold of 10% (between maximum and minimum intensity values) was applied to all pixels in the grid and only those above the threshold were included in the COM or error calculations.

For the BRW fiducial system, typical values of  $f_k$  in Equation 6.1 are 130 mm, *i.e.*, the distance of a diagonal fiducial rod from the centre of the fiducial system. For a target chosen at the centre of the fiducial system (*i.e.*,  $d_k = 0$ ) and using the three diagonal fiducial rods to calculate the STM (*i.e.*,  $N=3$ ), Equation 6.1 gives the  $TRE=3.6 \mu\text{m}$ . For a target where all values of  $d_k=50$  mm, the  $TRE=3.9 \mu\text{m}$ . As the target itself will be chosen on the scale of a pixel, the  $TRE$  in targets calculated from CT images is negligible.

Although it would be expected that the major contribution to  $FLE$  in MR images would be spatial distortion, it is useful to obtain a measure for  $FLE$  in MR images assuming no spatial distortion. MR images also were acquired of the stereotactic phantom for the work presented in Chapter 5 using a Siemens 1.5 T Vision MR scanner. In this case, images acquired using a standard spin warp spin echo sequence were used, with a bandwidth per point in the frequency encoding direction of 130 Hz. The voxel size in the images was  $1.0 \times 1.0 \times 3.0$  mm. A typical mean intensity of water in the images was 550 with a variance of 104. A typical intensity of a fiducial rod (tap water) was 1900 with a diameter of 4 pixels. Typical  $FLE$ 's measured by the computer program were  $27.0 \mu\text{m}$ . Although larger than the  $FLE$  measured from CT images, this is still much smaller than the size of a pixel. Substituting this value into Equation 6.1 as before, for a target at the centre of the fiducial system, the  $TRE$  would be  $15.6 \mu\text{m}$ . For a target where all values of  $d_k=50$  mm,  $TRE=17.4 \mu\text{m}$  where a typical  $f_k$  is 110 mm for the MRI compatible fiducial frame.

This section has outlined a method for estimating the  $FLE$  in images using a

## 6. Propagation of Errors in Stereotaxis

---

centre of mass method. In practice, this error is far smaller than that often used in perturbation studies to evaluate the propagation of errors in the stereotactic process. When used in combination with the equation derived by Fitzpatrick *et al.* to relate the *FLE* to the *TRE*, a *TRE* of less than 0.01 mm is obtained from CT images, and less than 0.02 mm from MR images. This suggests that the *TRE* of targets chosen from images is negligible compared to other errors in the stereotactic process, such as those summarized in Section 6.1 above. It also demonstrates that the centre of mass method is adequate for the detection of the centre of fiducial rods.

### 6.3 TRE due to FLE and TLE in MRI

Fitzpatrick *et al.*<sup>30</sup> have derived an equation (Equation 6.1) relating the *TRE* to the *FLE*. It would be useful to have a similar expression relating the *TRE* to both the *FLE* and the *TLE*, however deriving such an expression along the lines of Equation 6.1 was not the approach taken in this thesis. In Chapter 5, a phantom was used to measure errors in the *TRE* when calculated from MR images. Both the fiducial rods and target points were localized using a centre of mass method. In Section 6.2 above, it has been shown that the *FLE* in CT images is negligible when a centre of mass method is used to detect the centre of the fiducial rods. If the target point in CT images was also selected by a centre of mass method, as is possible with certain structures in a phantom and as was done with the phantom used in this work, then it would be expected that the *TRE* would remain negligible. Therefore, the difference between the target coordinate in stereotactic space of the same phantom point, calculated from both CT and MR images, will yield the *TRE* due to any spatial distortion present in the MR images. In this case, the *TRE* from MRI will include the effects from the *TLE* as well as the *FLE*. Although an analytical expression for *TRE* which depends on both *FLE* and *TLE* is not available, its properties may still be examined experimentally. In Chapter 5, Chang & Fitzpatrick's single slice reversed gradient correction method was used to measure the spatial distortion in both the fiducial rods and the phantom they surrounded. This may be considered a direct measurement of *FLE* and *TLE* due to spatial distortion. Assuming

## 6. Propagation of Errors in Stereotaxis

---

that  $TLE=0$ , the measured  $FLE$  may be substituted into Equation 6.1 and the resultant  $TRE$  calculated. This can be compared with the directly measured  $TRE$  and differences may be attributed to the (unknown) effect of the  $TLE$ .

For the work in this section, only one typical MR image of the phantom will be considered, in order to demonstrate the technique. A slice was chosen from the data presented in Section 5.4 with slice position  $z=20$  mm as a typical slice in which the multiple edge detection required to identify all the fiducial rods, had worked well. Only the non-diagonal phantom rods will be considered as their in-slice position is less likely to change with through-slice distortion. The diagonal phantom rods could also have their in-plane position changed by through-slice distortion. This was felt to be appropriate and consistent because the single slice reversed gradient correction method used to measure the  $FLE$  and  $TLE$  only corrects (and hence measures) in-slice spatial distortion.

### 6.3.1 TLE and FLE in MR Images from Reversed Gradient Correction

By application of Chang & Fitzpatrick's reversed gradient correction method to the MR images of the stereotactic phantom (see Section 5.4), the in-slice  $TLE$  and  $FLE$  could be measured directly. The values quoted are the mean distortion values over a rod, calculated by the stereotactic computer program. For the rods in the phantom which appear as regions of low signal in the MR images, the mean distortion around the rods was measured and this was taken as the distortion at the centre of the rod. The results for the fiducial rods are shown in Table 6.1, for the phantom rods in Table 6.2, and graphically in Figure 6.2. The pixel coordinates of each rod are also given, with their origin shifted to the centre of the fiducial system. The pixel coordinates are given as measured in the distorted MR image, and after correction using the reversed gradient method; the difference between these two coordinates (*i.e.*, the distortion) also is listed. All results in these tables have been converted to millimetres, using the pixel dimensions quoted by the MR scanner.

From Tables 6.1 and 6.2, along with Figure 5.18, it can be seen that the spatial distortion measured in the fiducial rods is much larger (by a factor of

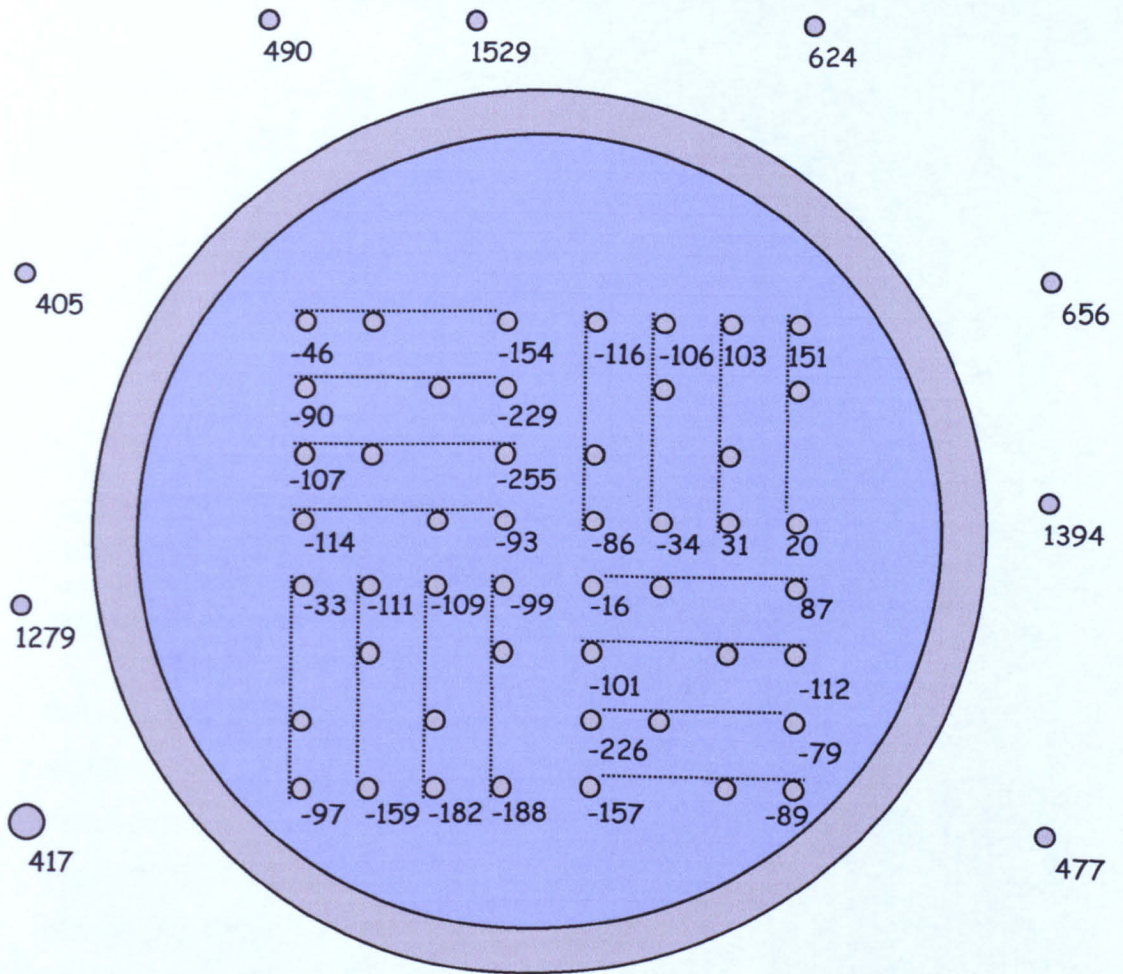


**Figure 6.2** Distortion of the fiducial rods and target points in the phantom measured from MRI using the reversed gradient correction method.

Values are in micrometres, for a typical MRI slice ( $z=-20$  mm scanning sequence se\_12b130.wkc voxel size  $1 \times 1 \times 3$  mm).

The frequency encoding axis was horizontal. Positive distortion is to the right. It is interesting to note that the distortion of the diagonal fiducial rods is larger than the straight fiducial rods.

## 6. Propagation of Errors in Stereotaxis

Fiducial rod number	Uncorrected $x$ pixel coordinate	$x$ distortion	Corrected $x$ pixel coordinate	$y$ pixel coordinate
0	-99.016	0.417	-98.599	60.971
1	-101.134	1.279	-99.855	-41.538
2	-100.696	0.405	-100.291	-58.202
3	-61.090	0.490	-60.600	-104.370
4	42.159	1.529	43.688	-104.952
5	59.149	0.624	59.773	-105.316
6	99.979	0.656	100.635	-60.939
7	100.440	1.394	101.834	40.243
8	101.675	0.477	102.152	58.170

Table 6.1: Coordinates of the centre of mass of each fiducial rod. The mean distortion of each rod, measured by the reversed gradient correction method, is listed and a corrected  $x$  coordinate (frequency encoding axis) is calculated. The fiducial rod numbering starts with the largest diameter rod, 0, and increments clockwise.

between 5 and 10) than that throughout the phantom. This suggests that in practice, the  $FLE$  will be larger than the  $TLE$  in MRI. Two factors appear to be working in opposition in MR images used for stereotactic planning. Equation 6.1 suggests that to minimize the  $TRE$  the fiducial markers should be as far from the centre of the fiducial system as possible (*i.e.*, increasing the  $f_k$ 's), while increasing the distance of the fiducial markers from the magnet's isocentre will increase the spatial distortion that they experience, thus increasing their  $FLE$  and the associated  $TRE$ .

It is also apparent that the fiducial rods which cross the imaging plane diagonally (namely rods 1, 4, and 7) exhibit larger amounts of spatial distortion along the frequency encoding axis, despite being slightly closer to the magnet's isocentre than the other fiducial rods. This may be explained by considering a cylinder of differing magnetic susceptibility to its surroundings (such as a fiducial rod) placed in a static magnetic field,  $B_0$ , with its long axis parallel to the direction of  $B_0$ . This configuration results<sup>19,94</sup> in no perturbation of the magnetic field outside the cylinder and a constant  $B_e$  inside the cylinder of  $\frac{\Delta\chi}{3}B_0$ , where  $\Delta\chi$  is the difference in magnetic susceptibility between the material inside and outside the cylinder. This will result in spatial shifting of the cylinder along the frequency encoding axis of a spin warp MRI acquisition. If the cylinder is considered to be made of water ( $\chi_{water} \approx -9 \times 10^{-6}$  ppm) and surrounded by air ( $\chi_{air} \approx 0$ ) then at a static magnetic field strength of 1.5 T, the inside of a fiducial

## 6. Propagation of Errors in Stereotaxis

Phantom rod number	Uncorrected $x$ pixel coordinate	$x$ distortion	Corrected $x$ pixel coordinate	$y$ pixel coordinate
0	-53.629	-0.046	-53.675	-47.616
2	-7.425	-0.154	-7.579	-48.785
3	6.512	-0.116	6.396	-52.758
4	20.627	-0.106	20.524	-53.511
5	34.768	0.103	34.871	-53.756
6	48.293	0.151	48.444	-53.933
7	-53.462	-0.090	-53.552	-33.684
9	-7.013	-0.229	-7.242	-34.657
14	-52.864	-0.107	-52.971	-19.463
16	-6.505	-0.255	-6.760	-20.753
17	7.266	-0.086	7.180	-7.268
18	21.296	-0.034	21.262	-7.444
19	34.897	0.031	34.928	-8.036
20	49.118	0.020	49.138	-8.211
21	-52.510	-0.114	-52.624	-5.604
23	-6.142	-0.093	-6.235	-6.739
24	7.355	-0.016	7.339	6.199
26	53.597	0.087	53.684	5.636
27	-48.229	-0.033	-48.262	8.098
28	-34.054	-0.111	-34.165	7.220
29	-20.022	-0.109	-20.131	7.228
30	-5.278	-0.099	-5.377	6.429
31	8.190	-0.101	8.089	20.646
33	53.974	-0.112	53.862	19.795
38	8.751	-0.226	8.525	34.582
40	54.343	-0.079	54.264	33.652
41	-46.989	-0.097	-47.086	53.724
42	-32.865	-0.159	-33.024	53.563
43	-18.786	-0.182	-18.968	53.425
44	-4.834	-0.188	-5.022	52.933
45	9.100	-0.157	8.943	49.873
47	54.917	-0.089	54.828	47.381

Table 6.2: Coordinates of the centre of mass of each phantom rod. The mean distortion around each rod, measured by the reversed gradient correction method, is listed and a corrected  $x$  coordinate (frequency encoding axis) is calculated. The phantom rod numbers are shown in Figure 5.4.

## 6. Propagation of Errors in Stereotaxis

---

rod will experience  $B_e \approx -4.5 \times 10^{-6}$  T. Expressed as a frequency offset,  $\Delta f \approx (-4.5 \times 10^{-6}) \times (42.57 \times 10^6) = -191$  Hz. For the spin warp MRI acquisition used the bandwidth per pixel was 130 Hz and one pixel had dimensions of 1 mm in the frequency encoding direction. Therefore the expected spatial distortion of a fiducial rod would be 1.5 mm along the frequency encoding axis. This compares with a typical measured spatial distortion of fiducial rods with long axes parallel to  $B_0$  of 0.5 mm. The difference is likely to be due to an incorrect value for  $\Delta\chi$  being used, as the fiducial rod is constructed of a plastic rod filled with tap water.

If all fiducial rods were parallel to  $B_0$  the spatial distortion described above would not be a problem for the case of the stereotactic phantom used. The phantom is also a cylinder parallel to  $B_0$  and so its interior would also be spatially distorted by the same amount as the fiducial rods. However, this would not be the case for other objects, such as a human head.

If the cylinder is tilted around one of its short axes away from its long axis being parallel to  $B_0$  then a magnetic field exterior to the cylinder will be created as well as the constant field inside the cylinder. In the extreme case of the cylinder being tilted by  $90^\circ$  (*i.e.*, so that its long axis is perpendicular to  $B_0$ ), the solution of both the internal and external  $B_e$  fields is well known.<sup>19,62,94</sup> In particular, the internal field is  $-\frac{\Delta\chi}{6}B_0$  to a first approximation.<sup>19</sup> For intermediate angles, the internal field would be expected to range between  $\frac{\Delta\chi}{3}B_0$  and  $-\frac{\Delta\chi}{6}B_0$ . The result of this, applied to MRI of fiducial systems containing rods in 'N' configurations is that it is expected that rods will undergo differing amounts of spatial distortion depending on their individual orientation to  $B_0$ . The rods parallel to  $B_0$  (and the cylindrical phantom) all will be shifted by the same distance along the frequency encoding axis, while the diagonal fiducial rods will experience a different  $B_e$  and so be shifted by a different amount. This explains the differential spatial distortion measured in the parallel and diagonal fiducial rods.

The majority of the NMR signal will come from water in the main phantom. This will dominate the automatic measurement of resonant frequency performed by the MR scanner. This NMR signal will be offset due to the  $B_e$  inside the phantom of  $\frac{\Delta\chi}{3}B_0$  and this will be largely compensated for by the adjustment of

## 6. Propagation of Errors in Stereotaxis

---

resonant frequency. This will reduce the distorting effect of  $B_e$  on the phantom and fiducial rods parallel to it. The diagonal fiducial rods experience a different internal  $B_e$  and they will have little effect on the setting of resonant frequency. Therefore, the setting of resonant frequency will compensate less of the internal  $B_e$  of the diagonal rods, and may even emphasize it. This explains why the measured spatial distortion is worse in the diagonal fiducial rods relative to the parallel rods.

### 6.3.2 Calculation of STM's and TRE's

From the results presented in Tables 6.1 and 6.2, two STM's may be calculated from MR images, and final treatment coordinates calculated for each phantom rod. The difference between these coordinates will highlight the effects of  $FLE$  and  $TLE$ .

Using the uncorrected fiducial rod coordinates from Table 6.1 and the calculations from Section 5.2.2, an 'uncorrected' STM may be calculated. It gives

$$\text{STM}_u = \begin{pmatrix} 0.9950 & -0.007141 & -123.8 \\ -0.007479 & -1.0226 & 136.3 \\ -0.004004 & -0.006171 & 48.87 \end{pmatrix} \quad (6.11)$$

Using the fiducial rod coordinates corrected by the distortion value calculated from the reversed gradient correction method gives a 'corrected' STM as

$$\text{STM}_c = \begin{pmatrix} 0.9970 & -0.01334 & -124.6 \\ -0.007489 & -1.0228 & 136.3 \\ -0.0008248 & -0.01363 & 49.46 \end{pmatrix} \quad (6.12)$$

In either case, the treatment point  $(x,y,z)$  is calculated from the in-slice pixel coordinates  $(X,Y)$  by

$$\begin{pmatrix} x \\ y \\ z \end{pmatrix} = \text{STM} \times \begin{pmatrix} X \\ Y \\ 1 \end{pmatrix} \quad (6.13)$$

and the  $TRE$  calculated as the difference between the coordinates of the same treatment point calculated from MR and CT images.

## 6. Propagation of Errors in Stereotaxis

---

These can be applied to give various  $TRE$ 's, relative to CT, for the phantom rods and the results are shown in Tables 6.3, 6.4, and 6.5. If  $STM_u$  is applied to uncorrected phantom rod coordinates,  $TRE_{uu}$  is obtained, quantifying the  $TRE$  from uncorrected fiducial rods and uncorrected phantom rods. If  $STM_c$  is applied to the uncorrected phantom rod coordinates,  $TRE_{cu}$  is obtained, *i.e.*, the  $TRE$  from corrected fiducial rods and uncorrected phantom rods. Finally, if  $STM_c$  is applied to the corrected phantom rod coordinates,  $TRE_{cc}$  is obtained. While the  $TRE$ 's are quoted as the total in-slice error,  $TRE_x$  and  $TRE_y$  are also tabulated separately. All calculations were performed by the computer program written to analyse the stereotactic images (see Chapter 5).

For comparison with other published results, both the mean  $TRE$  across the slice was calculated and the 'worst case' error (taken at the 99.9% confidence interval, assuming a normal distribution). For the  $TRE_{uu}$  these were 1.454 mm and 2.168 mm respectively, and for  $TRE_{cc}$  the corresponding values were 0.497 mm and 0.929 mm.

From considering the STM's above with Equation 6.13, it can be seen that the final  $x$  coordinate will depend mostly on the  $X$  pixel coordinate and the final  $y$  coordinate will depend mostly on the  $Y$  pixel coordinate. This is because the first two diagonal terms are close to unity while the off diagonal terms are small, as a result of the orientation of the fiducial system relative to the MR images. This explains why, for the orientation of the fiducial system to image axes chosen, correcting the spatial distortion along the horizontal frequency encoding  $x$  axis improved the  $TRE_x$  but made little difference to the  $TRE_y$ . Although already suggested in Section 5.5.4 and shown in Figure 5.24 that there might be a preferable orientation of the fiducial system to the imaging axes, this is a subject that should be investigated further.

Equation 6.1 was also applied to these data. A weakness of this equation would appear to be that it only considers one value for  $FLE$  throughout each slice. This may be reasonable in consideration of  $FLE$ 's from CT images where the  $FLE$  may depend on a global parameter such as noise or the centre of marker localization method used. However, in MR images it might be expected, and indeed has been shown in Table 6.1 and argued in Section 6.3.1, that the

## 6. Propagation of Errors in Stereotaxis

Fiducial rod number	$TRE_{uu}$ (mm)			$TRE_F$ (mm)
	x	y	$\sqrt{x^2 + y^2}$	
0	1.180	-0.588	1.318	0.354
2	1.078	-0.554	1.212	0.337
3	0.823	-0.657	1.053	0.340
4	0.885	-0.667	1.108	0.343
5	0.752	-0.773	1.050	0.348
6	0.604	-0.788	0.993	0.355
7	1.267	-0.402	1.329	0.348
9	1.247	-0.582	1.376	0.330
14	1.303	-0.389	1.360	0.342
16	1.205	-0.557	1.327	0.325
17	1.270	-0.509	1.368	0.323
18	1.228	-0.629	1.380	0.325
19	1.088	-0.484	1.190	0.330
20	1.227	-0.598	1.365	0.338
21	1.430	-0.336	1.469	0.340
23	1.309	-0.574	1.429	0.323
24	1.427	-0.372	1.475	0.323
26	1.227	-0.648	1.387	0.341
27	1.599	-0.276	1.622	0.338
28	1.597	-0.312	1.627	0.330
29	1.579	-0.356	1.619	0.325
30	1.610	-0.389	1.656	0.322
31	1.453	-0.346	1.493	0.325
33	1.362	-0.468	1.440	0.343
38	1.663	-0.453	1.724	0.330
40	1.486	-0.524	1.576	0.348
41	1.760	-0.348	1.823	0.354
42	1.815	-0.265	1.834	0.347
43	1.880	-0.242	1.896	0.343
44	1.685	-0.377	1.727	0.340
45	1.743	-0.381	1.784	0.339
47	1.433	-0.501	1.518	0.355
mean			1.454	
standard deviation			0.238	

Table 6.3: The directly measured uncorrected  $TRE$  ( $TRE_{uu}$ ) taken as the difference between the treatment point of each phantom rod calculated from MR and CT images. The phantom rod numbers are shown in Figure 5.4. Also, the  $TRE_F$  calculated by Equation 6.1.

## 6. Propagation of Errors in Stereotaxis

Fiducial rod number	$TRE_{cu}$ (mm)		
	x	y	$\sqrt{x^2 + y^2}$
0	0.029	-0.586	0.587
2	0.025	-0.555	0.556
3	-0.174	-0.657	0.680
4	-0.080	-0.670	0.674
5	-0.186	-0.729	0.752
6	-0.307	-0.786	0.843
7	0.035	-0.400	0.401
9	0.109	-0.586	0.596
14	-0.014	-0.391	0.391
16	-0.011	-0.564	0.564
17	-0.008	-0.516	0.516
18	-0.023	-0.639	0.639
19	-0.132	-0.491	0.509
20	0.033	-0.607	0.607
21	0.028	-0.339	0.340
23	0.003	-0.579	0.579
24	0.067	-0.378	0.384
26	-0.042	-0.660	0.661
27	0.120	-0.276	0.301
28	0.135	-0.313	0.340
29	0.158	-0.359	0.393
30	0.222	-0.395	0.453
31	0.003	-0.351	0.351
33	0.008	-0.478	0.478
38	0.132	-0.458	0.477
40	0.047	-0.533	0.535
41	0.022	-0.360	0.361
42	0.067	-0.294	0.302
43	0.142	-0.262	0.298
44	0.003	-0.389	0.389
45	0.108	-0.394	0.408
47	-0.093	-0.507	0.516
mean			0.496
standard deviation			0.141

Table 6.4:  $TRE_{cu}$  calculated using the  $STM_c$  corrected for spatial distortion in the fiducial rods, but with no correction for spatial distortion in the phantom rods.

## 6. Propagation of Errors in Stereotaxis

Fiducial rod number	$TRE_{cu}$ (mm)		
	x	y	$\sqrt{x^2 + y^2}$
0	-0.017	-0.585	0.586
2	-0.128	-0.554	0.568
3	-0.289	-0.656	0.717
4	-0.186	-0.669	0.694
5	-0.134	-0.729	0.741
6	-0.157	-0.787	0.802
7	0.035	-0.400	0.401
9	-0.119	-0.584	0.596
14	-0.121	-0.390	0.408
16	-0.265	-0.562	0.622
17	-0.094	-0.515	0.524
18	-0.057	-0.639	0.641
19	-0.101	-0.492	0.502
20	0.053	-0.607	0.609
21	-0.085	-0.338	0.349
23	-0.090	-0.578	0.585
24	0.051	-0.378	0.381
26	0.045	-0.661	0.662
27	0.088	-0.275	0.289
28	0.024	-0.312	0.313
29	0.050	-0.359	0.362
30	0.124	-0.394	0.413
31	-0.098	-0.350	0.364
33	-0.104	-0.477	0.488
38	-0.093	-0.456	0.466
40	-0.032	-0.532	0.533
41	-0.075	-0.360	0.367
42	-0.091	-0.293	0.307
43	-0.039	-0.261	0.264
44	-0.184	-0.388	0.429
45	-0.049	-0.393	0.396
47	-0.182	-0.507	0.538
mean			0.497
standard deviation			0.144

Table 6.5:  $TRE_{cc}$  calculated using the  $STM_c$  and target coordinates corrected for spatial distortion.

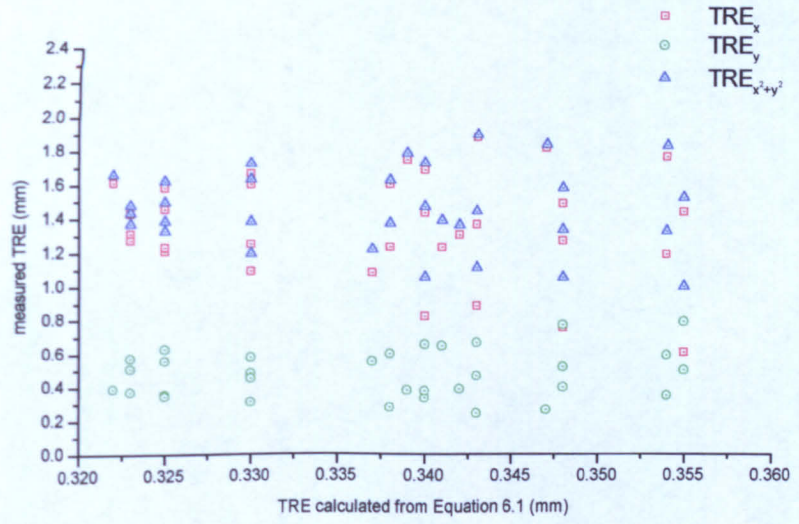
## 6. Propagation of Errors in Stereotaxis

---

$FLE$  due to spatial distortion is fiducial marker specific, and so the use of a single global  $FLE$  may not be so wise. The  $TRE$  calculated from Equation 6.1 is termed  $TRE_F$ . From Table 6.1,  $\langle FLE^2 \rangle$  was calculated to be  $0.311 \text{ mm}^2$ . The results for  $TRE_F$  are shown in the right hand column in Table 6.3. As  $\langle FLE^2 \rangle$  was calculated from the uncorrected fiducial rod pixel coordinates, it might be expected that  $TRE_F$  would correlate with the observed  $TRE_{uu}$ . However, as can be seen from Table 6.3 and the scatter plots in Figure 6.3, this does not appear to be the case. This could be explained by the relatively large variation in  $FLE$  between individual fiducial rods in MRI.

From the results presented in this section, it would appear that the main cause of  $TRE$  calculated from MR images is the spatial distortion in the fiducial rods. Correction of this distortion by the reversed gradient correction method decreases the measured  $TRE$  by a factor between 2 and 6. Similar results have been reported on a patients,<sup>27</sup> although as discussed in Chapter 4, it is not thought that the use of anatomical landmarks is suitable for the evaluation of  $TRE$ . The near elimination of  $TRE$  along the frequency encoding direction by the reversed gradient correction method (see Table 6.4) suggests that the implementation of the reversed gradient correction method with multiple edge detection works well. As mentioned above, for the orientation of fiducial system to imaging axes used for these measurements, it would be expected that distortions along an imaging axis would mainly affect the  $TRE$  along the same axis after being transformed by the STM. This is borne out by the observation that correction of distortion along the frequency encoding axis in the image predominantly affects the  $TRE$  along the  $x$  axis; the  $TRE$  along the  $y$  axis remains unaffected by the correction. The magnitude of the  $TRE$  along the  $y$  axis is surprising as it would not be expected that distortion would be observed along the phase encoding axis. As it remains fairly constant throughout the phantom (and in fact becomes the dominant source of  $TRE$  after application of the reversed gradient correction method), it may be that it is due to a mechanical difference in the set up of the apparatus between MR and CT image acquisitions. It is interesting to note that this error is comparable to that which would be estimated from the work of Maciunas *et al.*<sup>63</sup> for the weight of the phantom (180 N). The difference could

**Figure 6.3** Plots of TRE measured from a phantom against TRE calculated by Equation 6.1. No correlation is seen.



## 6. Propagation of Errors in Stereotaxis

---

also partly be explained from the difference in set up of the apparatus between CT and MR imaging. For CT imaging, the GTC head ring was rigidly attached to the couch, supporting both the phantom and fiducial system. During MR imaging, the apparatus was placed in the RF head coil resulting in most of the weight being supported by the fiducial system. It would not be surprising if the position of the phantom relative to the fiducial system changed between these two set ups. This would be an important consideration for future experiments and apparatus design, especially for MR imaging where rigid attachment of the head ring to the couch without stressing the fiducial system against the head coil could be relatively difficult.

Inclusion of correction of the relatively small amount of spatial distortion of the target points made no noticeable difference to the  $TRE$ . While it is encouraging to see that a small  $TLE$  does not lead to a large  $TRE$ , unfortunately no further insight into the relationship between  $TRE$  and  $TLE$  can be gained. However, this is an area which may benefit from the use of computer perturbation studies. As seen above, the application of perturbation studies examining the effect of random shifts of all fiducial rods to spatial distortion in MR images may not be valid. This is because the fiducial rods which are not parallel to  $B_0$  would be expected to experience larger amounts of distortion than those parallel to  $B_0$ . Also, the distortion due to this effect is in the same direction along the frequency encoding axis for all fiducial rods; both these effects result in a non-random pattern of distortion of the fiducial rods. However, in the case of the examination of the effect of  $TLE$  on  $TRE$  in MRI, perturbation studies may be more useful as they would only consider the perturbations of a single point.

### 6.4 Discussion and Conclusions

The major sources of error in a frame based stereotactic process, from imaging to treatment, have been outlined and their magnitude assessed with reference to previously published literature.

A method for estimating the error in localization of the centre of a fiducial rod,  $FLE$ , using a centre of mass method, has been described. This demonstrates that the centre of mass method results in a typical  $FLE$  of less than 0.05 mm

## 6. Propagation of Errors in Stereotaxis

---

in an undistorted image.

The spatial distortion of the fiducial rods in MR images was measured and found to be of the order of one millimetre. It was observed that the diagonal fiducial rod in the 'N' configurations experienced between two and three times more spatial misregistration than the parallel rods. A possible reason for this due to magnetic susceptibility differences was discussed. This observation suggests that studies examining the effect of *FLE* in MRI should consider systematic and anisotropic as well as random perturbations of the *FLE*.

The error in the final target coordinate, *TRE*, planned from MRI has been examined in more detail for a single slice than was done in Chapter 5, using a phantom. By use of Chang & Fitzpatrick's reversed gradient correction method it was found that the major source of *TRE* was spatial distortion of the fiducial rods. Correcting the distortion in the fiducial rods reduced the *TRE* in the phantom from between 1.0 mm and 1.9 mm to between 0.3 mm and 0.8 mm. This results in the *TRE* being comparable, and in some cases less than, errors from other portions of the stereotactic process. It also is comparable to the *TRE*'s measured elsewhere; in particular to those measured of rods in a cadaver's head by Sumanaweera *et al.*<sup>107</sup> using a 1.5 T MRI system, who quote uncorrected *TRE*'s of between 1.5 mm and 2.6 mm, reduced to between 0.4 mm and 0.5 mm after reversed gradient correction. Correction of MR images by the reversed gradient method has been ruled out in clinical practice due to the potential induction of artefacts (see Chapter 4). However, as the main source of *TRE* appears to be the distortion in the fiducial rods, it could be advantageous to quickly manually segment the fiducial rods and object in the MR images and apply the reversed gradient correction to the fiducials rods alone. This would remove a major contribution to the *TRE* without the risk of introducing artefacts into the images which will be clinically interpreted.

To judge the importance of the *TRE* from MRI, it is necessary to compare this error with other expected errors from the stereotactic process. The following values are qualitative estimates of typical values reported in various publications, along with the *TRE* measured here. The list is far from exhaustive; in particular errors reported by Maciunas *et al.*<sup>63</sup> associated with weight-bearing have been

## 6. Propagation of Errors in Stereotaxis

	mean	'worst case'
Clinical target selection	1.0	4.0
Frame reapplication	0.3	0.8
Mechanical inaccuracies (including brain motion or linac isocentre movement)	1.0	4.0
TRE from MRI (uncorrected / corrected)	1.5 / 0.5	2.2 / 0.9
Treatment error (uncorrected / corrected)	2.1 / 1.5	6.1 / 5.8
Treatment error (assuming TRE=0)	1.4	5.7

Table 6.6: Estimation of typical values of errors of various processes in a stereotactic treatment. All values are in millimetres.

excluded. This is not because they are considered unimportant but because their source is unclear and may be compensated for in many existing stereotactic procedures. For example, the devices for rigidly attaching the head ring to couches in Nottingham have adjustments to allow the frame to be brought to the vertical, as defined by calibrated isocentric lasers. Once this has been performed, it would be expected that any deformations of the head ring due to effects of the patient's weight would be constant between imaging and treatment. The estimated values are summarized in Table 6.6. The final treatment error is estimated by assuming that the individual errors are independent and may be added in quadrature. The treatment error arising if  $TRE=0$  is also included for comparison, to allow the size of the contribution of error from the  $TRE$  from MRI to be judged. These values are comparable to estimates of treatment errors published elsewhere, and summarized in earlier sections of this chapter.

Table 6.6 suggests that a  $TRE$  of 0.5 mm from MRI would not contribute significantly to the treatment error, assuming that reasonable values for the other errors have been chosen. Even if the  $TRE$  is larger than 1 mm, it only results in a relatively small increase in the treatment error. Although these estimates of the various errors involved are only approximate, they demonstrate the point that in order to judge the significance of a calculated  $TRE$ , it must be compared to other errors in the stereotactic process. In particular, values such as these should be borne in mind by the clinician when planning stereotactic treatments.

It is interesting to note that the errors in  $TRE$  arising from MR images acquired in the presence of a stereotactic head ring and fiducial system are of

## 6. Propagation of Errors in Stereotaxis

---

the order of  $TRE$  reported elsewhere from the three dimensional registration of MR to CT images.<sup>41,42,115,118</sup> It should be mentioned, however, that a range of measures of the success of the registrations was used in these works. That used by West *et al.*<sup>118</sup> is probably the closest to the  $TRE$  used in this chapter. This suggests that the perceived advantages (*i.e.*, increased accuracy) of using a frame based fiducial system for both MR and CT imaging may not materialize in practice. If this is the case, then many benefits would be obtained by removing the constraint of having to acquire MR images of the patient with the stereotactic apparatus, not least the increased comfort of the patient, the increased flexibility of the schedule for performing the MRI scan, and the potential of registering post-treatment images to the images used for planning in order to assess the success and accuracy of the actual treatment. This conclusion has been reached by many researchers several years ago and investigated further, to the extent that the suppliers of the BRW stereotactic system, Radionics, currently market a package to register MR images acquired in the absence of a fiducial system to CT images acquired with the BRW head ring and fiducial attached, with the USA's FDA approval.

Despite the amount of work published in recent years regarding the use of MRI for stereotactic planning, it is felt that the point raised by Maciunas *et al.*<sup>63</sup> and mentioned in Section 6.1 above, regarding the importance of the 'worst case' error still stands and has not been fully addressed. It is felt that what will finally convince the majority of clinicians involved in stereotactic treatments of the validity of the use of MRI in stereotaxis is not the numerical accuracy alone, but the quantification of any addition risk to their patients compared to their experience of planning from CT.

# Chapter 7

## Conclusion

The main aim of the work presented in this thesis was to implement a thorough method for quantifying the errors introduced in a neurosurgical frame-based stereotactic procedure by the use of MR rather than CT imaging techniques. To do so, Chang & Fitzpatrick's reversed gradient correction method was implemented, validated, and used.

Spatial distortion in MR images typically led to an error in the final target coordinates of between 1 mm and 2 mm. The main source of this distortion was identified as the MRI compatible GTC head ring used.

Correction of the spatial distortion was possible; this reduced the typical error in the final target coordinate to less than 0.5 mm. However, artefacts were observed in some corrected images produced by the reversed gradient method. The main source of these were believed to be imperfect edge detection in the MR images. Due to the potential problems of artefacts in corrected images, interfering with clinical interpretation of the images, it was concluded that the reversed gradient correction method should not be used to produce corrected images for stereotactic procedures. Its use was limited to the production of quantified distortion maps. Typical values of distortion in localized regions in the vicinity of the final target coordinate may be provided to the clinician to aid the planning process.

In order to study some of the effects of spatial distortion in MRI, a phantom was constructed to mimic a head, containing a number of spatially discrete points. By comparison with CT images, assumed to contain no spatial distortion, the

## 7. Conclusion

---

error in the final target coordinate then could be measured directly. The use of the phantom as a reasonable substitute for a brain was verified, in terms of distortive properties. The phantom was used to demonstrate the additional distortion caused by the stereotactic apparatus, in particular the GTC head ring.

The effect of different MRI acquisition schemes on *spatial distortion* of the final target coordinate was studied. It was found that the amount of distortion varied with the bandwidth per point of the acquisition only, and not with the sequence type. These measurements were repeated, with similar findings, on a second MRI scanner with the same magnetic field strength of 1.5 T but with a different construction. No significant difference was seen between spatial distortion on both MRI scanners, for comparable image acquisitions. This study highlighted the importance of quoting MRI acquisition parameters, in particular bandwidth per pixel, when publishing or discussing results. Without these details, comparison between imaging centres is difficult, reducing the ability to appreciate the results and conclusions of others in a local setting.

Once the error in the final target coordinate, determined from MR images, was measured, it could be considered along with other errors which occur in a stereotactic process. This was investigated, with reference to errors published elsewhere, to allow the effect of the error introduced by spatial distortion in MRI to be considered on the coordinate of the actual point treated. This brief analysis found that the use of MR rather than CT images would increase the mean error in typical treatment coordinate from about 1.4 mm to 2.1 mm.

The use of MRI for planning frame-based stereotactic procedures increases the error in the treatment coordinate. However, whether this is important will need to be judged clinically on a case by case basis. It also should be viewed with the findings published elsewhere, that the accuracy of the actual treatment point in a neurosurgical stereotactic procedure planned using CT images is unlikely in itself to be sub-millimetric.

With the contribution of spatial distortion in MRI quantified, it would appear that three courses of action may be taken regarding the use of MR images in stereotactic planning -

1. Accept the additional error in the treatment coordinate due to spatial dis-

## 7. Conclusion

---

tortion present in MRI. For many clinical cases, an error of a few millimetres may be acceptable. In particular, it may be that an increased contribution to the treatment error from spatial distortion is offset by improved localization of some targets due to the improved soft tissue contrast in MRI. While the contribution to the treatment error from spatial distortion in CT images is negligible, the error in visually locating the target often may be greater. Considerations such as these are difficult to quantify, yet may be an important contribution to the treatment error. They are usually ignored in the conclusions of studies considering the accuracy of stereotaxis and thus may not allow a true comparison between the use of MRI and CT to be assessed.

2. Application of a distortion correction method prior to performing the stereotactic planning. Both the reversed gradient and phase map correction methods have been applied to MRI previously in other centres. The reversed gradient correction method has been used in this work. It was concluded that while the reversed gradient correction method could be applied to MR images acquired in a stereotactic setting, it was not wise to use it to produce corrected images to be interpreted clinically due to the potential of introducing artefacts. Although not studied in detail here, the phase map correction method also suffers from limitations in application to MR images of stereotactic apparatus. Limitations of both techniques may be overcome by further work.
3. Frameless MRI stereotaxis. As mentioned in Chapter 6, the additional error introduced by using MR images in stereotactic planning is similar to the error measured after frameless co-registration has been performed between MR and CT images. This raises the possibility of acquiring MR images without the presence of any stereotactic apparatus and registering these images to CT images acquired of a patient attached to the stereotactic apparatus. This has been investigated and implemented in a few centres and its use becoming more generally accepted. This method has a number of advantages. The patient is not attached to the stereotactic apparatus

## 7. Conclusion

---

for the MRI scan. This results in less discomfort to the patient, eliminates the sources of spatial distortion associated with the stereotactic apparatus, and allows more flexibility in the scheduling of the MRI scan. Discomfort to the patient is reduced not only due to a reduction in the duration for which they must be attached to the stereotactic apparatus, but as the apparatus no longer needs to be MRI compatible (in particular, physically small enough to fit within the RF head coil), its design may facilitate patient comfort. The possibility also exists of registering images acquired after surgery to those acquired before, to observe the accuracy of the treatment. It would appear that this route, with or without MRI distortion correction, will result in the best practical implementation for incorporating MRI into the stereotactic planning process.

It also was possible to use the reversed gradient method to correct spatial distortion and demonstrate a resulting improvement in accuracy of two contemporary echo planar based MRI techniques, namely BOLD fMRI and the production of ADC maps. A large improvement in the quality of ADC maps was observed when the reversed gradient method was used to correct EP images acquired on a Siemens Vision MR scanner. This improvement was dependent on the properties of the Vision magnet system which allowed the effects of the diffusion weighting gradients to be considered as constant throughout the EPI acquisition. However, this may not be the case for other MRI systems. The method used to apply the reversed gradient method to correct distortion in EPI fMRI data appears to be valid, although no significant improvement in the overlay of areas of activation was observed.

Finally, a comparison was performed between the reversed gradient correction method and a phase map correction method. This highlighted the strengths and weaknesses of both methods, as well as identifying some important MRI acquisition parameters. In particular, the reversed gradient method introduces unacceptable artefacts in the corrected image if applied to MR images acquired with gradient echoes or half Fourier techniques. The phase map correction method introduces fewer artefacts in to the corrected images and would appear to be the more robust method for image correction in a general MRI setting.

# Acknowledgements

I would like to acknowledge and thank the following people, without whose help the work presented here would not have been possible.

**Richard Bowtell & Brian Worthington** For their supervision and support throughout this work, from both a physics and medical perspective (Magnetic Resonance Centre, Physics Department & Academic Radiology respectively, Nottingham University).

**Dominick McIntyre** For the basic implementation details of the reversed gradient correction method as a computer program.

**Yao Ng** For implementing the phase map correction method and for collaboration for the comparison of the two distortion correction methods (Magnetic Resonance Centre).

**Ian Theakston & Bob Plant** For the construction of the stereotactic phantom and other apparatus (Magnetic Resonance Centre and Nottingham City Hospital).

**Andy Maloney** For support of this project from a medical physics perspective and his contribution to setting up a stereotactic treatment planning system in Nottingham (Nottingham City Hospital).

**Tim Jaspens & Paul Byrne** For support of this project from a clinical perspective, their contribution to setting up a stereotactic treatment planning system in Nottingham, and allowing me to acquire additional MR images on their patients (Queen's Medical Centre).

**Steve Evans & Andy Cooper** For providing radiographic support and guidance in using the clinical MRI scanners (Queen's Medical Centre).

and all the other members of the Magnetic Resonance Centre and Nottingham Hospitals who have taught me, provided me with advice and assistance, and who were responsible for providing and maintaining the equipment used. I especially would like to thank all those who volunteered to be subjects for my MRI experiments.

This document was prepared using  $\text{\LaTeX}$  2 $\epsilon$ . The diagrammatic figures were produced using Microsoft Office '97 and the graphs produced with Microcal Origin version 5.

# Bibliography

- [1] Standards Publication 300, American College of Radiologists / National Electrical Manufacturers Association, 1988.
- [2] A. L. Alexander, J. S. Tsuruda, and D. L. Parker. Elimination of eddy current artefacts in diffusion-weighted echo-planar images: The use of bipolar gradients. *Magnetic Resonance in Medicine*, 38(6):1016–1021, 1997.
- [3] George Arfken. *Mathematical Methods for Physicists*. Academic Press, third edition, 1985.
- [4] Peter J. Basser and Carlo Pierpaoli. A simplified method to measure the diffusion tensor from seven MR images. *Magnetic Resonance in Medicine*, 39:928–934, 1998.
- [5] Mark F. Bear, Barry W. Connors, and Michael A. Paradiso. *Neuroscience: Exploring the Brain*. Williams & Wilkins, 1996.
- [6] F. Bloch, W. W. Hansen, and Martin Packard. Nuclear induction. *Physical Review*, 69:127, February 1946.
- [7] C. Boesch, R. Gruetter, and E. Martin. Temporal and spatial analysis of fields generated by eddy currents in superconducting magnets – optimization of corrections and quantitative characterization of magnet gradient systems. *Magnetic Resonance in Medicine*, 20(2):268–284, 1991.
- [8] Richard W. Bowtell, Dominick J. O. McIntyre, M-J. Commandre, Paul M. Glover, and Peter Mansfield. Correction of geometric distortion in echo planar images. In *Proceedings of the SMR. 2<sup>nd</sup> Meeting*, page 411, 1994.
- [9] W. G. Bradley. A categorical course in diagnostic radiology: MR imaging. The Radiological Society of North America, 1988.
- [10] T. J. Brady. Future prospects for MR imaging. In *Proceedings of the SMRM. 10<sup>th</sup> Annual Meeting*, page 2, San Francisco, USA, 1991.
- [11] R. A. Brown. A computerized tomography-computer graphics approach to stereotactic localization. *Journal of Neurosurgery*, 50:715–720, 1979.

## BIBLIOGRAPHY

---

- [12] R. A. Brown. A stereotactic head frame for use with CT body scanners. *Investigative Radiology*, 14:300, 1979.
- [13] R. A. Brown, T. S. Roberts, and A. G. Osborn. Stereotactic frame and computer software for CT-directed neurosurgical localization. *Investigative Radiology*, 15:308–312, 1980.
- [14] Fernando Calamante, David A. Porter, David G. Gadian, and Alan Connelly. Correction for eddy current induced  $B_0$  shifts in diffusion-weighted echo-planar imaging. *Magnetic Resonance in Medicine*, 41(1):95–102, January 1999.
- [15] Paul T. Callaghan. *Principles of Nuclear Magnetic Resonance in Microscopy*. Oxford University Press, 1993.
- [16] H. Y. Carr and E. M. Purcell. Effects of diffusion on free precession in nuclear magnetic resonance experiments. *Physics Review*, 94(3):630–638, May 1954.
- [17] Hsuan Chang and J. Michael Fitzpatrick. A technique for accurate magnetic resonance imaging in the presence of field inhomogeneities. *IEEE Transactions on Medical Imaging*, 11(3):319–329, September 1992.
- [18] B. Chapman, R. Turner, R. J. Ordidge, M. Doyle, M. Cawley, R. Coxon, P. Glover, and P. Mansfield. Real-time movie imaging from a single cardiac cycle by NMR. *Magnetic Resonance in Medicine*, 5:246–254, 1987.
- [19] Simon C.-K. Chu, Yan Xu, James A. Balschi, and Charles S. Springer, Jr. Bulk magnetic susceptibility shifts in NMR studies of compartmentalized samples: Uses of paramagnetic reagents. *Magnetic Resonance in Medicine*, 13:239–262, 1990.
- [20] Stuart Clare. PhD thesis, Nottingham University, 1997.
- [21] Richard H. Clarke and Victor Horsley. On a method of investigating the deep ganglia and tracts of the central nervous system. *British Medical Journal*, 2:1799–1800, 1906.
- [22] F. Colombo, A. Benedetti, A. Pozza, R. C. Arango, G. Chiarego, and C. Marchetti. Stereotactic radiosurgery utilizing a linear accelerator. *Applied Neurophysiology*, 48:133–145, 1985.
- [23] R. Damadian. Tumour detection by nuclear magnetic resonance. *Science*, 171:115, 1971.
- [24] René Descartes. *Discours de la Méthode pour Bien Conduire sa Raison, et Chercher la Vérité dans les Sciences*. Leiden, 1637. Discourse on the Method of Rightly Conducting One's Reason, and Seeking the Truth in the Sciences.

## BIBLIOGRAPHY

---

- [25] W. C. Dickinson. Dependence of the  $F^{19}$  nuclear magnetic resonance position on chemical compound. *Physics Review*, 77(5):736–737, March 1950.
- [26] Medical Device Directorate. Guidelines for magnetic resonance diagnostic equipment in clinical use with particular reference to safety. Technical report, Department of Health, 1993.
- [27] Shan Dong, J. Michael Fitzpatrick, and Robert J. Maciunas. Rectification of distortion in MRI for stereotaxy. In *Proceedings of the 5<sup>th</sup> Annual IEEE Symposium on Computer-based Medical Systems*, pages 181–189, Durham, NC, USA, 14<sup>th</sup>–17<sup>th</sup> June 1992.
- [28] W. A. Edelstein, J. M. S. Hutchison, G. Johnson, and T. Redpath. Spin warp NMR imaging and applications to human whole-body imaging. *Physics in Medicine and Biology*, 25:751–756, 1980.
- [29] Ephraim Feig, Fred Greenleaf, and Mark Perlin. Magnetic resonance imaging with non-uniform fields. *Physics in Medicine and Biology*, 31(10):1091–1099, 1986.
- [30] J. Michael Fitzpatrick, Jay B. West, and Calvin R. Maurer, Jr. Predicting error in rigid-body point-based registration. *IEEE Transactions on Medical Imaging*, 17(5):694–702, October 1998.
- [31] A. N. Garroway, P. K. Grannell, and Peter Mansfield. *Journal of Physics C*, 7:L457, 1974.
- [32] A. Haase, J. Frahm, D. Matthaei, W. Hanicke, and K. D. Merboldt. FLASH imaging – rapid NMR imaging using low flip-angle pulses. *Journal of Magnetic Resonance*, 67(2):258–266, 1986.
- [33] E. L. Hahn. Spin echoes. *Physics Review*, 80(4):580–594, November 1950.
- [34] Joseph V. Hajnal, Nadeem Saeed, Elaine J. Soar, Angela Oatridge, Ian R. Young, and Graeme M. Bydder. A registration and interpolation procedure for subvoxel matching of serially acquired MR images. *Journal of Computer Assisted Tomography*, 19(2):289–296, March/April 1995.
- [35] P. Harting. Le képhalographe: Nouvel instrument destiné à déterminer la figure et les dimensions du crane ou de la tête humaine. The University of Utrecht, 1861. The Képhalographe: A New Device for Determining the Shape and Dimensions of the Human Skull or Head.
- [36] G. H. Hartmann, W. Schlegel, V. Sturm, B. Kober, O. Pastyr, and W. J. Lorenz. Cerebral radiation surgery using moving field irradiation at a linear accelerator facility. *International Journal of Radiation, Oncology, Biology, Physics*, 11:1185–1192, 1985.

## BIBLIOGRAPHY

---

- [37] R. C. Hawkes, G. N. Holland, W. S. Moore, and B. S. Worthington. *Journal of Computer Assisted Tomography*, 4:577, 1980.
- [38] M. D. Heifetz, M. Wexler, and R. Thompson. Single-beam radiotherapy knife: A practical theoretical model. *Journal of Neurosurgery*, 60:814–818, 1983.
- [39] J. Hennig. Multiecho imaging sequences with low refocusing flip angles. *Journal of Magnetic Resonance*, 78:397–407, 1987.
- [40] J. Hennig, A. Nauerth, and H. Friedburg. RARE imaging: A fast imaging method for clinical MR. *Magnetic Resonance in Medicine*, 3:823–833, 1986.
- [41] Derek L. G. Hill, David J. Hawkes, Michael J. Gleeson, Tim C. S. Cox, Anthony J. Strong, Wai-Lup Wong, Clifford F. Ruff, Neil Kitchen, David G. T. Thomas, John E. Crossman, Colin Studholme, Advait J. Gandhe, Sandra E. M. Green, and Glynn P. Robinson. Accurate frameless registration of MR and CT images of the head: Applications in surgical and radiotherapy planning. *Radiology*, 191:447–454, 1994.
- [42] Derek L. G. Hill, David J. Hawkes, Zahid Hussain, Sandra E. M. Green, Clifford F. Ruff, and Glynn P. Robinson. Accurate combination of CT and MR data of the head: Validation and applications in surgical and therapy planning. *Computerized Medical Imaging and Graphics*, 17(4/5):357–363, July–October 1993.
- [43] Derek L. G. Hill, Calvin R. Maurer, Jr., Robert J. Maciunas, John A. Barwise, J. Michael Fitzpatrick, and Matthew Y. Wang. Measurement of intraoperative brain surface deformation under a craniotomy. *Neurosurgery*, 43(3):514–526, September 1998.
- [44] M. A. Horsefield, M. L. Lai, S. L. Webb, G. J. Barker, P. S. Tofts, R. Turner, P. Rudge, and D. H. Miller. Apparent diffusion coefficients in benign and secondary progressive multiple sclerosis by nuclear magnetic resonance. *Magnetic Resonance in Medicine*, 36:393–400, 1996.
- [45] Victor Horsley and Richard H. Clarke. The structure and functions of the cerebellum examined by a new method. *Brain*, 31:45–124, 1908.
- [46] D. I. Hoult. The solution of the Bloch equations in the presence of a varying  $B_1$  field – an approach to selective pulse analysis. *Journal of Magnetic Resonance*, 35:69–86, 1979.
- [47] A. M. Houseman, M. K. Stehling, B. Chapman, R. Coxon, R. Turner, R. J. Ordidge, M. G. Cawley, P. Glover, P. Mansfield, and R. E. Coupland. Improvements in snap-shot nuclear magnetic resonance imaging. *British Journal of Radiology*, 61(729):822–888, 1988.

## BIBLIOGRAPHY

---

- [48] J. Iizuka. Development of a stereotactic endoscopy of the ventricular system. *Confina Neurologica*, 37:141–149, 1975.
- [49] Peter Jezzard and Robert S. Balaban. Correction of geometric distortion in echo planar images from  $B_0$  field variations. *Magnetic Resonance in Medicine*, 34:65–73, 1995.
- [50] Peter Jezzard, Alan S. Barnett, and Carlo Pierpaoli. Characterization of and correction for eddy current artifacts in echo planar diffusion imaging. *Magnetic Resonance in Medicine*, 39:801–812, 1998.
- [51] H. E. Johns and J. R. Cunningham. *The Physics of Radiology*. Charles Thomas, Illinois, fourth edition, 1983.
- [52] S. A. R. Kannenießer, Y. Wang, and E. M. Haacke. Geometric distortion correction of gradient echo images using dynamic time warping. In *Proceedings of the International Society for Magnetic Resonance in Medicine. Sixth Scientific Meeting and Exhibition*, page 573, Sydney, Australia, 1998.
- [53] D. M. Kean and M. A. Smith. *Magnetic Resonance Imaging. Principles and Applications*. William Heinemann Medical Books, London, 1986.
- [54] M. Kirschner. Die Punktionstechnik und die Electrokoagulation des Ganglion Gasseri. über <<gezielte>> Operationen. *Archiv der Klinische für Chirurgie*, 176:581–620, 1933.
- [55] Anil Kumar, Dieter Welti, and Richard R. Ernst. NMR fourier zeugmatography. *Journal of Magnetic Resonance*, 18:69–83, 1975.
- [56] K. K. Kwong, J. W. Belliveau, D. A. Chesler, I. E. Goldberg, R. M. Weisskoff, B. P. Poncelet, D. N. Kennedy, B. E. Hoppel, M. S. Cohen, R. Turner, H. M. Cheng, T. J. Brady, and B. R. Rosen. Dynamic magnetic resonance imaging of human brain activity during primary sensory stimulation. *Proceedings of the National Academy of Sciences of the United States of America*, 89:5675–5679, 1992.
- [57] P. C. Lauterbur. Image formation by induced local interactions: Examples employing nuclear magnetic resonance. *Nature*, 242:190–191, 1973.
- [58] D. LeBihan, E. Breton, D. Lallemand, P. Grenier, E. Cabanis, and M. Laval-Jeantet. MR imaging of intravoxel incoherent motions: Applications to diffusion and perfusion in neurological disorders. *Radiology*, 161:401–407, 1986.
- [59] Lars Leksell. A stereotactic apparatus for intercerebral surgery. *Acta Chirurgica Scandinavica*, 99:229–233, 1949.
- [60] Lars Leksell. Cerebral radiosurgery. 1. gammathalamotomy in two cases of intractable pain. *Acta Chirurgica Scandinavica*, 134:585–595, 1968.

## BIBLIOGRAPHY

---

- [61] Louis Lemieux and Roger Jagoe. Effect of fiducial marker localization on stereotactic target coordinate calculation in CT slices and radiographs. *Physics in Medicine and Biology*, 39(11):1915–1928, November 1994.
- [62] K. M. Lüdeke, P. Röschmann, and R. Tischler. Susceptibility artifacts in NMR imaging. *Magnetic Resonance Imaging*, 3(4):329–343, 1985.
- [63] Robert J. Maciunas, Robert L. Galloway, Jr., and Jim W. Latimer. The application accuracy of stereotactic frames. *Neurosurgery*, 35(4):682–695, October 1994.
- [64] Peter Mansfield. Multi-planar image formation using NMR spin-echoes. *Journal of Physics C*, 10:L55–L58, 1977.
- [65] Peter Mansfield and Barry Chapman. Active magnetic screening of gradient coils in NMR imaging. *Journal of Physics E*, 15:235–239, 1986.
- [66] Peter Mansfield and P. K. Grannell. NMR 'diffraction' in solids? *Journal of Physics C*, 6:L422–L426, 1973.
- [67] Paul Margosian, Franz Schmitt, and David Purdy. Faster MR imaging: Imaging with half the data. *Health Care Instrumentation*, 1:195–197, 1986.
- [68] R. Mathur-De Vré. The NMR studies of water in biological systems. *Progress in Biophysics and Molecular Biology*, 35:103–134, 1979.
- [69] Calvin R. Maurer, Jr., George B. Aboutanos, Benoit M. Dawant, Srikanth Gadamsetty, Richard A. Margolin, Robert J. Maciunas, and J. Michael Fitzpatrick. Effect of geometrical distortion correction in MR on image registration accuracy. *Journal of Computer Assisted Tomography*, 20(4):666–679, 1996.
- [70] Calvin R. Maurer, Jr., J. Michael Fitzpatrick, Matthew Y. Wang, Robert L. Galloway, Jr., Robert J. Maciunas, and G. S. Allen. Registration of head volume images using implantable fiducial markers. *IEEE Transaction in Medical Imaging*, 16:447–462, 1997.
- [71] Calvin R. Maurer, Jr., Derek L. G. Hill, Alastair J. Martin, Haiying Liu, Michael McCue, Daniel Rueckert, David Lloret, Walter A. Hall, Robert E. Maxwell, David J. Hawkes, and Charles L. Truwit. Investigation of intraoperative brain deformation using a 1.5-T interventional MR syetem: Preliminary results. *IEEE Transactions on Medical Imaging*, 17(5):817–825, October 1998.
- [72] S. Meiboom and D. Gill. Modified spine echo method for measuring nuclear relaxation times. *Rev. Sci. Instr.*, 29:688–691, 1958.

## BIBLIOGRAPHY

---

- [73] Johan Michiels, H. Bosmans, P. Pelgrims, D. Vandermeulen, J. Gybels, G. Marchal, and P. Suetens. On the problem of geometric distortion in magnetic resonance images for stereotactic neurosurgery. *Magnetic Resonance Imaging*, 12(5):749–765, 1994.
- [74] Johan Michiels, H. Bosmans, D. Vandermeulen, P. Suetens, G. Marchal, and A. L. Baert. An overview of geometric distortion in fast MR images. In *Scientific Program and Book of Abstracts. ESMRMB '96 13<sup>th</sup> Annual Meeting*, volume 4, page 164, June 1996. MAG\*MA Supplement.
- [75] M. A. Moerland, R. Beersma, R. Bhagwandien, H. K. Wijrdeman, and C. J. G. Bakker. Analysis and correction of geometric distortions in 1.5 T magnetic resonance images for use in radiotherapy treatment planning. *Physics in Medicine and Biology*, 40(10):1651–1664, October 1995.
- [76] Paul S. Morgan, Richard W. Bowtell, and Brian S. Worthington. Correction of distortion in three dimensional MR volume image sets. In *Proceedings of the International Society for Magnetic Resonance in Medicine. Fifth Scientific Meeting and Exhibition*, page 2022, Vancouver, B.C., Canada, 12<sup>th</sup>–18<sup>th</sup> April 1997.
- [77] Paul S. Morgan, Richard W. Bowtell, and Brian S. Worthington. Quantification of the effect of spatial distortion from various MR sequences on errors in stereotaxy. In *Proceedings of the International Society for Magnetic Resonance in Medicine. Fifth Scientific Meeting and Exhibition*, page 50, Vancouver, B.C., Canada, 12<sup>th</sup>–18<sup>th</sup> April 1997.
- [78] Paul S. Morgan, Yao T. Ng, Dominick J. O. McIntyre, Brian S. Worthington, and Richard W. Bowtell. Comparison of two methods for correction of geometric distortion in echo planar images. In *Scientific Program and Book of Abstracts. ESMRMB '96 13<sup>th</sup> Annual Meeting*, volume 4, page 163, June 1996. MAG\*MA Supplement.
- [79] Peter G. Morris. *Nuclear Magnetic Resonance Imaging in Medicine and Biology*. Oxford University Press, 1986.
- [80] M. E. Moseley, Y. Cohen, J. Mintorovitch, L. Chileuit, H. Shimizu, J. Kucharczyk, M. F. Wendland, and P. R. Weinstein. Early detection of regional cerebral ischemia in cats: Comparison of diffusion- and  $T_2$ -weighted MRI and spectroscopy. *Magnetic Resonance in Medicine*, 14:330–346, 1990.
- [81] Moriel NessAiver. *All You Really Need to Know About MR Physics*. Simply Physics, Baltimore, MD, USA, 1997.
- [82] Yao T. Ng. *Magnetic Field Effects in Echo Planar Imaging at 3T*. PhD thesis, Nottingham University, 1998.

## BIBLIOGRAPHY

---

- [83] Yao T. Ng, Paul S. Morgan, Dominick J. O. McIntyre, Brian S. Worthington, and Richard W. Bowtell. Comparison of two methods for correction of geometric distortion in echo planar images. In *Proceedings of the International Society for Magnetic Resonance in Medicine. Fourth Scientific Meeting and Exhibition*, page 1603, New York, N.Y., U.S.A., 27<sup>th</sup> April – 3<sup>rd</sup> May 1996.
- [84] S. Ogawa, T. M. Lee, A. R. Kay, and D. W. Tank. Brain magnetic resonance imaging with contrast dependent on blood oxygenation. *Proceedings of the National Academy of Sciences of the United States of America*, 87:9868–9872, 1990.
- [85] R. J. Ordidge et al. *Magnetic Resonance in Medicine*, 10:227, 1989.
- [86] D. Ottoson. *Physiology of the Nervous System*. Macmillan, London, 1983.
- [87] Wilder Penfield and E. Boldrey. Somatic motor and sensory representation in the cerebral cortex of man as studied by electrical stimulation. *Brain*, 60:389–443, 1937.
- [88] C. Picard, A. Olivier, and G. Bertrand. The first human stereotactic apparatus: The contribution of Aubrey Mussen to the field of stereotaxis. *Journal of Neurosurgery*, 59:673–676, 1983.
- [89] B. P. Poncelet, V. J. Wedeen, R. M. Weisskoff, and M. S. Cohen. Brain parenchyma motion: Measurement with cine echoplanar MR imaging. *Radiology*, 185:645–651, 1992.
- [90] Manfred G. Prammer, John C. Haselgrove, Meir Shinnar, and John S. Leigh. A new approach to automatic shimming. *Journal of Magnetic Resonance*, 77:40–52, 1988.
- [91] W. H. Press, S. A. Teukolsky, W. T. Vetterling, and B. P. Flannery. *Numerical Recipes in Fortran: The Art of Scientific Computing*. Cambridge University Press, second edition, 1992.
- [92] W. G. Proctor and F. C. Yu. The dependence of a nuclear magnetic resonance frequency upon chemical compound. *Physics Review*, 77(5):717, March 1950.
- [93] E. M. Purcell, H. C. Torrey, and R. V. Pound. Resonance absorption by nuclear magnetic moments in a solid. *Physics Review*, 69:37–38, January 1946.
- [94] John R. Reitz, Frederick J. Milford, and Robert W. Christy. *Foundations of Electromagnetic Theory*. Addison-Wesley, third edition, 1979.
- [95] T. Riechert and F. Mundinger. Beschreibung und Anwendung eines Zielgerätes für stereotaktische Hirnoperationen (II. Modell). *Acta Neurochirurgica*, 3:308–337, 1955. Supplement.

## BIBLIOGRAPHY

---

- [96] T. Riechert and M. Wolff. Die technische Durchführung von gezielten Hirnoperationen. *Archiv für Psychiatrie und Zeitschrift Neurologie*, 190:297–316, 1953.
- [97] T. S. Roberts and R. Brown. Technical and clinical aspects of CT-directed stereotaxis. *Applied Neurophysiology*, 43:170–171, 1980.
- [98] Janet S. Ross and Kathleen J. W. Wilson. *Anatomy and Physiology in Health and Illness*. Churchill Livingstone, seventh edition, 1990.
- [99] G. Rossolimo. Zur Symptomatologie und chirurgischen Behandlung einer eigentümlichen Grosshirncyste Deutsche Zeitschrift für Nervenheilkunde. 6:76–94, 1895.
- [100] Lothar Schad, Sam Lott, Franz Schmitt, Volker Sturm, and Walter J. Lorenz. Correction of spatial distortion in MR imaging: A prerequisite for accurate stereotaxy. *Journal of Computer Assisted Tomography*, 11(3):499–505, May/June 1987.
- [101] F. Schmitt, M. K. Stehling, and R. Turner. *Echo-Planar Imaging: Theory, Technique, and Application*. Springer-Verlag, 1998.
- [102] K. Sekihara, M. Kuroda, and S. Matsui. Image restoration from non-uniform magnetic field influence for direct Fourier NMR imaging. *Physics in Medicine and Biology*, 29(1):15–24, 1984.
- [103] K. Sekihara, S. Matsui, and H. Kohno. A new method of measuring static-field distribution using modified Fourier NMR imaging. *Journal of Physics E*, 18(3):224–227, 1985.
- [104] K. Sekihara, S. Matsui, and H. Kohno. NMR imaging for magnets with large nonuniformities. *IEEE Transactions on Medical Imaging*, 4:193–199, December 1985.
- [105] E. A. Spiegel, H. T. Wycis, M. Marks, and A. J. Lee. Stereotactic apparatus for operations on the human brain. *Science*, 106:349–350, 1947.
- [106] Colin Studholme, Derek L. G. Hill, and David J. Hawkes. Using voxel similarity as a measure of medical image registration. In *Proceedings of the British Machine Vision Conference*, pages 235–244, 1994.
- [107] Thilaka S. Sumanaweera, Gary H. Glover, Paul F. Hemler, Petra A. van den Elsen, David Martin, John R. Adler, and Sandy Napel. MR geometric distortion correction for improved frame-based stereotactic target localization accuracy. *Magnetic Resonance in Medicine*, 34:106–113, 1995.
- [108] Thilaka S. Sumanaweera, Gary H. Glover, S. M. Song, John R. Adler, and Sandy Napel. Quantifying MRI distortion in tissue. *Magnetic Resonance in Medicine*, 31:40–47, 1994.

## BIBLIOGRAPHY

---

- [109] J. Talairach, H. Hecan, M. David, M. Monnier, and J. de Ajuriaguerra. Recherches sur la coagulation thérapeutique des structures sous-corticales chez l'homme. *Revue Neurologique*, 81:4–24, 1949. Research on Therapeutic Coagulation in the Human sub-cortical Regions.
- [110] D. G. Taylor and M. C. Bushell. The spatial mapping of translational diffusion coefficients by the NMR imaging technique. *Physics in Medicine and Biology*, 30:345–349, 1985.
- [111] D. G. Taylor, R. Inamdar, and M.-C. Bushell. NMR imaging in theory and in practice. *Physics in Medicine and Biology*, 33(6):635–670, 1988.
- [112] David G. T. Thomas, editor. *Stereotactic and Image Directed Surgery of Brain Tumours*. Churchill Livingstone, 1993.
- [113] R. Turner. Gradient coil design: A review of methods. *Magnetic Resonance Imaging*, 11:903–920, 1993.
- [114] A. M. Ulug, N. Beauchamp, R. N. Bryan, and P. C. M. van Zijl. Absolute quantitation of diffusion constants in human stroke. *Stroke*, 28(3):483–490, 1997.
- [115] Marcel van Herk and Hanne M. Kooy. Automatic three-dimensional correlation of CT-CT, CT-MRI, and CT-SPECT using chamfer matching. *Medical Physics*, 21(7):1163–1178, July 1994.
- [116] R. M. Weisskoff and T. L. Davis. Correcting gross distortion on echo planar images. In *Proceedings of the SMRM. 11<sup>th</sup> Annual Meeting*, page 4515, Berlin, 1992.
- [117] D. J. Werring, C.A. Clark, G. J. Barker, D. H. Miller, G. J. M. Parker, M. J. Brammer, E. T. Bullmore, V. P. Giampietro, and A. J. Thompson. The structural and functional mechanisms of motor recovery: Complementary use of diffusion tensor and functional magnetic resonance imaging in a traumatic injury of the internal capsule. *Journal of Neurology, Neurosurgery and Psychiatry*, 65:863–869, 1998.
- [118] Jay West, J. Michael Fitzpatrick, Matthew Y. Wang, Benoit M. Dawant, Calvin R. Maurer, Jr., Robert M. Kessler, Robert J. Maciunas, Christian Barillot, Didier Lemoine, André Collignon, Frederik Maes, Paul Suetens, Dirk Vandermeulen, Petra A. van den Elsen, Sandy Napel, Thilaka S. Sumanaweera, Beth Harkness, Paul F. Hemler, Derek L. G. Hill, David J. Hawkes, Colin Studholme, J. B. Antoine Maintz, Max A. Viergever, Gregoire Malandain, Xavier Pennec, Marilyn E. Noz, Gerald Q. Maguire, Jr., Michael Pollack, Charles A. Pelizzari, Richard A. Robb, Dennis Hanson, and Roger P. Woods. Comparison and evaluation of retrospective inter-modality brain image registration techniques. *Journal of Computer Assisted Tomography*, 21(4):554–566, 1997.

## BIBLIOGRAPHY

---

- [119] H. Rodney Withers. Biological basis of radiation therapy for cancer. *The Lancet*, 339:156–159, 18<sup>th</sup> January 1992.